Dynamics in Cold Atomic Gases: Resonant Behaviour of the Quantum Delta-Kicked Accelerator and Bose-Einstein Condensates in Ring Traps

PAUL LEE HALKYARD

Dynamics in Cold Atomic Gases: Resonant Behaviour of the Quantum Delta-Kicked Accelerator and Bose-Einstein Condensates in Ring Traps

Paul Lee Halkyard

A thesis submitted in partial fulfilment
of the requirements for the degree of
Doctor of Philosophy

Department of Physics
Durham University

15^{th} October, 2010

Dynamics in Cold Atomic Gases: Resonant Behaviour of the Quantum Delta-Kicked Accelerator and Bose-Einstein Condensates in Ring Traps

Paul Lee Halkyard

Abstract

In this thesis, the dynamics of cold, trapped atomic gases are investigated, and the prospects for exploiting their nonlinear dynamics for inertial sensing are discussed.

In the first part, the resonant and antiresonant dynamics of the atom-optical quantum delta-kicked accelerator with an initial symmetric momentum distribution are considered. The system is modeled as an ideal, non-interacting atomic gas, with a temperature-dependence governed by the width of the initial momentum distribution. The existence of resonant and antiresonant behaviour is established, and analytic expressions describing the dynamics of momentum moments of the time-evolved momentum distribution are derived. In particular, the momentum moment dynamics in both the resonant and antiresonant regimes depend strongly on the width of the initial momentum distribution. The resonant dynamics of all even-ordered momentum moments are shown to exhibit a power-law growth with an exponent given by the order of the moment in the zero-temperature regime, whereas for a broad, thermal initial momentum distribution the exponent is reduced by one. The cross-over in the intermediate regime is also examined, and a characteristic time is determined up to which the system exhibits dynamics associated with the zero-temperature regime. A similar analysis is made for the temperature-dependence of the antiresonant dynamics. This general behaviour is demonstrated explicitly by considering a Maxwell-Boltzmann and uniform momentum distribution, allowing exact expressions describing the dynamics of the second- and fourth-order momentum moments, and momentum cumulants, to be obtained. The relevance of these results to the potential of using this system in accurate determinations of the local gravitational acceleration is discussed.

In the second part, the dynamics of one- and two-component Bose-Einstein Condensates prepared in a counter-rotating superposition of flows in a quasi-1D toroidal trap are studied. Particular attention is paid to the dynamical stability of the initial state in the presence of atom-atom interactions, included via a mean-field description within the Gross-Pitaevskii equation. A broad regime of dynamical stability using a two-component BEC is identified, in which a typical implementation using ^{87}Rb is predicted to lie. A proof-of-principle Sagnac atom-interferometer using a two-component ^{87}Rb BEC is then presented, and the accumulation of the Sagnac phase is shown to be possible via relative pop-

ulation measurement or, alternatively, through the continuous monitoring the precession of atomic density fringes. In contrast to conventional Sagnac interferometers, the accumulation of the Sagnac phase is independent of the enclosed area of the interferometer. The prospects of using this system for high-precision determinations of rotation is discussed.

Declaration

I confirm that no part of the material offered has previously been submitted by myself for a degree in this or any other University. Where material has been generated through joint work, the work of others has been indicated.

Paul Lee Halkyard
Durham, November 25, 2010

Preface

This thesis is structured as follows:

Part I is concerned with the study of quantum delta-kicked accelerators. Chapters 1-3 are mostly comprised of introductory material, which can be found in Refs. [1, 2]. Original results are presented in Chapters 4 and 5, the majority of which are contained in the publications [3, 4]. The work regarding fractional resonances contributed to the publication [5].

Part II presents work on one- and two-component Bose-Einstein Condensates in quasi-1D toroidal traps. Chapters 7 and 8 consist of introductory material, and Chapter 8 contains original work, resulting in the publication [6].

Acknowledgements

First and foremost, I must thank my supervisor Simon Gardiner. His support, mentorship, and encouragement has been deeply appreciated, and I am tremendously grateful to have had been given the opportunity to work for him, and to have benefited from his patient (often very patient!) efforts to help me develop into a better scientist. Simon's door has rarely been closed, and I have been fortunate enough to have enjoyed many enlightening, and often impromptu, discussions with him, as well as being the recipient of his often well-timed and thoughtful advice.

I am also extremely grateful to my co-supervisor Ifan Hughes, with whom I have also shared many and long, valuable discussions, and who's deep physical intuition has always amazed me. I have greatly benefited from many coffee-time discussions with Ifan on a range of general physics, and will miss such conversations in the future.

Much of science is a collaborative effort, and the work in this thesis is no exception. The first part was completed in collaboration with Mark Saunders and Katharine Challis, whilst Matt Jones who had a large input into the work of the second part. I am very grateful to have worked with all three, and thank them for their valuable contributions.

I am also grateful for all the varied, useful and stimulating discussions with the members of Durham AtMol, particularly Charles Adams, Simon Cornish, Ulrich Krohn, Alexandre Gauguet, Mark Bason, James Millen, and Jon Pritchard. I am grateful for discussions with Vernon Armitage from Durham Mathematics Department.

I must also thank my office-mates Steven Wrathmall, Tom Billam, and Mark

Saunders for not only stimulating, but often wildly meandering conversation, which will always be fondly misremembered.

Work and life are never as well-separated as perhaps many of us would like them to be, and sometimes life's events can begin to overtake us. Without the help, encouragement, and support of the Halkyards, the Rowes, the Browns, and the Cleasbys, I could not have kept up.

Finally, I thank my parents for encouraging me to go this far, and my wife Elizabeth for her ceaseless love and support, my keystone without whom all would have fallen.

Contents

Part I

AOKAs/AOKRs

Chapter 1

Introduction

1.1 Motivation

The study of the atom has motivated a plethora of discoveries in modern physics. It was the consideration of the structure of elemental hydrogen that first led Niels Bohr to formulate what is now referred to as "old quantum theory"[7]. These early ideas later developed into modern quantum mechanics, arguably one of the most successful theories in modern physics.

The ramifications of these first considerations are still being explored today. Aided by recent advancements in laser cooling and magnetic and optical trapping [2, 8–11], it is now possible to trap relatively small samples of particular species of cold atoms and ions in highly-controllable environments. Generally, such environments consist of magnetic and electric fields, and light fields. Each of these can be controlled with great precision, in a time-dependent fashion if required, to create the conditions desired for the study of interest [1, 12]. Local inertial effects can be altered by using drop-towers [13], parabolic flight-paths [14, 15], and turntables [15, 16]; indeed, even the interaction of atoms with other atoms can be predictably altered by the exploitation of Feshbach resonances [17–21]. With such exquisite control, it is possible to perform fundamental tests in physics [22–24], precision measurements of the atoms and their environment [25], and explore new areas of science such as quantum information science [26], quantum simulation [27], and aspects of chaos theory [28, 29].

1.2 Classical Chaos

Chaos theory is concerned with the dynamics of non-integrable, deterministic systems, and the properties that are at the root of their characteristic behaviour [28, 30–33]. By definition, a deterministic system has a known rule, often expressed as an iterative map, that will produce the full dynamics from some initial condition. Therefore, it is tempting to believe that, with sufficient computing power[1], and a complete knowledge of some state at an instant in time, it is possible to completely determine the past and future dynamics. This deterministic philosophy is optimistically expressed in a quote by Laplace [34]:

> Given for one instant an intelligence which could comprehend all the forces by which nature is animated and the respective situation of the beings who compose it - an intelligence sufficiently vast to submit these data to analysis - it would embrace in the same formula the movements of the greatest bodies of the universe and those of the lightest atom; for it, nothing would be uncertain and the future, as the past, would be present before its eyes.

It is now known that this deterministic view of the universe is false [28, 32, 35, 36]. There are some classes of systems where the predicted dynamics rapidly deviate from the observed dynamics despite an overall governance by a deterministic rule, no matter how well-known the starting point. In such systems, the dynamics can be so unpredictable that they appear random; such is the degree of complexity that these systems are described as chaotic.

The apparent failure to obey a deterministic rule may be explained by considering the propagation of uncertainty (round-off error, for example) from one iteration to the next. In any calculation, there is always some inherent uncertainty, but its mere existence is not enough to ensure that chaotic dynamics ensue. Rather, the critical issue is the response of the system due to this uncertainty.

Chaos in classical mechanics is commonly examined using trajectories in a dimensionless position-momentum phase space (expressed in action-angle variables). In a regular system, i.e. non-chaotic, a set of similar initial conditions will spawn a bundle of trajectories that will closely follow one another. In a

[1] In reality, the computing power required for a typical many-body system would be unfeasibly large, but this is irrelevant to this discussion.

chaotic system, this bundle rapidly diverges to fill all of the energetically accessible phase space; it quickly becomes impossible to associate a given trajectory with an initial condition. In fact, what is is termed an initial condition is arbitrary, and it is enough that two or more diverging trajectories pass sufficiently close to each other at some instant of time for a long-term prediction to be unfeasible, since it would not be possible to distinguish them at all times. This strong exponential dependence on propagation error is called *sensitivity to initial conditions* [37].

It must be stressed that this divergence cannot be avoided with any finite amount of computing power, because trajectories in chaotic systems diverge exponentially. Consequently, a large increase in computational resources can always be outdone by a modest increase in observation time.

The sensitivity of the trajectories to initial conditions is often cited as a prerequisite for chaos. However, this is often invoked as an operational requirement, since there is no single, universally accepted definition of chaos [38]. A conceptually pleasing definition of chaos is Devaney's definition [39], which includes sensitivity to initial conditions as a manifestation of more fundamental, topological properties [40].

Unlike chaotic dynamics, where bundles of trajectories become inexorably tangled, regular dynamics are associated with motion along invariant tori in phase space, which are assigned a winding number denoting the ratio of the angular frequencies of the angular coordinates. For the dynamics to be constrained to surfaces of tori, a system with N degrees of freedom must have N independent constants of motion so that trajectories in the $2N$-dimensional phase space are restricted to a N-dimensional subspace. Systems that satisfy this requirement are called integrable, and tend to comprise of one or two degrees of freedom. One of the few integrable systems with three degrees of freedom or more is the Toda lattice [28, 41].

Systems with many degrees of freedom tend to contain fewer symmetries, and, courtesy of Noether's theorem [42], contain fewer constants of motion; it is unsurprising then that these systems display chaotic dynamics. It is therefore of great interest that similarly complex dynamics arise from systems with only few degrees of freedom. Indeed, some authors specify that a chaotic system must be relatively simple [32], i.e., it must be composed of one or two degrees of freedom, and possibly include a time-dependence of some sort [31, 35]. Moreover, such

systems may become chaotic with the addition of a small perturbation, and the availability of this kind of adjustment allows the onset of chaos to be investigated. Models which are susceptible to this methodology serve as valuable paradigms in the study of chaos.

1.3 The Classical Kicked-Rotor

The kicked-rotor[2] is one such important paradigm of chaos [28], and has been extensively studied over the last few decades [43–47]. It describes a constrained mass, free to rotate without friction, subjected to periodic driving by some constant vector-force[3]. Although the periodic force is instantaneous the impulse imparted to the system is finite. The Hamiltonian for the classical kicked-rotor is,

$$H = \frac{J^2}{2I} + \kappa \cos(\theta) \sum_{j=-\infty}^{\infty} \delta(t - nT) \tag{1.1}$$

where J and θ are the canonically conjugate angular momentum and angle, respectively, κ is the stochasticity parameter (or kicking strength), T is the kick-period, and I is the moment of interta of the constrained mass.

Although there is not general analytic solution for the dynamics of the kicked-rotor, it is possible to derive the kick-to-kick dynamics, i.e. as a kick-to-kick mapping of one of the phase space trajectories. This discrete-time solution is given by the mapping [28, 29, 31],

$$\begin{aligned} J_{n+1} &= J_n + \kappa \sin(\theta_n) \\ \theta_{n+1} &= \theta_n + J_n, \end{aligned} \tag{1.2}$$

where J_n and θ_n are the dimensionless angular momentum and its canonically conjugate angle, respectively, at the n-th iteration, with $I = T = 1$. The mapping (1.2) is known as the Standard Map [28, 44], so-called because of its applicability as a local description in a wide range of chaotic systems.

There is a rectilinear equivalent of the kicked-rotor that extends over the whole real line, namely the kicked-particle, whose kick-to-kick dynamics are still prescribed by the Standard Map. For the kicked-particle, it is appropriate to consider the linear momentum and its canonical conjugate position in lieu of J

[2] Also known as the kicked-rotator.

[3] A force of constant magnitude and unchanging orientation.

and θ, respectively. To emphasise, the underlying phase spaces are identical, but the physical manifestations of the dynamics are different.

Figure 1.1 shows phase space portraits for certain values of the stochasticity parameter, κ, using the Standard Map. For weak kicking, the trajectories form orbits through the phase space, and the dynamics appear predictable. As the kicking strength increases, tori with rational winding numbers (which, for systems with few spatial dimensions correspond to circular trajectories) are destroyed, whilst those corresponding to irrational numbers are preserved as dictated by KAM theorem [31]. These latter tori have irrational winding numbers, and correspond to quasi-periodic motions in which small perturbations tend to average out over many cycles. Chaos manifests between the preserved tori (called KAM tori), but trajectories spawned in the chaotic regions are confined to this small volume of phase space. Essentially, the chaotic dynamics are sandwiched between islands of regular orbits associated with the existence of fixed points. Rigourously, it has been shown that the last KAM torus, with a winding number equal to the golden ratio, is destroyed for $\kappa \approx 0.971635$, resulting in global mixing of initially well-separated trajectories [45]. Mixing of this kind is demonstrated in Fig. 1.1(b). For very strong kicking, small islands of stability corresponding to quasi-periodic motions may emerge over narrow ranges of κ, but most of the phase space is overwhelmingly chaotic.

The transition to chaos is an interesting topic in its own right, but the relevant point here is that varying degrees of chaos may arise from a simple physical system, depending on the adjustment of a single parameter, and such systems may serve to allow universal aspects of chaotic dynamics to be uncovered. Additionally, when chaos does manifest it allows the unbounded growth of momentum since the whole phase space becomes mixed. Well into the chaotic regime, the kick imparted to the rotor may be modelled as being uniformly distributed on $[-\kappa, \kappa]$. The resultant trajectories may be interpreted as diffusing through phase space on a random walk, leading to the well-known result that the mean kinetic energy of a classical ensemble increases linearly.

1.3.1 Accelerator Modes

The apparently random diffusion of trajectories through phase space may seem to be the only behaviour a system can exhibit far into the chaotic regime, especially if one examines only the phase spaces in Fig. 1.1 with large κ. A typical

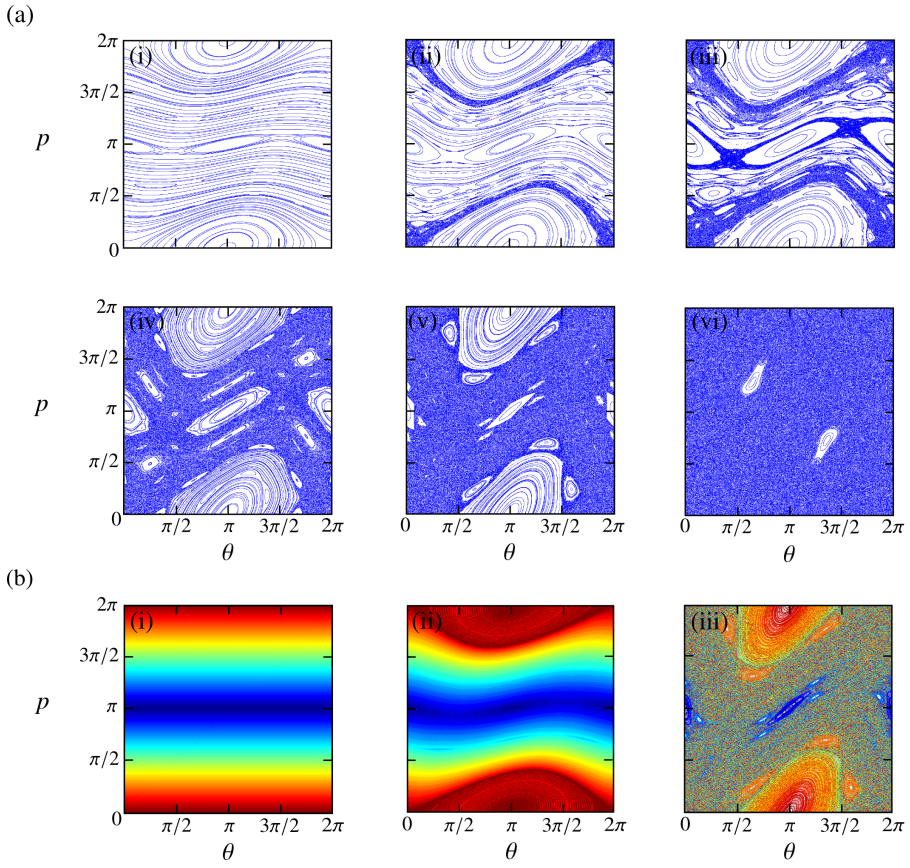

Figure 1.1: Typical phase spaces for the kicked-rotor generated by iterating the standard map with the stochasticity parameter set as (a) (i) $\kappa = 0.4$, (ii) $\kappa = 0.8$, (iii) $\kappa = 0.971635$, (iv) $\kappa = 1.2$, (v) $\kappa = 1.6$, and (vi) $\kappa = 5$. For weak kicking strengths, panels (i) and (ii) demonstrate that regular dynamics, observed as orbits, dominate the dynamics. As the kicking strength increases, chaos emerges as regions of densely-packed, disconnected trajectories constrained to small regions of phase space. Panel (iii) corresponds to the critical value of κ corresponding to the destruction of the last KAM torus [45]. Panels (iv-vi) show that progressively stronger kicking results in global chaos, with islands of stability centered on fixed points that become less frequent. Panel (b)(i) shows families of unperturbed trajectories corresponding to $\kappa = 0$, identified by a colour, and uses them as initial conditions for (ii) $\kappa = 0.4$ and (iii) $\kappa = 1.6$, to demonstrate that initially well-separated trajectories become strongly mixed in the chaotic regions. Panels (a)(i) and (a)(v) are directly comparable to panels (b)(ii) and (b)(iii), respectively.

signature of this occurring is that the momentum growth scales as $\sqrt{n}$, where n is the kicknumber (number of kicks). However, for special initial conditions, the momentum may scale linearly with n. Orbits which exhibit this property are known as accelerator modes [28], and occur only in the chaotic regime. For example, choosing $K = 2\pi$, $x_0 = \pi/2$, and $p_0 = 0$, and iterating the Standard Map for n kicks gives $p \sim n$; subsequently, the kinetic energy grows quadratically in time.

Initial conditions spawned near accelerator modes surrounded by stable periodic orbits may also undergo similar growth. Commonly, nearby trajectories are described as "sticking" to the accelerator mode, thereby gaining energy quadratically, before returning to diffusive behaviour [48]. Such dynamics may occur infrequently, and diffusive trajectories can be interrupted by large, but shortlived, momentum growth, resulting in behaviour described as Lévy flights [31]. Dynamics of this sort further encourage momentum transport, and are unique to chaotic dynamics.

1.3.2 Observing Chaos

As aforementioned, systems with more than two degrees of freedom are generally not integrable, and most systems have at least some chaotic character, the degree of which depends on the parameters defining the system. Despite the small number of dimensions, these systems typically defy analytic solutions except in some cases [49]. Many initial theoretical studies are numerical experiments, especially in the light of the fact there is no test of integrability. Although chaotic dynamics are ubiquitous in the natural world, the inherent complexity of chaotic systems makes physical realisations difficult; observing chaos is straightforward, but exerting a high-degree of control over a chaotic system, which is highly susceptible to small perturbations, is not.

Fortunately, the field of atom-optics presents itself as a means to observe chaos in physical systems, and at at the same time enforce a high-degree of control. The ability to trap ensembles of cold atoms in well-characterised, isolated environments where their mutual interactions can be reduced so much as to be negligible, and the precise control over the laser light comprising the fields, permits direct investigations of chaotic dynamics. The added complication, however, is that the atoms can be cooled to such a degree that their de Broglie is comparable to the interatomic separation, leading to prominent quantum effects. Such

investigations under these conditions do not probe classical chaos, but, rather, they probe *quantum chaos*.

1.4 Quantum Chaos

Quantum chaos [29, 48, 50–52] is concerned with the pursuit of chaos in quantum systems. A common approach is to study classically chaotic systems that have been canonically quantised[4]. At first glance, it may seem to be a distinct avenue to the investigation into classical chaos. On the contrary, the correspondence principle dictates that classical mechanics must be recovered in some limit of quantum mechanics. Quantum mechanics is more general than classical mechanics, which is seen to be a consequence of the former. As such, the quantum counterparts of classically chaotic systems must somehow contain the essential ingredients for chaos to manifest. Much work has been done in this area (See Ref. [53] and references therein), but the problem of quantum-classical correspondence is still not resolved fully.

In light of this, quantum systems whose classical counterparts exhibit chaos may be used as test cases, where chaos is thought, somehow, to be a common feature. In attempting to describe the origin of chaos in quantum systems, the hope is that understanding of quantum-classical correspondence will be yielded.

Frequently, however, the systems of choice exhibit such interesting behaviour that they merit study in their own right. Owing to its prominence in classical chaos, the kicked-rotor again takes a central role, and has been a paradigm of quantum chaos since the field's inception.

As already stated, a related system is the quantum delta-kicked particle (QDKP), and is often more applicable than its rotor equivalent because of the nature of the physical implementations. The Hamiltonian for the QDKP is,

$$\hat{H} = \frac{\hat{p}^2}{2M} - \kappa \cos(K\hat{z}) \sum_{j=-\infty}^{\infty} \delta(t - jT), \tag{1.3}$$

where $\hat{p}$ and z are the quantised momentum and position, respectively, and M is the mass. The equation of motion for this Hamiltonian is the time-dependent Schrödinger equation (TDSE), which is linear in the wavefunction, and admits a superposition principle which guarantees well-behaved trajectories. In contrast,

[4]Canonical quantisation refers to the process by which canonical momenta and position coordinates are exchanged for their Heisenberg equivalents.

chaos is associated with non-linear systems where there is no superposition principle. Consequently, the wavefunction in the TDSE cannot exhibit chaos in the sense described above. Moreover, the evolution of the wavefunction is unitary, which guarantees than the 'separation' of the initial states, i.e. the overlap, is a constant of the motion; thus, there can be no sensitivity to initial conditions in the same way as for classical chaos. Furthermore, the evolution of states cannot be represented in a momentum-position phase space since single-particle trajectories are prohibited by the Heisenberg uncertainty principle, and the phase-space picture developed above is not directly applicable[5]. It is still conceptually useful to consider the underlying classical phase space, and instead imagine the dynamics of a distribution of trajectories.

It is important to note that the wavefunction is never directly observed, rather, one observes expectations of operators, calculated using the wavefunction. An equivalent equation is the Heisenberg equation, which describes the evolution of observables. This may take a nonlinear form, and so it not correct to say that the linearity of the TDSE prohibits chaos arising in these systems. The important point, rather, is that the chaotic behaviour of the underlying classical system manifests itself differently when one considers phase space distributions. Indeed, a much related field is that of wave chaos [33].

An extra complication in quantum chaos is the requirement to obey Heisenberg Uncertainty. This prohibits meaningful structures below scales of order $\hbar^N$ (for N degrees of freedom), and so the self-similar structures that are ubiquitous in classical chaos [33] do not appear below these scales. Furthermore, the distributions of initial states that are considered in quantum chaos are distributions of probability amplitudes, which allows interference phenomena to participate. Therefore, the dynamics of the quantised system can be expected to be quite different from its classically chaotic counterpart.

It is often stated that the term "quantum chaos" is a misnomer, since there is no sensitive dependence to initial conditions in the wavefunction, and to avoid confusion some prominent researchers advocate the usage of "quantum chaology" to make the distinction between classical chaos, and its manifestation in quantum systems [55, 56]. Others resolve this ambiguity by defining different categories of chaos [29]. In all cases, however, the distinction is an arbitrary

[5]Some quasi phase-space distributions do exist, and are extensively used to examine systems in quantum chaos, but the choice of distribution depends on the objectives of the study [54].

one if we accept that the origin of chaos may be more fundamental that its original observations in classical systems would seem to suggest. Therefore, although quantum systems do not exhibit chaos in the conventional sense, they do have unique properties not seen in quantum systems with no classically chaotic counterpart. The nature of this more general chaos means that the tools and concepts of classical chaos are not directly applicable. The modus operandi, then, when studying quantum chaos is to examine *signatures* of quantum chaos [29, 35].

1.5 Signatures of Quantum Chaos

1.5.1 Energy Level Statistics

One of the mostly commonly mentioned signatures of quantum chaos are related to the energy level distribution of the quantised classical system [29, 35]. At first, if a quantum system is thought to exhibit chaos, it might be expected that its energy level structure would demonstrate large disorder, and essentially appear random. The consequence of such an assumption is that the separation of nearest-neighbour energy levels tend to cluster, with a probability distribution that exponentially decreases with energy. However, this expectation is false, and one instead observes energy level repulsion.

Wigner resolved this with the introduction of random matrix theory [29, 57–59]. The concept behind random matrix theory in quantum chaos postulates that, since quantum mechanics can be formulated in terms of matrices, it might be reasonable to replace the operators of quantised chaotic systems with operators that have have minimal coherence, i.e. maximal entropy, but with the correct symmetry and transformation properties [59]. The predicted nearest-neighbour distribution was called the Wigner distribution, and correctly predicted energy level repulsion. However, in order to properly characterise the energy level statistics of a system, many energy levels are needed. Originally, these methods were applied to the energy levels of heavy nuclei and atoms, but the advent of precision atomic physics, where single atoms could be confidently manipulated, allowed simpler systems to be investigated. These have included hydrogen atoms in strong magnetic fields [60]. These experiments involved the ionisation of hydrogen, which allowed the nearest-neighbour statistics of the energy levels to be computed. For experiments on neutral systems with a time-evolution, this

is clearly more difficult.

1.5.2 Dynamical Localisation

A second fingerprint of chaos is exemplified in the kicked-rotor. In the chaotic regime, strong stochasticity results in dynamics that are approximated by a random walk in phase space. Therefore, the mean kinetic energy of the ensemble grows linearly, and the system is said to be in the diffusive regime. In the quantum delta-kicked rotor (QDKR), the mean kinetic energy grows linearly until a quantum break time, after which quantum interference effects suppress the classically predicted chaotic diffusion. The eventual state is dynamically localised in momentum, and further kicks do not increase the mean kinetic energy of the ensemble. Soon after, a mapping was established [61] that described this phenomenon in terms of Anderson localisation [62], which describe the localisation of electron wavepackets in disordered lattices.

Dynamical localisation in the QDKR was first observed experimentally in the group of Raizen, whose experiments used pulsed standing-waves of light to periodically drive the atoms in a cold atomic gas. It had been proposed [63] and experimentally demonstrated [64, 65] that a standing wave of light could diffract atomic beams, thereby allowing momentum to be precisely imparted an atomic gas. These advances were used by the group of Raizen to demonstrate dynamical localisation of a diffracted atomic sample [66], and later these methods were suitably adapted in seminal experiments of the first atom-optics realisation of a delta-kicked rotor [67]. These experiments clearly showed dynamical localisation of the resulting atomic momentum distribution.

These experiments inspired a generation of research on dynamical localisation in the QDKR [68–76], which included the effects of dissipation and noise on the system. In general, it was found that the addition of amplitude noise or dissipation was to destroy dynamical localisation thereby demonstrating that it was indeed a quantum effect relying upon the coherent properties of its constituents.

1.5.3 Quantum Resonances

In some sense, dynamical localisation represents the default behaviour of the QDKR in the chaotic regime. However, it had been known since 1979 that for special kicking periodicities, one may observe the effect of quantum reso-

nances [46] whereby momentum growth is enhanced. Specifically, the momentum growth is linear, and should be observable as a quadratic increase in the kinetic energy of the ensemble. However, this effect was predicted for momentum eigenstates, and the temperature of these initial experiments was too high for these effects to properly resolved.

Shortly after the atom-optics realisation of the QDKR, the phenomenon of quantum antiresonance, and its link to dynamical localisation, was investigated theoretically [77]. Antiresonances describe the phenomenon of periodic revival of momentum expectation values, and for plane waves means that the wavefunction reconstructs periodically. Both quantum antiresonance and quantum resonance are quantum phenomena with no classical analogue, and it is therefore interesting that these occur in the chaotic regime of these systems.

A related phenomenon is the quantum accelerator mode, so-called in analogy with the classical accelerator modes. These occur close to quantum resonances, and also demonstrate enhanced momentum transfer. However, unlike quantum resonances, they only affect a portion of the atomic distribution, and leave most of the trapped sample otherwise unperturbed. The first observation of a quantum accelerator mode (then called referred to as anomalous diffusion) was again in the group of Raizen [78], and other studies soon followed [79–85].

Quantum resonances and antiresonances, on the other hand, affect the entire atomic sample, albeit to a varying degree. The limitations in the ability to obtain a sufficiently narrow momentum distribution meant that most experiments observed a linear increase in kinetic energy, and the observation of quadratic energy increase was not observed until 2000 when Oskay *et al* [86] were able to resolve the differences between resonant and antiresonant behaviour. However, this was quickly suppressed after approximately 10 kicks due the finite spread over momentum eigenstates in the initial atomic sample. In 2004 Duffy *et al* observed resonant and antiresonant behaviour in a BEC, but only for very low kick-numbers due to experimental limitations.

The first part of this thesis aims to investigate quantum resonances and antiresonances of the QDKR when the effect of finite-temperature is considered. The dynamics will be characterised in terms of the moments of the time-evolved momentum distribution, and the observation of linear kinetic growth in a finite-temperature regime will be explained, and a timescale over which ballistic growth would be observed is given. Furthermore, asymptotes of higher-order

moments will be derived, and the linear and quadratic growths seen in earlier experiments will be shown to be examples of a more general power-law behaviour. In particular, the dynamics of initially uniform and Gaussian momentum distributions for varying initial widths will be investigated, and exact expressions for the second-order and fourth-order momentum moments will be given, in both the resonant and antiresonant regimes.

Chapter 2

Review of Atom-Light Interactions

The development of atomic physics has relied heavily upon the availability of techniques to confine, cool, and manipulate dilute, atomic alkali gases. The mechanical effect of light on matter had been known a long time, but only since the 1960s has been it known that intensity gradients could exert forces upon atoms [87] and possibly trap them [88–90]. In 1975 these early ideas were brought to fruition, and Doppler cooling [91, 92] was proposed, so-named because it exploited the Doppler effect to selectively cool hot atoms. Later this technique was successfully used for manipulating atomic gases, and inspired a generation of research into bringing thermal atoms to rest [9].

Originally, cooling experiments were performed on atomic beams of sodium, since the hyperfine structure of sodium was well-known, and certain atomic transitions could be targeted with laser light. Unfortunately, atomic beams are inherently comprised of high-temperature atoms whose Doppler shifts become appreciably different as they slow. This necessitated the development of techniques to slow the constituent atoms such that they remained on resonance with the cooling light. With the development of chirp cooling [93–95] and Zeeman slowing [96], these difficulties were overcome. In the 1980s, optical molasses, where slowed thermal atoms are bathed in a viscous force provided by a 3D configuration of lasers, were implemented [97]. These innovations directly led to the discovery of sub-Doppler cooling mechanisms [98–102] and the construction of the first magneto-optical traps [103] (MOTs). These landmark develop-

ments allowed atoms to be cooled, confined, and coherently manipulated, thus beginning an era of ultracold atom-optics [9–12].

The work presented in this thesis tacitly assumes a laser-cooled, confined atomic gas as a starting point, and employs specially chosen laser-fields to induce desirable dynamical effects. A thorough understanding of the fundamentals behind laser-cooling and confining atoms is not required here, but it would be remiss to entirely neglect the methods used to bring about these crucial conditions.

In this chapter, the relevant physics behind the optical forces required to cool, and control, atoms will be summarised, following the treatments in Refs. [1, 12]. Firstly, the optical force between a non-interacting gas of atoms and a single laser beam will be introduced. This will necessitate a brief overview of the two-level description of the atom, which will suggest a decomposition of the optical force as the sum of a dipole force and a radiation pressure force, the latter of which can be made negligible under certain conditions. This important step will allow atoms in the light-field to be placed in a variety of tailored conservative potentials.

2.1 The Optical Force

A dilute atomic gas is considered to be isolated from its environment and addressed by a single laser beam. The light-field of the laser will be considered to be sufficiently populated in a single mode that it can be treated classically. In this classical picture, the atom-light interaction may be modelled as a deformation of a charge distribution by an electromagnetic wave. Using the Lorentz force law, the energy of the charge distribution is,

$$U = -\mathbf{d}\cdot\mathbf{E} - \mu\cdot\mathbf{B} + \ldots, \tag{2.1}$$

where $\mathbf{d}$ and μ are the electric- and magnetic-dipole moment, respectively, and where successively higher-order terms are negligible. The interaction energies can be estimated using first-order perturbation theory to imply,

$$\frac{\langle\mathbf{d}\cdot\mathbf{E}\rangle}{\langle\mu\cdot\mathbf{B}\rangle} = \frac{2}{\alpha} \approx 274, \tag{2.2}$$

where α is the fine structure constant. Thus, the dominant interaction with the atom is via the electric dipole moment, giving rise to a force whose expectation

is given by Ehrenfest's theorem [7, 104] as,

$$\langle \mathbf{F} \rangle = \langle \nabla(\mathbf{d} \cdot \mathbf{E}) \rangle. \tag{2.3}$$

A typical optical wavelength is of order 500nm, which is 100 times larger than the typical extent of an atom in low-lying electronic states. Consequently, the electric field varies little over the extent of the atom, and to a good approximation the induced atomic dipole can be considered to be pointlike. Thus, interpreting ∇ to act on the spatial part of the electric field, and taking the electric field to have the form $\mathbf{E} = \tilde{\mathbf{e}}E$, where $\tilde{\mathbf{e}}$ is the unit polarisation, implies

$$\langle \mathbf{F} \rangle = \langle (\hat{\mathbf{d}} \cdot \tilde{\mathbf{e}} \nabla E) \rangle. \tag{2.4}$$

For a rarefied gas, it is reasonable to assume that the external field due to the laser is much greater than the induced field of the atoms, and therefore the induced dipole is parallel to the electric field, giving,

$$\langle \mathbf{F} \rangle = \langle \hat{\mathbf{d}} \rangle \nabla E. \tag{2.5}$$

For a classical charge distribution, the dipole may be taken to be of the form $\mathbf{d} = \alpha \mathbf{E}$, where α is the permittivity of the charge distribution. Consequently, the force is

$$\mathbf{F}_{\text{Class}} = \alpha E \nabla E = \frac{\alpha}{2} \nabla E^2, \tag{2.6}$$

Therefore, the force on a charge distribution arising from the interaction of the electric dipole with the light-field varies with the gradient of the intensity of the electric field. In the case of atoms, the evaluation of the induced electric dipole moment is not so straightforward, and requires a quantum mechanical description. For simplicity, and to attain an understanding of the basic physics, the two-level model of the atom is used.

2.2 Two-Level Model of the Atom

2.2.1 Model Hamiltonian for an Atom in a Classical Light-Field

Alkali atoms have a single valence electron, which is convenient for a theoretical description. In addition, modern lasers have a well-known frequency and a narrow linewidth (< 100Mhz) compared to the hyperfine structure of the atom,

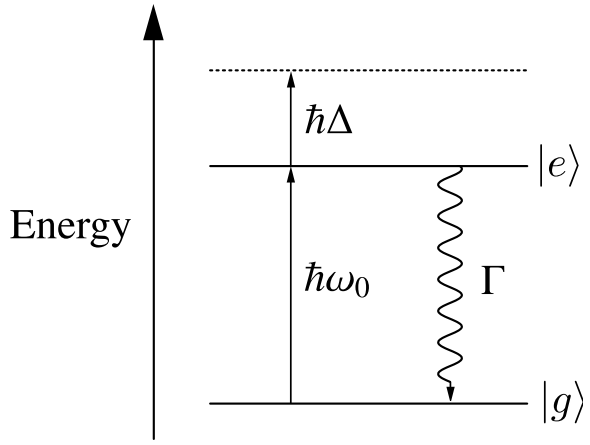

Figure 2.1: Under some circumstances, an atom may be modelled as a two-level system, with ground- and excited-states $|g\rangle$ and $|e\rangle$, respectively, with a transition frequency ω_0, and where the applied light-field may have a detuning Δ. Atoms in the excited state $|e\rangle$ spontaneously decay back to the ground state $|g\rangle$ at a characteristic rate Γ.

which essentially makes them monochromatic sources. Therefore, for two atomic levels with a closed transition, and an incident light-field having a frequency close to the transition frequency, an atom may be treated as a two-level system[1].

The corresponding Hamiltonian is taken to be of the form

$$\hat{H} = \hat{H}_0 + \hat{H}_{\text{int}} \tag{2.7}$$

where H_0 is the Hamiltonian for a single atom of mass M in some potential V, and $\hat{H}_{\text{int}}$ describes the atom-light interaction, with

$$\hat{H}_0 = \frac{\hat{p}^2}{2M} + \hat{V}_{\text{ext}} + \hbar\omega_0 \left[|e\rangle\langle e| - |g\rangle\langle g|\right], \tag{2.8}$$

where $\hbar\omega_0$ is the energy splitting between the ground state $|g\rangle$ and the excited state $|e\rangle$. Note that the zero of the potential has been implicitly set to coincide with the ground state. Since the electric dipole interaction dominates the atom-light interaction, $\hat{H}_{\text{int}} = -\mathbf{d}\cdot\mathbf{E}$, which leads to

$$\hat{H} = \frac{\hat{p}^2}{2M} + \hat{V}_{\text{ext}} + \hbar\omega_0 \left[|e\rangle\langle e| - |g\rangle\langle g|\right] - \hat{\mathbf{d}}\cdot\mathbf{E}. \tag{2.9}$$

In writing the Hamiltonian in this way, it is tacitly assumed that atom-atom interactions play no role. This can be a valid assumption for cold atom experiments, where the atomic gas can be made very dilute. In addition, where

[1]Note that a two-level description is inadequate when considering cooling mechanisms where polarisation plays a role, such as in the Sisyphus effect [9, 10]

the atomic density is high enough to play a role, the judicious exploitation of a Feshbach resonance, in principle, allows the s-wave scattering length, which governs the mutual interaction of cold atoms, to be tuned arbitrarily close to zero [19].

The electric field of the light-field is assumed to be,

$$\mathbf{E} = \hat{\mathbf{e}} E_0 e^{i(\theta - \omega t)}, \tag{2.10}$$

where ω is the angular frequency, $\mathbf{k}$ is the wavevector, and $\tilde{\mathbf{e}}$ is the unit polarisation vector. The parameter θ takes account for travelling waves, e.g., for a plane wave, $\theta = \mathbf{k} \cdot \mathbf{r}$. The electric dipole moment, $\hat{\mathbf{d}}$, is given by $\hat{\mathbf{d}} = -q\hat{\mathbf{r}}'$, where q is the electronic charge, and $\hat{\mathbf{r}}'$ represents the displacement of the charges and acts only in the Hilbert space spanned by $\{|g\rangle, |e\rangle\}$. The interaction Hamiltonian is then

$$\hat{H}_{\text{int}} = -qE_0 e^{i(\theta - \omega t)} \hat{\mathbf{r}}', \tag{2.11}$$

since the electric field and induced dipole have been assumed to be parallel. Using Eq. (2.11), Hamiltonian (2.9) becomes,

$$\hat{H} = \frac{\hat{p}^2}{2M} + \hat{V}_{\text{ext}} + \hbar\omega_0 \left[|e\rangle\langle e| - |g\rangle\langle g|\right] + \hbar\Omega e^{i(\theta - \omega t)} \left(|g\rangle\langle e| + |e\rangle\langle g|\right), \tag{2.12}$$

where the Rabi frequency $\Omega = -eE_0\langle e|\hat{r}|g\rangle/\hbar$ has been introduced. The Hamiltonian (2.12) is more conveniently expressed in the interaction picture as

$$\hat{H} = \frac{\hbar\Omega}{2} \left(e^{i\Delta t}|g\rangle\langle e| + e^{-i\Delta t}|e\rangle\langle g|\right), \tag{2.13}$$

where terms with angular frequencies $\omega_0 + \omega$ have been omitted using the rotating wave approximation.

2.2.2 Spontaneous Emission

So far, spontaneous emission has been omitted, and to include this effect it is convenient to use a density operator formalism. In this formalism, Eq. (2.12) is equivalent to

$$\frac{d\hat{\rho}}{dt} = \frac{i}{\hbar}[\hat{\rho}, \hat{H}]. \tag{2.14}$$

where $\hat{\rho}$ is the density operator. Equation (2.14) is known as Liouville's equation, and is exactly equivalent to the TDSE. The advantage of using Eq. (2.14)

in lieu of the TDSE is that spontaneous emission may be included as a phenomenological modification. With the necessary alteration, Eq. (2.14) becomes [105]

$$\frac{d\hat{\rho}}{dt} = \frac{i}{\hbar}[\hat{\rho}, \hat{H}] + \hat{L}(\hat{\rho}), \tag{2.15}$$

where, in matrix form,

$$\hat{L}(\hat{\rho}) = \begin{pmatrix} -\Gamma\rho_{ee} & -\Gamma\rho_{ge}/2 \\ -\Gamma\rho_{eg}/2 & \Gamma\rho_{ee} \end{pmatrix} \tag{2.16}$$

The diagonal terms of $\hat{L}(\hat{\rho})$ are chosen to ensure that the population of the excited state relaxes exponentially with a decay rate Γ, implying a corresponding increase in the ground state population. The coherences are modified so allow this choice to be consistent. For a two-state system with wavefunction,

$$|\psi\rangle = a|a\rangle + b|b\rangle, \tag{2.17}$$

the corresponding density operator in matrix form is given by,

$$\rho \equiv \begin{pmatrix} \rho_{gg} & \rho_{ge} \\ \rho_{eg} & \rho_{ee} \end{pmatrix} = \begin{pmatrix} |b|^2 & ba^\star \\ ab^\star & |a|^2 \end{pmatrix}. \tag{2.18}$$

The factor of $\Gamma/2$ can be roughly understood by considering the superposition state $|\psi\rangle$. If the objective is to introduce a decay of the excited state population at a rate Γ, then this may be achieved by $b \to b\exp(-\Gamma t/2)$. To retain the normalisation of the wavefunction, $a \to \sqrt{1 - |b|^2\exp(-\Gamma t)}$. Allowing $a = b = 1/\sqrt{2}$ for simplicity (and for normalisation), then the coherence is

$$\rho_{eg} = \rho_{ge} = \frac{1}{\sqrt{2}} e^{-\Gamma t/2}\left(1 - e^{-\Gamma t}\right)^{1/2}, \tag{2.19}$$

which, after some algebra, is written

$$\frac{\partial \rho_{eg}}{\partial t} = -\frac{\Gamma}{2}\rho_{eg} \tag{2.20}$$

Therefore, introducing a decay Γ to the excited state population in a coherent state introduces a decay of $\Gamma/2$ into the coherences, and one would expect this to continue to be true for statistical mixtures of coherent superposition states.

The Hamiltonian (2.12) can be expressed as

$$\hat{H}(\hat{\rho}) = \frac{\hbar}{2}\begin{pmatrix} 0 & \Omega e^{-i\Delta t} \\ \hbar\Omega e^{i\Delta t} & 2\Delta \end{pmatrix} \tag{2.21}$$

Using Hamiltonian (2.21) in the Liouville equation (2.15) implies

$$\frac{d\rho_{gg}}{dt} = -\frac{d\rho_{ee}}{dt} = \Gamma\rho_{ee} - \frac{i\Omega}{2}\left(\rho_{eg}e^{-i\Delta t} - \rho_{ge}e^{i\Delta t}\right) \tag{2.22a}$$

$$\frac{d\rho_g e}{dt} = \frac{d\rho^{\star}_{eg}}{dt} = -\frac{\Gamma}{2}\rho_{ge} + \frac{i\Omega}{2}\left(\rho_{gg} - \rho_{ee}\right)e^{-i\Delta t}. \tag{2.22b}$$

These are the optical Bloch equations [1, 104]. Equation (2.22) is subject to the constraints $\mathrm{Tr}(\hat{\rho}) = 1$ (following from unitarity of Eq. (2.14)) and $\hat{\rho}^{\dagger} = \hat{\rho}$ (following from the Hermiticity of the Hamiltonian (2.12)), which allows the system (2.22) to be reduced to a description with just three unknowns, chosen to be

$$u = \frac{1}{2}(\rho_{eg} + \rho_{ge}) \tag{2.23a}$$

$$v = \frac{i}{2}(\rho_{eg} - \rho_{ge}) \tag{2.23b}$$

$$w = \frac{1}{2}(\rho_{ee} - \rho_{gg}). \tag{2.23c}$$

In these new variables, the optical Bloch equations become [1],

$$\frac{du}{dt} = \Delta v - \frac{\Gamma}{2}u \tag{2.24a}$$

$$\frac{dv}{dt} = -\Delta u - \frac{\Gamma}{2}v + \Omega w \tag{2.24b}$$

$$\frac{dw}{dt} = -\Omega v - \Gamma(w - 1). \tag{2.24c}$$

The optical force in Eq. (2.5) represents an ensemble average, which is not well-described by the time-dependent dynamics of Eq. (2.24). Instead, using the fact that the solutions to Eq. (2.24) are oscillatory[2], and assuming that the dynamics of interest take place over many optical cycles, the average force can be shown to be equal to the force exerted in the steady-state. The steady-state solutions of Eq. (2.24) are

$$\tilde{u} = \frac{\Delta}{\Omega}\frac{S}{1+S} \tag{2.25a}$$

$$\tilde{v} = \frac{\Gamma}{2\Omega}\frac{S}{1+S} \tag{2.25b}$$

$$\tilde{w} = -\frac{1}{2}\frac{1}{1+S} \tag{2.25c}$$

where the saturation parameter S is given by,

$$S = \frac{2\Omega^2}{4\Delta^2 + \Gamma^2}. \tag{2.26}$$

The dipole expectation $\langle\hat{\mathbf{d}}\rangle$ can be expressed differently using the steady state solutions of the Optical Bloch Equation. In a density matrix formalism,

$$\langle\hat{\mathbf{d}}\rangle = \mathrm{Tr}(\hat{\rho}\hat{d}) = d_{eg}(\rho_{eg} + \rho_{ge}). \tag{2.27}$$

[2]This may be seen by solving Eq. (2.24) numerically.

using $d_{ee} = d_{gg} = 0$ and $d_{eg} = d_{ge}$. Using the above equation with Eq. (2.11), the steady state solutions (2.25), and transforming back into density matrix elements using Eq. (2.23), then the optical force on a two-level atom is revealed to be

$$\mathbf{F} = -\frac{\hbar}{2}\frac{S}{1+S}\left(\frac{\Delta}{\Omega^2}\nabla\Omega^2 - \Gamma\nabla\theta\right), \tag{2.28}$$

where the dependence on the properties of the light-field and the atom is now evident.

2.3 The Optical Force on a Two-Level Atom

2.3.1 The Dipole Force

The optical force has two contributions, with different dependencies on the system parameters. The first term in Eq. (2.28) represents the force due to the interaction of the electric field with the induced electric dipole moment in the atom. This is analogous to the classical dipole force on an atom, and is given by,

$$\mathbf{F} = -\frac{\hbar}{2}\frac{S}{1+S}\frac{\Delta}{\Omega^2}\nabla\Omega^2. \tag{2.29}$$

The dipole force is parallel to the gradient of the intensity of light (the intensity is proportional to Ω^2), with a direction determined by the sign of the detuning. For red-detuned light ($\Delta < 0$), the force is directed towards high-intensity regions, and vice versa for blue-detuned light. On resonance, there is no dipole force.

The degree of control over the light-fields used, both spatially and temporally, means that a wide range of tailored conservative potentials can be applied to an atomic gas. The dipole force is commonly used to create optical lattices [106], dipole traps, and to sculpt the effective potential in traps, such as in the case where blue-detuned "plug beams" were used in the first demonstrations of Bose-Einstein Condensation [107]. Other notable examples include time-averaged dipole traps that vary sufficiently rapidly that more exotic confining geometries, such as ring lattices, can be created [108].

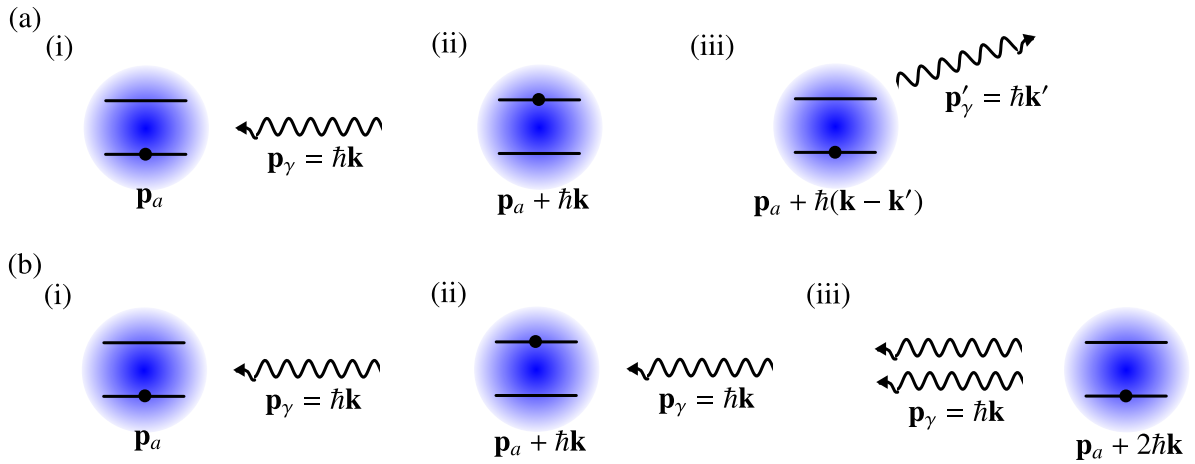

Figure 2.2: A semi-classical interpretation of the optical force: (a) A schematic of the scattering force, showing (i) a moving atom in a light-field, which (ii) absorbs a photon, followed by (iii) a spontaneous emission of a photon in a random direction. On average, the emission of photons perpendicular to $\mathbf{p}_\gamma$ cancel, and the momentum transfer can be essentially modelled by letting $\mathbf{k}' = \mathbf{k}$ or $\mathbf{k}' = -\mathbf{k}$ half of the time. On a shot-to-shot basis, however, the atom undergoes a random walk. (b) A schematic of the dipole force, where in juxtaposition to panel (a)(ii), the stimulated emission of a photon occurs resulting in (iii) a gain of $2\hbar\mathbf{k}$ to the momentum of the atom. For a pair of counter-propagating laser beams detuned so that oncoming atoms are Doppler-shifted to the red of the atomic resonance, the scattering force and the dipole force act as a frictional (dissipative) force and a restoring (conservative) force, respectively.

2.3.2 The Scattering Force

The second term in Eq. (2.28) is the radiation pressure or scattering force on the atom, and is given by,

$$\mathbf{F}_{\text{scatt}} = \frac{\hbar\Gamma}{2}\frac{S}{1+S}\nabla\theta. \tag{2.30}$$

This represents the force on the atom during the spontaneous emission of a photon. Spontaneous emission is a random process, and Eq. (2.30) is interpreted as an expectation of these events, and therefore represents an ensemble average. As such, it does not describe a single emission process (except probabilistically), and gives the average force after many emissions.

For a single beam, where $\theta = \mathbf{k}\cdot\mathbf{R}$, the scattering force becomes,

$$\mathbf{F}_{\text{scatt}} = \frac{\hbar\Gamma}{2}\frac{S}{1+S}\mathbf{k}. \tag{2.31}$$

In the limit of high-intensity, for which $\Omega^2 \gg \Delta^2$ and $\Omega^2 \gg \Gamma^2$, the saturation parameter S becomes large, and the scattering force rapidly saturates at the maximum force

$$\mathbf{F}_{\text{scatt,max}} = \frac{\hbar\Gamma}{2}\mathbf{k}. \tag{2.32}$$

Figure (2.2) considers the absorption of a photon of momentum $\hbar\mathbf{k}$, and its subsequent emission. After absorption, the atom recoils with additional momentum $\hbar\mathbf{k}$. After some characteristic time $1/\Gamma$, the atom relaxes, and emits a photon in a random direction. Since the direction of the spontaneous emissions is spherically distributed about the atom, and occur with a rate Γ, the atom will emit in the $-\mathbf{k}$ direction half of the time, gaining an overall additional momentum $2\hbar k$ on average. Similarly, emissions in the direction $\mathbf{k}$ return the atom to its initial momentum. Thus, on average, the atom gains $\hbar\mathbf{k}/2$ for each emission event, yielding the rate of momentum change (the force) as $\Gamma\hbar\mathbf{k}/2$.

For a standing wave configuration, $\theta = 0$, and the scattering force is zero; this is equivalent to having equal and opposite forces applied by two beams with $\theta = \mathbf{k}.\mathbf{R}$ and $\theta = -\mathbf{k}\cdot\mathbf{R}$. Therefore, the scattering force does not contribute to the net force in a standing wave (or an optical lattice). Importantly, however, the force is still present, and any emitted photons introduce dissipative effects. These emitted photons are not included in the model, but they can be intuitively understood to instigate a series of further absorption-emission events throughout the gas, resulting in a loss of coherence, and undesirable heating effects.

2.3.3 The Far-Detuned Limit

It is often desirable to maintain the coherence of a trapped sample, but the dissipative effect of the scattering force may seem to make this unachievable. Fortunately, the detuning presents itself as a parameter that can control the balance of the dipole and scattering forces. In the large detuning limit ($\Delta^2 \gg \Omega^2 \gg \Gamma^2$), the saturation parameter becomes

$$S_{\Delta^+} = \frac{\Omega^2}{2\Delta^2}, \tag{2.33}$$

implying that,

$$F_{\text{scatt},\Delta^+} = \frac{\hbar\Gamma\Omega^2}{4\Delta^2}\nabla\theta \tag{2.34a}$$

$$F_{\text{dip},\Delta^+} = -\frac{\hbar}{\Delta}\mathbf{4}\nabla\Omega^2. \tag{2.34b}$$

Equations (2.34) show that the scattering force diminishes more rapidly for large detunings than the dipole force. This has the consequence that the scattering force has a negligible contribution to the optical force for a far-off resonance light-field. Large detunings[3], therefore, allow the total optical force to be considered to be conservative. The average scattering force in the far-detuned limit [see Eq. (2.34)] corresponds to an absorption or emission rate of $\Gamma\Omega^2/4\Delta^2$ photons per second. In typical experiments, $\Gamma \approx 10$MHz, $\Omega \approx 1$MHz, and $\Delta \approx 10$GHz, which corresponds to less than one photon emission per second.

[3]For the force on the atoms to remain appreciable, there must be a concomitant increase in the light-intensity.

Chapter 3

Model System for the Atom-Optical Delta-Kicked Accelerator

The aim of this chapter is three-fold. Firstly, the Hamiltonian for a quantum delta-kicked accelerator (QDKA) will be derived from the perspective of an idealised atom-optical experiment. In this context the QDKA is often referred to as the atom-optical kicked accelerator (AOKA). This will assume the atoms to be sufficiently well-described within a two-level atom approximation, and will employ a judiciously chosen configuration of laser beams to arrive at the desired Hamiltonian.

The second objective will be to outline the derivation of the kick-to-kick time-evolution operator, namely, the Floquet operator. To do this, the system Hamiltonian will be transformed into a spatially-periodic form, allowing some simplifications to be made with Bloch theory. Notably, the concept of quasimomentum will be introduced, which will become important in later analyses.

Finally, the existence of quantum resonances in the Floquet operator will be brought to notice, and the resonant kick-to-kick dynamics of a momentum eigenstate will be shown.

The content of this chapter is a summary of existing work, and is included here for completeness and to place into context the original work that follows in later chapters. Further details can be found in refs. [3, 109].

3.1 Atom-Optical Delta-Kicked Accelerator

3.1.1 Model Hamiltonian

A laser-cooled gas of two-level atoms is considered to be initially confined in a MOT, and atom-atom interactions are assumed to be negligible. There are avenues of study that study the effect of atom-atom interactions in kicked-systems comprised of Bose-condensed atoms [110], but the focus of this work is on the temperature dependence of the dynamics. The atomic sample is treated as an ensemble of single-particle two-level systems with Hamiltonian

$$\hat{H} = \frac{\hat{p}^2}{2M} + \frac{1}{2}\hbar\omega_0 \left[|e\rangle\langle e| - |g\rangle\langle g|\right] + V(\hat{\mathbf{r}}, t) \tag{3.1}$$

where M is the mass of one atom, $|g\rangle$ and $|e\rangle$ are the ground- and excited-states respectively, ω_0 is the frequency difference between the two internal states, t is the time, $\hat{\mathbf{r}} = (\hat{x}, \hat{y}, \hat{z})$ is the centre of mass position operator with its conjugate momentum operator given by $\hat{p}$, and V is the external potential.

The atomic gas is then released from its confining potential, and is addressed by a vertically-oriented, sinusoidal potential formed by an appropriate configuration of counter-propagating laser-beams of similar frequency. The laser-beams are assumed to be sufficiently far-detuned that spontaneous emission may be neglected. Furthermore, degrees of freedom orthogonal to the laser-beams are considered to be unimportant in the ensuing dynamics; hence, the system is treated one-dimensionally along the axis of the laser beams. This is a direct consequence of neglecting atom-atom interactions, causing the wavefunction corresponding to $\hat{H}$ to be separable in x, y, and z, which, in turn, means that the dynamics in each degree of freedom can be individually determined. Within these considerations, the system Hamiltonian is

$$\begin{aligned}\hat{H} =& \frac{\hat{p}^2}{2M} + \frac{1}{2}\hbar\omega_0 \left[|e\rangle\langle e| - |g\rangle\langle g|\right] + mg\hat{z} \\ &+ \frac{1}{2}\hbar\Omega_1 e^{i(k_L\hat{z} - \omega_L t) + \phi_1}|e\rangle\langle g| + \frac{1}{2}\hbar\Omega_1 e^{-i(k_L\hat{z} - \omega_L t + \phi_1)}|g\rangle\langle e| \\ &+ \frac{1}{2}\hbar\Omega_2 e^{-i(k_L\hat{z} + \omega_L t + \phi_2)}|e\rangle\langle g| + \frac{1}{2}\hbar\Omega_2 e^{i(k_L\hat{z} + \omega_L t + \phi_2)}|g\rangle\langle e|\end{aligned} \tag{3.2}$$

where the two laser-beams have Rabi frequencies Ω_1 and Ω_2, phases ϕ_1 and ϕ_2, g is the local gravitational acceleration, and the wave-number k_L, and frequency ω_L of each beam is identical. Upon choosing the beams to have equal intensity

$\Omega = \Omega_1 = \Omega_2$, then

$$\begin{aligned}\hat{H} =& \frac{\hat{p}^2}{2M}\frac{1}{2}\hbar\omega_0\left[|e\rangle\langle e| - |g\rangle\langle g|\right] + Mg\hat{z} \\ &+ \hbar\Omega\cos(k_L\hat{z} + \phi_-)\left[|e\rangle\langle g|e^{-i(\phi_+ + \omega_L t)} + |g\rangle|e\rangle e^{i(\omega_L t + \phi_+)}\right],\end{aligned} \tag{3.3}$$

where $\phi_- = (\phi_1 - \phi_2)/2$ and $\phi_+ = (\phi_1 + \phi_2)/2$.

The explicit time-dependence of this Hamiltonian can be removed, and the zero-energy shifted to the atomic ground state, with the application of the unitary transformation

$$\hat{U}_1 = \exp\left(it[\omega_L|e\rangle\langle e| - \omega_0(|e\rangle\langle e| + |g\rangle\langle g|/2)]\right), \tag{3.4}$$

to give,

$$\hat{H} = \frac{\hat{p}^2}{2M} + Mg\hat{z} + \hbar\Delta|e\rangle\langle e| + \frac{1}{2}\hbar\Omega\cos(k_L\hat{z} + \phi_-)\left(e^{i\phi_+}|e\rangle\langle g| + e^{-i\phi_+}|g\rangle\langle e|\right), \tag{3.5}$$

where $\Delta = \omega_0 - \omega_L$ is the detuning from the atomic transition.

The effective gravitational acceleration experienced by the atoms may be altered by adjusting the phase of the counter-propagating lasers in a time-dependent way [5, 84, 111]. This causes the optical lattice, formed by the interference of the beams, to have a constant drift velocity, thereby imparting a net, vertically-oriented force on the atoms.

To achieve this, the phase difference of the beams, ϕ_- is chosen to be $\phi_- = k_L a_\phi t^2$ [5, 111]. To move into the frame accelerating with the walking wave, the unitary transformation

$$\hat{U} = \exp\left(i[Ma_\phi\hat{z}t - a_\phi\hat{p}t^2/2 + \zeta(t)]/\hbar\right), \tag{3.6}$$

is applied to Hamiltonian (3.5), and making use of $\hat{U}\hat{z}\hat{U}^\dagger = \hat{z} - a_\phi t^2/2$ and $\hat{U}\hat{p}\hat{U}^\dagger = \hat{p} - Ma_\phi t$, this yields the transformed Hamiltonian

$$\hat{H} = \frac{\hat{p}^2}{2M} + Ma\hat{z} + \hbar\Delta|e\rangle\langle e| + \frac{1}{2}\hbar\Omega\cos(k_L\hat{z})\left(|e\rangle\langle g| + |g\rangle\langle e|\right), \tag{3.7}$$

where $a = g - a_\phi$, and $\zeta(t) = Ma_\phi t^3(a_\phi - 2g)/12$ is imposed for algebraic convenience [5].

3.1.2 Adiabatic Elimination of the Excited State

In the limit of far-detuning, where $\Omega/\Delta \ll 1$, the population of the excited state changes negligibly. This is a consequence of high-frequency, low amplitude

oscillations of the excited- and ground-state populations close to their initial values. If, initially, the entire atomic population is in the ground state, then to a good approximation the excited state dynamics are unimportant, and may be removed using adiabatic elimination [49].

Adiabatic elimination is a mathematical procedure that expresses the solution to the two-level system as an asymptotic series in Ω/Δ, which, for large detunings, can be truncated to second order. Essentially, the procedure decouples the dynamics of the atomic levels, resulting in a different effective Hamiltonian for each atomic level. Since the system is assumed to begin entirely in the ground state, only the ground state Hamiltonian is relevant to the subsequent dynamics.

The adiabatic elimination is carried out in detail in Appendix A, and allows Hamiltonian (3.5) in the far-detuned limit to be reduced to

$$\hat{H} = \frac{\hat{p}^2}{2M} + Ma\hat{z} - \frac{\hbar\Omega^2}{8\Delta}\cos(K\hat{x}), \tag{3.8}$$

where $K = 2k_L$.

3.1.3 Introduction of a Delta-Kicked Potential

To construct a system to mimic the QDKA, the potential that the atoms experience must be time-modulated. This is achieved by periodically pulsing the 1-D lattice formed by the laser beams. The time required for the switching[1] is typically of order 1ns, and the inertia of the atoms is sufficiently high to ensure that there are no transient effects due to switching. Furthermore, the duration of the pulse is typically of order 100ns, which is short enough that the Raman-Nath approximation is valid. Such a pulse, or kick, will be modelled by a Dirac delta-function. Note that although the pulses are infinite, the impulse imparted by them is related to their norm, which is finite.

The effect of finite pulse duration is essentially to change the kicking strength experienced by the atoms; for long pulses, the kicking strength increases. Also, when the momentum of an atom is sufficiently high that atoms move over an appreciable lengthscale of the light-wave, the Raman-Nath approximation is no longer valid. Therefore, in experiments there is an upper bound on the momentum of the atoms before the model breaks down. Typically, this is approximately 60 photon recoils for sodium, and 200 photon recoils for Caesium [112]. There-

[1] For purely practical reasons, the lasers are not actually switched on and off, but are periodically blocked, which allows very short switching times.

fore, finite-pulse effects are expected to become important when considering the long-term dynamics of situations resulting in efficient momentum growth.

The pulse-train is introduced by modulating the lattice potential in Hamiltonian (3.8) as,

$$\hat{H} = \frac{\hat{p}^2}{2M} + Ma\hat{z} - \frac{\hbar\Omega^2}{8\Delta}\cos(K\hat{x})f(t) \tag{3.9}$$

with the dimensionless modulation function, $f(t)$, where,

$$f(t) = t_p \sum_{j=-\infty}^{\infty} \delta(t - jT). \tag{3.10}$$

The parameter t_p is chosen as the pulse duration of the corresponding, idealised square pulse, since these are closer to what will be used experimentally. Choosing t_p in this way ensures that the same impulse is imparted by the pulse as in the delta-kicked case.

Thus, the Hamiltonian corresponding to the AOKA is,

$$\hat{H} = \frac{\hat{p}^2}{2M} - \hbar\phi_d \cos(K\hat{z}) \sum_{n=0}^{\infty} \delta(t - nT) + Ma\hat{z}. \tag{3.11}$$

where $\phi_d = \Omega^2 t_p/8\Delta$. In accordance with the experiments performed in Oxford, ϕ_d is taken to be $\phi_d = 0.8\pi$

3.2 Derivation of the Floquet Operator

It is convenient to partition the dynamics of atom-optical kicked-accelerator into a kicked-part and a free-evolution part. The Hamiltonian for the free-evolution part is,

$$\hat{H} = \frac{\hat{p}^2}{2M} + Ma\hat{z}, \tag{3.12}$$

which, by standard methods, has the time-evolution operator,

$$\hat{E} = \exp\left[-it\left(\frac{\hat{p}^2}{2M} + Ma\hat{z}\right)/\hbar\right]. \tag{3.13}$$

The kicked-evolution may be determined by integrating the Schrödinger equation over a small interval of time around the n-th kick, occurring at time $t = nT$; this implies,

$$\int_{nT-\epsilon}^{nT+\epsilon} dt\hat{H}|\psi(t)\rangle = i\hbar \int_{nT-\epsilon}^{nT+\epsilon} dt \frac{d|\psi(t)\rangle}{dt}. \tag{3.14}$$

The left-hand side of Eq. (3.14) becomes,

$$\int_{nT-\epsilon}^{nT+\epsilon} dt\hat{H}|\psi(t)\rangle = \int_{nT-\epsilon}^{nT+\epsilon} dt \left[\frac{\hat{p}^2}{2M}|\psi(t)\rangle + Ma\hat{z}|\psi(t)\rangle \right.$$
$$\left. - \hbar\phi_d \cos(K\hat{z}) \sum_{n=-\infty}^{\infty} \delta(t-nT)|\psi(t)\rangle \right].$$

For small ϵ, the contributions from the $\hat{p}^2|\psi(t)\rangle$ and $\hat{z}|\psi(t)\rangle$ terms are negligible and only the term accompanying the delta-function contributes, yielding,

$$\lim_{\epsilon\to 0} \int_{nT-\epsilon}^{nT+\epsilon} dt\hat{H}|\psi(t)\rangle = -\hbar\phi_d \cos(K\hat{z})|\psi(nT)\rangle. \tag{3.15}$$

The right-hand side of Eq. (3.14) can be formally integrated to give,

$$i\hbar \int_{nT-\epsilon}^{nT+\epsilon} dt \frac{d|\psi(t)\rangle}{dt} = i\hbar \left(|\psi(nT+\epsilon)\rangle - |\psi nT-\epsilon\rangle \right). \tag{3.16}$$

The presence of the delta-kicks causes $\frac{d|\psi(t)\rangle}{dt}$ to contain an infinite discontinuity at $t = nT$. In the limit $\epsilon \to 0$, Eq. (3.16) describes the jump across the discontinuity. Now, if one reconsiders Eq. (3.14) with the kinetic energy and gravitational potential terms omitted, then the same jump will be obtained due to the kicking. Thus, with these same omissions in the TDSE, the change in the wavefunction across the discontinuity is given by the solution to,

$$\frac{d|\psi(t)\rangle}{dt} = \frac{i\phi_d}{2\epsilon} \cos(K\hat{z})|\psi(t)\rangle, \tag{3.17}$$

which has the solution,

$$|\psi(t)\rangle = \exp\left(\frac{i\kappa t}{2\epsilon\hbar} \cos(K\hat{z}) \right) |\psi(t_0)\rangle. \tag{3.18}$$

Noting that this is only valid in describing the wavefunction immediately before and after the kick, given by $|\psi^-\rangle$ and $|\psi^+\rangle$, respectively, then,

$$|\psi^+\rangle = \exp\left(i\phi_d \cos(K\hat{z}) \right) |\psi^-\rangle. \tag{3.19}$$

where the limit $2\epsilon = t \to 0$ has been taken. This reveals the kick-evolution operator to be,

$$\hat{K} = \exp\left(i\phi_d \cos(K\hat{z}) \right). \tag{3.20}$$

The free-evolution and the kick-evolution operators [Eqs. (3.13) and (3.20), respectively] may be combined to represent a kick-to-kick time evolution operator, given by

$$\hat{F} = \exp\left[-\frac{it}{\hbar} \left(\frac{\hat{p}^2}{2M} + Mg\hat{z} \right) \right] \exp\left(\frac{i\kappa}{\hbar} \cos(K\hat{z}) \right). \tag{3.21}$$

This time-evolution operator describes a single kick followed by a free-evolution. The time-evolution for n kicks, i.e., following an evolution for $t = nT$, is therefore,

$$\hat{\mathcal{F}}_n = \hat{F}^n. \tag{3.22}$$

The time-evolution operator (3.21) is an example of a Floquet operator, which is used to describe systems with discrete time-invariance, in analogy to Bloch theory in solid state physics.

3.2.1 Transformation into the Falling Frame

The repeated application of a spatially periodic potential, followed by free-evolutions, suggests that there is merit in transforming to a spatially periodic frame, where Bloch theory may be of use. The unitary transformation,

$$\hat{U}_2 = \exp\left(\frac{it}{\hbar} Ma\hat{z}\right) \tag{3.23}$$

may be used to transform the model Hamiltonian

$$\hat{H} = \frac{\hat{p}^2}{2M} + Ma\hat{z} - \hbar\phi_d \cos(K\hat{z}) \sum_{n=0}^{\infty} \delta(t - nT), \tag{3.24}$$

into the spatially periodic form,

$$\hat{H} = \frac{(\hat{p} - Mat)^2}{2M} - \hbar\phi_d \cos(K\hat{z}) \sum_{n=0}^{\infty} \delta(t - nT). \tag{3.25}$$

The transformation (3.23) introduces a non-trivial time-dependence to the Hamiltonian, and complicates the determination of its corresponding time-evolution operator, if direct methods were applied to Eq. (3.25). However, the time-evolution may be determined by applying the transformation (3.23) to the Floquet operator (3.21), to determine the transformed Floquet operator as $\hat{F}' = \hat{U}_2 \hat{F} \hat{U}_2^\dagger$.

In order to do this, it is first convenient to rewrite Eq. (3.21) so that the position- and momentum-dependent parts act separately. Using the identity

$$\exp\left(\left[a\hat{p}^2 + b\hat{z}\right] t\right) = \exp\left(a\hat{p}^2 t + i\hbar ab\hat{p}t^2 - \hbar^2 ab^2 t^3/3\right) \exp\left(bt\hat{z}\right), \tag{3.26}$$

it is found that [3, 109]

$$\hat{F}'(nT, (n-1)T) = \exp\left(-\frac{i}{\hbar}\left[\hat{p}^2 T/2M - \hat{p}a(2n-1)T^2/2\right]\right) \exp\left(i\phi_d \cos(K\hat{z})\right) \tag{3.27}$$

where $\hat{F}'$ has been redefined to include the global phase,

$$\exp\left(-iMa^2[3n^2-3n+1]T^3/6\hbar\right), \tag{3.28}$$

which is unimportant to any subsequent dynamics.

3.2.2 Bloch Theory

The time-evolution operator in Eq. (3.27) is spatially periodic, and allows Bloch theory [113] to be used. A useful conceptual picture in the theory of crystals, where Bloch theory is frequently used, is that of quasimomentum[2]. Bloch's theorem asserts that the system wavefunction can be described within the first Brillouin zone, determined by the periodicity of the system, up to a multiplicative plane wave, whose associated momentum is defined to be the quasimomentum. Thus, the wavefunction in other Brillouin zones is identical, up to a phase, and quasimomentum is said to be conserved from one zone to the next. Concisely, knowledge of the first Brillouin zone allows a complete determination of the system.

To exploit these concepts, it is convenient to decompose the momentum and position operators as,

$$\begin{aligned}\hat{p} &= \hbar K(\hat{k}+\hat{\beta})\\ \hat{z} &= \frac{1}{K}\left(2\pi\hat{J}+\hat{\theta}\right).\end{aligned} \tag{3.29}$$

for which the eigenvalues of $\hat{k}$ and $\hat{J}$ are integers, but the eigenvalues of $\hat{\beta}$ and $\hat{\theta}$ are continuous, and are given by $\beta \in [-1/2, 1/2)$ and $\theta \in [-\pi, \pi)$, respectively. The continuous momentum component, β, is called the quasimomentum, in analogy with Bloch theory. The quasimomentum operator can be shown [114, 115] to commute with Eq. (3.25), and is therefore conserved. Thus, $\hat{\beta}$ may be replaced by its eigenvalue β, and the momentum operator $\hat{p} = \hbar K(\hat{k}+\beta)$ may only act to couple momentum eigenstates having eigenvalues differing by an integer amount of $\hbar K$ [81]. Alternatively, the system does not act to mix initial states with different initial quasimomentum, and therefore one may consider the system to comprise of many non-interacting kicked-rotors.

Given this simplification, the Floquet operator corresponding to a particular quasimomentum subspace may be determined; by substituting the decomposi-

[2]Also known as crystal momentum.

tions Eq. (3.29) into the transformed Floquet operator Eq. (3.27), one obtains,

$$\hat{F}(\beta)_n = \exp\left(-\frac{i}{\hbar}\left[\hbar^2 K^2(\hat{k}+\beta)^2 T/2M - \hat{k}\beta a(2n-1)T^2/2\right]\right)\exp\left(i\phi_d\cos(\hat{\theta})\right). \tag{3.30}$$

3.2.3 Quantum Resonances and Antiresonances

The dynamics determined by repeated applications of the Floquet operator (3.30) may be quite different depending on the chosen parameters. Previous work has shown that when the time-period is chosen to be,

$$T = \ell\frac{T_T}{2} = \frac{2\pi M}{\hbar K^2}\ell \tag{3.31}$$

quantum antiresonances and resonances in the dynamics of the time-evolved state are observed [80]. The parameter T_T is called the Talbot time, in analogy with the Talbot effect in optics [116]. Related work exists where T is some rational multiple of the Talbot time, but these higher-order quantum resonances [117, 118] are not considered here.

With this choice of the time-period, Eq. (3.30) becomes,

$$\hat{F}_n(\beta) = e^{-i\pi[\beta\ell-\Omega(2n-1)]}e^{-i\pi[\ell-\Omega(2n-1)+2\ell\beta]\hat{k}}e^{i\phi_d\cos(\hat{\theta})}, \tag{3.32}$$

where $\Omega = KaT^2/2\pi$. Choosing ℓ to be an even integer, $\Omega = 0$, and $\beta = 0$ or $\beta = 1/\ell$ gives, and ignoring the unimportant global phase,

$$\hat{F}_n(\beta) = e^{i\phi_d\cos(\hat{\theta})}, \tag{3.33}$$

so that

$$\hat{\mathcal{F}}_n = \hat{F}^n = e^{ni\phi_d\cos(\hat{\theta})}. \tag{3.34}$$

Therefore, for this choice of parameters, repeated application of the Floquet operator is equivalent to one application with a kicking strength n times larger. This regime of reinforced growth is called a quantum resonance.

Similarly, for odd ℓ, and Ω and β one can also have,

$$\hat{F}_n^2(\beta) = \mathbb{1}. \tag{3.35}$$

Therefore, an even number of kicks will result in total reconstruction of the initial state, whereas an odd number will demonstrate the equivalent growth to a single kick. Such behaviour is described as antiresonant behaviour, and has been exploited as a means of splitting and recombining a wavepacket for interferometric purposes [119, 120].

3.3 Time-Evolution of a Single Momentum Eigenstate

The time-evolution of a general initial state governed by the Floquet operator (3.32) may be complicated. A sensible starting point is to consider an initial momentum eigenstate corresponding to a particular quasimomentum subspace. The time-evolution corresponding to n kicks is given by,

$$\hat{\mathcal{F}}_n(\beta) = \hat{F}_n(\beta)\hat{F}_{n-1}(\beta)\dots\hat{F}_1(\beta). \tag{3.36}$$

Therefore, for an initial momentum eigenstate $|k+\beta\rangle$, the evolved state is,

$$|\Psi(t=nT)\rangle = \hat{\mathcal{F}}_n(\beta)|k+\beta\rangle \tag{3.37}$$

which may be decomposed into the momentum basis as,

$$|\Psi(t=nT)\rangle = \sum_{j=-\infty}^{\infty} c_{kj}(\beta, nT)|j+\beta\rangle, \tag{3.38}$$

where the probability amplitudes are given by

$$c_{kj}(\beta, nT) = \langle j+\beta|\hat{\mathcal{F}}_n(\beta)|k+\beta\rangle. \tag{3.39}$$

3.3.1 Application of the transformed Floquet operators

Firstly, the effect of the Floquet operator for the n-th kick on a momentum eigenstate $|k+\beta\rangle$ will be determined. From Eq. (3.27)

$$\begin{aligned}\tilde{F}_n(\beta)|k+\beta\rangle =& \int_{-\infty}^{\infty} dz \tilde{F}_n(\beta)|z\rangle\langle z|k+\beta\rangle \\ =& e^{i[\pi(1+\beta)\ell - K\gamma_n]\beta}\int_{-\infty}^{\infty} dz e^{-i\hat{k}K\gamma_n}e^{i\phi_d\cos(K\hat{z})}|z\rangle\langle z|k+\beta\rangle,\end{aligned} \tag{3.40}$$

where

$$K\gamma_n \equiv \pi\left[(1+2\beta)\ell - \Omega\left(2n-1\right)\right]. \tag{3.41}$$

By using the displacement operation $\exp(-i\hat{k}K\gamma_n)|z\rangle = \exp(i\beta K\gamma_n)|z+K\gamma_n\rangle$, and using the position representation of a momentum eigenstate $\langle z|k+\beta\rangle = \sqrt{K/2\pi}\exp[i(k+\beta)Kz]$, it follows from Eq. (3.40) that

$$\hat{F}_n(\beta)|k+\beta\rangle = \sqrt{\frac{K}{2\pi}}e^{i\pi\beta(1+\beta)\ell}\int_{-\infty}^{\infty} dz|z+\gamma_n\rangle e^{i(k+\beta)Kz}e^{i\phi_d\cos(Kz)}. \tag{3.42}$$

The effect of a further kick is calculated in a similar fashion to obtain,

$$\begin{aligned}\tilde{F}_{n+1}(\beta)\tilde{F}_n(\beta)|k+\beta\rangle =& \sqrt{\frac{K}{2\pi}}e^{i2\pi\beta(1+\beta)\ell}\int_{-\infty}^{\infty} dz|z+\gamma_n+\gamma_{n+1}\rangle \\ &\times e^{i(k+\beta)Kz}e^{i\phi_d[\cos(Kz)+\cos(Kz+K\gamma_n)]}.\end{aligned} \tag{3.43}$$

Hence, the full time evolution of the initial momentum eigenstate, given by successive, time-ordered Floquet operators as $\tilde{\mathcal{F}}_n(\beta) = \tilde{F}_n(\beta)\tilde{F}_{n-1}(\beta)\ldots\tilde{F}_1(\beta)$, is

$$\begin{aligned}\tilde{\mathcal{F}}_n(\beta)|k+\beta\rangle =& \sqrt{\frac{K}{2\pi}} e^{in\pi\beta(1+\beta)\ell} \int_{-\infty}^{\infty} dz \left| z + \sum_{n'=1}^{n} \gamma_{n'} \right\rangle e^{i(k+\beta)Kz} \\ & \times \exp\left(i\phi_d \left[\cos(Kz) + \sum_{j=1}^{n-1} \cos\left(Kz + \sum_{j'=1}^{j} K\gamma_{j'} \right) \right] \right).\end{aligned} \tag{3.44}$$

3.3.2 Spatial representation

To proceed further, it is convenient to determine the position representation of Eq. (3.44):

$$\begin{aligned}\langle z|\tilde{\mathcal{F}}_n(\beta)|k+\beta\rangle =& \sqrt{\frac{K}{2\pi}} e^{in\pi\beta(1+\beta)\ell} e^{i(k+\beta)\left(Kz - \sum_{n'=1}^{n} K\gamma_{n'}\right)} \\ & \times \exp\left(i\phi_d \left[\cos\left(Kz - \sum_{n'=1}^{n} K\gamma_{n'} \right) \right.\right. \\ & \left.\left. + \sum_{j=1}^{n-1} \cos\left(Kz - \sum_{n'=1}^{n} K\gamma_{n'} + \sum_{j'=1}^{j} K\gamma_{j'} \right) \right] \right).\end{aligned} \tag{3.45}$$

Using the definition of $K\gamma_n$ in Eq. (3.41), it is found that

$$\sum_{n'=1}^{n} K\gamma_{n'} = n\pi\left[(1+2\beta)\ell - \Omega n\right], \tag{3.46}$$

with which Eq. (3.45) can be simplified, to yield

$$\begin{aligned}\langle z|\tilde{\mathcal{F}}_n(\beta)|k+\beta\rangle =& \sqrt{\frac{K}{2\pi}} e^{in\pi\beta(1+\beta)\ell} e^{i(k+\beta)(Kz-q_0)} \\ & \times \exp\left(i\phi_d \sum_{j=0}^{n-1} \cos(Kz - q_j) \right),\end{aligned} \tag{3.47}$$

where the definition $q_j \equiv (n-j)\pi\left[(1+2\beta)\ell - \Omega(n+j)\right]$ has been introduced for compactness. Finally, defining $\xi \equiv \sum_{j=0}^{n-1}\cos q_j$ and $\zeta \equiv \sum_{j=0}^{n-1}\sin q_j$, Eq. (3.47) further simplifies to

$$\begin{aligned}\langle z|\tilde{\mathcal{F}}_n(\beta)|k+\beta\rangle =& \sqrt{\frac{K}{2\pi}} e^{in\pi\beta(1+\beta)\ell} e^{i(k+\beta)(Kz-q_0)} \\ & \times e^{i\phi_d\xi\cos(Kz) + i\phi_d\zeta\sin(Kz)}.\end{aligned} \tag{3.48}$$

3.3.3 Probability amplitudes

The Jacobi-Anger identities [121] allow exponentials of cosines and sines to be rewritten in terms of Bessel functions as,

$$e^{ia\cos(bx)} = \sum_{j=-\infty}^{\infty} i^j J_j(a) e^{ijKx} \tag{3.49a}$$

$$e^{ia\sin(bx)} = \sum_{j=-\infty}^{\infty} J_j(a) e^{ijKx}. \tag{3.49b}$$

These identities permit Eq. (3.48) to be written more simply as

$$\langle z|\tilde{\mathcal{F}}_n(\beta)|k+\beta\rangle = \sqrt{\frac{K}{2\pi}} e^{in\pi\beta(1+\beta)\ell} e^{i(k+\beta)(Kz-q_0)} \sum_{j=-\infty}^{\infty} e^{ijKz} J_j(\omega) e^{ij\chi}, \tag{3.50}$$

where ω and χ are real and defined by $\omega e^{i\chi} \equiv \phi_d(i\xi+\zeta)$. To evaluate the matrix element

$$\langle j+\beta'|\tilde{\mathcal{F}}_n(\beta)|k+\beta\rangle = \sqrt{\frac{K}{2\pi}} \int_{-\infty}^{\infty} dz e^{-i(j+\beta')Kz} \langle z|\tilde{F}_n(\beta)|k+\beta\rangle, \tag{3.51}$$

Eq. (3.50) is substituted into Eq. (3.51) to yield

$$\begin{aligned}\langle j+\beta'|\mathcal{F}_n(\beta))|k+\beta\rangle =& e^{-i\pi n\alpha k} e^{-in^2\pi(k+\beta)\Omega} e^{-in\pi\beta^2\ell} \sum_{j'=-\infty}^{\infty} J_{j'}(\omega) \\ &\times e^{ij'\chi} \frac{K}{2\pi} \int_{-\infty}^{\infty} dz e^{i(k+j'-j+\beta-\beta')Kz},\end{aligned} \tag{3.52}$$

where $\alpha = (1+2\beta)\ell$.

The probability amplitudes may now calculated by considering the expansion

$$|\Psi(t=nT)\rangle \equiv \hat{\mathcal{F}}_n(\beta)|k+\beta\rangle = \sum_{j=-\infty}^{\infty} c_{kj}(\beta, nT)|j+\beta\rangle, \tag{3.53}$$

and realising that $c_{kj}(\beta, nT)$ are given by $c_{kj}(\beta, nT)\delta(\beta-\beta') = \langle j+\beta'|\hat{\mathcal{F}}_n(\beta)|k+\beta\rangle$. Evaluating the integral in Eq. (3.52), the probability amplitudes are determined to be

$$c_{kj}(\beta, nT) = J_{j-k}(\omega) e^{i(j-k)\chi} e^{-i\pi n\alpha k} e^{-in^2\pi(k+\beta)\Omega} e^{-in\pi\beta^2\ell}. \tag{3.54}$$

Note that the normalisation condition $\sum_{j=\infty}^{\infty} |c_{kj}(\beta, nT)|^2 = 1$ is satisfied. It is convenient to define $\phi_d\nu = \omega e^{i\chi}$, so that

$$\nu \equiv i\xi + \zeta = i\sum_{j=0}^{n-1} e^{-iq_j}. \tag{3.55}$$

Upon substitution of q_j into Eq. (3.55), it is found that

$$\nu = ie^{-i\pi(\alpha n - \Omega n^2)} \sum_{j=0}^{n-1} e^{i\pi(\alpha j - \Omega j^2)}. \tag{3.56}$$

The prefactor of the summation is a global phase, which is only relevant to the determination of χ. In turn, χ is irrelevant to the dynamics of a given initial state. Hence, this unimportant phase can be absorbed into the definition of ν, giving

$$\nu = \sum_{j=0}^{n-1} e^{i\pi(\alpha j - \Omega j^2)}, \tag{3.57}$$

The parameter ω may be determined via the magnitude $\eta \equiv |\nu| = |\omega|/\phi_d$. Finally, the time-evolution of an initial momentum eigenstate $|k+\beta\rangle$ following n kicks is revealed to be

$$|\Psi(t=nT)\rangle = \sum_{j=-\infty}^{\infty} J_{j-k}(\omega) e^{i(j-k)\chi} e^{-i\pi n\alpha k} e^{-in^2\pi(k+\beta)\Omega} e^{-in\pi\beta^2\ell} |j+\beta\rangle. \tag{3.58}$$

Chapter 4

Momentum Moment Dynamics for General Symmetric Initial Momentum Distributions

In the previous chapter, an idealised physical system whose dynamics are described by the QDKA was described, and it was shown how its Floquet operator can be used to determine the time-evolution of a momentum eigenstate. In this chapter, the dynamics of an initial momentum eigenstate will be described in terms of the moments of the resulting momentum distribution. This will be generalised to include initial distributions of momentum eigenstates. These calculations will motivate the importance of the Gauss sum ν to the dynamics, and will allow the regimes resulting in resonant or antiresonant behaviour to be identified. Lastly, the limiting behaviour of the momentum moments in the ultracold limit, and the broad momentum-width limit, will be calculated, in both the resonance and antiresonant regimes.

4.1 Momentum Moment Dynamics of Momentum Eigenstates

The result from the previous chapter shows how successive kicks repeatedly diffract the initial state, coupling a given momentum eigenstate before the kick to all other momentum eigenstates separated by $\hbar K$ after the kick. Hence, despite starting with a simple initial state, the dynamics soon become very complicated. For more general initial conditions, represented by distributions of momentum eigenstates, the evolved state will quickly become difficult to interpret. To describe the dynamics more straightforwardly, it is convenient to study statistical quantities of the evolving distribution, such as the moments.

The momentum expectation can be calculated from Eq.(3.58) to be

$$\langle \hat{p} \rangle_n = \langle \Psi(nT) | \hat{p} | \Psi(nT) \rangle = (\hbar K) \sum_{j=-\infty}^{\infty} J_{j-k}^2 [\phi_d \eta(n)](j+\beta). \tag{4.1}$$

which can be generalised straightforwardly to give the evolution of the m-th momentum moment as

$$\langle \hat{P}^m \rangle_n = \sum_{j=-\infty}^{\infty} J_{j-k}^2 [\phi_d \eta(n)](j+\beta)^m, \tag{4.2}$$

where $\hat{P} = \hat{p}/\hbar K$ is the dimensionless momentum.

4.1.1 Bessel Function Summations

The Bessel function summation in Eq. (4.2) must be computed in order to determine the momentum moment evolution. Firstly, the more compact notation

$$S_m(p,q) \equiv \sum_{j=-\infty}^{\infty} J_{j+p}(x) J_{j+q}(x) j^m, \tag{4.3}$$

is introduced, where the dependence of $S_m(p,q)$ on x will be left implicit. An immediate observation, using the identity $J_{-n}(x) = (-1)^n J_n(x)$, is

$$S_{2m+1}(0,0) \equiv \sum_{j=-\infty}^{\infty} j^{2h+1} J_j^2 \equiv 0, \tag{4.4}$$

and therefore all odd moments are zero at all times. Intuitively, this is a trivial result, and expected for a symmetric initial state driven by a symmetric potential when the centres of symmetry coincide.

The starting point for computing $S_m(p,q)$ for all values is the Bonêt recursion relation for Bessel functions [121]

$$J_{j-1}(x) + J_{j+1}(x) = \frac{2j}{x} J_j(x). \tag{4.5}$$

Squaring both sides of Eq. (4.5) yields

$$J_{j-1}^2(x) + J_{j+1}^2(x) + 2J_{j-1}(x)J_{j+1}(x) = \frac{4j^2}{x^2} J_j^2(x) \tag{4.6}$$

which may be multiplied by j^{2m-2}, rearranged, and summed over j:

$$\begin{aligned}\sum_{j=-\infty}^{\infty} j^{2m} J_j^2(x) =& \frac{x^2}{4} \sum_{j=-\infty}^{\infty} j^{2m-2} \left[J_{j-1}^2(x) + J_{j+1}^2(x)\right. \\ &\left. + 2J_{j-1}(x)J_{j+1}(x)\right].\end{aligned}$$

Using the definition Eq. (4.3), Eq. (4.7) may be rewritten as,

$$S_{2m}(0,0) = \frac{x^2}{2}\left[S_{2m-2}(-1,-1) + S_{2m-2}(1,1) + 2S_{2m-2}(-1,1)\right] \tag{4.7}$$

Neumann's addition theorem states that

$$\sum_{j=-\infty}^{\infty} J_j(x)J_{j+k}(y) = J_k(x-y), \tag{4.8}$$

where k is an integer. There are two relevant special cases, which occur when $x = y$, implying

$$\sum_{j=-\infty}^{\infty} J_j^2(x) = 1 \tag{4.9}$$

and, for $k \neq 0$,

$$\sum_{j=-\infty}^{\infty} J_j(x)J_{j+k}(x) = 0. \tag{4.10}$$

In the notation introduced in Eq. (4.3), this implies,

$$S_0(p,q) = \begin{cases} 1 & \text{if } |p = q| = 1 \\ 0 & \text{if } p \neq q. \end{cases} \tag{4.11}$$

and, consequently, for $m = 1$ Eq. (4.7) is reduced to

$$S_2(0,0) = \frac{x^2}{2}. \tag{4.12}$$

Leading-Order Growth

Higher-order summations may be determined by repeated substitution of the recursion identity (4.5); one may consider jJ_{j-k},

$$jJ_{j-k} = \frac{x}{2}\left(J_{j-k-1} + J_{j-k+1}\right) + kJ_{j-k} \tag{4.13}$$

substituted into $j^2 J_{j-k}$, to give,

$$\begin{aligned} j^2 J_{j-k} =& \frac{x}{2}\left(jJ_{j-k-1} + jJ_{j-k+1}\right) + jkJ_{j-k} \\ =& \left(\frac{x}{2}\right)^2 \left(J_{j-k-2} + 2J_j + J_{j-k+2}\right) + k\frac{x}{2}\left(J_{j-k-1} + J_{j-k+1}\right). \end{aligned} \tag{4.14}$$

Further such substitutions reveal that it is possible to render $j^m J_{j-p}$ in the form,

$$j^m J_{j-k} = \sum_{p=1}^{m} \left(\frac{x}{2}\right)^p \sum_{q=-p}^{p} a(p,q) J_{j-k-q}. \tag{4.15}$$

This may be simplified by restricting attention to even values of m only [see Eq. (4.4)], and selecting k to be zero[1]. Moreover, for even m, it may noticed that the index q, and therefore p, only takes even values. In addition, multiplying by J_j and summing over j reveals the general form of $S_{2m}(0,0)$ to be,

$$\sum_{j=-\infty}^{\infty} j^{2m} J_j^2 = \sum_{p=1}^{m} \left(\frac{x}{2}\right)^{2p} \sum_{q=-2p}^{2p} a(2p,2q) \sum_{j=-\infty}^{\infty} J_{j-2q} J_j. \tag{4.16}$$

The application of Eqs. (4.9) and (4.10) to Eq. (4.16) implies that only those terms for $q = 0$ contribute nonzero terms to the summation; consequently,

$$\sum_{j=-\infty}^{\infty} j^{2m} J_j^2(x) = \sum_{p=1}^{m} x^{2p} \frac{a(2p,0)}{2^{2p}} \equiv R_{2m}(x) \tag{4.17}$$

The crucial observation in Eq. (4.16) is that $S_{2m}(0,0)$ takes the form of an even polynomial with leading order x^{2m}. The leading-order coefficient is always nonzero, and may be determined explicitly as $(2m)!/(m!)^2 2^{2m}$. The generation of the coefficients $a(p,q)$ is possible, in principle, via a recursive procedure using the identities above; it is found that

$$\sum_{j=-\infty}^{\infty} j^2 J_j^2(x) = \frac{x^2}{2}, \tag{4.18}$$

and

$$\sum_{j=-\infty}^{\infty} j^4 J_j^2(x) = \frac{3x^4}{8} + \frac{x^2}{2}. \tag{4.19}$$

[1]This was required to be nonzero until now to allow the continued substitution of the rescursion relation (4.5) into $j^m J_j$.

m	x^2	x^4	x^6	x^8	x^{10}	x^{12}	x^{14}
1	$\frac{1}{2}$	0	0	0	0	0	0
2	$\frac{1}{2}$	$\frac{3}{8}$	0	0	0	0	0
3	$\frac{1}{2}$	$\frac{15}{8}$	$\frac{5}{16}$	0	0	0	0
4	$\frac{1}{2}$	$\frac{63}{8}$	$\frac{35}{8}$	$\frac{35}{128}$	0	0	0
5	$\frac{1}{2}$	$\frac{255}{8}$	$\frac{735}{16}$	$\frac{525}{64}$	$\frac{63}{256}$	0	0
6	$\frac{1}{2}$	$\frac{1023}{8}$	440	$\frac{21945}{128}$	$\frac{3465}{256}$	$\frac{231}{1024}$	0
7	$\frac{1}{2}$	$\frac{4095}{8}$	$\frac{65065}{16}$	$\frac{26025}{8}$	$\frac{36063}{128}$	$\frac{21021}{1024}$	$\frac{429}{2048}$

Table 4.1: Nonzero Coefficients of the polynomial $R_{2m}(x)$

Generating Higher-Order Summations

This tedious recursive procedure may be cast into a form more amenable to computational methods by considering

$$\begin{aligned} S_m(p,q) &\equiv \sum_{j=-\infty}^{\infty} j^m J_{j+p} J_{j+q} \\ &= \sum_{j=-\infty}^{\infty} j^{m-1}(j+p) J_{j+p} J_{j+q} - p \sum_{j=-\infty}^{\infty} j^{m-1}(j+p) J_{j+p} J_{j+q}, \end{aligned} \tag{4.20}$$

which, upon using the recursion identity (4.5), yields,

$$S_m(p,q) \equiv \frac{x}{2}\left[S_{m-1}(p-1,q) + S_{m-1}(p+1,q)\right] - pS_{m-1}(p,q). \tag{4.21}$$

Using Eq. (4.11) to provide initial values, Eq. (4.21) may be used to generate the coefficients of all higher-order summations. For example, choosing $m = 1$, this leads to

$$S_1(p,q) = \frac{x}{2}\left[S_0(p-1,q) + S_0(p+1,q)\right] - pS_0(p,q) = \begin{cases} x/2 & \text{if } |p-q| = 1 \\ -p & \text{if } p = q \\ 0 & \text{Otherwise.} \end{cases} \tag{4.22}$$

The results from a simple computational routine using the recursion relation (4.21) are shown in Table (4.1), and corroborate the assertion that the leading order growth of $S_{2m}(0,0)$ is $\left[(2m)!/(m!)^2 2^{2m}\right] x^{2m}$.

The momentum moments, obtained from Eq. (4.2), may now be expressed as,

$$\langle \hat{p}^{2m} \rangle = R_{2m}(\eta), \tag{4.23}$$

where $R_{2m}(\eta)$ is an even polynomial in η of order $2m$. In this form, it is clear that η plays a vital role in the dynamics of single momentum eigenstates.

4.2 Incoherent Mixtures of Momentum Eigenstates

An atomic gas which has been laser-cooled, confined, and allowed to thermalise, may be treated as an incoherent ensemble of momentum eigenstates, denoted $D_k(\beta)$. The corresponding density operator, $\hat{\rho}$, is then diagonal in the momentum basis, and given by

$$\begin{aligned}\hat{\rho} &= \int_{-\infty}^{\infty} dp|p\rangle D(p)\langle p| \\ &= \int_{-1/2}^{1/2} \sum_{k=-\infty}^{\infty} d\beta|k+\beta\rangle D_k(\beta)\langle k+\beta|.\end{aligned} \tag{4.24}$$

In the Heisenberg picture, and using Eq. (3.58) this evolves after a time $t = nT$ to,

$$\begin{aligned}\hat{\rho} &= \int_{-\infty}^{\infty} dp|p\rangle D(p)\langle p| \\ &= \int_{-1/2}^{1/2} d\beta \sum_{k=-\infty}^{\infty} \left(\sum_{j=\infty}^{\infty} c_{kj}(\beta, nT)|j+\beta\rangle \right) D_k(\beta) \left(\sum_{j'=-\infty}^{\infty} c^{\star}_{j'k}(\beta, nT)\langle j'+\beta| \right),\end{aligned} \tag{4.25}$$

where, for brevity, the probability amplitudes have been left in their general form. The objective is to calculate the momentum distribution at some later time, meaning that only the diagonal terms in Eq. (4.25) are relevant. Considering only the diagonal elements gives

$$\begin{aligned}D_k(\beta, nT) &= \sum_{j=-\infty}^{\infty} |c_{kj}|^2 D_j(\beta, 0) \\ &= \sum_{j=-\infty}^{\infty} J^2_{j-k}[\phi_d \eta(n)] D_j(\beta, 0).\end{aligned} \tag{4.26}$$

Therefore, by definition, the m-th moment of the evolved momentum distribution is given by

$$\langle \hat{p}^m \rangle_n = \int_{-1/2}^{1/2} d\beta \sum_{j,k=-\infty}^{\infty} J^2_{j-k}[\phi_d \eta(n)] D_k(\beta)(j+\beta)^m. \tag{4.27}$$

It is sometimes useful to write this in terms of the continuous momentum P:

$$\langle \hat{p}^m \rangle_n = \int_{-\infty}^{\infty} dP \sum_{j=-\infty}^{\infty} J^2_{j}[\phi_d \eta(n)] D(P)(j+P)^m. \tag{4.28}$$

The case where the initial state is described by a single momentum eigenstate $|k' + \beta'\rangle$ is reclaimed by taking $D(P) = \delta(P - k' - \beta')$.

4.2.1 Time-Evolution of Incoherent Mixtures

Using Eq. (4.28), and binomially expanding the term $(j+P)^m$ yields,

$$\langle \hat{p}^m \rangle_n = \int_{-\infty}^{\infty} dP \sum_{j=-\infty}^{\infty} \sum_{h=0}^{m} \binom{m}{h} J_j^2[\phi_d \eta(n)] D(P) j^h P^{m-h}, \tag{4.29}$$

where the summation over j may be treated separately to the integration. From section 4.1.1, this may be rewritten using the general form of the Bessel summations, as

$$\langle \hat{p}^m \rangle_n = \langle \hat{p}^m \rangle_0 + \int_{-\infty}^{\infty} dP \sum_{h=1}^{m} \binom{m}{h} R_{2h}(\phi_d \eta) D(P) P^{m-h}. \tag{4.30}$$

where the first term of the summation over h has been explicitly evaluated to give the initial momentum moment. It should be noted that η is dependent on β, which complicates the evaluation of the integral. Furthermore, the momentum moment dynamics for both single momentum eigenstates and incoherent mixtures [See Eq. (4.1.1) and Eq. (4.30)] are strongly dependent on the behaviour of η. For Eq. (4.30), this dependence can be seen more easily when the second- and fourth-order moments are considered. Selecting $m = 2$ and $m = 4$, and using Eq. (4.18) and Eq. (4.19), gives the second-order momentum moment to be

$$\langle \hat{p}^2 \rangle_n = \langle \hat{p}^2 \rangle_0 + \frac{\phi_d^2}{2} \int_{-\infty}^{\infty} dp D(p) \eta^2 \tag{4.31}$$

and, similarly, the fourth-order momentum moment,

$$\langle \hat{p}^4 \rangle_n = \langle \hat{p}^4 \rangle_0 + \frac{\phi_d^2}{2} \int_{-\infty}^{\infty} dp D(p) \left[\frac{3}{8} \phi_d^4 \eta^4 + \frac{1}{2} \phi_d^2 \eta^2 + 3p^2 \phi_d^2 \eta^2 \right]. \tag{4.32}$$

4.3 Resonances, Anti-Resonances, and Fractional Resonances of η

In this section, the behaviour of the function η will be examined in detail, and the parameter regimes resulting in resonant, fractionally resonant, or antiresonant behaviour will be revealed. The consequent growth in these regimes will also be calculated where possible, and these results will then interpreted in the context of the momentum moment dynamics.

Previously, η was defined as the magnitude $\eta = |\nu|$. To examine the behaviour of η, it is more convenient to work with the complex function ν, defined by

$$\nu = \sum_{j=0}^{n-1} \exp[i\pi(\alpha j - \Omega j^2)], \tag{4.33}$$

where $\alpha = (1 + 2\beta)\ell$, with $\beta \in [-1/2, 1/2)$, and $\Omega \geq 0$. Notably, ν has the form of a Gauss sum [122, 123], and has merited study for its own right in number theoretical fields [124–126], as well as enjoying use in some proof of principle experiments for number factorisation[127]. In particular, the work of Berry [125] is pertinent, where it was shown that $|\nu| \sim n$ for $\alpha = 0$ and $\Omega = p/q$ with pq an even integer. Similarly, $|\nu|$ was shown to retrace itself through the complex plane for pq equal to odd integer. Both of these conditions are exactly equivalent to the resonance and antiresonance criteria derived below. However, the focus of Berry's work was such that nonzero α was not considered, and the behaviour of the recurrences of $|\nu|$ was not examined at all. Also, given that α depends on a physically interesting quantity (the quasimomentum), it is therefore appropriate to re-examine $|\nu|$ in the context of the QDKR.

4.3.1 Symmetry Properties

To compute the momentum moments, the integral in Eq. (4.30) must be evaluated explicitly. As written, η is a function of the quasimomentum, β, only, whereas the integral refers directly to the continuous momentum P. Furthermore, intuition suggests that a symmetric driving force, as is the case here, should preserve the symmetry of the initial distribution, but this is not explicitly obvious in Eq. (4.30). Consequently, an understanding of some basic symmetry properties of η is desirable before attempting to derive the momentum moment dynamics.

Invariance Under $\beta \to \beta + k$

A change of variables which is useful in this work is change from the continuous momentum to the corresponding continuous and discrete components, given by $p = k + \beta$, and it is fortuitous that $\eta(\beta)$ is invariant under this change of variables. This can be shown straightforwardly by applying the transformation directly, to give,

$$\eta(k + \beta) = \sum_{j=0}^{n-1} \exp[i\pi(\alpha j + 2k\ell - \Omega j^2)], \tag{4.34}$$

which, since $2k\ell$ is an even integer, gives,

$$\eta(k + \beta) = \eta(\beta). \tag{4.35}$$

Invariance Under $\beta \to -\beta$

The symmetry under $\beta \to -\beta$ is expected on intuitive grounds. To determine the conditions where this symmetry property is obeyed, it is convenient to first consider $\nu(\beta)$ at the $(n+1)$-th kick, $\nu_{n+1}(\beta)$,

$$\nu_{n+1}(\beta) = \sum_{j=0}^{n} e^{i\pi\left[(1+2\beta)\ell j - rj^2/s\right]} \tag{4.36}$$

for which $\Omega = r/s$. Then, reordering the summation (so that j is exchanged for $n-j$), and considering $\nu_{n+1}(-\beta)$ implies,

$$\nu_{n+1}(-\beta) = e^{i\pi n[(1-2\beta)\ell - rn/s]} \sum_{j=0}^{n} e^{-i\pi\left[(1-2\beta)\ell j - 2rnj/s + rj^2/s\right]}. \tag{4.37}$$

The total number of kicks is now taken to be an integer multiple of s, i.e., $n = \tau s$ for integer τ, so that,

$$\nu_{n+1}(-\beta) = e^{i\pi\tau s[(1-2\beta)\ell - r\tau]} \sum_{j=0}^{\tau s} e^{-i\pi\left[(1-2\beta)\ell j + rj^2/s\right]}, \tag{4.38}$$

where the term $2r\tau$ in the exponential has been neglected because it contributes a 2π phase to the sum. Since ℓj is an integer, the identity $\exp(-i\pi\ell j) = \exp(i\pi\ell j)$ can be used to imply,

$$\nu_{n+1}(-\beta) = e^{i\pi\tau s[(1-2\beta)\ell - r\tau]}\nu_{n+1}(\beta). \tag{4.39}$$

Thus, since $\eta = |\nu|$, the symmetry $\eta_{n+1}(\beta) = \eta_{n+1}(-\beta)$ is observed when $\Omega = r/s$ and $n = \tau s + 1$. For $n = \tau s$, using

$$\nu_{n+1}(\beta) = \nu_n(\beta) + e^{i\pi\left[(1+2\beta)\ell\tau s - rs\tau^2\right]} \tag{4.40}$$

then, by Eq. (4.39)

$$\nu_{\tau s+1}(-\beta) = e^{i\pi\tau s[(1-2\beta)\ell - r\tau]} \left[\nu_n(\beta) + e^{i\pi\left[(1+2\beta)\ell\tau s - rs\tau^2\right]}\right]. \tag{4.41}$$

Therefore, the symmetry property for $|\nu_{n+1}(\beta)|$ also applies to $|\nu_n(\beta)|$ when the additional exponential term is β-independent. This occurs whenever $(1+2\beta)\ell s\tau$ is an integer, which later will be shown to be satisfied as a prerequisite in the antiresonant and resonant regimes.

In summary then, both $\eta_{n+1}(\beta)$ and $\eta_n(\beta)$ are invariant under $\beta \to -\beta$ for $\Omega = r/s$ and $n = \tau s$. The symmetry property may have wider validity, but only the latter symmetry property will be used in this work since only the kick-to-kick dynamics every s-th kick are obtained.

4.3.2 Resonances

Resonances are characterised by parameter sets that result in unbounded growth of $|\eta|$ with increasing n. A trivial example is the case where $\alpha = \Omega = 0$, giving the maximum value $|\eta| = n$. Here, a resonance will be defined according to a set of choices $\{\alpha, \Omega\}$ that gives $|\eta| = n$.

For a resonance to exist, the summand of ν must be periodic with respect to the counting index j. To determine this period, let $j \to j + T$, so that

$$\nu = \sum_{j=0}^{n-1} \exp[i\pi(\alpha j + \alpha T - \Omega j^2 - 2\Omega j T - \Omega T^2)]. \tag{4.42}$$

For ν to be periodic, the period T must be independent of the counting index j. Therefore, ΩT must be an integer. For the case where Ω is rational, such that $\Omega = r/s$, then T must be a multiple of s, i.e., the period is $T = s$. Moreover, if the period is to be associated with periodic growth, then the summand must be left invariant. Imposing this determines that the resonance condition

$$\alpha T - \Omega T^2 = s(\alpha - r) = 2A \tag{4.43}$$

must be satisfied, for any integer A, for η to experience resonant growth. However, for this growth to be resonant (rather than fractionally resonant), the equality $\eta = n$ must hold, which in turn implies $T = 1$. Therefore, resonances in this sense only occur for $r = s$, i.e., when Ω is integer.

Integer Ω

In the special case of integer values of Ω, η can be calculated analytically. Choosing $s = 1$ in Eq. (4.42) yields

$$\nu = \sum_{j=0}^{n-1} \exp[i\pi(\alpha j - r j^2)]. \tag{4.44}$$

Importantly, rj^2 is an integer by definition, and only its parity influences η. Exploiting the fact that the parity of rj^2 is the same as rj, then

$$\nu = \sum_{j=0}^{n-1} \exp[i\pi(\alpha j - r j)], \tag{4.45}$$

which takes the form of a geometric sum; thus,

$$\nu = \frac{1 - \exp[i\pi n(\alpha - r)]}{1 - \exp[i\pi(\alpha - r)} = \exp[i\pi(n-1)(\alpha - r)/2] \frac{\sin[n\pi(\alpha - r)/2]}{\sin[\pi(\alpha - r)/2]}, \tag{4.46}$$

which, may be written

$$\eta = \frac{\sin[n\pi(\alpha - r)/2]}{\sin[\pi(\alpha - r)/2]}. \tag{4.47}$$

Interestingly, Eq. (4.47) has the form of a Chebyshev polynomial of the second kind [128, 129], which implies that it may be possible to cast η into a more convenient form; this observation will be put to good effect in Chapter 5, where η will be expanded as finite cosine series[2].

4.3.3 Fractional Resonances

Note that for $T = s > 1$, the magnitude of η is necessarily sub-maximal, i.e., $\eta < n$. Although this sort of growth still scales linearly, it is reduced by increasing s. Hence, parameter sets corresponding to this regime, where $s > 1$, are called fractional resonances. Although they scale with n similarly to resonances, they are distinguished by describing weaker growths.

The evaluation of η for kick numbers is difficult except for specific values of n. To see the partial resonance corresponding to $\Omega = r/s$, the number of kicks must exceed s, i.e. $n > s$. By choosing $n = \tau s + \lambda$, and partitioning η appropriately, one obtains

$$\nu = \tau \sum_{j=0}^{s-1} \exp\left(i\pi[\ell j - (r/s)j^2]\right) + \sum_{j=0}^{\lambda-1} \exp\left(i\pi[\ell j - (r/s)j^2]\right). \tag{4.48}$$

In this form, the growth of η is decomposed into a number of complete cycles with a remainder term, which is bounded by s and becomes negligible for many kicks.

The summation representing the complete cycles can be rewritten using the reciprocity formula[3] [124] as

$$\begin{aligned} \sum_{j=0}^{|C|-1} \exp(i\pi[Aj^2 + Bj]/C) =& \sqrt{\left|\frac{C}{A}\right|} \exp(i\pi[(|AC| - B^2)/4AC]) \\ &\times \sum_{j=0}^{|A|-1} \exp(-i\pi[Cj^2 + Bj]/A), \end{aligned} \tag{4.49}$$

[2]This is equivalent to writing Chebyshev's polynomial of the second kind, $U_{n-1}(\cos[(\ell - r)\pi/2])$, in terms of Chebyshev's polynomial of the first kind, which is also equivalent to an analytic discrete Fourier transform.

[3]This is a more generalised version of the Landsberg-Schaar formula that appears most often in the literature.

where A, B, and C are integers such $AC - B$ is even. Note that this constraint is equivalent to the resonance condition (4.43) above. Thus,

$$\begin{aligned}\nu =&\tau\sqrt{\frac{s}{r}}\exp(i\pi[\ell^2 s/4r - rs])\sum_{j=0}^{r-1}\exp\left(i\pi[sj^2 + slj/r]\right)\\ &+\sum_{j=0}^{\lambda-1}\exp\left(i\pi[\ell j - (r/s)j^2]\right).\end{aligned} \tag{4.50}$$

where now only kicks that are integer multiples of s are considered; that is, those kicks where the remainder term in Eq. (4.48) is zero, although, as noted, it can be made negligible for many kicks.

In writing ν in this form, it may be evaluated identically as for integer Ω provided $r = 1$, i.e. for the case where $\Omega = 1/s$. For this choice,

$$\eta = \tau\sqrt{s} = \frac{n}{\sqrt{s}}, \tag{4.51}$$

where the kicknumber n has the form $n = \tau s$.

4.3.4 Anti-resonances

Anti-resonances are characterised by exact revivals in η. For this to occur, η must be periodic with respect to n, i.e., the summand, $\exp(i\pi[\alpha j - \Omega j^2])$ must be oscillatory. Formally,

$$\exp(i\pi[\alpha(j+Q) - \Omega(j+Q)^2]) = -\exp(i\pi[\alpha j - \Omega j^2]) = \exp(i\pi[\alpha j - \Omega j^2 + 1]). \tag{4.52}$$

Using similar reasoning as for the resonance case, the equality $Q = s$ must hold, with the condition

$$s(\alpha - r) = 2A + 1 \tag{4.53}$$

where A is an arbitrary integer. This condition is the anti-resonance condition for η, i.e., $\eta = 0$ when n is an even multiple of s. In this instance, $2s$ is the revival period of the antiresonance.

For a given $\Omega = r/s$, we may also deduce high-order antiresonances for varying α. Following similar lines to that above,

$$\begin{aligned}&\exp(i\pi[\alpha(j+Q) - \Omega(j+Q)^2]) = \exp(i\pi[N_r/N_s])\exp(i\pi[\alpha j - \Omega j^2])\\ &= \exp(i\pi[\alpha(j+N_sQ) - (r/s)(j^2 + 2jN_sQ + N_s^2Q^2)]).\end{aligned} \tag{4.54}$$

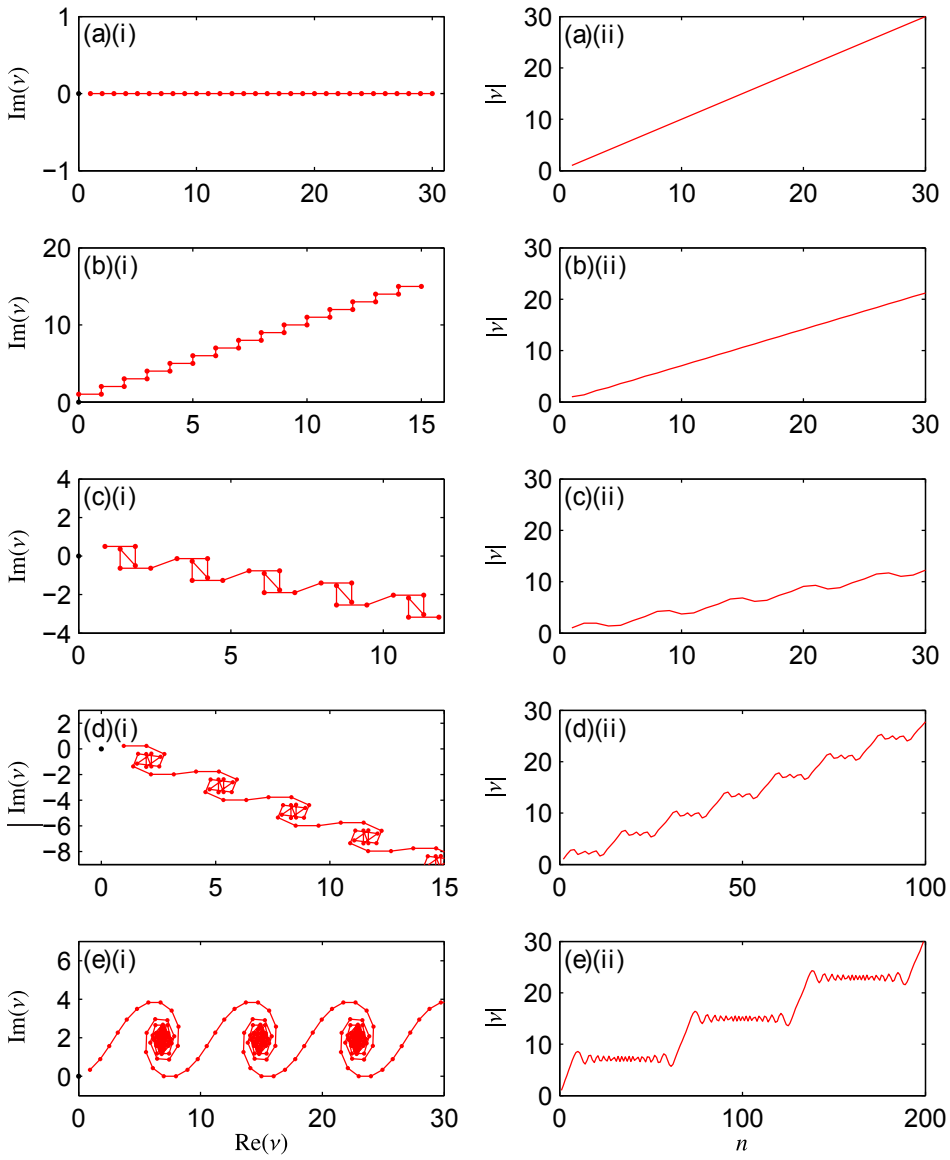

Figure 4.1: The parameter ν as a function of n for (a) $\beta = 0$, $\ell = 3$, $r = s = 1$, (b) $\beta = 1/4$, $\ell = 2$, $r = 1$, $s = 2$, (c) $\beta = 1/12$, $\ell = 2$, $r = 1$, $s = 6$, (d) $\beta = 1/28$, $\ell = 2$, $r = 1$, $s = 14$, and (e) $\beta = 1/32$, $\ell = 2$, $r = 1$, $s = 64$. In all cases, $s(\alpha - r)$ is even, the behaviour is resonant. Panels (b)-(d) are examples of fractional resonance, whereas panel (a) demonstrates a full resonance evidenced by a maximum growth in $|\nu|$. Series (i) shows ν in the complex plane and series (ii) shows the magnitude of ν, measured from the origin. Panels (a)-(c) show ν and its corresponding magnitude up to $n = 30$ whereas panels (d-e) shows a high-order fractional resonance where large n is required to reveal the repeating structure. Units are dimensionless.

Again, it is found that $Q = s$, but now the revival period is $2N_s s$. The antiresonance condition becomes,

$$s(\alpha - r) = 2A + \frac{N_r}{N_s}. \tag{4.55}$$

Resonances and Anti-Resonances in Quasimomentum Space

The location of resonances and antiresonances in quasimomentum space can be determined from the condition $s(\alpha - r) = 2A + N_r/N_s$, where resonances correspond to the instance where $N_r = 0$. It is found that resonances occur when

$$\beta = \frac{2A + s(r - \ell)}{2\ell s} \tag{4.56}$$

and, for antiresonances,

$$\beta = \frac{2A + N_r/N_s + s(r - \ell)}{2\ell s}. \tag{4.57}$$

It is clear that antiresonances and fractional resonances are dense in the quasimomentum space, whereas resonances are not. Figures (4.3) and (4.4) show the (Ω, β) parameter space for η with $\ell = 1$ and $\ell = 2$ for a varying number of kicks. The width of resonances can be seen to dramatically diminish for increasing kicknumbers, and η appears to become increasingly insensitive to the parameters. This may be understood by considering the average behaviour of high-order antiresonances. For n kicks, a particular antiresonance with period $s \gg n$ will initially mimic resonant growth, until it eventually reaches half of its revival time, and begins the revival stage. With increasing n, more antiresonances participate in this competing effect, and the overall growth is curtailed. Therefore, long observation times result in resonances that become narrower as high-order antiresonances become distinguishable from their nearby resonances. A similar mechanism takes place around partial resonances, but because of their inherently reduced growth, the diminishing effect of increasing n is even more apparent.

Also noticeable in Figs. (4.3) and (4.4) is that the effect of increasing ℓ is to scale and translate the parameter space. This is a direct consequence of the fact that $2\beta\ell s$ must be an integer for antiresonances or resonances to be observed, which affects the number of resonances in the parameter space. This will have ramifications in chapter 5 where it will be shown distributions of momentum

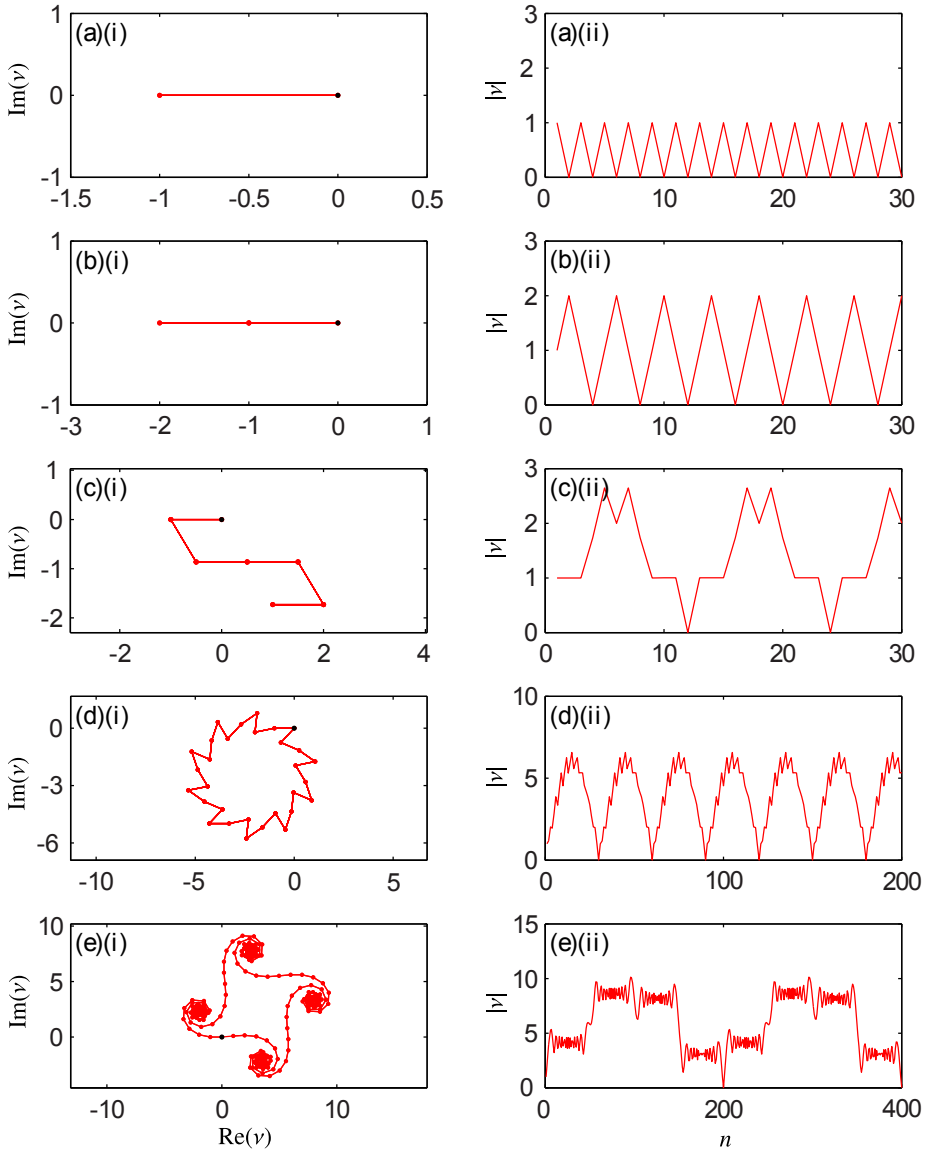

Figure 4.2: The parameter ν as a function of n for (a) $\beta = 0$, $\ell = 2$, $r = s = 1$, (b) $\beta = 1/4$, $\ell = 1$, $r = 1$, $s = 2$, (c) $\beta = 1/12$, $\ell = 1$, $r = 1$, $s = 6$, (d) $\beta = -1/10$, $\ell = 2$, $r = 1$, $s = 3$, and (e) $\beta = -19/200$, $\ell = 5$, $r = 1$, $s = 50$. In all cases, $s(\alpha - r) = 2A + N_r/N_s$, and the behaviour is anti-resonant. Panels (b)-(e) are examples of high-order anti-resonances, whereas panel (a) demonstrates a simple anti-resonance evidenced by a simple periodic revivals in $|\nu|$. Series (i) shows ν in the complex plane and series (ii) shows the magnitude of ν, measured from the origin. Panels (b)-(e) demonstrate how antiresonances may initially mimic resonant behaviour. In particular, antiresonances exist whose initial growth can be made arbitrarily long before a revival event becomes obvious. Units are dimensionless.

around resonances or antiresonances have a timescale over which they behave resonantly or antiresonantly set by ℓ.

4.3.5 Irrational Parameters

The dependence of a physical system on the rationality of some experimentally-determined parameter may be intuitively displeasing. However, the interpretation of these assertions requires the realisation that experimentally-determined parameters will always fluctuate around some mean value, even though those fluctuations may be negligible for experimental purposes. Consider, for example, $\tilde{\Omega} \in [1/s - \epsilon, 1/s + \epsilon]$. Assuming all values in this range are equally likely, one would observe the average growth of η of all $\tilde{\Omega}$, which will be dominated by the resonances corresponding to $1/s$, and its nearby high-order antiresonances. In comparison, contributions from irrational values of $\tilde{\Omega}$ are associated with ν performing random-walks in the complex plane, and these contributions are therefore quickly masked by the much larger high-order antiresonances. In fact, one can think of approximating an irrational parameter with a rational approximate, written as a continued fraction expansion. The quicker the rational approximate of a parameter converges, the more it will behave as if it were indeed rational. That is, there is no way to distinguish between a rational and an irrational value of $\tilde{\Omega}$, since a finite observation time could always correspond to a rational approximate of the irrational parameter.

4.4 Limiting Behaviours of the Momentum Moments

4.4.1 Zero-Temperature Limit

The time-evolution of a single momentum eigenstate is recovered in the zero-temperature, or ultracold, limit of an initial momentum distribution. In this regime, all the atoms are in the $P = 0$ state; in principle, the ultracold limit may admit nonzero quasimomentum values, common to all atoms in the sample, but only symmetric initial momentum distributions are considered in this work. In contrast to the dynamics for initial momentum eigenstates presented thus far, these considerations are reinforced by the understanding of resonant and antiresonant regimes developed in the previous section, which will allow the

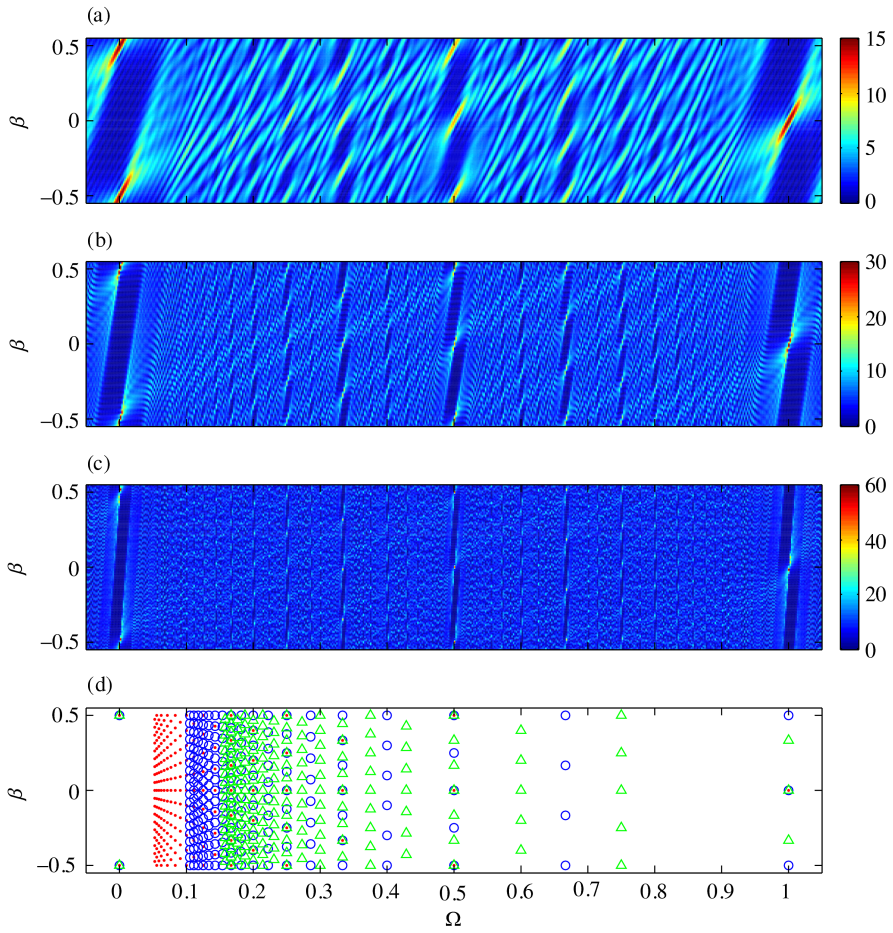

Figure 4.3: The parameter η as a function of Ω and β for $\ell = 1$ at (a) 15 kicks, (b) 30 kicks, and (c) 60 kicks. An antiresonance of order $2N_s$ will initially mimic exactly resonant growth for $N_s s$ kicks. The dimishing finite size of the resonances in (a)-(c) is due to nearby high-order antiresonances which become apparent as n increases. Panel (d) shows the locations of those resonances for which ($\cdot$) $\Omega = 1/s$, ($\circ$) $\Omega = 2/s$, and ($\triangle$) $\Omega = 3/s$, where $s = 1, 2, 3, \ldots, 20$. The resonances become infinite in number as $\Omega \to 0$, but their intensity diminishes. At $\Omega = 0$, there are only two resonances. Units are dimensionless.

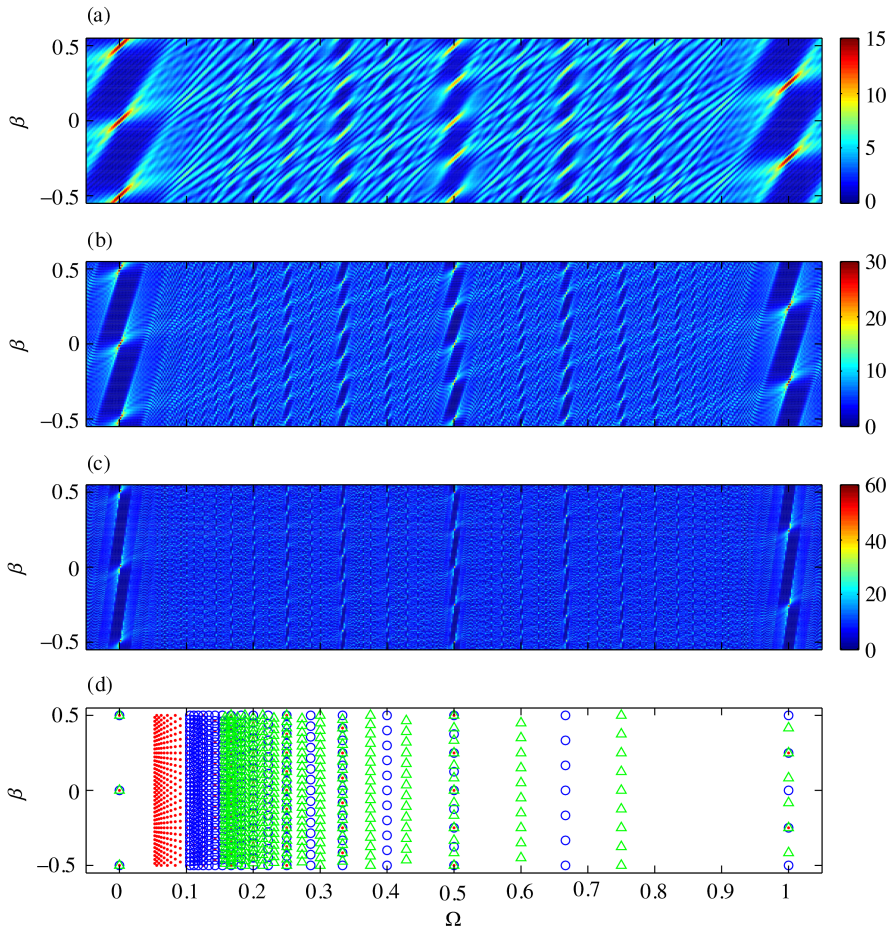

Figure 4.4: The parameter η as a function of Ω and β for $\ell = 2$ at (a) 15 kicks, (b) 30 kicks, and (c) 60 kicks. An antiresonance of order $2N_s$ will initially mimic exactly resonant growth for $N_s s$ kicks. The dimishing finite size of the resonances in (a)-(c) is due to nearby high-order antiresonances which become apparent as n increases. Panel (d) shows the locations of those resonances for which ($\cdot$) $\Omega = 1/s$, ($\circ$) $\Omega = 2/s$, and ($\triangle$) $\Omega = 3/s$, where $s = 1, 2, 3, \ldots, 20$. The resonances become infinite in number as $\Omega \to 0$, but their intensity diminishes. At $\Omega = 0$, there are only three resonances. Units are dimensionless.

dynamics to be characterised in more detail.

The ultracold limit is obtained by setting the initial momentum distribution to be $D(P) = \delta(P)$ in Eq. (4.30) to give the result

$$\langle \hat{p}^{2m} \rangle_n = R_{2m}(\phi_d \eta), \tag{4.58}$$

meaning that, in the zero-temperature limit, the growth of the $2m$-th momentum moment scales as $(\phi_d \eta)^{2m}$ to leading order.

Integer Resonances

From section (4.3.2), for integer Ω and $\beta = 0$,

$$\eta = \left| \frac{\sin[n(\ell - r)\pi/2]}{\sin[(\ell - r)\pi/2]} \right|. \tag{4.59}$$

which may be identified as the modulus of Chebyshev's polynomial of the second kind, $U_{n-1}(\cos[(\ell - r)\pi/2])$. Imposing the resonance condition (4.43) with $\beta = 0$, $s = 1$, and $(\ell - r) = 2A$, gives $\eta = n$. Hence,

$$\langle \hat{p}^{2m} \rangle_n = R_{2m}(\phi_d n), \tag{4.60}$$

and, specifically, for $m = 1$ and $m = 2$, using Eqs.(4.18) and (4.19),

$$\langle \hat{p}^2 \rangle_n = \frac{\phi_d}{2} n^2, \tag{4.61a}$$

$$\langle \hat{p}^4 \rangle_n = \frac{3\phi_d^4}{8} n^4 + \frac{\phi_d^2}{2} n^2. \tag{4.61b}$$

Integer Antiresonances

Similarly, for integer Ω, enforcing the antiresonance condition $(\ell - r) = 2A + N_r/N_s$ gives,

$$\eta = \left| \frac{\sin\left(n\pi N_r/2N_s\right)}{\sin\left(\pi N_r/2N_s\right)} \right|. \tag{4.62}$$

The simplest antiresonance corresponds to $N_r = N_s = 1$, which may be obtained by selecting β, ℓ, and r appropriately. The magnitude of ν is

$$\eta = \left| \sin\left(\frac{n\pi}{2}\right) \right|. \tag{4.63}$$

and therefore,

$$\eta^2 = \sin^2(n\pi/2) = \frac{1}{2}\left[(-1)^{n+1} + 1\right]. \tag{4.64}$$

Consequently, for the simplest antiresonance, $\langle \hat{p}^{2m} \rangle$ oscillates with a period of two kicks, with an amplitude that scales as ϕ_d^{2m}. Explicitly, the second- and fourth-order moments are,

$$\langle \hat{p}^2 \rangle_n = \frac{\phi_d^2}{4} \left[(-1)^{n+1} + 1 \right], \tag{4.65a}$$

$$\langle \hat{p}^4 \rangle_n = \left(\frac{3\phi_d^4}{16} + \frac{\phi_d^2}{4} \right) \left[(-1)^{n+1} + 1 \right]. \tag{4.65b}$$

Note that any combination of even powers of $\left[(-1)^{n+1} - 1 \right]$ may be written as $a \left[(-1)^{n+1} - 1 \right]$, for some constant a. Thus, this antiresonant behaviour is also seen in the cumulants, but with a different amplitude of oscillation. This would be expected to hold for $s > 1$ at every s-th kick, but not necessarily for all n.

Fractional resonances: Rational values of Ω

For rational values of Ω, for which $s > 1$, the resonant growth was found to be $\eta = n/\sqrt{s}$ [See Eq. (4.51)], where $n = \tau s$. Consequently,

$$\langle \hat{p}^m \rangle_n = R_{2m}(\phi_d n/\sqrt{s}), \tag{4.66}$$

and, in particular,

$$\langle \hat{p}^2 \rangle_n = \frac{\phi_d^2}{2s} n^2, \tag{4.67a}$$

$$\langle \hat{p}^4 \rangle_n = \frac{3\phi_d^4}{8s^2} n^4 + \frac{\phi_d^2}{2s} n^2. \tag{4.67b}$$

As in the resonant case, the leading-order growth of $\langle \hat{p}^{2m} \rangle$ with respect to n is n^{2m}, but that growth is now diminished by the additional factor of s^m.

Equivalent Dynamics in the Kicked-Rotor

The dynamics of the kicked-rotor, or kicked-particle, are recovered for $\Omega = 0$. Studies in this chapter have shown that, for integer Ω, only the parity is important, and the magnitude of Ω does not influence the dynamics. Since the dynamics corresponding to integer Ω can be mapped onto $\Omega = 0$, with an appropriate choice of ℓ, then the QDKA dynamics for integer Ω map directly to the kicked-rotor dynamics. Since the fractional resonances presented in this chapter rely upon non-integer Ω, these are in addition to the well-known kicked-rotor resonances.

4.4.2 High-Temperature Limit

In this section, the high-temperature limit of the momentum moment dynamics will be derived. In this context, a high-temperature limit refers to a symmetric, broad momentum distribution which has a well-described initial width. That is, the distribution has a maximum close to $P = 0$, and an envelope that decreases for increasing P, both of which are typical characteristics of a thermal momentum distribution. One might imagine a Gaussian distribution, but, for the results that follow, this need not be the case.

General form of η^{2q}

The integral in Eq. (4.30) contains even powers of η, and it would be inconvenient to calculate with this form. Instead, a general even power, η^{2q}, may be written as

$$\eta^{2q} = \left| \sum_{j=0}^{n-1} e^{i\pi(\alpha j - \Omega j^2)} \right|^{2q} = \sum_{\mathbf{j}_q, \mathbf{j}'_q = 0}^{n-1} e^{i\pi[F(\mathbf{j}_q) + \beta G(\mathbf{j}_q) - F(\mathbf{j}'_q) - \beta G(\mathbf{j}'_q)]} \tag{4.68}$$

where the shorthand notation $\sum_{\mathbf{j}_q, \mathbf{j}'_q = 0}$ has been used to denote the $2q$ sums, with $\mathbf{j}_q = (j_1, ..., j_q)$ and $\mathbf{j}'_q = (j'_1, ..., j'_q)$, and,

$$F(\mathbf{j}_q) = \sum_{r=1}^{q} (\ell j_r - \Omega j_r^2) \tag{4.69a}$$

$$G(\mathbf{j}_q) = 2\ell \sum_{r=1}^{q} j_r. \tag{4.69b}$$

It should be noted that the parameters are unconstrained, and that the dynamics are not necessarily resonant or anti-resonant. Substituting Eq. (4.68) into Eq. (4.30) gives,

$$\begin{aligned} \langle \hat{P}^{2m} \rangle = & \langle \hat{P}_0^{2m} \rangle + \sum_{h=1}^{m} \binom{2m}{2h} \sum_{q=1}^{h} a_q \phi_d^{2q} \sum_{\mathbf{j}_q, \mathbf{j}'_q = 0}^{n-1} e^{i\pi[F(\mathbf{j}_q) - F(\mathbf{j}'_q)]} \\ & \times \int_{-\infty}^{\infty} dP D(P) P^{2(m-h)} e^{i\pi P[G(\mathbf{j}_q) - G(\mathbf{j}'_q)]}, \end{aligned} \tag{4.70}$$

where the general expansion $R_{2h}(\phi_d \eta) = \sum_{q=1}^{h} a_q (\phi_d \eta)^{2q}$ has been inserted. In this form, the convenience of rewriting η as a single summation is clearer; the quasimomentum-independent terms can be separated from the integral. However, this comes at the cost of further abstraction, and the meaning of the partition is not immediately obvious.

In general, each integrand is oscillatory, which may lead to cancellation of terms in the summation. This is indeed the aim, and by consideration of the method of stationary phase, it is expected that many terms would make a negligible contribution to the momentum moment evolution. To show this, the integrals with no oscillation are extracted from the integral; these include exclusively those terms where $G(\mathbf{j}_q) = G(\mathbf{j}'_q)$. A immediate consequence of imposing this constraint is that $F(\mathbf{j}_q) - F(\mathbf{j}'_q) = 2\Omega\rho(\mathbf{j}_q, \mathbf{j}'_q)$ where $\rho(\mathbf{j}_q, \mathbf{j}'_q)$ is an integer given by[4]

$$\rho(\mathbf{j}_q, \mathbf{j}'_q) = \sum_{x=1}^{q} \sum_{y=x+1}^{q} (j'_x j'_y - j_x j_y). \tag{4.71}$$

Partitioning Eq. (4.70) in this way, and using Eq. (4.71), yields

$$\begin{aligned}
\langle \hat{P}^{2m} \rangle_n =& \langle \hat{P}^{2m} \rangle_0 + \sum_{h=1}^{m} \binom{2m}{2h} \langle P^{2(m-h)} \rangle_0 \\
&\times \sum_{q=1}^{h} a_q \phi_d^{2q} \sum_{\substack{\mathbf{j}_q, \mathbf{j}'_q \\ G(\mathbf{j}_q)=G(\mathbf{j}'_q)}} e^{i2\pi\Omega\rho(\mathbf{j}_q, \mathbf{j}'_q)} \\
&+ \sum_{h=1}^{m} \binom{2m}{2h} \sum_{q=1}^{h} a_q \phi_d^{2q} \sum_{\substack{\mathbf{j}_q, \mathbf{j}'_q \\ G(\mathbf{j}_q)\neq G(\mathbf{j}'_q)}} e^{i\pi[F(\mathbf{j}_q)-F(\mathbf{j}'_q)]} \\
&\times \int_{-\infty}^{\infty} dP D(P) P^{2(m-h)} e^{i\pi P[G(\mathbf{j}_q)-G(\mathbf{j}'_q)]},
\end{aligned} \tag{4.72}$$

where the dependence on n is now left implicit. In this form, the contribution according to the initial quasimomentum has been extracted from the momentum moment evolution. It is useful as an aid to understanding to draw upon an analogy at this stage; the latter term in Eq. (4.72) may be thought of as associating each initial quasimomentum value with the dynamics of a momentum eigenstate. Each eigenstate has a frequency dependent on the quasimomentum value and the kicking period, with the states weighted accordingly. In the ultracold limit, only one eigenstate contributes to the dynamics. In the high-temperature limit, there is a spread over many different quasimomentum values, and they effectively cancel leaving only the oscillations due to the kicking-period, which is identical for all eigenstates. Thus, provided the distribution, $D(P)$, is sufficiently broad to cover many different values of quasimomentum with weightings sufficient to allow significant cancellation, then contribution of the latter term is zero. This will now be demonstrated more rigourously.

[4] A simple example is for $q = 2$ where we have the constraint $j_1 + j_2 = j'_1 + j'_2$. Considering $(j_1 + j_2)^2 = (j'_1 + j'_2)^2$ leads to the conclusion that $j_1^2 + j_2^2 - {j'_1}^2 - {j'_2}^2 = 2(j'_1 j'_2 - j_1 j_2)$.

If integer values of Ω are considered, since $\rho(\mathbf{j}_q), \mathbf{j}'_q)$ is also an integer, $\exp(i2\pi\Omega\rho(\mathbf{j}_q), \mathbf{j}'_q)$ simplifies to unity, and the sum over such terms is equal to the number of terms in the sum. Therefore, it is necessary to determine the number of ways $G(\mathbf{j}_q) = G(\mathbf{j}'_q)$ can be satisfied.

Counting Terms Where $G(\mathbf{j}_q) = G(\mathbf{j}'_q)$

To find the number of terms where $G(\mathbf{j}_q) = G(\mathbf{j}'_q)$, it is necessary to examine the constraint [see Eq. (4.69b)]

$$(j_1 + j_2 + \ldots + j_q - j'_1 - j'_2 - \ldots - j'_q) = 0, \tag{4.73}$$

where $j_q, j'_q \in [0, n-1]$, and determine the number of permutations that allow this to be satisfied. A well-known number theoretical approach, which is described in detail in Ref. [130] is that this problem is isomorphic to the problem of evaluating the x-independent term in

$$\left(1 + x + x^2 + \ldots + x^{n-1}\right)^q \left(1 + \frac{1}{x} + \frac{1}{x^2} + \ldots + \frac{1}{x^{n-1}}\right)^q. \tag{4.74}$$

An equivalent problem, given by multiplying by $x^{q(n-1)}$, is find the coefficient $x^{q(n-1)}$

$$\left(1 + x + x^2 + \ldots + x^{n-1}\right)^{2q}. \tag{4.75}$$

This is given by[5] [131], given as

$$\begin{aligned} W(2q, n) &= \sum_{j=0}^{q} (-1)^j \binom{2q}{j} \binom{n(q-j) + q - 1}{2q - 1} \\ &= \sum_{j=0}^{q} (-1)^j \binom{N + q - 1}{N - q} \binom{2q}{j}, \end{aligned} \tag{4.76}$$

where $N = n(q - j)$, and the identity $\binom{x}{y} = \binom{x}{x-y}$ has been used. The only n-dependent part of $W(2q, n)$ is the binomial coefficient

$$\binom{N + q - 1}{N - q} = \frac{(N + m - 1)(N + m - 2)\ldots(N - m + 1)}{(2q - 1)!}, \tag{4.77}$$

the numerator of which is a polynomial in N of degree $2q-1$. Thus, $W(2q, n) = S_{2q-1}(n)$ where

$$S_{2q-1}(n) = \sum_{r=1}^{2q-1} b_r n^r \tag{4.78}$$

[5] This is equivalent to considering $2q$ n-sided dice and finding the number of ways $W(2q, n)$ of totalling $q(n-1)$.

and represents a polynomial in n of degree $2q-1$. In principle, the coefficients b_r can be computed for a specific q, but are left general for the purposes required of them. Therefore,

$$\sum_{\substack{\mathbf{j}_q,\mathbf{j}'_q \\ G(\mathbf{j}_q)=G(\mathbf{j}'_q)}} e^{i2\pi\Omega\rho(\mathbf{j}_q,\mathbf{j}'_q)} = \sum_{\substack{\mathbf{j}_q,\mathbf{j}'_q \\ G(\mathbf{j}_q)=G(\mathbf{j}'_q)}} 1 = S_{2q-1}(n), \tag{4.79}$$

which, upon substitution into Eq. (4.72), yields,

$$\begin{aligned}\langle \hat{P}^{2m}\rangle_n =& \langle \hat{P}^{2m}\rangle_0 + \sum_{h=1}^{m}\binom{2m}{2h}\langle P^{2(m-h)}\rangle_0 \sum_{q=1}^{h} a_q \phi_d^{2q} S_{2q-1}(n) \\ &+ \sum_{h=1}^{m}\binom{2m}{2h}\sum_{q=1}^{h} a_q\phi_d^{2q} \sum_{\substack{\mathbf{j}_q,\mathbf{j}'_q) \\ G(\mathbf{j}_q)\neq G(\mathbf{j}'_q)}} e^{i\pi[F(\mathbf{j}_q)-F(\mathbf{j}'_q)]} \\ &\times \int_{-\infty}^{\infty} dP D(P) P^{2(m-h)} e^{i\pi P[G(\mathbf{j}_q)-G(\mathbf{j}'_q)]}.\end{aligned} \tag{4.80}$$

It is convenient to rewrite the oscillatory term in the integrand as

$$e^{i\pi P[G(\mathbf{j}_q)-G(\mathbf{j}'_q)]} = e^{i2\pi P\ell\sum_{r=1}^{q}[j_r-j'_r]}, \tag{4.81}$$

Written in this form, it is apparent that the maximum period of the oscillatory terms is $1/\ell$. Therefore, by the method of stationary phase, distributions that are approximately constant over one such period cause the integral to average approximately to zero. The distribution that satisfies this requirement is more general than the physical problem permits. Therefore, this result should be interpreted to mean that suitable distributions must be broad, that is, have a characteristic width, w, such that $w \gg 1/\ell$. The only surviving contribution is

$$\langle \hat{P}^{2m}\rangle_n = \langle \hat{P}^{2m}\rangle_0 + \sum_{h=1}^{m}\binom{2m}{2h}\langle P^{2(m-h)}\rangle_0 \sum_{q=1}^{h} a_q \phi_d^{2q} S_{2q-1}(n), \tag{4.82}$$

demonstrating that the growth of the $2m$-th momentum moment of an initially broad momentum distribution has a leading order which scales as n^{2m-1}.

In choosing Ω to be integer, neither resonant nor antiresonant behaviour is necessarily specified, and in the high-temperature limit, resonant and antiresonant behaviours are indistinguishable. Although not shown here, it is reasonable to expect that this is also true for rational values of Ω. This may be deduced because, firstly, the summation (4.79) with general Ω, is bounded above by $S_{2q-1}(n)$, and, secondly, the scaling with respect to n is identical for momentum eigenstates in both the rational and integer Ω cases. Both points imply that the expected growth in the high-temperature limit for rational Ω scales

with n in the same way as for integer Ω, but with a reduced growth resulting from smaller coefficients.

4.5 Momentum Cumulants

In principle, complete knowledge of the moments allows the distribution to be reconstructed. In practice, however, there are an infinite number of moments, and increasingly higher-orders may diverge. Moreover, the m-th order moment depends on all lower-order moments. Consequently, moments of different order are not independent quantities, which appears to limit their usefulness.

Fortunately, the information regarding lower-order moments can be systematically removed to generate quantities, called cumulants [132], that are independent. The first-, second-, third- and fourth-order cumulants are the mean, variance, skew, and kurtosis, respectively, and are given in terms of the moments as:

$$\langle\langle \hat{P} \rangle\rangle = \langle \hat{P} \rangle, \tag{4.83a}$$

$$\langle\langle \hat{P}^2 \rangle\rangle = \langle \hat{P}^2 \rangle - \langle \hat{P} \rangle^2, \tag{4.83b}$$

$$\langle\langle \hat{P}^3 \rangle\rangle = \langle \hat{P}^3 \rangle - 3\langle \hat{P} \rangle \langle \hat{P}^2 \rangle + 2\langle \hat{P} \rangle^3, \tag{4.83c}$$

$$\langle\langle \hat{P}^4 \rangle\rangle = \langle \hat{P}^4 \rangle - 4\langle \hat{P} \rangle \langle \hat{P}^3 \rangle - 3\langle \hat{P}^2 \rangle^2 + 12\langle \hat{P} \rangle^2 \langle \hat{P}^2 \rangle - 6\langle \hat{P} \rangle^4. \tag{4.83d}$$

where the m-th order momentum cumulant is denoted $\langle\langle \hat{P}^m \rangle\rangle$.

The skew quantifies the asymmetry of the distribution about the mean, and the kurtosis quantifies the degree to which the distribution is peaked. For example, a Gaussian (or δ-function, which can be defined as a zero-variance limit of a Gaussian) has zero kurtosis, whereas a distribution which is more sharply peaked or cusp-like has positive kurtosis, and a distribution which is more "blunt" has negative kurtosis. The consideration of distributions that are symmetric means that, as for the moments, the odd cumulants are zero at all times, and therefore the relevant quantities are

$$\langle\langle \hat{P}^2 \rangle\rangle = \langle \hat{P}^2 \rangle, \tag{4.84a}$$

$$\langle\langle \hat{P}^4 \rangle\rangle = \langle \hat{P}^4 \rangle - 3\langle \hat{P}^2 \rangle^2. \tag{4.84b}$$

Trivially, the second-order moment is equal to the second-order cumulant, but, the fourth-order cumulant is

$$\langle\langle \hat{p}^4 \rangle\rangle = \frac{\phi_d^2 n^2}{2} - \frac{3}{8}\phi_d^4 n^4. \tag{4.85}$$

In contrast to the fourth-order moment, which is monotonically increasing, and positive for all kicks, the fourth-order cumulant may initially be positive before tending to large negative values corresponding to very delocalised momentum distributions.

Although the cumulants are formally useful, it may be convenient experimentally to use moments, since experimental errors may aggregate in constructing the cumulants. In addition, the cumulants have a more complicated structure than the moments in the finite-temperature regime. Therefore, for clarity, the moments will be referred most often, with the cumulants being calculated when most appropriate.

4.5.1 Cumulants as Physical Quantities

The first-order momentum moment is the expectation of the momentum of the ensemble, and since the odd moments are identically zero, this means that the mean momentum of the ensemble is zero at all times. Likewise, the quantity $\langle\hat{p}^2\rangle/2M$ is the mean kinetic energy of the ensemble, and represents the energy transfer from the kicking potential to the atomic gas.

The interpretation of the higher-order moments is difficult, and therefore the cumulants are considered instead. Since the distribution is symmetric, the quantity $\langle\langle\hat{p}^2\rangle\rangle/2M$ also represents the mean kinetic energy of the ensemble, with a corresponding variance given by $\langle\langle\hat{p}^4\rangle\rangle/2M$, which may be taken to be a measure of how the kinetic energy is distributed amongst the atoms in the sample. A large fourth-order cumulant implies that few atoms have relatively high kinetic energy, and vice versa. For example, the fact that Eq. (4.85) is negative follows from the realisation that a momentum eigenstate is a localised state, and repeated kicks in the resonant regime will inevitably delocalise the state.

In the high-temperature limit, $\langle\langle\hat{p}^4\rangle\rangle/2M$ is cubic, although it is not clear from the analysis presented so far whether this will be increasing or decreasing for high kicknumbers. To determine the second- and fourth-order cumulants for thermal distributions, it is necessary to consider specific distributions, and obtain the analytic forms of the moments.

Chapter 5

Momentum Moment Dynamics for Specific Distributions for Integer Ω

In this chapter, the second- and fourth-order momentum moments for two physically reasonable initial momentum distributions for integer Ω will be examined in detail. The adherence to the general results derived in the previous chapter will first be confirmed, in both the resonant and antiresonant cases. In addition, the specific choice of an initial momentum distributions will allow an examination of finite-temperature effects. Finally, the results from both distributions will be compared and contrasted, and the cumulant behaviour in both cases will be examined.

5.1 Uniform Distribution

The simplest momentum distribution that may be considered is a uniform distribution of momentum over some finite interval, $D(P) = \Theta(P)$, where,

$$\Theta(P) = \begin{cases} 1/2\epsilon & \text{if } |P| \leq \epsilon; \\ 0 & \text{otherwise.} \end{cases} \tag{5.1}$$

where the parameter ϵ characterises the width of the distribution. Physically, a similar distribution may result from velocity-selective cooling methods, such as Raman cooling, where the high-velocity wings are removed from a thermal

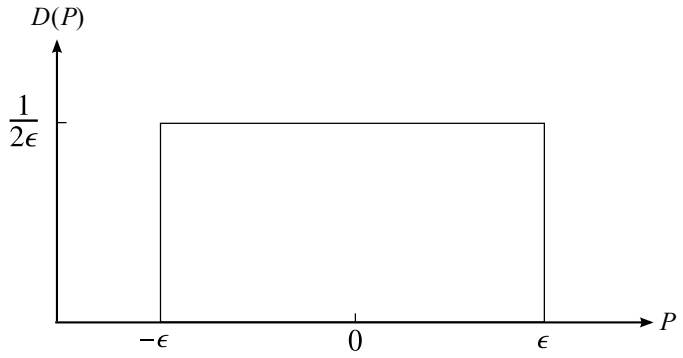

Figure 5.1: The normalised uniform momentum distribution with a width 2ϵ.

distribution [102]. The remaining momentum distribution has a slowly varying distribution of momentum up to some momentum cut-off. Therefore, the distribution $\Theta(P)$ is an adequate description of such a system, but is sufficiently simple that some insight into the dependence of the dynamics on the initial temperature may be gained.

5.1.1 General Second-Order Momentum Moment

The second-order momentum moment for integer Ω is determined from Eq. (4.31) with $D(P) = \Theta(P)$, to give,

$$\langle \hat{p}^2 \rangle_n = \frac{\epsilon^2}{3} + \frac{\phi_d^2}{4\epsilon} \int_{-\epsilon}^{\epsilon} dP \frac{\sin^2[n(\pi\ell P + (\ell - r)\pi/2)]}{\sin^2[\pi\ell P + (\ell - r)\pi/2]}, \tag{5.2}$$

where the initial second moment can be shown to be $\epsilon^2/3$. In order to compute the integral (5.2), it is convenient to cast the integrand in Eq. (4.59) in a more useful form. The link between different kinds of Chebyshev polynomial was remarked upon previously, and this insight suggests that Eq. (4.59) may be expanded as a series of cosines. Appendix B demonstrates that this is indeed the case, and the expansion in terms of cosines is,

$$\eta^2 = \frac{\sin^2(n\pi\ell P + n(\ell - r)\pi/2)}{\sin^2(\pi\ell P + (\ell - r)\pi/2)} = n + 2\sum_{q=1}^{n-1} (-1)^{q(\ell - r)} (n - q) \cos(2q\pi\ell P). \tag{5.3}$$

Therefore, Eq. (5.2) becomes,

$$\begin{aligned} \langle \hat{p}^2 \rangle_n =& \frac{\epsilon^2}{3} + \frac{\phi_d^2}{2} n + \frac{\phi_d^2}{2\epsilon} \sum_{q=1}^{n-1} (-1)^{q(\ell - r)} (n - q) \int_{-\epsilon}^{\epsilon} dP \cos(2q\pi\ell P) \\ =& \frac{\epsilon^2}{3} + \frac{\phi_d^2}{2} n + \frac{\phi_d^2}{2\pi\epsilon\ell} \sum_{q=1}^{n-1} (-1)^{q(\ell - r)} \frac{(n - q)}{q} \sin(2q\pi\ell\epsilon) \end{aligned} \tag{5.4}$$

Before examining the dependence of the moments on ϵ, the general results for general symmetric momentum distributions will first be verified. The initial uniform distribution $\Theta(P)$ does not have a well-defined temperature since this is not a distribution that describes the atomic gas in thermal equilibrium. However, the parameter ϵ that characterises the width of the distribution loosely corresponds to an effective temperature. Therefore, the low-temperature regime is presumed to occur when $\epsilon \to 0$.

5.1.2 Low-Temperature Limit of Second-Order Moment

In the low-temperature regime, the second-order momentum moment becomes,

$$\langle \hat{p}^2 \rangle_n = \frac{\phi_d^2}{2} n + \phi_d^2 \sum_{q=1}^{n-1} (-1)^{q(\ell - r)} (n - q) \tag{5.5}$$

where the limit $\sin(nx)/x \to n$ as $x \to 0$ has been used.

Resonance

Since Ω has been chosen to be integer, the resonance condition (4.43) is satisfied when $\ell - r$ is even. Therefore, on resonance, and using the identity $\sum_{q=1}^{n-1} q = (n-1)n/2$,

$$\begin{aligned} \langle \hat{p}^2 \rangle_n =& \frac{\phi_d^2}{2} n + \phi_d^2 n(n-1) - \phi_d^2 \sum_{q=1}^{n-1} q \\ =& \frac{\phi_d^2}{2} n^2, \end{aligned} \tag{5.6}$$

and therefore the time-evolution for an initial momentum eigenstate given in Eq. (4.61a) is recovered.

Anti-Resonance

Anti-resonant behaviour manifests when $\ell - r$ is odd, suggesting

$$\langle \hat{p}^2 \rangle_n = \frac{\phi_d^2}{2} n + \phi_d^2 \sum_{q=1}^{n-1} (-1)^q (n - q) \tag{5.7}$$

For odd n, the summations can be computed by pairing consecutive terms, to obtain

$$\sum_{q=1}^{n-1} (-1)^q = 0 \tag{5.8}$$

$$\sum_{q=1}^{n-1} (-1)^q q = \frac{n-1}{2}. \tag{5.9}$$

Similarly, for even n,

$$\sum_{q=1}^{n-1}(-1)^q = -1 \tag{5.10}$$

$$\sum_{q=1}^{n-1}(-1)^q q = -\frac{n}{2}. \tag{5.11}$$

Combining these results implies,

$$\langle\hat{p}^2\rangle_n = \begin{cases} \phi_d^2/2 & n \text{ odd} \\ 0 & n \text{ even.} \end{cases} \tag{5.12}$$

which has the more compact form

$$\langle\hat{p}^2\rangle_n = \frac{\phi_d^2}{4}\left[(-1)^{n-1}+1\right], \tag{5.13}$$

in agreement with Eq. (4.65a).

High-Temperature limit of the Second-Order Moment

The high-temperature limit of the uniform distribution corresponds to a broad distribution, which is attained by in the large ϵ limit. In this limit, Eq. (5.4) becomes,

$$\langle\hat{p}^2\rangle_n = \frac{\epsilon^2}{3} + \frac{\phi_d^2}{2}n. \tag{5.14}$$

This has the power-law predicted in Eq. (4.82), and, as expected, it is independent of the parity of $\ell - r$. This independence may be understood by considering Figs. 4.3. For a sufficiently broad coverage of initial quasimomenta, so that many resonances are included, then a translation of the space by changing the parity of Ω does not affect the coverage of resonant and antiresonant behaviours in the initial distribution. In this sense, all behaviours are included and one observes an average of all of them.

An immediate observation from Eq. (5.14) is that the dynamics in the limit $\epsilon \to \infty$ are ill-defined since Eq. (5.14) contains information regarding the initial width of the distribution. However, if only the change with respect to the initial state, $\langle\hat{p}^2\rangle_n^\star = \langle\hat{p}^2\rangle_n - \epsilon^2/3$, is considered, then the dynamics are well-defined. Consequently, in the high-temperature limit,

$$\langle\hat{p}^2\rangle_n^\star = \frac{\phi_d^2}{2}n. \tag{5.15}$$

5.1.3 Fourth-Order Momentum Moment

In an identical fashion, Eq. (4.32) with $D(P) = \Theta(P)$ implies,

$$\langle \hat{p}^4 \rangle_n = \frac{\epsilon^4}{5} + \frac{1}{2\epsilon} \int_{-\epsilon}^{\epsilon} dP \left[\frac{3\phi_d^4}{8} \eta^4 + \frac{\phi_d^2}{2} \eta^2 + 3\phi_d^2 P^2 \eta^2 \right] \tag{5.16}$$

where $\langle \hat{p}^4 \rangle_0 \epsilon^4/5$ has been inserted. As for the second-order moment, it is convenient to expand η^4 in a cosine series [see Appendix B] to obtain

$$\begin{aligned} \eta^4 =& \frac{n}{3}(2n^2+1) + \sum_{q=1}^{n-1} (-1)^{q(\ell-r)} \left(q^3 - 2nq^2 - q + \frac{2n}{3}(2n^2+1) \right) \cos(2q\pi\ell P) \\ & - \sum_{q=n}^{2n-2} (-1)^{q(\ell-r)} \left[\frac{q^3}{3} - 2nq^2 + \left(4n^2 - \frac{1}{3} \right) q + \frac{2n}{3}(1-4n^2) \right] \cos(2q\pi\ell P). \end{aligned} \tag{5.17}$$

Substituting the expansions given in Eqs. (5.17) and (5.3) into Eq. (5.16), and evaluating the integrals using

$$\int_{-\epsilon}^{\epsilon} P^2 \cos(2q\pi\ell P) dP = \frac{\epsilon^2 \sin(2q\pi\ell\epsilon)}{q\pi\ell} - \frac{\sin(2q\pi\ell\epsilon)}{2(q\pi\ell)^2} + \frac{\epsilon \cos(2q\pi\ell\epsilon)}{(q\pi\ell)^2} \tag{5.18}$$

reveals,

$$\begin{aligned} \langle \hat{p}^4 \rangle_n =& \frac{\epsilon^4}{5} + \phi_d^4 \frac{2n^2+1}{8} n + \frac{3\phi_d^4}{16\pi\ell\epsilon} \sum_{q=1}^{n} a(q) \sin(2q\pi\ell\epsilon) \\ & - \frac{3\phi_d^4}{16\pi\ell\epsilon} \sum_{q=n}^{2n-2} b(q) \sin(2q\pi\ell\epsilon) + \frac{\phi_d^2 n}{2} + \phi_d^2 \sum_{q=1}^{n-1} \frac{c(q)}{2q\pi\ell\epsilon} \sin(2q\pi\ell\epsilon) + \phi_d^2 \epsilon^2 n \\ & + \frac{3\phi_d^2}{\epsilon} \sum_{q=1}^{n-1} c(q) \left[\frac{\epsilon}{(q\pi\ell)^2} \cos(2q\pi\ell\epsilon) + \frac{\epsilon^2}{q\pi\ell} \sin(2q\pi\ell\epsilon) \right. \\ & \left. - \frac{1}{2(q\pi\ell)^3} \sin(2q\pi\ell\epsilon) \right], \end{aligned} \tag{5.19}$$

where,

$$\begin{aligned} a(q) =& (-1)^{q(\ell-r)} \left[q^2 - 2nq - 1 + \frac{2n}{3q}(2n^2+1) \right], \\ b(q) =& (-1)^{q(\ell-r)} \left[\frac{q^2}{3} - 2nq + \left(4n^2 - \frac{1}{3} \right) + \frac{2n}{3q}(1-4n^2) \right], \\ c(q) =& (-1)^{q(\ell-r)} (n-q). \end{aligned} \tag{5.20}$$

5.1.4 Low-Temperature Limit of Fourth-Order Moment

For $\epsilon \to 0$, Eq. (5.19) can be shown straightforwardly to reduce to

$$\langle \hat{p}^4 \rangle = \phi_d^4 \frac{(2n^2+1)n}{8} + \frac{3\phi_d^4}{8} \sum_{q=1}^{n-1} a(q) q - \frac{3\phi_d^4}{8} \sum_{q=n}^{2n-2} b(q) q + \frac{\phi_d^2 n}{2} + \phi_d^2 \sum_{q=1}^{n-1} c(q) \tag{5.21}$$

Resonance

The summations in Eq. (5.21) can be computed using the identities

$$\sum_{q=1}^{n-1} q^2 = \frac{1}{6}\left(2n^3 - 3n^2 + n\right), \tag{5.22}$$

$$\sum_{q=1}^{n-1} q^3 = \frac{1}{4}\left(n^4 - 2n^3 + n^2\right). \tag{5.23}$$

to obtain,

$$\langle \hat{p}^4 \rangle = \frac{3\phi_d^4}{8} n^4 + \frac{\phi_d^2}{2} n^2, \tag{5.24}$$

as expected from Eq. (4.61b). Note that higher-order summations can be computed using Bernouilli's Formula[1] for sums of powers, and these merely generate the polynomial $R_{2m}(\phi_d n)$ defined previously.

Anti-Resonance

The antiresonant case in the ultracold limit can be verified using

$$\sum_{q=1}^{n-1} (-1)^q q^2 = (-1)^{n-1} \frac{n(n-1)}{2} \tag{5.25}$$

and

$$\sum_{q=1}^{n-1} (-1)^q q^3 = (-1)^{n-1} \frac{n^2(3-2n)}{4} - \frac{\left[(-1)^{n-1} - 1\right]}{8}, \tag{5.26}$$

with Eq. (5.21) to give,

$$\langle \hat{p}^4 \rangle = \left(\frac{3\phi_d^4}{16} + \frac{\phi_d^2}{4}\right)\left[(-1)^{n-1} + 1\right]. \tag{5.27}$$

5.1.5 High-Temperature Limit of Fourth-Order Moment

In the high-temperature limit, Eq. (5.19) becomes,

$$\begin{aligned}\langle \hat{p}^4 \rangle_n =& \frac{\epsilon^4}{5} + \phi_d^4 \frac{2n^2+1}{8} n + \phi_d^2 \epsilon^2 n + \frac{\phi_d^2 n}{2} \\ &+ 3\phi_d^2 \sum_{q=1}^{n-1} c(q) \left[\frac{1}{(q\pi\ell)^2} \cos(2q\pi\ell\epsilon) + \frac{\epsilon}{q\pi\ell} \sin(2q\pi\ell\epsilon)\right],\end{aligned} \tag{5.28}$$

In contrast to the second-order moment, Eq. (5.28) has a dependence on the parity of $\ell - r$, and will therefore undergo different growth in the resonant and antiresonant regimes. An additional complication at fourth-order, is that the

[1] This is sometimes known as Faulhaber's Formula.

limit $\epsilon \to \infty$ is less obvious since terms involving ϵ-dependent sines and cosines survive. Consequently, a more intelligent limit must be used to examine the high-temperature regime.

Peculiarities of the Uniform Distribution

As discussed in section (3.2.1), Bloch theory implies that all of the dynamics are encapsulated in the quasimomentum subspace corresponding to $k = 0$, namely, the first Brillouin zone. In addition, the Floquet operator $\tilde{F}_n(\beta)$ [See Eq. (3.30)] is periodic in β, with period $1/\ell$, up to a β-dependent phase. This implies that the Brillouin zone can be divided into ℓ Brillouin subzones, where each individually describes the entire dynamics of the system.

Given this, it can be seen that increasing ϵ for an initial uniform momentum distribution periodically reproduces the same moment dynamics as narrower initial distributions, except for a different initial condition. This property is peculiar to a uniform initial distribution; increasing ϵ includes more Brillouin subzones, potentially from different k-subspaces, but with equal weights. Therefore, an appropriate high-temperature limit is[2] $\epsilon = \tilde{\epsilon}/2\ell$ for some positive integer $\tilde{\epsilon}$. In this new limit, Eq. (5.19) becomes,

$$\begin{aligned}\langle \hat{p}^4 \rangle_n =& \frac{\epsilon^4}{5} + \phi_d^4 \frac{2n^2+1}{8} n + \frac{\phi_d^2 \tilde{\epsilon}^2}{4\ell^2} n + \frac{\phi_d^2}{2} n \\ &+ 3\frac{\phi_d^2}{\pi^2 \ell^2} \sum_{q=1}^{n-1} (-1)^{q(\ell-r)} \frac{n-q}{q^2},\end{aligned} \tag{5.29}$$

Clearly, this diverges for $\tilde{\epsilon} \to \infty$, as one would expect of a momentum moment in this limit. As aforementioned, a better quantity for that limit would be the corresponding cumulant; however, the choice $\epsilon = \tilde{\epsilon}/2\ell$ includes all orders of antiresonance and resonance with equal weightings, and therefore adequately mimics the high-temperature limit $\epsilon \to \infty$ without the diverging momentum moment.

The evaluation of the summation is made difficult by the presence of a reciprocal power of q; however, only the growth with respect to n is crucial here. A useful approach is to examine the upper bound. On resonance,

$$\sum_{q=1}^{n-1} \frac{n-q}{q^2} = n \sum_{q=1}^{n-1} \frac{1}{q^2} - \sum_{q=1}^{n-1} \frac{1}{q} \leq \frac{\pi^2}{6} n \tag{5.30}$$

On antiresonance, the contribution will be even smaller; in both cases, the maximum contribution to the fourth-order moment from the corresponding summa-

[2]Note that the uniform distribution ranges from $-\epsilon$ to ϵ.

tion is linear, and will therefore be neglected. Thus, the fourth-order moment in the high-temperature regime is

$$\langle \hat{p}^4 \rangle_n = \frac{\epsilon^4}{5} + \frac{\phi_d^4}{8}(2n^2+1)n + \phi_d^2\epsilon^2 n + \frac{\phi_d^2}{2}n, \tag{5.31}$$

and the corresponding fourth-order momentum cumulant is given by

$$\langle\langle \hat{p}^4 \rangle\rangle_n = -\frac{2\epsilon^4}{15} + \frac{\phi_d^4}{8}(2n^2+1)n - \frac{3\phi_d^4}{4}n^2 + \frac{\phi_d^2}{2}n. \tag{5.32}$$

5.1.6 Intermediate Initial Momentum Widths

Although the width of uniform momentum distribution does not correspond directly to a temperature, its extremes can be associated with the low- and high-temperature regimes. In the context used here, the uniform momentum distribution mainly serves to provide a mixture of different initial quasimomenta. The fact that the mixture does not represent a thermal distribution over such states should not be crucial since the effect of finite-temperature in this model is simply to provide a distribution of quasimomenta. It is expected, therefore, that the examination of initial momentum widths of an initial uniform momentum distribution may yield some insight into the temperature dependence of the momentum moment dynamics, whilst retaining the relative simplicity of the calculations.

Resonance

The dependence on ϵ is studied by numerically evaluating the second- and fourth-order moments given by Eqs. (5.4) and (5.4), respectively. Figures 5.2(a)(i) and 5.2(b)(i) show the momentum moments in the resonant regime for a range of initial widths. These initial widths are chosen to firstly represent the range of behaviour observable in this system, but also so that they fall within the reach of current experiments, although to obtain such low temperatures it has been necessary to use Bose-Einstein Condensates. Experiments using non-degenerate gases [69, 133, 134] had initial standard deviations of the momentum distribution between approximately $2\hbar K$ and $4\hbar K$ (2 and 4 in the dimensionless units used in this work). However, later BEC experiments [135] obtained momentum standard deviations of approximately $0.01\hbar K$.

The initial growth for the momentum moments follows closely the asymptotic behaviour in the ultracold regime, in agreement with the results from Sec. 4.4.

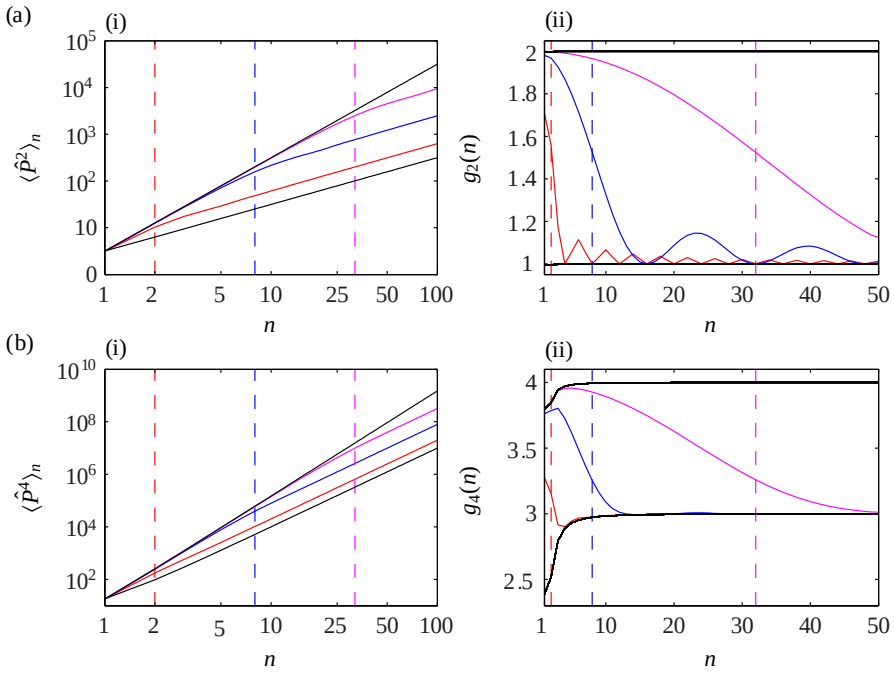

Figure 5.2: The resonant momentum moment dynamics for an initial uniform distribution with width 2ϵ, with $\ell = 2$, $r = 0$, and $\phi_d = 0.8\pi$. Panels (a) and (b) demonstrate the growth of the second- and fourth-order momentum moments [See Eqs. (5.4) and (5.19)], respectively, for (-) $\epsilon = 1/8$, (-) $\epsilon = 1/32$ (-) $\epsilon = 1/128$, with the corresponding break times, given by $n^\star = 1/2L\epsilon$, indicated with vertical dashed lines. Series (i) graph the momentum moments directly, whereas series (ii) shows the numerical gradient of the corresponding log-log data in series (i), and is therefore indicates the dominant power-law growth. Solid black lines are given by the asymptotic behaviour in the ultracold and high-temperature regimes [See Eqs.(4.61a) and (4.61b)]. Units are dimensionless.

At some time, $n^\star$, the growth of the moments significantly diminishes, and approaches the asymptote representing the high-temperature limit. For initially narrower distributions, the break time, $n^\star$, is delayed. Initially narrower distributions, therefore, behave similarly to initial momentum eigenstates on resonance until $n = n^\star$, before averaging effects, due to widespread population of the Brillouin subzone, eventually curtail the growth.

The break time can be estimated by considering the value of n such that the summation in Eqs. (5.4) first becomes negative. This occurs when $n = n^\star = 1/2\ell\epsilon$, and represents the characteristic timescale over which a mixture of momentum eigenstates may mimic growth in the ultracold regime. For example, initial distributions that fill an entire Brillouin subzone, such that $\epsilon \geq 1/2\ell$ break before the first kick and will always be observed in the high-temperature regime.

Figures 5.2(a)(ii) and 5.2(b)(ii) show the numerically calculated gradients[3], $g_2(n)$ and $g_4(n)$, for $\langle \hat{P}^2 \rangle_n$ and $\langle \hat{P}^4 \rangle_n$, respectively, which represent the index of the prevailing power-law growth. It is clear that, initially, the power-law growth of $\langle \hat{P}^{2m} \rangle_n$ $(m = 1, 2)$ for very narrow distributions is n^{2m}. The power $g_2(n)$ gradually decreases, until at the break time $g_2(n^\star) \approx 1.5$, before undergoing damped oscillations to $g_2(n) = 1$ from above. Similarly,, the power of the fourth-order moment, $g_4(n)$, experiences a transient decay from $g_4(n) \approx 4$ to $g_4(n) = 3$, but with stronger damping. Note that in the low- and high-temperature regimes of the fourth-order momentum moment, the power-law growth also undergoes a transient. This is a consequence of the dependence on more than one order of n; by $n = 10$ the order n^4 sufficiently dominates n^2 that the growth is mostly fourth-order in n.

The break times, given by $\epsilon = 1/2\ell$, predict the onset of thermal effects in the second-order momentum moments consistently, and seem to occur approximately half-way between the two regimes. However, for the fourth-order momentum moments, they appear to occur after significant deviation from the power-law for the ultracold regime. This is reasonable since the fourth-order moments included second-order effects, and will therefore be susceptible to competition of second-order effects at the break time, and purely fourth-order effects which are still driving resonant growth.

[3]Note that since the moment dynamics are discrete, it is impossible to improve the smoothness of the derivatives.

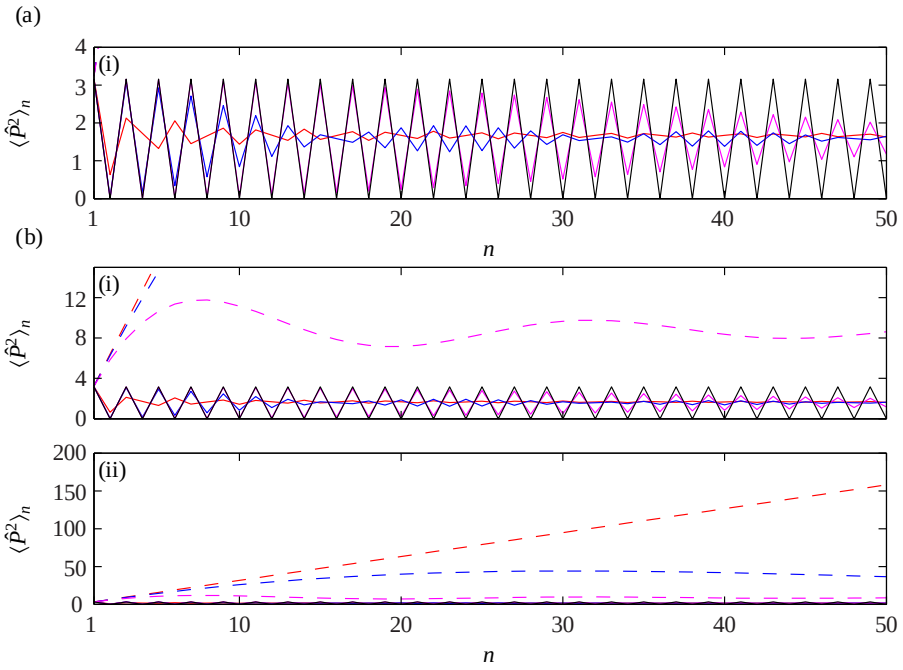

Figure 5.3: The antiresonant dynamics of the second-order moment for an initial uniform distribution [See Eqs. (5.4) and (5.19)] with width 2ϵ, with $\ell = 1$, $r = 0$, and $\phi_d = 0.8\pi$. Panel (a) shows the dependence on ϵ close to the ultracold regime, for (-) $\epsilon = 1/8$, (-) $\epsilon = 1/32$ (-) $\epsilon = 1/128$. The solid black line corresponds to ideal antiresonant behaviour [See Eq. (4.65a)]. Panel (b) shows the small scale (i) and the large scale (i) dependence on ϵ close to the high-temperature regime, for (- -) $\epsilon = w^\star$, (- -) $\epsilon = 0.98w^\star$ (–) $\epsilon = 0.92w^\star$, where $w^\star = 1/2L$ is half the width of the Brillouin subzone. Units are dimensionless.

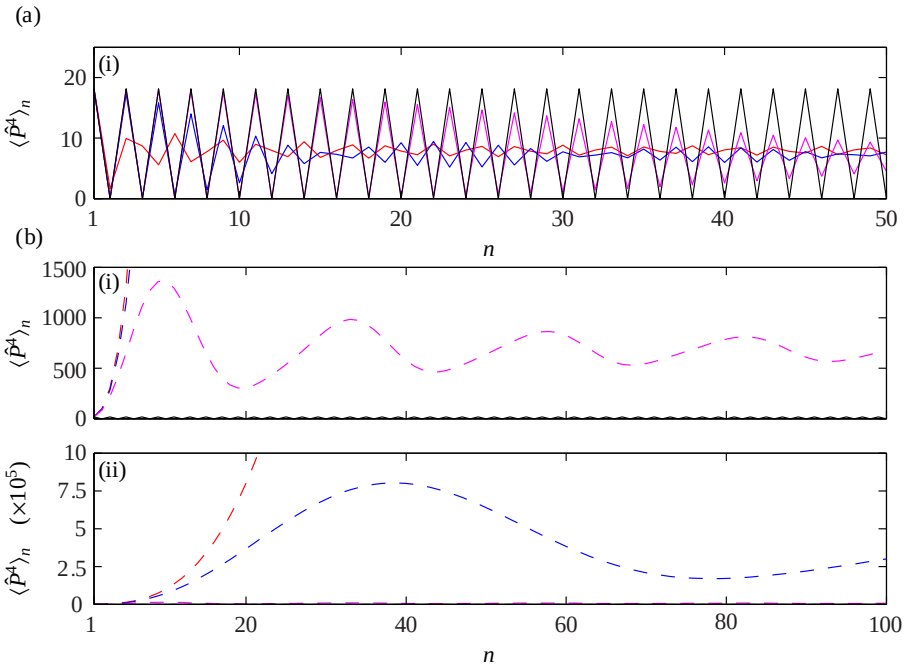

Figure 5.4: The antiresonant dynamics of the fourth-order moment for an initial uniform distribution [See Eqs. (5.3) and (5.27)] with width 2ϵ, with $\ell = 1$, $r = 0$, and $\phi_d = 0.8\pi$. Panel (a) shows the dependence on ϵ close to the ultracold regime, for (-) $\epsilon = 1/8$, (-) $\epsilon = 1/32$ (-) $\epsilon = 1/128$. The solid black line corresponds to ideal antiresonant behaviour [See Eq. (4.65b)]. Panel (b) shows the small scale (i) and the large scale (i) dependence on ϵ close to the high-temperature regime, for (- -) $\epsilon = w^\star$, (- -) $\epsilon = 0.98w^\star$ (- -) $\epsilon = 0.92w^\star$, where $w^\star = 1/2L$ is half the width of the Brillouin subzone. Units are dimensionless.

Anti-Resonance

Antiresonant behaviour of the second- and fourth-order momentum moments are shown in Figs. (5.3) and (5.4), respectively. Panel (a) in both figures shows the nearly ultracold behaviour, and demonstrates that initially very narrow distributions closely follow ideal antiresonant dynamics. After some time, they finally decay to an average value, dictated mainly by the initial width. Upon examination of the mechanisms in the relevant summations, these damped dynamics can be seen to correspond to very weak linear growth. However, over the timescales examined here, the growth is so weak that it can neglected. To support this claim, panel (b) shows the long-term behaviour for the same initial conditions, where now the dynamics close to the high-temperature regime can be seen. In the sense described above, the high-temperature regime is accessed by choosing $\epsilon = \epsilon^\star = 1/2L$ so that one Brillouin subzone is completely occupied. For the timescales considered here, the growth in the near-ultracold regime appears totally saturated.

The growths shown in Fig. (5.3)(b)(i)-(ii) show that initially broad momentum distributions experience rapid growth, which scales as n^{2m-1}, until reaching saturation. For broader distributions, this can be delayed for arbitrarily long times. The mechanism for this can be understood by considering widths of the form $\epsilon = 1/2L - \delta$, for some small parameter δ, so that an entire Brillouin subzone is almost entirely filled. After a little algebra, and imposing the antiresonance condition, Eqn. (5.4) suggests that,

$$\begin{aligned}\langle \hat{P}^2 \rangle_n - \langle \hat{P}^2 \rangle_0 =& \frac{\phi_d^2}{2} n - \frac{\phi_d^2}{\pi(1-2\ell\delta)} \left[n \sum_{q=1}^{n-1} (-1)^q \frac{\sin(2q\pi\ell\delta)}{q} \right. \\ & \left. - \sum_{q=1}^{n-1} (-1)^q \sin(2q\pi\ell\delta) \right], \end{aligned} \tag{5.33}$$

For $\delta < 1/2\ell n$, the initial growth can be approximated by

$$\begin{aligned}\langle \hat{P}^2 \rangle_n - \langle \hat{P}^2 \rangle_0 \approx& \frac{\phi_d^2}{2} n - \frac{2\ell\delta\phi_d^2}{(1-2\ell\delta)} \left[n \sum_{q=1}^{n-1} (-1)^q - \sum_{q=1}^{n-1} (-1)^q q \right] \\ =& \frac{\phi_d^2}{2} n + \frac{\ell\delta\phi_d^2}{2(1-2\ell\delta)} \left[2n - (-1)^{n-1} - 1 \right] \\ \approx& \frac{\phi_d^2}{2} n + \ell\delta\phi_d^2 n, \end{aligned} \tag{5.34}$$

which is linear in n, up to $n \approx 1/2\ell\delta$. Generally, this holds when $2q\pi\ell\delta$ modulo

2π is approximately zero. For large n, such that $2q\pi\ell\delta$ modulo $2\pi \approx \pi$,

$$\langle \hat{P}^2 \rangle_n - \langle \hat{P}^2 \rangle_0 \approx \frac{\phi_d^2}{2} n - \ell\delta\phi_d^2 n, \tag{5.35}$$

which also expresses linear growth.

For large n, such that $\delta < 1/2\ell n$ no longer holds, the oscillatory nature of the summand begins to have an influence. For mathematical convenience, the limit $n \to \infty$ is taken, and using the identity [136],

$$\sum_{q=1}^{\infty} \frac{(-1)^q}{q} \sin(qx) = -\frac{x}{2}, \tag{5.36}$$

Eq. (5.4) may be written as

$$\langle \hat{P}^2 \rangle_n - \langle \hat{P}^2 \rangle_0 = -\sum_{q=1}^{\infty} (-1)^q \sin(2q\pi\ell\epsilon), \tag{5.37}$$

which describes a oscillatory evolution of the momentum moments that is small in comparison with the initial growth, thereby explaining the observed saturation of the moments. However, it should be noted that the saturation depends critically on the properties of $\Theta(P)$. Specifically, there is a cut-off in the momentum range included initially, which permits only a fraction of the Brillouin subzone to participate in the dynamics.

The strong influence of widths close to the width of a Brillouin subzone allows the effect of high-order antiresonances in the quasimomentum subspace to be explored in a systematic way. However, this dependence is in some sense pathological, and depends on the discontinuous cutoff introduced by the uniform distribution, and is not necessarily typical of dynamics that will be observed in physical implementations.

5.2 Gaussian Distribution

A physically more reasonable initial momentum distribution is one with a Gaussian form. This is a commonly encountered momentum distribution following cooling of an ideal atomic gas, provided there is sufficient time to reach thermal equilibrium. Unlike the uniform momentum distribution, it covers many Brillouin subzones initially, even for narrow momentum widths, and is therefore not subject to the peculiarities mentioned in the previous section. In this section, the dynamics resulting from an initial Gaussian momentum distribution will be examined in detail, and the effect of different initial temperatures, corresponding the standard deviation, will be studied.

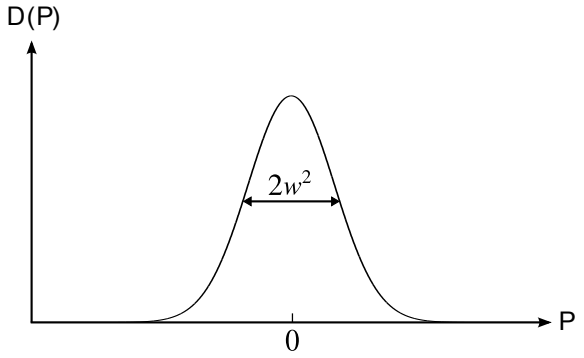

Figure 5.5: The Gaussian momentum distribution with a variance w^2.

The initial momentum distribution, $D(P)$, is assumed to be

$$D(P) = \frac{1}{\sqrt{2\pi w^2}} \exp(-P^2/2w^2), \tag{5.38}$$

where w is the standard deviation, and the corresponding Boltzmann temperature is given by $\mathcal{T}_w = \hbar^2 K^2 w^2 / M k_B$, where k_B is Boltzmann's constant.

As for the case where $D(P) = \Theta(P)$, Ω is constrained to take integer values, therefore fractional quantum resonances derived for $\Omega = 1/s$ in the ultracold limit [see Sec. 4.4.1] are not considered here. The procedure for deriving the moments in the resonant or antiresonant regimes is identical to that in Sec. (5.1) and uses similar identities, although the algebra is more involved. For brevity, only final results are given, and all intermediate results, if already stated in Sec. (5.1), are tacitly assumed.

5.2.1 Second-Order Momentum Moment

Using Eq. (4.31) with Eq. (5.38), and using the cosine expansion in Eq. (5.3), yields

$$\langle \hat{P}^2 \rangle_n = w^2 + \frac{\phi_d^2}{2} n + \phi_d^2 \sum_{q=1}^{n-1} (-1)^{q(\ell - r)} (n-q) e^{-2q^2 \ell^2 \pi^2 w^2}, \tag{5.39}$$

where it has been necessary to evaluate the integral [136]

$$\frac{1}{\sqrt{2\pi w^2}} \int_{\infty}^{\infty} dP P^2 \cos(2q\pi\ell P) e^{-P^2/2w^2} = w^2 (1 - 4q^2 \ell^2 \pi^2 w^2) e^{-2q^2 \ell^2 \pi^2 w^2}. \tag{5.40}$$

5.2.2 Low-Temperature Limit of the Second-Order Moment

In the limit $w \to 0$, Eq. (5.39) becomes,

$$\langle \hat{P}^2 \rangle_n = \frac{\phi_d^2}{2} n + \phi_d^2 \sum_{q=1}^{n-1} (-1)^{q(\ell - r)} (n - q). \tag{5.41}$$

In the resonant, and antiresonant cases, both Eq. (4.61a) and Eq. (4.65a) are recovered, as expected.

5.2.3 High-Temperature Limit of the Second-Order Moment

Unlike the high-temperature limit of the uniform distribution, one may simply allow $w \to \infty$ for initial Gaussian momentum distributions; increasing P still includes more Brillouin subzones, but for a Gaussian distribution they have a decreasing weight relative to the subzones corresponding to smaller discrete momentum values, k. Therefore, the limit is well-defined.

Imposing this limit in Eq. (5.41) gives

$$\langle \hat{P}^2 \rangle_n = w^2 + \frac{\phi_d^2}{2} n, \tag{5.42}$$

which, except for the trivially different initial condition, agrees with Eq. (5.15).

5.2.4 Fourth-Order Momentum Moment

Similarly, upon substitution Eq.(5.38) into Eq. (4.32), one obtains,

$$\begin{aligned}
\langle \hat{P}^4 \rangle =& 3w^4 + \frac{\phi_d^4}{8}(2n^2 + 1)n + \frac{\phi_d^2}{2} n + 3w^2 \phi_d^2 n \\
&+ \frac{3\phi_d^4}{8} \sum_{q=1}^{n-1} (-1)^{q(\ell - r)} e^{-2q^2 \ell^2 \pi^2 w^2} \left[q^3 - 2nq^2 - q + \frac{2n}{3}(2n^2 + 1) \right] \\
&- \frac{3\phi_d^4}{8} \sum_{q=n}^{2n-2} (-1)^{q(\ell - r)} e^{-2q^2 \ell^2 \pi^2 w^2} \left[\frac{q^3}{3} - 2nq^2 + \frac{(12n^2 - 1)}{3} q + \frac{2n}{3}(1 - 4n^2) \right] \\
&+ \phi_d^2 \sum_{q=1}^{n-1} (-1)^{q(\ell - r)} (n - q) e^{-2q^2 \ell^2 \pi^2 w^2} \\
&+ 6\phi_d^2 \sum_{q=1}^{n-1} (-1)^{q(\ell - r)} (n - q) w^2 (1 - 4w^2 q^2 \ell^2 \pi^2) e^{-2q^2 \ell^2 \pi^2 w^2}.
\end{aligned} \tag{5.43}$$

where the integral [136],

$$\frac{1}{\sqrt{2\pi w^2}} \int_{\infty}^{\infty} dP \cos(2q\pi \ell P) e^{-P^2/2w^2} = e^{-2q^2 \pi^2 \ell^2 w^2}, \tag{5.44}$$

has been used. Note that in the ultracold limit both the resonance and antiresonance behaviours expressed in Eqs.(4.61b) and (4.65b), respectively, are reproduced, serving as a validation of Eq. (5.44).

5.2.5 High-Temperature Limit of the Fourth-Order Momentum Moment

In the high-temperature limit, for which $\epsilon \to \infty$, it is straightforward to see that the fourth-order moment is,

$$\langle \hat{P}^4 \rangle = 3w^4 + \frac{\phi_d^4}{8}(2n^2+1)n + \frac{\phi_d^2}{2}n + 3w^2\phi_d^2 n. \tag{5.45}$$

which is independent of $\ell - r$.

5.2.6 Transient Temperatures

Resonances

As for an initial uniform momentum distribution, the dependence on the initial standard deviation can be investigated by numerically evaluating Eqs.(5.39) and (5.43). Figure (5.6) shows the second- and fourth-order momentum moments in the resonant regime for the same initial standard deviations as the dynamics described in Sec. 5.1. The momentum moments adopt similar behaviour as that for an initial uniform momentum distribution, and also agree with the asymptotic limits. In contrast, however, the approach to the limiting behaviour of $g_2(n)$ and $g_4(n)$ is monotonic, rather than the oscillatory approach in Sec. 5.1, and appears less strongly damped. The consequence of this is that dynamics derived from an initial Gaussian distribution approach the high-temperature regime more slowly than for an initial uniform momentum distribution for identical initial standard deviations. The reason for this is that many Brillouin subzones are initially populated, with weights distributed as a Gaussian across each subzone. On resonance, the peak of the Gaussian is centered on the resonance, and therefore resonant effects are able to compete more strongly with high-order antiresonant effects until eventually succumbing to averaging effects.

Similar to Sec. 5.1 it is possible to discern a break time in the second-order moment. For a Gaussian distribution, the criterion for a break time is less forthcoming but a good approximation is to consider when the exponential term in Eq. (5.39) becomes small. A reasonable choice is decide that this occurs when

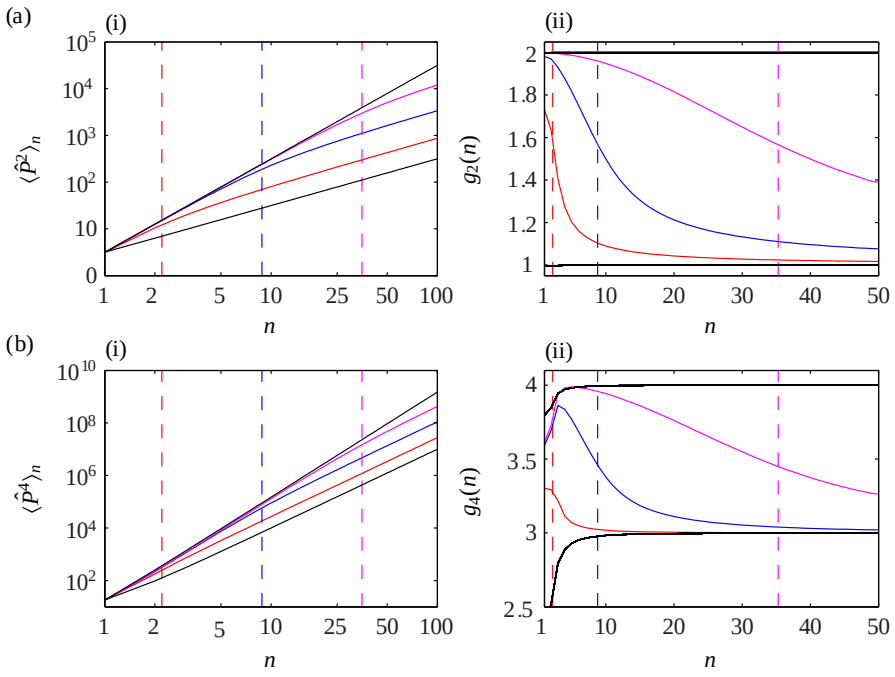

Figure 5.6: The resonant momentum moment dynamics for an initial Gaussian distribution with standard deviation w, with $L = 2$, $r = 0$, and $\phi_d = 0.8\pi$. Panels (a) and (b) demonstrate the growth of the second- and fourth-order momentum moments [See Eqs. (5.39) and (5.43)], respectively, for (-) $w = 1/8\sqrt{(3)}$, (-) $w = 1/32\sqrt{(3)}$ (-) $w = 1/128\sqrt{(3)}$, with the corresponding break times, given by $n^\star = 1/\pi L w$, indicated with vertical dashed lines. Series (i) graph the momentum moments directly, whereas series (ii) shows the numerical gradient of the corresponding log-log data in series (i), and is therefore indicative of the dominant power-law growth. Solid black lines are given by the asymptotic behaviour in the ultracold and high-temperature regimes [See Eqs.(4.61a) and (4.61b)]. Units are dimensionless.

$n = n_G^\star = 1/\pi \ell w$, and these times are indicated by vertical dashed lines in Fig. (5.6). As for the case of an initial uniform distribution, the break times mark approximately half-way between the limiting regimes, where the prevaling power-law growth is $n^{3/2}$, and adequately describe the transition between regimes in the fourth-order momentum moment.

Antiresonances

Antiresonant behaviour of the second- and fourth-order momentum moments for an initial Gaussian momentum distribution are shown in Figs. 5.7 and 5.8, respectively. It is clear that the effect of the initial width is, as for an initial uniform momentum distribution, to set a timescale over which the oscillations mimicking ideal antiresonant dynamics decay. In contrast to the dynamics in Sec. 5.1, growth of the moments can be seen once oscillations have significantly decayed, although the growth is particularly weak. In Figs.5.7 and 5.8, panels (b) show the long-term dynamics of panels (a), and demonstrates the continued linear growth of the second-order moments long after oscillations are no longer observable. This is a direct consequence of the unequal weighting of quasimomentum in the initial distribution, and should be expected of all smooth initial momentum distributions. The dynamics of the fourth-order momentum moment proceed along similar lines, except the surviving growth approaches cubic growth for large widths.

5.3 Summary

For both initial momentum distributions examined in this chapter, the power-law growths in the ultracold limit and the high-temperature limit, as derived in the previous chapter, are obeyed. The general power-laws were shown to depend only on some characteristic width, σ, of the distribution exceeding $1/2\ell$, provided the distributions were symmetric, and were generally well populated about $P = 0$. These results have been demonstrated to hold for two initial momentum distributions where the characteristic width represents a different quantity.

Considering Gaussian and uniform initial momentum distributions, it has been possible to examine in detail the transient effect of varying the initial width of the distribution. In the former case, this corresponded directly to a change in initial temperature. In the resonant regime, the temperature dependence of the second- and fourth-order momentum moments for both distributions is similar, and can be seen to switch significantly from the ultracold regime to the high-temperature regimes at a characteristic time $n^\star \sim 1/\ell$. However, in the antiresonant regime, the dynamics approach the limiting behaviours in qualitatively different ways. For uniform distributions, it is possible to populate

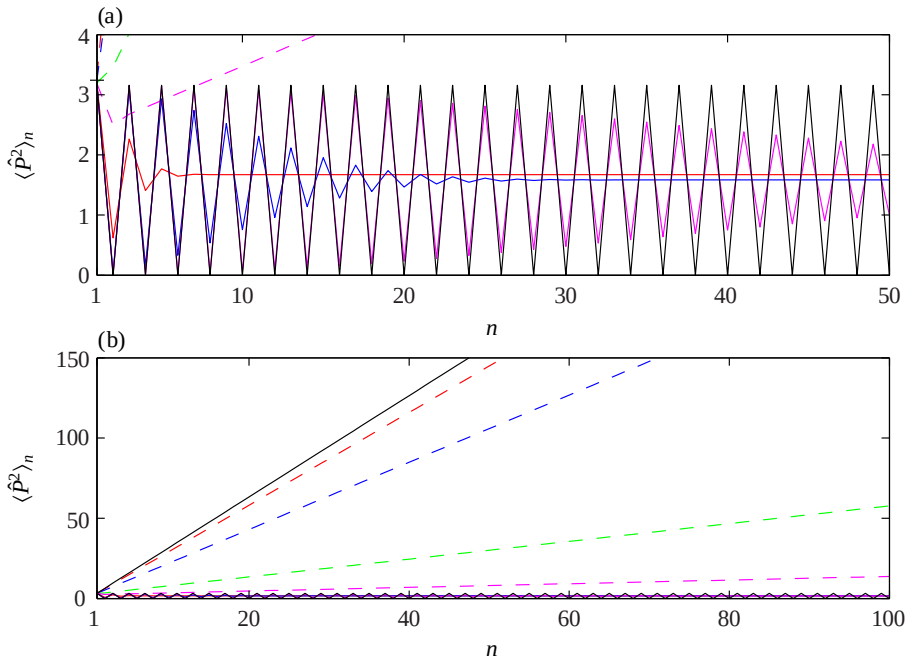

Figure 5.7: The antiresonant dynamics of the second-order moment for an initial Gaussian distribution [See Eq. (5.39)] with standard deviation w, with $L = 1$, $r = 0$, and $\phi_d = 0.8\pi$. The dependence on w is shown, for (-) $w = 1/8\sqrt{3}$, (-) $w = 1/32\sqrt{3}$, (-) $w = 1/128\sqrt{3}$, (- -) $w = 0.4$, (- -) $w = 0.3$, (- -) $w = 0.3$, and (- -) $w = 0.1592$. The value of $w = 0.1592$ correspond to a break time occurring at the first kick. The solid black line corresponds to ideal antiresonant behaviour [See Eq. (4.65a)]. Panel (b) shows the large scale behaviour of the moments. Units are dimensionless.

momentum eigenstates in a single Brillouin subzone only, and mimic the effect of the high-temperature regime, but only until some time where the growth of the momentum moments completely saturates. For initial widths much larger than $1/2L$, the correct power-law growth is recovered.

Figure 5.9 shows a comparison of the fourth-order cumulants for both Gaussian and uniform initial momentum distributions, for equal initial standard deviations. The fourth-order cumulant represents the partition of kinetic energy amongst the ensemble (with respect to a Gaussian distribution). Unlike the moments, which are necessarily positive, cumulants may be negative, and indeed, $\langle\langle \hat{P}^4 \rangle\rangle$ is negative initially. This may be interpreted as a degree of localisation of kinetic energy, i.e., few atoms move quickly - these are the ballistic peaks

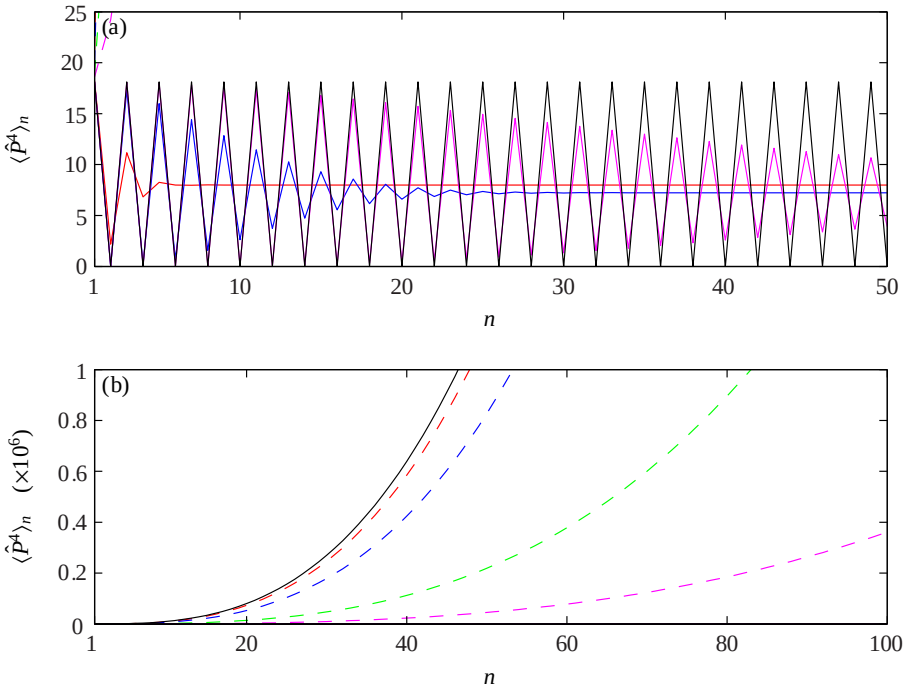

Figure 5.8: The antiresonant dynamics of the fourth-order moment for an initial Gaussian distribution [See Eq. (5.19)] with standard deviation w, with $L = 1$, $r = 0$, and $\phi_d = 0.8\pi$. The dependence on w is shown, for (-) $w = 1/8\sqrt{3}$, (-) $w = 1/32\sqrt{3}$, (-) $w = 1/128\sqrt{3}$, (- -) $w = 0.4$, (- -) $w = 0.3$, (- -) $w = 0.3$, and (- -) $w = 0.1592$. The value of $w = 0.1592$ correspond to a break time occurring at the first kick. The solid black line corresponds to ideal antiresonant behaviour [See Eq. (4.65b)]. Panel (b) shows the large scale behaviour of the moments. Units are dimensionless.

referred to in Ref. [86]. As the initial temperature increases, the kinetic energy is more equally spread through the ensemble, given by a large, positive value of $\langle\langle \hat{P}^4 \rangle\rangle$. The turning point appears to begin to manifest at the break time; in this instance, however, this is not simply a manifestation of second-order effects, since the fourth-order cumulant is an independent quantity. Physically, one can imagine that the transition from quadratic growth to linear growth in the kinetic energy signals the onset of an underlying averaging effect which subsequently results in the redistribution of kinetic energy, hence increasing $\langle\langle \hat{P}^4 \rangle\rangle$. Also observable is that the onset of thermal effects is prolonged for Gaussian momentum distributions, and increasingly so for broader initial momentum distributions. Additionally, in the low- and high-temperature limit, the cumulant obeys the

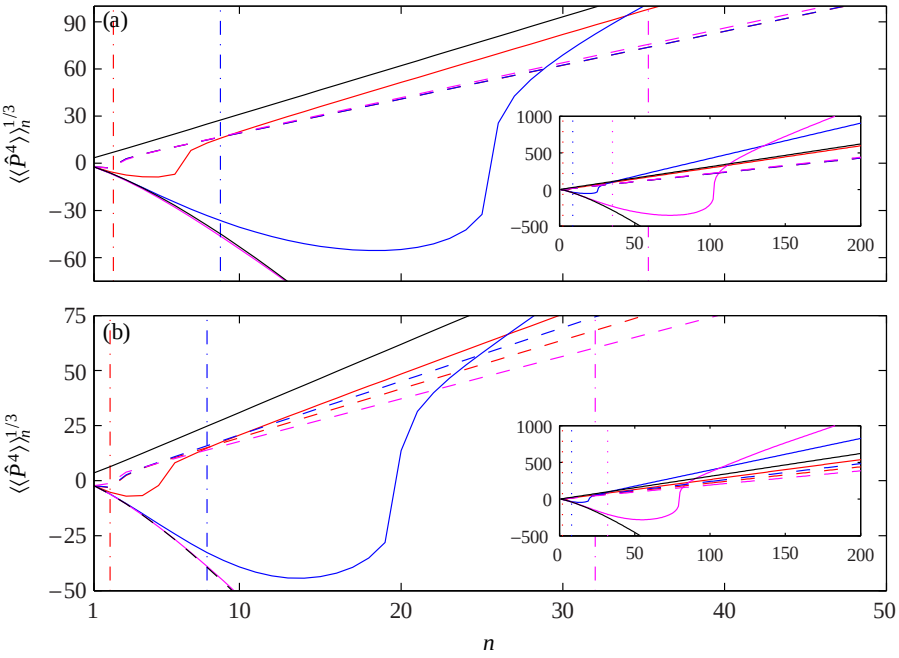

Figure 5.9: The resonant dynamics of the fourth-order cumulant for (a) an initial gaussian distribution with standard deviation w and (b) an initial uniform distribution with width 2ϵ, where $L = 2$, $r = 0$, and $\phi_d = 0.8\pi$. The dependence on w is shown, for (-) $w = 1/8\sqrt{3}$, (-) $w = 1/32\sqrt{3}$, (-) $w = 1/128\sqrt{3}$, (- -) $w = 0.4$, (- -) $w = 0.3$, (- -) $w = 0.3$. The solid black lines correspond to ideal resonant behaviour in the ultracold and high-temperature regimes. Insets in both panels demonstrate the long-term behaviour of the cumulants. Units are dimensionless.

same general power laws showing that these effects are not manifestations of lower-order effects.

In both momentum distributions, resonant and antiresonant behaviour is rapidly suppressed by finite-temperature effects. For Gaussian distributions, very low temperatures are required to observe these effects for appreciable kick-numbers. This is clearly shown in the initial experiments on the AOKA, where $\sigma \approx 2$, and linear growth in the kinetic energy was observed. Although it had previously been shown that asymptotic linear growth was expected in a thermal regime, a timescale for these dynamics was not predicted. For the initial temperature reported in Ref. [86], assuming initial an initial Gaussian momentum distribution, the break time on resonance is $n^\star = 1/\pi\ell w < 1$. To observe

quadratic growth of the kinetic energy (i.e. the second momentum moment) for up to 10 kicks, assuming $\Omega = 0$, one would require $w \approx 0.015$. The observation in Ref. [86] of quadratic growth was qualitative only, and the results of this chapter suggest that they observed sub-quadratic growth, such as that in the vicinity of the break time. In later experiments using Bose-Einstein Condensates for which $w = 0.002\hbar K$, quantitative measurements were made that clearly showed quadratic growth up to 20 kicks. In this instance, $n^\star \approx 80$ kicks, which is consistent with these observations. Indeed, in that work, it is stated that in their own numerical simulations the deviation from the growth corresponding to an initial momentum eigenstate is less than 10% from their experimental data.

Similarly narrow initial distributions are required to distinguish antiresonant effects. However, an inherent advantage is that since $\ell = 1$ for the first antiresonance, the break time may be twice that of the resonant case. In light of proposals to exploit quantum resonant and antiresonant dynamics for interferometric purposes [119, 120, 137, 138], it is evident that finite-temperature effects dramatically limit the interrogation time of any measurement. For example, proposals relying upon the sensitivity of Ω to the local gravitational acceleration require a clear measurement of quadratic growth to signal the selection of a resonance. Taking the results presented here into account, and also considering what effect atom-atom interactions might have if they were included, it would appear that finite-temperature effects may be overwhelmingly detrimental to such schemes.

However, the use of antiresonances as an atom-optical analogue of a beamsplitter and recombiner may be advantageous; only two kicks would be required for such a sequence. On antiresonance, ℓ may be unity, and therefore the break time may be doubled, permitting a significant delay to deleterious effects. In addition, large momenta are not encountered, and the problem of finite-pulse effects is averted. Moreover, the atomic sample remains trapped, permitting more control over its interaction with other constituents in any proposed interferometer. Such an experiment has recently been demonstrated [139].

Chapter 6

Conclusion

In this first part, the momentum moment dynamics of the atom-optical delta-kicked accelerator on resonance, without atom-atom interactions, for an initial state described by an incoherent ensemble of momentum eigenstates has been examined, for general symmetric initial momentum distributions in the ultracold and high-temperature regimes. General power-laws describing momentum moment growth were derived, and then verified for two experimentally feasible initial momentum distributions, where, importantly, it was possible to study the effect of finite-temperatures on the momentum moment dynamics.

The dynamics were determined stroboscopically (from kick-to-kick), with a time-period of the pulsed laser taken to integer multiples, ℓ, of the half-Talbot time. For this choice, the dynamics no longer undergo dynamical localisation, but instead may exhibit unbounded growth in momentum (resonances) or periodic revivals (antiresonance). Exact analytical expressions describing the time-evolution of the momentum moments were given. The importance of Gauss sums to the dynamics was stressed, and the conditions under which resonant and antiresonant behaviour manifested were derived in terms of the parity of ℓ and the rescaled local gravitational acceleration, Ω.

For general symmetric distributions with integer Ω, where only even momentum moments are nonzero, it was shown that on resonance in the ultracold limit, the $2m$-th momentum moment scaled with the number of kicks, n, as n^m. Exact expressions describing this growth were calculated. Likewise, on resonance in the high-temperature regime, it was shown that the momentum moments scale as n^{2m-1}. These results were extended to describe fractional resonances

in the ultracold regime, for which $\Omega = 1/s$, and showed that on resonance, the power-law growth of the momentum moments is n^{2m}/s^m.

The momentum cumulants, which are independent quantities unlike momentum moments, were calculated where feasible. In all cases, the leading order growth obeyed the derived power-laws in the ultracold and high-temperature regimes, suggesting that these laws were not simply manifestations of lower-order effects.

To illustrate these behaviours for experimentally feasible momentum distributions, the second- and fourth-order momentum moments for integer values of Ω were calculated for uniform and Gaussian initial momentum distributions. In both cases, the power-laws were obeyed in the limit where the initial characteristic width, σ, of the distribution was larger than $1/\ell$. In addition, the effect of finite-temperature, interpreted here as characteristic widths between the limiting behaviours, was examined in detail, for both resonant and antiresonant conditions. Under antiresonant conditions, the fourth-order momentum moments for both momentum distributions differed significantly, which was suggested to be a result of using an idealised uniform momentum distribution, where there is a cutoff in the included momentum range, rather than gradually decreasing tails as for a smooth distribution.

When including finite-temperature effects, antiresonant and resonant dynamics were quickly suppressed after a characteristic time $n^\star \sim 1/\ell\sigma$. The utility of the atom-optical kicked accelerator for sensitive measurements was discussed, and it was concluded that finite-temperature effects inhibit the use of resonances for such purposes. In contrast, quantum antiresonances, as already alluded to in recent experiments, may be useful as beamsplitting and recombination devices in matter-wave interferometry.

Part II

Bose-Einstein Condensates in Ring-Traps

Chapter 7

Introduction

Perhaps one of the most fundamental studies after the study of a single atom is the study of how atoms interact with other atoms. Many-body physics plays a role in many systems of practical and academic interest, and has generated a great deal of research in many different areas of science. Indeed, consideration of the three-body problem [34] eventually led to the beginnings of chaos theory [28, 30, 32, 33] which, arguably, is an important cornerstone of contemporary science.

Technological developments in the last few decades have allowed atomic and optical physics experiments to show what the original pioneers of quantum mechanics once thought impossible [140, 141]. The confinement of single-species atomic gases in well-characterised, finely-tuned trapping potentials [9–11] has allowed quantum systems to be tailor-made at an experimental level. With such control, it is possible to implement systems that are described, to an excellent approximation, by a prescribed Hamiltonian allowing particular many-body systems to be systematically explored both experimentally and theoretically [27]. Novel quantum phase transitions [142], the quantum Hall effect [143], Josephson oscillations [144, 145], many-body entanglement [146], and nonlinear wave-phenomena such as solitons [147–149] and quantised vortices [150, 151] are just a few examples of many-body phenomena observed in confined atomic gases. Although many-body effects can produce interesting nonlinear phenomena [27], they can also be deleterious in some applications [152–154]. It is sometimes possible to suppress their effect by, for example, using a magnetic Feshbach resonance [155, 156], or by reducing the atomic density to a level where 2-body

collisions are sufficiently rare that they do not play a part in the dynamics [152, 157]. The former method is not always possible to implement in practice, since in some species Feshbach resonances are associated with high inelastic losses [158], and the latter causes weaker signal to noise ratios in experimental signals [159]. In atom-interferometry, these drawbacks become more important, and can limit the accuracy and precision of the interferometer.

The theoretical treatment of many-body systems is, due to the many degrees of freedom involved, a difficult problem which often proves to be intractable. In many-body quantum mechanics, a range of different approaches has been developed to capture the essential physics at hand. Unfortunately, the inherent complexity of these systems means that these methods are inherently numerical, and are often very computationally intensive.

Given the difficulty of the general many-body problem, it is then desirable to study specific, simple many-body systems in order to investigate particular underlying physical effects. Using confined cold atomic gases is one way to do this, in a manner that allows equal progression of theory and experiment. The rapid advancement in the field of cold atomic physics is testament to the success of this partnership.

7.1 Bose-Einstein Condensation

One of the most straightforward many-body systems is a Bose-Einstein Condensate (BEC) [160, 161]. This was first predicted in 1925 by Einstein, who used Bose's statistical theory of bosons to predict the sudden macroscopic occupation of the ground state of an ideal gas of bosons below a certain temperature. The transition temperature, T_c, is given approximately by

$$T_c = \left[\frac{n}{\zeta(3/2)}\right]^{2/3} \frac{2\pi\hbar^2}{mk_B T}, \tag{7.1}$$

where n is the number density, m is the mass of an atom in the gas, T is the temperature, k_B is Boltzmann's constant, and $\zeta(x)$ is the Riemann Zeta function.[1] Atoms with an even number of nucleons can be considered as composite bosons, so that dilute atomic gases can be modelled as ideal Bose gases.

[1]The approximation (7.1) is valid only for a non-interacting gas, but it should be noted that atom-atom interactions are crucial for thermal equilibrium to be reached so that the atomic gas can be cooled.

For dilute atomic gases, T_c is on the order of 500nK, and required the development of sub-recoil laser cooling [9–11] and evaporative cooling [107] before there was any possibility of observing this phenomenon. Far below T_c, the atoms predominantly occupy, or *condense* into, the same state. The resultant gas is a coherent ensemble of all the atoms, and it therefore manifests distinctly quantum behaviour. The effect later became known as Bose-Einstein Condensation, and was verified experimentally in 1995 in work that later was awarded the Nobel prize for physics [162, 163].

In practice, a pure BEC does not exist, even at $T = 0$. A small non-condensed fraction of the atomic gas can persist because atom-atom interactions eventually become significant enough that it is not energetically favourable for all atoms to occupy the same quantum state. In some manifestations of BEC, this non-condensed fraction plays a significant role, and complicates the theoretical treatment. For instance, the first observation of BEC is considered to have been in Helium-4 [164, 165], which undergoes a superfluid phase transition below 2.17 K. Such a system has a density many orders of magnitude greater than an atomic gas, and strong many-body interactions are present. Nevertheless, a fraction of the fluid can be identified as a superfluid component but typically constitutes much less than half of the liquid. Consequently, any description of the dynamics requires the normal component to be included. Despite the complexity involved, the theoretical study of BECs close to the transition temperature is an active area of research. In contrast to superfluid Helium, in a dilute atomic atomic gas with a temperature much less than T_c, the non-condensed fraction typically constitutes less than 1% of the total, which simplifies the theoretical treatment of the dynamics considerably. Dilute atomic gases are therefore ideal systems in which to study BEC.

For a BEC with temperature $T \ll T_c$, it is common to neglect the temperature dependence completely, and to include atom-atom interactions as a mean-field interaction. As discussed above, the former is a good approximation in general, and the latter is valid for dilute atomic gases. The dynamics can then be modelled by the Gross-Pitaevskii equation (GPE),

$$\frac{i\partial\Psi(\mathbf{r},t)}{\partial t} = -\frac{\hbar^2}{2M}\nabla^2\Psi(\mathbf{r},t) + V(\mathbf{r},t)\Psi(\mathbf{r},t) + gN|\Psi(\mathbf{r},t)|^2\Psi(\mathbf{r},t), \qquad (7.2)$$

where $V(\mathbf{r},t)$ is an external potential, N is the total number of atoms in the BEC, and $g = 4\pi\hbar^2 a_s/M$ characterises the atom-atom interaction within the contact potential approximation, with a_s being the s-wave scattering length of

the atom-atom interactions. The dependence of atom-atom interactions on a single partial-wave scattering length is valid since the temperatures are so low that higher energy contributions are negligible.

The high occupation of a single quantum state means that the mean-field contribution is essentially a classical field, represented by the atomic density. The atomic density, however, is derived from the many-body wavefunction, which takes a particularly simple form in an ideal BEC, and is subject to quantum interference effects. As a consequence, the wave-like nature of matter can be directly observed in the atomic density, which is essentially a classical field. It is this remarkable property of BECs that offer a route to observing quantum effects on a macroscopic scale.

The presence of atom-atom interactions and the high degree of spatial coherence in BECs underlies a wide range of interesting dynamics. Notable phenomena include the manifestation of superfluid flow [166], solitons [147–149], quantised vortices [150, 151], Josephson oscillations [144, 167], and collective excitations [168]. Thus, BECs offer an opportunity to not only study fundamental quantum physics, but also to study interesting nonlinear effects with links to other areas of physics.

7.2 Atom Interferometry

The high degree of coherence in BECs makes them ideal candidates for interferometry. Atom-interferometry [23, 25, 102, 153, 169–178] exploits the wave-like nature of atoms to deduce the effect of the environment on the system in a way exactly analogous to optical interferometry. Although optical interferometry is a highly developed field, having found great success in commercial applications achieving extremely high sensitivity, atom-interferometry has the potential to be a superior alternative for inertial measurements. The sensitivity of atom-interferometers to phase shifts from inertial effects can be up to 10^{10} times greater than optical interferometers in equivalent configurations [153, 179].

Atom-interferometry is often performed with either beams of thermal atoms [23, 102, 170, 171, 175, 178, 180, 181], confined cold atoms [169, 182], or BECs [152, 153, 172, 177, 183–186], and each source has its own advantages and disadvantages. Atomic beams have high fluxes, which yields a high brightness, but a lack of coherence is accompanied by a low contrast. In addition, a typical

experimental apparatus is very large, which could limit the future usefulness of this approach in some practical applications. Interferometry with confined cold atoms involves much fewer atoms, but the coherence properties are much better, and because of the lower temperatures it is possible to obtain long interrogation times. When an ultracold gas, i.e. a BEC, is used in lieu of cold atoms the contrast of the measured signal is greatly enhanced because of the long range coherence. However, since BECs typically contain two orders of magnitude fewer atoms than cold atomic samples, the measured signal is weaker, but this can be overcome with larger samples of BEC. One avenue of research to overcome this deficiency is the pursuit of the atom-laser which proposes to continually output a high flux of coherent atoms [172, 187, 188].

Unfortunately, there are two major disadvantages to consider with atom-interferometers. The first is that the atom flux in typical implementations can be more than 10^7 times smaller than the photon flux from light sources, leading to a much reduced brightness in the signal. Secondly, unlike photons, atoms experience mutual interactions, resulting in nonlinear phase shifts that are difficult to take into account, which becomes more pronounced for high densities [152].

It is important to consider the inherent uncertainty in an interferometer, determined by quantum effects and not by experimental defects. The phase-uncertainty for classical input states (coherent states) is bounded below by $1/N$, where N is the number of atoms. This so-called standard quantum limit can only be beaten with the use of squeezed states, which reduce the uncertainty of, say, the phase at the expense of a concomitant increase in the number uncertainty. In this case, the minimum uncertainty in the phase can be reduced to $1/N^2$, which is the Heisenberg limit. If all possible k-body couplings are included, and the input state is a product state, then a phase uncertainty of $1/N^{k-1/2}$ is theoretically possible [189], thereby surpassing the Heisenberg limit. Counter-intuitively, nonlinear interactions may therefore provide a means of obtaining highly precise interferometers. This is, of course, assuming that one can harness the atom-atom interactions sufficiently well.

7.3 BEC Mixtures

A feature of early BEC experiments is the presence of a second trappable Zeeman state, allowing the formation of a BEC mixture. Each component of the mixture is associated with its respective Zeeman state, and hence separately trapped atoms are distinguishable. Therefore, there is no ambiguity in identifying two separate BECs, and one can therefore consider a two-component BEC [190]. Later experiments advanced this idea to create mixtures of different species of BEC [191, 192]. Other experiments featured degenerate Zeeman sublevels, allowing spin-exchange interactions to occur thus realising so-called spinor BECs [193, 194]. Although interesting, different-species and spin-dependent systems are not considered in this work.

Two separately formed BECs cannot have repeatable, known difference in their initial phase, which can be disadvantageous in atom-interferometry. Generally, this issue is avoided by using a single BEC to populate a second mode in the system. A frequently used approach is to split a BEC spatially by transforming the trapping potential into a double-well system with a long tunnelling lifetime [157, 174, 177, 185, 186]. The different modes, labelled by the individual wells, are then separately addressable, and can be used to subject one BEC-component to an interaction whose phase evolution can be inferred from the interference pattern obtained by reversing the splitting process to induce recombination. This scheme is particularly pleasing from a theoretical viewpoint since double-well systems have been extensively studied. However, the process of recombination can cause instabilities, even when performed adiabatically [154]
.

An alternative to spatially separating a single BEC is to create a BEC mixture instead. In such a mixure, each BEC is associated with a particular hyperfine sublevel, which can be achieved, for example, by using a microwave $\pi/2$ pulse to populate a state with a dipole-forbidden transition [190]. Subsequently, the BEC components can be controlled via their associated magnetic sublevels, and like the double-well scheme share a common initial phase. In contrast, however, atom-atom interactions have a greater role because the components of the BEC may overlap, and can lead to phase-separation. Such behaviour is associated with the presence of dynamical instabilities, and may appear to limit the usefulness of a binary mixture to atom-interferometry.

The GPE (7.2) can be generalised to describe a binary mixture of BECs. Neglecting spin-exchange collisions, and assuming different components interact only through their mean-fields, the dynamics can be modelled by the coupled GPEs (CGPEs),

$$i\hbar\frac{\partial\Psi_j(\mathbf{r},t)}{\partial t} = \Bigg[-\frac{\hbar^2}{2M}\nabla^2 + V_j(\mathbf{r}) + (-1)^j\frac{\hbar\omega_0}{2} + \frac{4\pi\hbar^2 N}{M}\sum_{k=1}^{2}a_{jk}|\Psi_k(\mathbf{r},t)|^2\Bigg]\Psi_j(\mathbf{r},t)$$

where $\hbar\omega_0$ is the energy separation between the two trapping states, $j = 1, 2$, and

$$g_{ij} = \frac{4\pi\hbar^2}{M}a_{jk} \tag{7.3}$$

where a_{jk} is the s-wave scattering length between atoms in state j and state k. Note that, since spin-exchange is not included, setting $\omega_0 = 0$ does not realise a spinor BEC.

Clearly, the inclusion of a second component greatly increases the complexity of the system; in addition to a second trapping potential, several parameters are now needed to describe the system. Moreover, the coupling between different components is nonlinear. However, such a system is susceptible to available computational resources, and the broad range of physics that it contains merits its study. In this respect, the added complexity of additional parameters can instead be seen as an opportunity to more thoroughly explore the dynamics of this system. Binary mixtures of BECs, as described by (7.3), have been used to investigate the stability properties of BECs [195], and to observe novel soliton [196] and vortex phenomena [150].

7.4 Ring-Traps

The control over the interfering paths in interferometry is crucial. For simplicity, atom-interferometry often deals with spatially separated paths that can be used to guide the trapped atomic gas through an interaction region [177]. The atom-optical equivalents to mirrors and beam-splitters have been demonstrated, and can be used to implement exact analogues of optical interferometry [12, 169].

The inclusion of atom-atom interactions may seem to preclude the usage of interpenetrating binary mixture for atom-interferometry; any guiding of one

BEC component relative to another would result in a nonlinear modulation of their respective spatial modes.

The problem of "drag" between the components can be alleviated by using a quasi-1D toroidal trap, or ring trap, considered to be identical for each BEC component. The periodicity of such a geometry allows separation and recombination to occur more naturally; the direction of travel around the ring trap determines the interferometric path. In addition, the periodic boundary conditions and the possibility to remove any angular dependence in the trapping potential is mathematically appealing. More important, however, is the possibility of suppressing nonlinear effects by uniformly filling the ring traps. In this case, the BEC-components are perfectly overlapped, and experience regular dynamics; ring-traps therefore offer the possibility to perform atom-interferometry with two-component BECs.

Ring geometries have been used in optical interferometry in accurate determinations of rotation for many decades. Such determinations exploit the Sagnac effect to infer the rotation of the external system. This necessitates the preparation of two coherent waves that, combined, enclose an area oriented orthogonally to the sense of rotation. In recent years, there has been interest in Sagnac atom-interferometry [178, 181–183, 197] in ring traps [179, 198–203] with the ultimate aim of creating a feasible atom gyroscope. In all cases, the modes used in interferometry undergo spatial separation, and efforts have been expended in avoiding regimes where atom-atom interactions are appreciable. Although the sensitivity attained by some interferometers is impressive, it is interesting to consider the feasibility of including atom-atom interactions as they allow the possibility to surpass the Heisenberg uncertainty limit, and thus may yield greater benefits in future implementations.

7.5 Two-Component BECs in Ring Traps

In this thesis, the dynamics of a two-component BEC in a quasi-1D toroidal trap will be investigated. The emphasis of these studies will be on the dynamics of states initially described by counter-propagating superfluid flows. For these particular initial conditions, and a particular choice of atomic species, it will be shown how the deleterious effect of atom-atom interactions can be suppressed, but without necessitating their exclusion. In some cases, they may

even be harnessed to enhance the dynamical stability of the dynamics. To demonstrate the feasibility of performing atom-interferometry in this regime, two idealised experimental protocols for performing Sagnac interferometry will then be presented. The first protocol will include atom-atom interactions in a trivial way, and demonstrate an idealised Sagnac atom-interferometer based on relative population measurements. The second will describe a continual precession of density fringes at a rate governed by the rotation of the external system. This second proposal has no direct area-dependence, unlike typical Sagnac interferometry where the measured phase difference is directly proportional to the area [204, 205].

Chapter 8

Description of a BEC in a Quasi-1D Toroidal Trap

A toroidal trapping geometry is theoretically appealing because it is a bounded system with periodic boundary conditions. Such confinement has been realised in a variety ways, from all-optical [108, 206] to all-magnetic potentials [183, 198–202], both time-averaged and static, as well as the more conventional magneto-optical traps [166, 182, 207, 208]. The lifetime, diameter and efficacy of the trapping potential depends on the respective method, and a large range of characteristics have been shown; trapping lifetimes of several minutes, diameters up to $\sim$ 7cm, and robust coherence properties have all been demonstrated.

For a general toroidal trapping potential, a full 3D treatment is required to describe the dynamics. This can be especially complicated since the nonlinear interaction in BECs couples orthogonal degrees of freedom. Although a full 3D simulation is computationally feasible, it is unnecessary to describe much of the physics that occurs in these systems; consequently, a quasi-1D regime is considered instead. In some circumstances, orthogonal degrees of freedom may be decoupled so that the effective dimensionality of the system is lowered. This can be achieved with very strong confinement in two degrees of freedom which effectively "freezes" the respective dynamics, leaving only the remaining degree of freedom. Following this, the theoretical description is given by an effective 1D GPE which permits some degree of analytic treatment whilst also retaining interesting nonlinear effects. This approach has been used frequently to probe dynamics of BECs in the quasi-1D and quasi-2D regimes.

It should be stressed that there are regimes of confined BEC in 1D that exhibit distinct effects not seen in 2D and 3D, but these typically occur for extremely tight trapping potentials and low atom number (~ 100). If the healing length of the BEC becomes less than the mean interatomic spacing then it is more appropriate to consider the system as a Tonks gas. Fortunately, an intermediate regime exists where the quasi-1D desciption is valid, and it is this regime that is considered in this work.

In this chapter, a BEC confined to a toroidal confinement potential will be considered in the quasi-1D regime. Firstly, a straightforward method for creating a toroidal trapping potential will be reviewed. This will be followed by a determination of the approximate axial and radial ground states in the quasi-1D regime, which will then be projected out of the 3D GPE leaving an effective 1D description of the dynamics; hence, the resultant dynamics will describe a two-component BEC on a ring. Finally, an appropriate set of rescaled units will be used to render the 1D GPE into a dimensionless form.

8.1 Formation of a Toroidal Trapping-Potential

A wide range of conservative potentials can be tailor-made with optical forces. Using methods of this sort, it is possible, in principle, to create an optical toroidal trap. Relying solely on optical means, however, can be technically difficult, as it requires good control of time-averaged, spatially dependent optical potentials [209]. A more straightforward method is to use a blue-detuned laser as a "plug beam" in a magnetic trap with a harmonic potential [166]. Provided the resultant energy barrier is high enough that the tunnelling between opposite sides of the harmonic trap can be neglected, the resultant trap can be considered to be multiply connected. Furthermore, adjustment of the plug beam's waist and intensity varies the diameter of the toroidal trap, allowing simple control over crucial trapping parameters.

One recent, and particularly relevant, experiment with ring traps created in this way was performed by the NIST atomic physics group, which was used to demonstrate persistent flow of a BEC around a quasi-1D ring trap [166]. The trapping potential was approximately

$$V(x,y,z) = \frac{1}{2}m\omega_x^2 x^2 + \frac{1}{2}m\omega_y^2 y^2 + \frac{1}{2}m\omega_z^2 z^2 + V_0 \exp\left(-\frac{2[x^2+y^2]}{w_0^2}\right) \quad (8.1)$$

where $\omega_{x,y,z}$ are the angular trapping frequencies along x, y, and z, respectively,

w_0 is the beam waist, and V_0 is related to the power of the plug-beam. The experimental parameters were reported to be $\Omega_{x,y,z}/2\pi = 25, 36$, and 51Hz, $V_0/\hbar = 3.6$KHz, and $w_0 = 8$ μm. Clearly, the trap is not exactly cylindrically symmetric, which introduces a small angular dependence on the potential. This dependence is approximately sinusoidal, and can be considered small for $\omega_x \approx \omega_y$. Its amplitude was reported to be less than $\mu/3$ (where μ is the chemical potential) so that, to a good approximation, this variation can be neglected. For simplicity then, cylindrical symmetry is assumed, i.e., $\omega_x = \omega_y = \omega$. In cylindrical coordinates, the confining potential (8.1) is

$$V(r,\theta,z) = \frac{1}{2}m\omega^2 r^2 + \frac{1}{2}m\omega_z^2 z^2 + V_0 \exp\left(-\frac{2r^2}{w_0^2}\right), \tag{8.2}$$

which has a minimum at $r = R$, and $z = 0$, where

$$R^2 = \frac{w_0^2}{2}\ln\left(\frac{4V_0}{m\omega^2 w_0^2}\right). \tag{8.3}$$

Taylor-expanding the potential (8.2) around this minimum yields

$$V(r,z) \approx V(R,0) + \frac{1}{2}\omega_r^2(r-R)^2 + \frac{1}{2}m\omega_z^2 z^2, \tag{8.4}$$

where $\omega_r = 2\omega R/w_0$ is the effective radial trapping frequency, and terms of order $(r-R)^3$ have been neglected. The potential (8.4) describes a toroidal trapping potential in the ideal case. The constant $V(R,0)$ has no bearing on the dynamics and can be removed, so that the Hamiltonian describing this system is given by

$$\hat{H} = \frac{\hat{p^2}}{2M} + \frac{M}{2}\left[\omega_r^2(r-R)^2 + \omega_z^2 z^2\right]. \tag{8.5}$$

It is possible that small imperfections, such as non-horizontal alignment of the trap, are present. With some technical effort, these can be sufficiently reduced that they do not impose any inherent limitation [208], and therefore they will not be considered here.

8.2 Reduction to a Quasi-1D Description

In some circumstances, it is possible to restrict attention to the azimuthal dynamics by "freezing out" the dynamics in the radial and axial directions. This is accomplished with tight radial and axial confinement, so that the energy separation between adjacent states is much larger in the axial and radial directions than in the angular direction. The advantage of this is that the mathematical

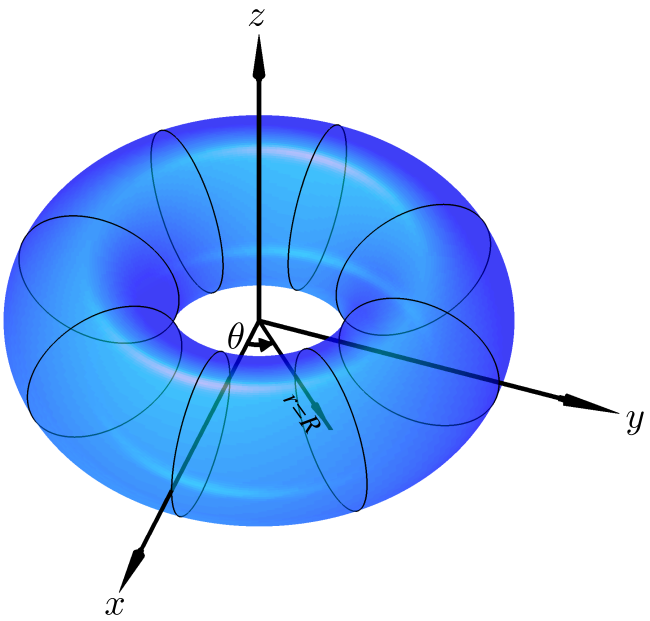

Figure 8.1: Coordinate system

description is reduced from 3D to 1D, making the system much more tractable. An important point to make is that this reduction is a mathematical convenience, and the physical system is still 3D; notably, the atom-atom interactions in the system are a consequence of 3D s-wave scattering events.

For sufficiently strong axial and radial confinement the total wavefunction, $\Psi(r, \theta, z; t)$, is approximately separable as

$$\Psi(r, \theta, z; t) \approx \psi(\theta, t)\rho(r)\phi(z). \tag{8.6}$$

In this regime, the radial and axial wavefunctions reside in their respective ground states, and can be projected out once they are known. It therefore remains to determine the ground states.

8.2.1 Calculation of the Radial and Axial Ground States

The ground states of a toroidal trap are difficult to calculate analytically in the GPE because the nonlinear term prohibits the separation of variables, even assuming the separation (8.6). However, for strong confinement or weak interactions so that $g|\psi|^2 \ll V_{\text{ext}}$, the ground states in the non-interacting case may serve as close approximations to the interacting ground states. Using the approximate separation (8.6) for the ground states, the appropriate time-

independent Schrödinger equation (TISE) in cylindrical coordinates is,

$$\begin{aligned}\mu\rho(r)\phi(z)\psi(\theta,t) =& -\frac{\hbar^2}{2M}\left[\psi(\theta,t)\phi(z)\frac{1}{r}\frac{\partial}{\partial r}\left(r\frac{\partial\rho(r)}{\partial r}\right)+\phi(z)\rho(r)\frac{1}{r^2}\frac{\partial^2\psi(\theta,t)}{\partial\theta^2}\right.\\ &\left.+\ \psi(z)\rho(r)\frac{\partial^2\phi(z)}{\partial z^2}\right]\\ &+\frac{M}{2}\left[\omega_r^2(r-R)^2+\omega_z^2z^2\right]\psi(\theta,t)\phi(z)\rho(r), \end{aligned} \tag{8.7}$$

where μ is the chemical potential. It is now possible for Eq. (8.7) to be written as,

$$-\frac{\hbar^2}{2M}\frac{\partial^2\psi}{\partial\theta^2} =\lambda\psi \tag{8.8a}$$

$$\frac{\hbar^2}{2M}\left[\frac{r}{\rho}\frac{\partial}{\partial r}\left(r\frac{\partial\rho}{\partial r}\right)+\frac{r^2}{\phi}\frac{\partial^2\phi}{\partial z^2}\right]-\frac{Mr^2}{2}\left[\omega_r^2(r-R)^2+\omega_z^2z^2\right]+\mu r^2 =\lambda, \tag{8.8b}$$

where λ is a constant of separation, having the physical dimensions of an energy, and the explicit coordinate dependences of the wavefunctions has been omitted for brevity. Although the angular eigenstates are not required for the reduction procedure, they are nonetheless relevant to later discussions. They are simply momentum eigenstates, given by,

$$\psi_0(\theta) = \frac{1}{\sqrt{2\pi}}\exp\left(i\ell\theta\right), \tag{8.9}$$

where $\lambda = \hbar^2\ell^2/2M$. The ground state corresponds to $\ell = 0$, which describes a uniformly distributed atomic density with no rotation. A further separation of variables in Eq. (8.8) gives,

$$-\frac{\hbar^2}{2M}\frac{\partial^2\phi}{\partial\phi^2}+\frac{M}{2}\omega_z^2z^2\phi =\kappa\phi \tag{8.10a}$$

$$\frac{\hbar^2}{2M}\frac{1}{r}\frac{\partial}{\partial r}\left(r\frac{\partial\rho}{\partial r}\right)-\frac{M}{2}\omega_r^2(r-R)^2\rho-\frac{\lambda}{r^2}\rho =(\kappa-\mu)\rho, \tag{8.10b}$$

where κ is a new constant of separation. The eigenstates of Eq. (8.10a) are harmonic oscillator states, admitting the ground state

$$\phi_0(z) = \left(\frac{m\omega_z}{\pi\hbar}\right)^{1/4}\exp\left(-\frac{M\omega_z z^2}{2\hbar}\right). \tag{8.11}$$

Equation (8.10b) can be re-expressed with the change of variable $\tilde{\rho} = \sqrt{r}\rho$, to yield the more revealing form,

$$-\frac{\hbar^2}{2M}\frac{\partial^2\tilde{\rho}}{\partial r^2}+\frac{M}{2}\omega_r^2(r-R)^2\tilde{\rho}+\frac{(4\ell^2-1)\hbar^2}{8Mr^2}\frac{\tilde{\rho}}{r^2} = E\tilde{\rho}, \tag{8.12}$$

where $E = (\kappa-\mu)$. In this form, Eq. (8.12) resembles the TISE for a harmonic oscillator with the centrifugal barrier term $(4\ell^2-1)\hbar^2/2Mr^2$. In the limit that $\ell \ll R/\sqrt{\hbar/M\omega_r}$ and $\sqrt{\hbar/M\omega_r} \ll R$, the effect of the centrifugal barrier on

the overall dynamics is negligible, and the eigenstates are closely related to the harmonic oscillator eigenstates. Under this approximation, and transforming back to the radial coordinates, the ground state is therefore

$$\rho_0(r) = \left(\frac{m\omega_r}{\pi\hbar r^2}\right)^{1/4} \exp\left(-\frac{m\omega_r(r-R)^2}{2\hbar}\right). \tag{8.13}$$

In arriving at this ground state, it has been assumed that the potential energy is greater than the self-interaction energy so that the ground states can be described as harmonic oscillator ground states. This is a good approximation for tight-trapping, but this is assumed as a matter of convenience rather than necessity; one could include the effect of the nonlinearity to determine the analytic ground state in terms of hypergeometric functions [210], which includes the asymmetry of the true ground state. Projecting out such states, however, is difficult, and would not alter the final result significantly. Figure 8.2 shows the ground states for the potential (8.10b) for different ℓ, R, and a_{HO}, where sa_{HO} is the harmonic oscillator length of the corresponding harmonic trapping potential. It can be seen that under the previous stipulations, the harmonic oscillator ground states are good approximation to the true ground states, even without strictly observing the bounds. The use of these approximations is not only accurate, therefore, but will also improve the clarity of the following analysis.

8.2.2 Projecting Out the Ground States

The 3D GPE with a toroidal confining potential is

$$\begin{aligned} i\hbar\frac{\partial\Psi(\mathbf{r},t)}{\partial t} =& -\frac{\hbar^2}{2M}\nabla^2\Psi(\mathbf{r},t) + \frac{M}{2}\left[\omega_r^2(r-R)^2+\omega_z^2z^2\right]\Psi(\mathbf{r},t) \\ &+ g|\Psi(\mathbf{r},t)|^2\Psi(\mathbf{r},t). \end{aligned} \tag{8.14}$$

Under the assumption that $\Psi(\mathbf{r},t) \approx \psi(\theta,t)\phi_0(z)\rho_0(r)$, this becomes,

$$\begin{aligned} i\hbar\rho_0\phi_0\frac{\partial\psi(t)}{\partial t} =& -\frac{\hbar^2}{2M}\phi_0\psi(t)\left[\frac{1}{r}\frac{\partial}{\partial r}\left(r\frac{\partial}{\partial r}\right)\rho_0\right] - \frac{\hbar^2}{2M}\frac{\phi_0\rho_0}{r^2}\frac{\partial^2\psi(t)}{\partial\theta^2} \\ &- \frac{\hbar^2}{2M}\rho_0\psi(t)\frac{\partial^2\phi_0}{\partial z^2} + \frac{M}{2}\left[\omega_r^2(r-R)^2+\omega_z^2z^2\right]\rho_0\phi_0\psi(t) \\ &+ g|\rho_0|^2|\phi_0|^2|\psi(t)|^2\rho_0\phi_0\psi(t), \end{aligned} \tag{8.15}$$

where the radial and axial ground states are momentarily left in their implicit form, and the explicit dependence of the functions on the coordinates has been omitted for brevity. The dependence on r and z may be projected out by multiplying Eq. (8.15) by $\phi_0^*(z)\rho_0^*(r)$ and integrating over the range of r and z.

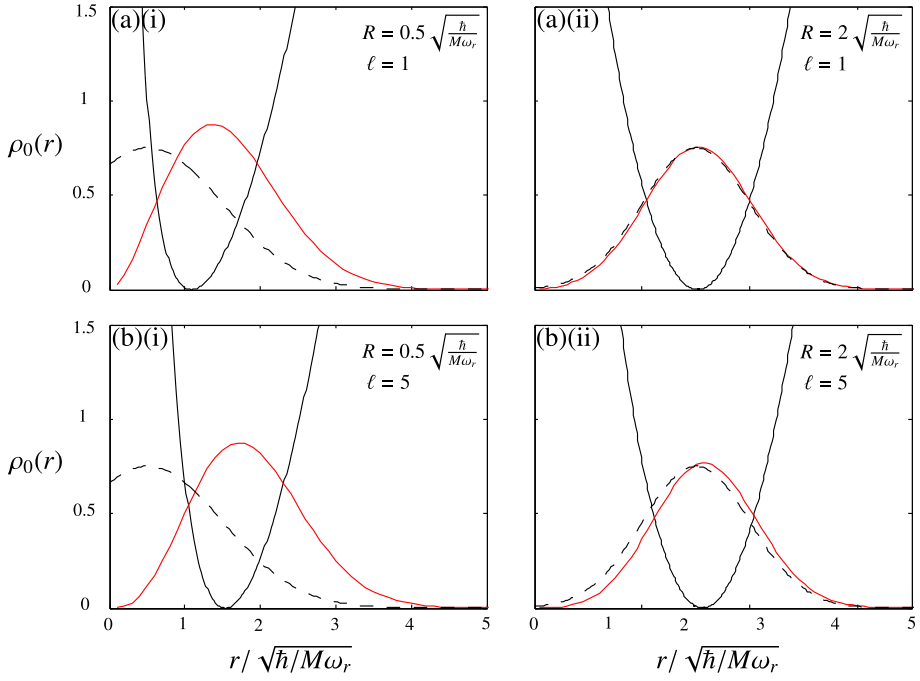

Figure 8.2: The radial ground states of Eq. (8.12) for (a) $\ell = 1$ and (b) $\ell = 2$ with the ring trap radii set as (i) $R = 0.5a_{HO}$ and (ii) $R = 2a_{HO}$, where $a_{HO} = \sqrt{\hbar/M\omega_r}$ is an harmonic oscillator length-unit. The exact solutions (red solid line), computed numerically using an imaginary-time propagation outlined in Appendix C, and the approximate ground state (black dashed line), as given by Eq. (8.13), as well as the trapping potential (solid black line) determined by R and ℓ, are shown. Strictly, the approximate solutions are valid for $R/a_{HO} \gg 1$ and $R/a_{HO} \gg \ell$, but it is clear from these simulations that the approximate solutions are in good agreement with the exact solutions for low R and relatively large ℓ.

This yields,

$$\begin{aligned}
& i\hbar\frac{\partial\psi(t)}{\partial t}\int_0^\infty\int_{-\infty}^\infty drdzr|\rho_0|^2|\phi_0|^2 \\
=& -\frac{\hbar^2}{2M}\psi(t)\int_0^\infty\int_{-\infty}^\infty drdz|\phi_0|^2\rho_0^*\left[\frac{\partial}{\partial r}\left(r\frac{\partial}{\partial r}\right)\rho_0\right] \\
& -\frac{\hbar^2}{2M}\frac{\partial^2\psi(t)}{\partial\theta^2}\int_0^\infty\int_{-\infty}^\infty drdz\frac{1}{r}|\phi_0|^2|\rho_0|^2 \\
& -\frac{\hbar^2}{2M}\psi(t)\int_0^\infty\int_{-\infty}^\infty drdzr|\rho_0|^2\phi_0^*\frac{\partial^2\phi_0}{\partial z^2} \\
& +\frac{M}{2}\psi(t)\int_0^\infty\int_{-\infty}^\infty drdzr\left[\omega_r^2(r-R)^2+\omega_z^2z^2\right]|\rho_0|^2|\phi_0|^2 \\
& +g|\psi(t)|^2\psi(t)\int_0^\infty\int_{-\infty}^\infty drdzr|\rho_0|^4|\phi_0|^4,
\end{aligned} \tag{8.16}$$

where it is convenient to leave the ground states implicit so that the normalisation conditions,

$$\begin{aligned}\int_0^\infty dr r|\rho_0|^2 = 1,\\ \int_{-\infty}^\infty dz|\phi_0|^2 = 1,\end{aligned} \tag{8.17}$$

can be invoked; consequently, Eq. (8.16) becomes,

$$\begin{aligned}i\hbar\frac{\partial\psi(t)}{\partial t} =& -\frac{\hbar^2}{2M}\psi(t)\int_0^\infty dr\rho_0^*\left[\frac{\partial}{\partial r}\left(r\frac{\partial}{\partial r}\right)\rho_0\right]\\ &-\frac{\hbar^2}{2M}\frac{\partial^2\psi(t)}{\partial\theta^2}\int_0^\infty dr\frac{1}{r}|\rho_0|^2 - \frac{\hbar^2}{2M}\psi(t)\int_{-\infty}^\infty dz\phi_0^*\frac{\partial^2\phi_0}{\partial z^2}\\ &+\frac{M\omega_r^2}{2}\psi(t)\int_0^\infty dr(r-R)^2 r|\rho_0|^2\\ &+\frac{M\omega_z^2}{2}\psi(t)\int_{-\infty}^\infty dz z^2|\phi_0|^2\\ &+g|\psi(t)|^2\psi(t)\int_0^\infty\int_{-\infty}^\infty drdzr|\rho_0|^4|\phi_0|^4.\end{aligned} \tag{8.18}$$

Inserting the explicit form for the radial and axial ground states, given by Eqs. (8.13) and (8.11), yields,

$$\begin{aligned}i\hbar\frac{\partial\psi(t)}{\partial t} =& -\frac{\hbar^2}{2M}\left(\frac{M\omega_r}{\pi\hbar}\right)^{1/2}\psi(t)\\ &\times\int_0^\infty dr\left[\frac{1}{4r^2} - \frac{M\omega_r}{\hbar} + \left(\frac{M\omega_r}{\hbar}\right)^2 R^2 - 2\left(\frac{M\omega_r}{\hbar}\right)^2 Rr + \left(\frac{M\omega_r}{\hbar}\right)^2 r^2\right]\\ &\times\exp\left(-\frac{M\omega_r}{\hbar}(r-R)^2\right)\\ &-\frac{\hbar^2}{2M}\left(\frac{M\omega_r}{\pi\hbar}\right)^{1/2}\frac{\partial^2\psi(t)}{\partial\theta^2}\int_0^\infty dr\frac{1}{r^2}\exp\left(-\frac{M\omega_r}{\hbar}(r-R)^2\right)\\ &-\frac{\hbar^2}{2M}\frac{1}{\sqrt{\pi}}\left(\frac{M\omega_z}{\hbar}\right)^{3/2}\psi(t)\int_{-\infty}^\infty dz\left[\left(\frac{M\omega_z}{\hbar}\right)z^2 - 1\right]\exp\left(-\frac{M\omega_z}{\hbar}z^2\right)\\ &+\left(\frac{M\omega_r}{\pi\hbar}\right)^{1/2}\frac{M\omega_r^2}{2}\psi(t)\int_0^\infty dr(r-R)^2\exp\left(-\frac{M\omega_r}{\hbar}(r-R)^2\right)\\ &+\left(\frac{M\omega_z}{\pi\hbar}\right)^{1/2}\frac{M\omega_z^2}{2}\psi(t)\int_{-\infty}^\infty dz z^2\exp\left(-\frac{M\omega_r}{\hbar}z^2\right)\\ &+g|\psi(t)|^2\psi(t)\int_0^\infty\int_{-\infty}^\infty drdzr\exp\left(-\frac{2M\omega_r}{\hbar}(r-R)^2\right)\exp\left(-\frac{2M\omega_z}{\hbar}z^2\right).\end{aligned} \tag{8.19}$$

Many of the integrals in Eq. (8.19) can be evaluated using the identities [136],

$$\int_0^\infty e^{-ax^2}dx = \frac{1}{2}\sqrt{\frac{\pi}{a}} \tag{8.20}$$

$$\int_0^\infty xe^{-ax^2}dx = \frac{1}{2a} \tag{8.21}$$

$$\int_0^\infty x^2e^{-ax^2}dx = \frac{1}{4}\sqrt{\frac{\pi}{a^3}}. \tag{8.22}$$

However, integrals containing reciprocal powers of r have singularities at $r = 0$, and therefore diverge. This is because the centrifugal barrier potential diverges at the origin, and this behaviour is not contained in the approximate ground state $\rho_0(r)$. Rather, $\rho_0(r)$ is valid only for a small interval around $r = R$ where $r \ll R$. Thus, in the interval $r \in [R - \epsilon, R + \epsilon]$,

$$\int_0^\infty dr \frac{1}{r^n} \exp\left(-\frac{M\omega}{\hbar}[r-R]^2\right) \approx \infty \int_{R-\epsilon}^{r+\epsilon} dr \frac{1}{R^n} \exp\left(-\frac{M\omega}{\hbar}[r-R]^2\right). \tag{8.23}$$

This approximation assumes that the contribution due to the tails of the exact ground state are negligible, and that the greatest contribution is provided by a wavefunction that closely resembles a harmonic oscillator ground state in a small interval around R. However, the limits of these integrals makes their evaluation complicated, and is contrary to the spirit behind the preceding approximations. This may be remedied by observing that the contribution from the tails of harmonic oscillator state is small, and since the reciprocal term is now assumed constant, the tails can be included in the limits of the integral to simplify the final result. Therefore,

$$\int_0^\infty \frac{1}{r^n} \exp\left(-s[r-R]^2\right) \approx \frac{1}{R^n} \int_{-\infty}^{\infty} \exp\left(-s[r-R]^2\right), \tag{8.24}$$

which is valid where $R \gg \sqrt{\hbar/m\omega}$. Finally, using Eqs. (8.20) and (8.24) yields

$$\begin{aligned} i\hbar\frac{\partial\psi(t)}{\partial t} = &-\frac{\hbar^2}{2MR^2}\frac{\partial^2\psi(t)}{\partial\theta^2} + \left(\frac{\hbar\omega_r}{2} + \frac{\hbar\omega_z}{2} - \frac{\hbar^2}{8MR^2}\right)\psi(t) \\ &+ \frac{m\sqrt{\omega_z\omega_r}}{2\pi\hbar R} g|\psi(t)|^2\psi(t). \end{aligned} \tag{8.25}$$

The constant shift of $(\omega_\rho + \omega_z)\hbar/2$ in the potential is a consequence of freezing the radial and axial wavefunctions in their ground states; these shifts are the ground state contributions to the total energy. Likewise, the shift of $-\hbar^2/8mR^2$ is a consequence of assuming the centrifugal barrier is small, which is effectively constant under the assumed regime. Adjusting the zero of the potential, these constant shifts can be removed, so that

$$i\hbar\frac{\partial\psi(t)}{\partial t} = -\frac{\hbar^2}{2MR^2}\frac{\partial^2\psi(t)}{\partial\theta^2} + \tilde{g}|\psi(t)|^2\psi(t). \tag{8.26}$$

This has the form of a 1D GPE, and describes the quasi-1D dynamics of a BEC in a toroidal trap. The interaction strength in this quasi-1D description is related to the 3D interaction strength via

$$\tilde{g} = \frac{M\sqrt{\omega_z\omega_r}}{2\pi\hbar R} g = \frac{2N\hbar\sqrt{\omega_r\omega_z}}{R} a_s, \tag{8.27}$$

where the number of atoms, N, has been absorbed into the definition of g.

Species	States ($\|F, m_F\rangle$)	N	a_s/a_0	λ	τ	Ref.
^{23}Na	$\|1,-1\rangle$:$\|1,-1\rangle$	2×10^5	52 ± 5	18800	0.07	[166, 211]
^{23}Na	$\|2,2\rangle$:$\|2,2\rangle$	2×10^5	85 ± 3	30730	0.07	[166, 211]
^{85}Rb (155G)	$\|2,-2\rangle$:$\|2,-2\rangle$	5×10^4	200	35601	0.13	[212]
^{85}Rb (0G)	$\|2,-2\rangle$:$\|2,-2\rangle$	5×10^4	-443	-78856	0.13	[212]
^{87}Rb	$\|1,-1\rangle$:$\|1,-1\rangle$	2800	100.44	1024	0.14	[213]
^{87}Rb	$\|2,1\rangle$:$\|1,-1\rangle$	2800	98.09	1000	0.14	[213]
^{87}Rb	$\|2,1\rangle$:$\|2,1\rangle$	2800	95.47	974	0.14	[213]

Table 8.1: Values of the dimensionless interaction strength λ for s-wave scattering between particular hyperfine sublevels. The precision of each value of a_s is taken directly from the corresponding reference, where it is given. For ^{23}Na, the radius $R = 13.9\ \mu m$, and the trapping frequency $2\pi \times 540$ Hz were used, whereas for ^{87}Rb, the radius and the trapping frequency was $R = 10\ \mu m$, and $2\pi \times 540$ Hz, respectively. The latter parameters were used as estimates for the remaining elements.

8.3 Rescaling to Dimensionless Form

It is convenient for the analyses that follow to recast Eq. (8.27) into a dimensionless form. Since the spatial coordinate is already dimensionless, this involves rescaling the time unit only. For $\tilde{t} = t/\tau$, the timescale $\tau = MR^2/\hbar$ is chosen, and the dimensionless quasi-1D GPE becomes,

$$i\frac{\partial\psi(t)}{\partial t} = -\frac{1}{2}\frac{\partial^2\psi(t)}{\partial\theta^2} + \lambda|\psi(t)|^2\psi(t), \tag{8.28}$$

where $\lambda = 2MNR\sqrt{\omega_r\omega_z}a/\hbar$. Table (8.1) gives a range of typical s-wave scattering lengths and their corresponding typical interaction strengths for different species. Note that λ depends on the details of the trapping potential used, and will vary from one experiment to another, particularly for ^{85}Rb which requires the use of a Feshbach resonance to form a stable BEC. Despite this, it is useful to consider similar trapping parameters so that a comparison of possible dimensionless values can be made. Typical experimental values give $\lambda \gg 1$, and admit a dimensionless time-unit equivalent to times on the order of 0.1s.

8.4 Generalisation to a Binary Mixture

The quasi-1D GPE (8.28) can be generalised straightforwardly to describe a two-component BEC in the same system. Assuming that the trapping potentials addressing each trapped BEC are identical, then the CGPEs for a quasi-1D toroidal trap are,

$$\begin{aligned} i\frac{\partial\psi_1(t)}{\partial t} &= -\frac{1}{2}\frac{\partial^2\psi_1(t)}{\partial\theta^2} - \frac{\hbar\omega}{2} + g_{11}|\psi_1(t)|^2\psi_1(t) + g_{12}|\psi_2(t)|^2\psi_1(t) \\ i\frac{\partial\psi_2(t)}{\partial t} &= -\frac{1}{2}\frac{\partial^2\psi_2(t)}{\partial\theta^2} + \frac{\hbar\omega}{2} + g_{21}|\psi_1(t)|^2\psi_2(t) + g_{22}|\psi_2(t)|^2\psi_2(t), \end{aligned} \tag{8.29}$$

where three interaction strengths are required to fully characterise the atom-atom interactions, and $\hbar\omega$ is the energy splitting between the magnetic sublevels associated with each BEC component, with the normalisation convention,

$$\int_0^{2\pi} \left[|\psi_1(\theta)|^2 + |\psi_2(\theta)|^2\right] = 1. \tag{8.30}$$

Note that symmetry implies that $g_{12} = g_{21}$. In principle, the relative populations affect the strength of interactions, but, for simplicity, it will be commonly be assumed in this work that the populations of the two BEC components are equal, and that any difference in interaction strength is encoded in the parameters g_{11}, g_{12}, and g_{22}.

Chapter 9

Dynamics of a BEC in a Ring Trap

In the previous chapter, the quasi-1D form of the GPE for a BEC in a toroidal trap was derived. The purpose of this chapter is to present numerical solutions to this system, followed by a qualitative discussion of the dynamics for both one- and two-component BECs.

Firstly, the choice of initial condition will be motivated, and its suitability with respect to a ring geometry will be made clear. Numerical solutions to Eq. (8.28) will then be discussed. It is useful to first consider one-component BEC dynamics since they are simpler than those in the two-component case, and therefore allow some insight to be developed. Particular attention will be paid to the fidelity of the evolved state, which will be used a measure of the dynamical stability, with a view to interpreting how interactions affect the longevity of the initial state. This will be followed by an examination of the dynamics in a two-component BEC system, using similar initial conditions. The fidelity of the initial state will once again be examined, and a regime of dynamical stability will be identified.

9.1 One-Component BEC

9.1.1 Initial Conditions

One striking property of a BEC is its lack of internal viscosity, a characteristic property of superfluids that allows persistent flows to be established. A ring trap is a natural geometry for observing superfluidity in BEC as it allows superfluid flow to be continue unhindered once it has been established. Another characteristic property is the observation of quantised vortices [150, 151], which were observed soon after the first BEC experiments, and served as experimental verifications of long-range order and coherence in BECs.

A persistent flow in a ring trap is equivalent to a single vortex state, with the vortex core coinciding with the centre of trap thus "pinning" the vortex and enhancing the lifetime of the state. Such configurations with singly charged vortices have been proposed as a possible source of qubits for use in quantum information processing [214], where the sign of the charge relates the boolean value of the qubit. The focus of this work, however, is in the use of superfluid flows around a ring trap as elements of an atom-interferometer.

In the 1D system developed in the previous chapter, persistent flows or vortex states can be modelled as angular momentum eigenstates where the charge is given by the angular momentum, i.e., a vortex state of charge m is equivalent to $\psi_{\mathrm{v}}(\theta) = \exp(im\theta)$ where m is the angular momentum. Such a state is a solution to the GPE, and investigations in the 3D regime [215] have shown these ground states to be stable in ring traps for a broad range of interaction strengths.

It is interesting to consider superpositions of angular momentum states of the form,

$$\psi(\theta) = \frac{1}{2\sqrt{\pi}}\left(e^{im\theta} - e^{-im\theta}\right) = \frac{1}{\sqrt{\pi}}\sin(m\theta) \tag{9.1}$$

where the prefactor ensures normalisation of the state. The state (9.1) represents a superposition of counter-propagating superfluid flow, and is interesting not only because it is an example of a dramatic quantum effect that is observable on a macroscopic scale, but also because it may also be interpreted as a superposition of vortex states and may be useful in quantum information processing. The creation of such a superposition was considered in Ref. [214], and is expected to be experimentally feasible.

The primary motivation behind this choice of initial condition lies in its utility

in an atom-interferometer. In any given interferometer, there must be two (or more) equally-accessible paths available. In a ring trap, two paths can be identified. These correspond to different traversing the ring trap in different orientations. Hence, the study of counter-propagating superfluid flows in this system is of immediate relevance to interferometric applications.

In the non-interacting regime, the GPE simply becomes the time-dependent Schrödinger equation (TDSE), and the superposition (9.1) is an eigenstate of the system. For nonzero interactions, however, this is no longer true, and the initial state will undergo a spatial modulation. Since it is not always possible to tune atom-atom interactions so that they are negligible [156, 184], it is important to consider the effect of these interactions on the dynamics of the initial-state, and to consider if they can be easily understood, or manipulated, to provide dynamics conducive to interferometry.

9.1.2 Stationary States

The stationary states of the 1D GPE with periodic boundary conditions and no external potential were investigated by Carr *et al* for both repulsive and attractive interactions [216]. They showed that the ground states of the system fall into three classes: constant amplitude solutions, real symmetry-breaking solutions, and complex symmetry-breaking solutions. The first class of solutions are angular momentum states, which are also eigenstates of the non-interacting system. The second and third classes describe dark and grey soliton solutions, respectively. In both these symmetry-breaking cases, there are a finite number of allowed solutions, corresponding to an allowed number of density notches $\{n_d\}$, in contrast to the family of constant amplitude solutions which contain an infinite number of states. This is because the density notches of the symmetry breaking solutions have an associated width which precludes many notches; once the density notches begin to overlap, a solution is no longer obtainable.

Only repulsive s-wave interactions are considered in this work. In this case, the real symmetry-breaking solutions have the form,

$$\psi(\theta) = \frac{\sqrt{2m}}{2g^2}\,[4jK(m)]\,\mathrm{sn}(4jK(m)\theta|m) \tag{9.2}$$

where $0 \leq m \leq 1$ is the elliptic modulus, $K(m)$ is an elliptic integral of the first kind, and j determines the number of nodes in the solution. In practice, m has to be determined numerically for a given j and g, if the solution exists, so that

normalisation of the solution is obeyed. In the limit $m \to 0$, the non-interacting solutions are recovered, and the number of allowed solutions increases to infinity. The complex symmetry breaking solutions are of the form,

$$\psi(\theta) = A\left[1 + \gamma \mathrm{dn}^2(2jK(m)\theta|m)\right]^{1/2} \exp(i\alpha(x)) \tag{9.3}$$

where A is a normalisation constant, γ relates to the depth and speed of the grey soliton, and $\mathrm{dn}(x|m)$ is another Jacobi elliptic function. Unfortunately, the normalisation, the phase $\alpha(x)$, and the parameters γ and m have to be determined self-consistently according to boundary conditions and the normalisation condition, thereby placing limits on their usefulness in analytics. Despite this, Carr *et al* showed that the number of density notches for a given interaction strength is bounded above by $j_{\max} = g^2/4\pi^2 - 1$ for even j and by $j_{\max} = g^2/2\pi^2 - 2$ for odd j.

The initial condition (9.1) may be considered to be related to the real symmetry-breaking solutions via a small perturbation (for an identical number of nodes). For large interaction strengths, this perturbation would become stronger, but one would expect that the dynamics would resemble the stationary state plus some excitation, in some regimes. For a linear system, this would certainly be the case, and it is interesting to consider if this is also true for the nonlinear system, at least in some parameter regimes.

9.1.3 Qualitative Dynamics

Figure 9.1 shows the time-evolution of a weakly-interacting one-component BEC evolved from the initial condition (9.1). For $g = 0$, $\psi(0)$ is an eigenstate, and can be clearly seen to evolve as expected. For small increases in the interaction strength, excitations are induced, which appear to manifest as identical pairs of soliton-like disturbances. This is inferred by noting that they appear to exhibit similar characteristics to soliton dynamics. Firstly, they appear to propagate without dispersion, i.e., they trace distinctive trajectories. It is useful to consider the timescale for a free Gaussian wavepacket of standard deviation $\sigma(x)$ to disperse to a lengthscale observable in this system[1]. For a 50% increase in $\sigma(0)$, with $\sigma(0)/R = 0.1$, the time taken in dimensionless units would be approximately 0.02 time-units, which is clearly much shorter than the duration

[1]The time-dependence of a Gaussian dispersing in free-space [104] is given by $\sigma(t) = \sqrt{\sigma^2(x) + \frac{\hbar^2}{4M^2\sigma^2(0)}t^2}$.

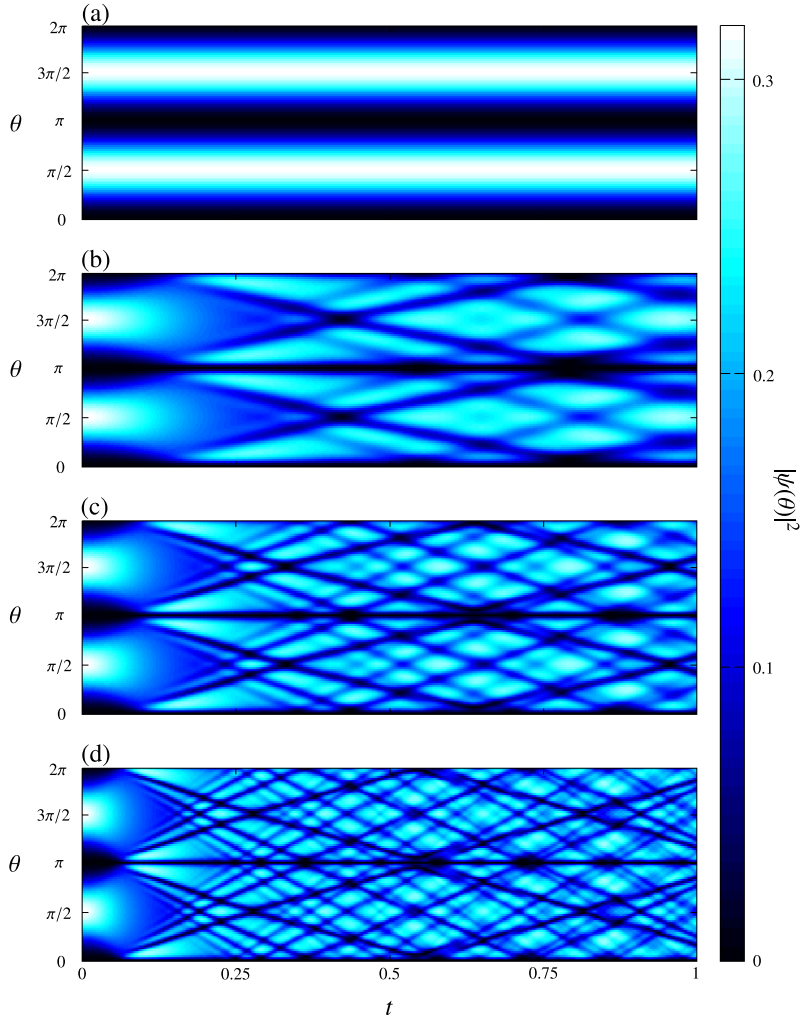

Figure 9.1: The time-evolved density, $|\psi(\theta, t)|^2$, given by the numerical solution to Eq. (8.28) for (a) $g = 0$, (b) $g = 100$, (c) $g = 250$, and (d) $g = 500$. Stronger interactions are associated with soliton-like disturbances that, due to repeated position-shifting during collisions, results in the rapid loss of the initial state. Units are dimensionless.

observed here. Secondly, the travelling density-notches of the excitations seem to survive collisions with other solitons relatively unscathed except for a position shift, another feature associated with solitons.

This latter property means that collisions between solitons serve to advance them an amount depending on the strength of their mutual interaction. In this system, the nonlinear interaction is mediated through a repulsive density interaction; for solitons associated with large density notches, i.e. for large density variations, one would expect higher interaction energies between collisions, and therefore larger position shifts following those collisions. Figure 9.2 shows a zoom of the region where the soliton-like disturbances first coincide. Indeed, each soliton-like disturbance can be seen to be advanced by an amount that increases with the depth of the density notches of the colliding solitons. Furthermore, one can see, at least to the resolution of these simulations, that the same number of density notches leave the interaction regions with the same speed and depth as those entering the same region, and that there does not appear to be any significant diffraction of the incoming disturbances. Due to the non-uniform background density on which they propagate, however, the trajectories of the soliton-like disturbances are not straight, and this is exacerbated by their proximity to other soliton-like disturbances.

Given that these disturbances are non-dispersive, at least over the timescales demonstrated, and appear to be robust under collisions with each other, and also given that there are eigenstates of this system that describe solitons, it is therefore not unreasonable to describe these disturbances as soliton-like. In light of this, the stationary density notch, associated with the node of the wavefunction, and the propagating density notches, of varying depths and speeds, will henceforth be described as dark- and grey-solitons, respectively. Note, however, that no strict claim is made here, and that this is done only as an aid to developing a conceptually useful picture.

Further increases in the interaction strength result in the manifestation of many pairs of solitons. As g increases, the first pair of grey solitons (i.e. the slowest moving disturbances) become deeper, and faster.[2] For the interactions considered here, the typical number of allowed grey solitons in the ground state, as described by Carr *et al*, is of the order 100, which is much greater than the number of soliton-like disturbances observed here. Although this bound has

[2]Generally, deep solitons move slower than shallow solitons in the same system, but here systems with different interaction strengths are being compared, so there is no contradiction.

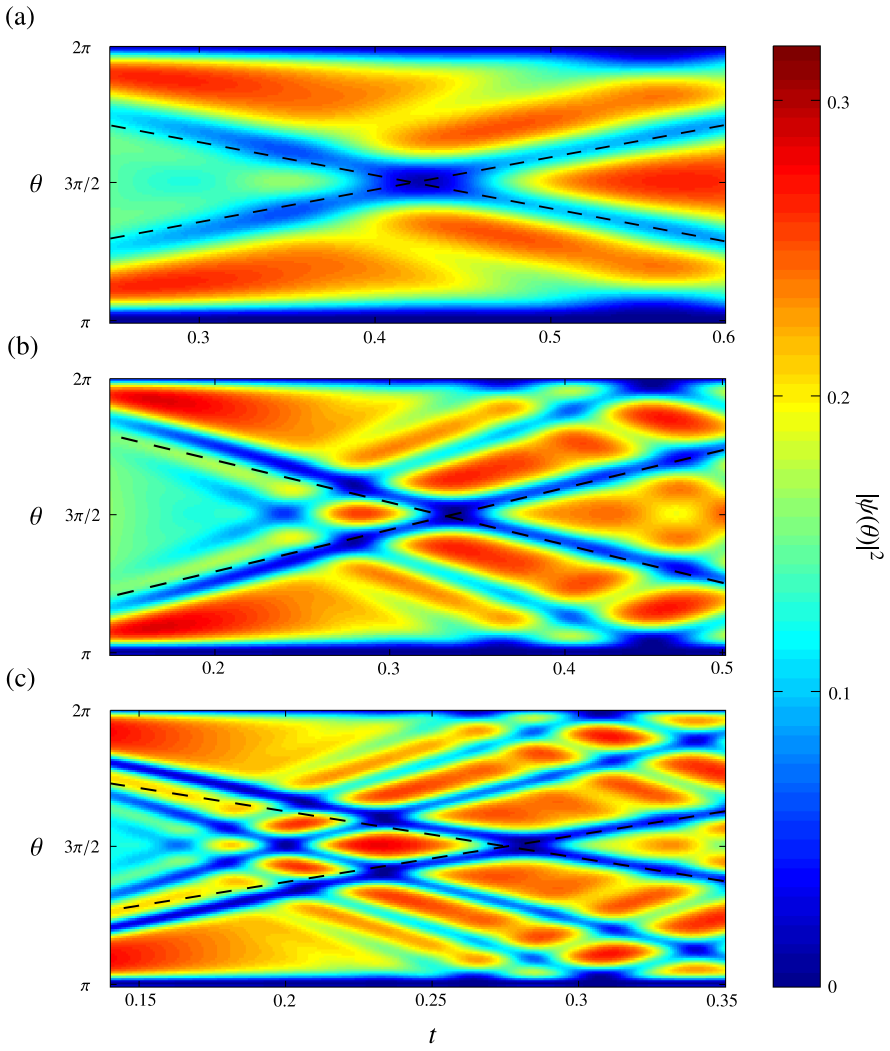

Figure 9.2: A close-up of the dynamics in fig. (9.1) for (a) $g = 100$, (b) $g = 250$, and (c) $g = 500$. Note the different spatial limits, and the different time-axes between subfigures, which are chosen to focus attention on the coincidences of propagating density notches. A different colourmap is also used to accentuate small differences. Coinciding density-notches appear to undergo position-shifts, to a degree proportional to their depth, and continue unscathed beyond the interaction region. Dashed lines have been added to guide the eye. Units are dimensionless.

no direct bearing on the time-dependent dynamics, it is a useful measure with which to consider the consistency of these numerics since one would expect the physics determining the bound to apply to the time-dependent system, i.e., one should expect there is a maximum number of allowed solitons for a given repulsive interaction in the time-dependent system as well for the ground states.

The existence of pairs is easily understood as following directly from the conservation of angular momentum in the system, or, more fundamentally, the preservation of the symmetry of the initial condition. However, the proximity of neighbouring soliton pairs makes it impossible to resolve them all, and, in any case, faster and shallower solitons have a negligible impact on the dynamics.

Only the dark-solitons and the two slowest moving pairs of grey-solitons (referred to as first- and second-order) are important because they dominate the dynamics after their first collisions. For very low g where only the first-order is important, collisions occur regularly with the stationary dark solitons seeded by the nodes of the initial state. However, as the second-order become important, the first-order undergoes position-shifts before completing a round trip of the ring. This, in turn, affects the next collision between the second- and first-orders, and, hence, there is an irregular cascade of position-shifting events that rapidly complicates the time-evolution. A short time after the first few collisions have taken place, the number of participating solitons is immaterial, and only a complex pattern of trajectories is seen.

The range of interaction strengths used in Fig. 9.1 corresponds to a very weakly interacting BEC, only found (at present) in a regime where a Feshbach resonance would be required, or where atomic densities are extremely low. For more typical BEC experiments, the interaction strengths are more than an order of magnitude of order greater than those used in Fig.(9.1) [see Table 8.1]. Consequently, the initial state $\psi(0)$ for more typical interaction strengths would deteriorate even more rapidly. For such a highly-excited state, one would also expect the depletion from the BEC to become significant.

9.1.4 Symmetry Considerations

For applications where high fidelities are advantageous, such as in interferometry, the existence of symmetries is useful because the range of possible dynamics are more restricted. An observation in Fig. 9.1 is that the minimum in the initial

density appears to be preserved throughout the evolution. This is a direct consequence of the fact that a node in the initial wavefunction introduces a reflection symmetry which is preserved by the GPE. That is, for $\psi(\theta, 0) = a\sin(m\theta)$, then $\psi(\theta^\star - \theta) = -\psi(\theta - \theta^\star)$, where $\theta^\star = n\pi$ for integer n. The GPE (8.28) is invariant under translations of θ, and may be written

$$-\frac{1}{2}\frac{\partial^2\psi(\theta^\star - \theta)}{\partial\theta^2} + g|\psi(\theta^\star - \theta)|^2\psi(\theta^\star - \theta) = i\frac{\partial\psi(\theta^\star - \theta)}{\partial t}, \tag{9.4}$$

from which the preservation of reflection symmetries can be readily seen.

Trivially, the preservation of the number of nodes may seem to follow from the conservation of angular momentum in this system. This would seem to imply that the angular momentum associated with the each direction around the ring is also constant. As is shown below, however, this is not the case. The creation of *pairs* of soliton-like disturbances ensures the net angular momentum is conserved whilst at the same time changing the angular momentum associated with each orientation. Given the potential importance of this system to Sagnac interferometry, where the velocity of counter-propagating flows is an important part, these effects are of direct relevance.

9.1.5 Angular Momentum Decomposition

Since the dynamics seem to be qualitatively described by a combination of multiple solitons, it would be desirable to decompose the time-evolved dynamics into a combination of an unperturbed stationary state [i.e., $\psi(0)$] plus a number of small amplitude solitons. Unfortunately, this is not straightforward since the nonlinearity in this system prohibits a superposition principle, and, additionally, soliton solutions do not form an orthonormal basis. Instead, one could alternatively perform a linear stability analysis of this system, and in doing so arrive at the Bogoliubov-de Gennes equations, to allow a numerical determination of the elementary excitations of this system. Such a study would be interesting in its own right, but a more natural basis in which to decompose the time-evolved dynamics is the angular momentum basis, where the angular momentum states are $\phi_k(\theta) = (1/\sqrt{2\pi})\exp(ik\theta)$. In this basis, the initial state corresponds to an equal superposition of ϕ_1 and ϕ_{-1}. The overlap with an angular momentum state of eigenvalue k is given by,

$$C_k(t) = \int_0^{2\pi} \psi(\theta, t)\phi_k(\theta). \tag{9.5}$$

Figure 9.3 shows the decomposition of the wavefunction in the angular momentum basis for a weakly-interacting BEC. Note that, following from momentum conservation, the occupation of the angular momentum modes is symmetric, and therefore only those with positive eigenvalues are shown. For very small g, the initial superposition persists, and shows sparse occupation of higher-momentum modes. The variation of the momentum components is not monotonic, and displays unpredictable oscillatory behaviour, except at very low values of g. At weak interaction strengths, the system undergoes quasi-periodic revivals, which is impeded by the occupation of higher angular momentum modes.

A further observation is that only odd angular momentum states (those for which n is odd) are occupied. This is a direct consequence of the discrete translational symmetry of the initial state of the system, with the consequence that angular momentum changes may only occur in integer multiples of $2n$. For example, for an initial state describe by $\psi(0) = (1/\sqrt{2})(\phi_2 + \phi_{-2})$, only even momentum modes would be occupied.

An important point to be drawn from these decompositions is that for small g only the lowest two occupied angular momentum modes appear sufficient to adequately account for the dynamics. Within the conceptual picture presented above, the occupation of higher-angular momentum modes is associated with the occurrence of soliton-like excitations. The occupation of higher angular momentum modes can therefore be taken as an indication of the degree of excitation in the system, and once they occur, the presence of the nonlinearity ensures that they permanently inhibit revivals of the initial state.

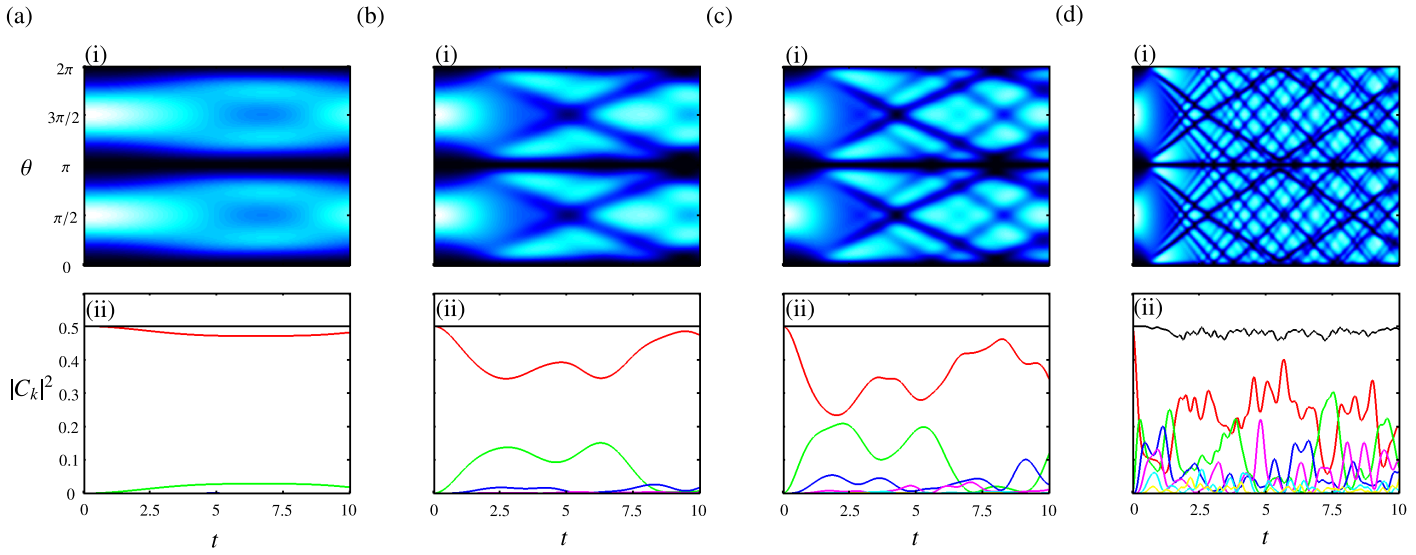

Figure 9.3: A comparison of the time-evolved dynamics of a one-component BEC in a ring trap, and their overlap, $|C_k|^2$, with angular momentum eigenstates with eigenvalue k [see Eq. (9.5)]for (a) $g = 10$, (b) $g = 50$, (c) $g = 100$, and (d) $g = 500$ where (–) $k = 1$, (–) $k = 3$, (–) $k = 5$, (–) $k = 7$, (–) $k = 9$, and (–) $k = 11$. Only angular momentum states separated by $\Delta k = 2$ are coupled, and the conservation of angular momentum ensures this occurs symmetrically, e.g., $|C_k|^2 = |C_{-k}|^2$, and therefore only overlaps with angular momentum with $k > 0$ are shown. The initial state corresponds to an antisymmetric superposition of momentum eigenstates with eigenvalues $k = 1, -1$ [see Eq. (9.1)]. The solid black line shows the sum of the angular momentum components. Few excitations occur for weak-interactions, whereas the occupation of higher angular momentum modes becomes significant for stronger interactions. The participation of few angular momentum modes in the weakly-interacting regime permits quasi-periodic motions to occur. Units are dimensionless.

9.1.6 The Fidelity of the Evolved State

A simple method to determine the dynamical stability is to evaluate the fidelity of the dynamics with respect to the initial state. The fidelity in this case is essentially an autocorrelation, and is given by

$$F(t) = \left| \int_0^{2\pi} \psi(\theta, t)\psi(\theta, 0)d\theta \right|^2 . \tag{9.6}$$

For the initial state (9.1), this takes the form of a Fourier integral, and picks out the common angular momentum components from the time-evolved state. Figure 9.4 shows the fidelity as a function of the interaction strength and time. Initially, the fidelity decreases, as expected, but experiences partial revivals at irregular intervals. This occurs approximately at the time the first-order grey-soliton excitations have completed one full revolution of the ring. For strong interactions, this revival occurs sooner; this is not surprising, since stronger interactions induce solitons to propagate more quickly. An interesting implication of Fig. 9.4 is that high-fidelity revivals appear to occur for all interaction strengths, although they are more short-lived for strong interactions. Also of importance is that the high-fidelity region for weak interactions is robust for long durations, and shows no observable narrowing.

Figure 9.5 shows the time-averaged fidelity after a time t for a given interaction strength, given by,

$$\overline{F} = \int_0^T dt \left| \int_0^{2\pi} \psi(\theta, t)\psi(\theta, 0)d\theta \right|^2 . \tag{9.7}$$

This corresponds to averaging the fidelity in horizontal scans across Fig.(9.4), but for different durations, and shows the decay of the fidelity for increasing interaction strengths. At first, the fidelity appears to deteriorate exponentially for increasing g, until saturating and oscillating around approximately 0.5.

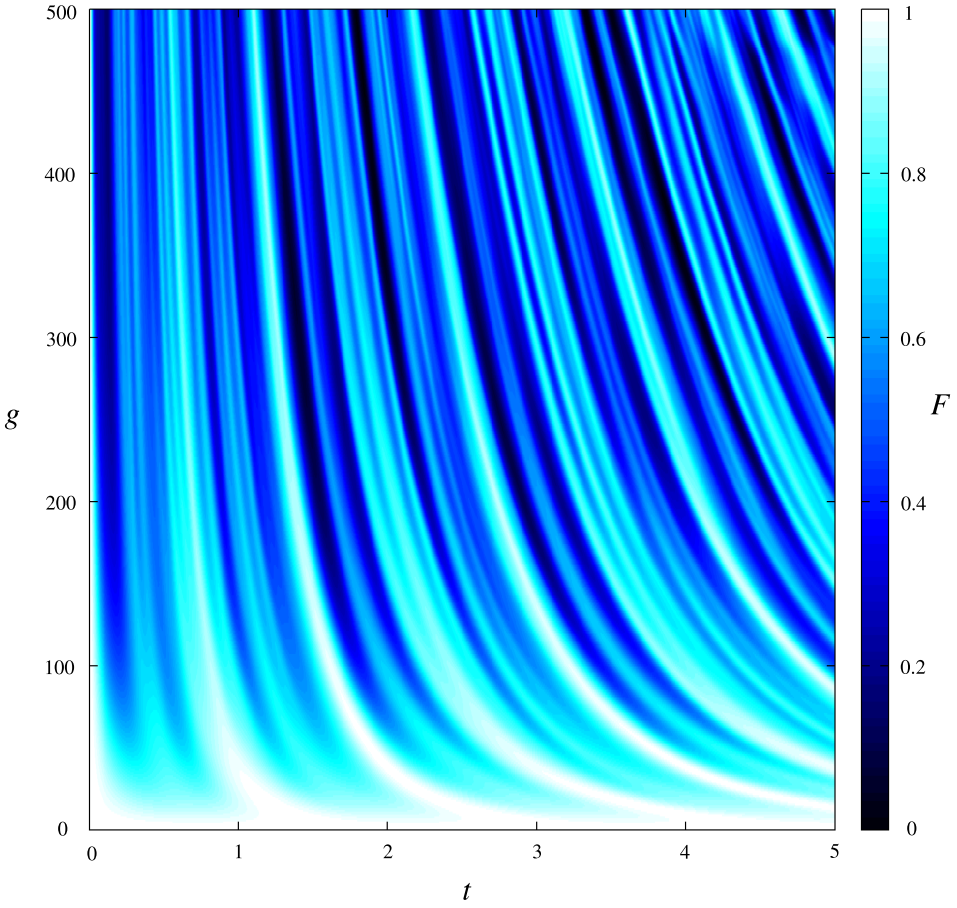

Figure 9.4: The fidelity with respect to the initial state [see Eq. (9.6)] of a weakly-interacting one-component BEC in a ring trap. The initial state corresponds to an antisymmetric superposition of momentum eigenstates with eigenvalues $k = 1, -1$ [see Eq. (9.1)]. For low interaction strengths, the fidelity remains consistently high, whereas for stronger interactions, the fidelity is low except during quasiperiodic revivals. Units are dimensionless.

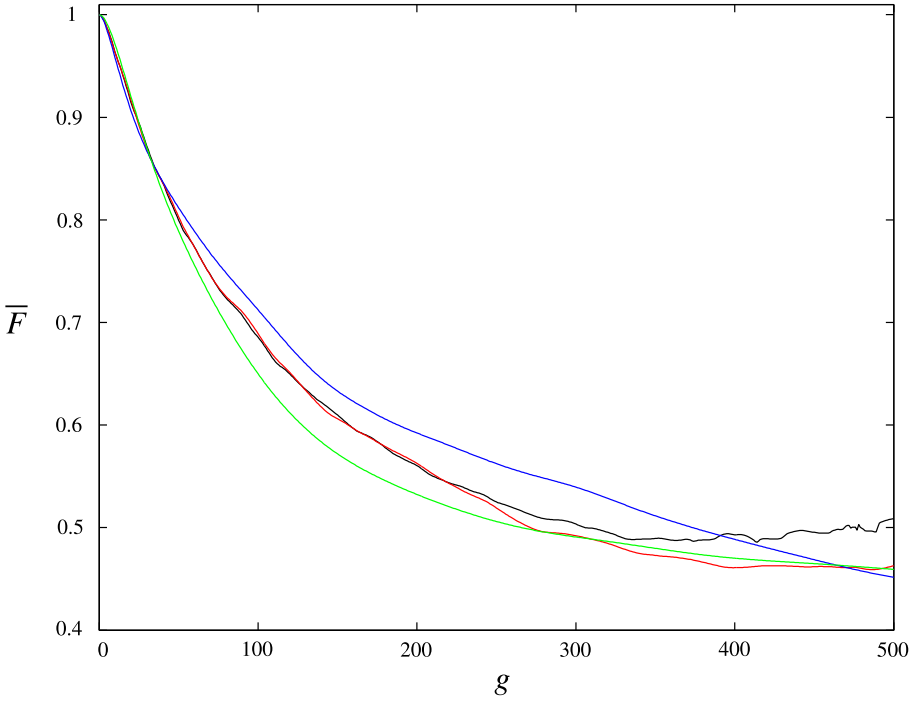

Figure 9.5: The time-averaged fidelity with respect to the initial state [see Eq. (reffidav)] for an increasing interaction strength, g, for dynamics for (-) $T = 10$, (-) $T = 5$, and (-) $T = 1$. The initial decay is exponential, but saturation occurs for low interaction strengths. The onset of saturation appears insensitive to the time duration of the time-averaging. Units are dimensionless.

9.1.7 Summary of One-Component Dynamics

For an initial state describing a superposition of two angular momentum states, the dynamics of a BEC in a ring trap exhibits complex dynamics. The description of these dynamics in terms of a stationary solution with some additional fluctuations, which manifest as soliton-like excitations, is conceptually useful in understanding the dynamics. A mathematical description in these terms, however, would be difficult, and would add little to the intuitive picture developed here. Instead, the qualitative picture was used to interpret numerical results. For moderate interaction strengths typically founded in experiments, the initial state quickly becomes scrambled by the dynamics. For very low interaction strengths, the discrete nature of the excitations allows the fidelity to remain high for relatively long times, but, except for very dilute conditions, a Feshbach resonance would be required to reach such a regime, in which case the objective would be to remove interactions totally. The rapid decay of the state therefore

suggests that a single-component BEC in a ring trap would be unsuitable for atom-interferometry unless direct control over the atom-atom interactions was exerted.

9.2 Two-Component BEC Mixture

For the purposes of atom-interferometry, it is useful to consider under what conditions the fidelity would remain high for typically encountered interaction strengths. Clearly, the excitations for one-component BECs are caused by variations in the atomic density which feed back into the dynamics through the nonlinearity in (8.28). It is interesting to consider the effect of a second BEC upon the dynamics to see if the decay of the fidelity can be mitigated by the presence of another atomic density.

In this section, the time-evolution of a two-component BEC, described by Eq. (8.29), prepared in a superposition of sinusoidal states will be considered. In a similar manner to the preceding section, the fidelity of the dynamics for variable interspecies and intraspecies interaction strengths will be used to quantify the dynamical stability of the system. Particular attention will be paid to an idealised experimental realisation using ^{87}Rb to demonstrate a typical operating regime for this system.

9.2.1 Initial Conditions

One way to avoid the effect of the nonlinearity, other than to make it small, is to make it constant. If the nonlinear terms remain constant during the dynamics then the time-evolution of the system can be derived straightforwardly. An example of an initial state that does this is

$$\psi_1(\theta, t=0) = \exp(in\theta), \tag{9.8a}$$

$$\psi_2(\theta, t=0) = \exp(-in\theta), \tag{9.8b}$$

where ψ_j $(j = 1, 2)$ are the wavefunctions of the BECs, and n is their angular momentum eigenvalue. These have uniform densities, and therefore the mean-field terms in (7.3) are constant, and the CGPEs resemble two uncoupled Schrödinger equations. The solutions of these are determined by applying the

effective unitary time-evolution operators,

$$\hat{U}_1(t) = \exp\left(-it\left[\frac{\hat{p}^2}{2} + g_{11} + g_{12}\right]\right), \tag{9.9}$$

$$\hat{U}_2(t) = \exp\left(-it\left[\frac{\hat{p}^2}{2} + g_{22} + g_{21}\right]\right), \tag{9.10}$$

to obtain,

$$\psi_1(\theta, t) = \exp\left(i\left[\frac{n^2}{2} + g_{11} + g_{12}\right]t\right)\exp\left(in\theta\right), \tag{9.11}$$

$$\psi_2(\theta, t) = \exp\left(i\left[-\frac{n^2}{2} + g_{22} + g_{21}\right]t\right)\exp\left(-in\theta\right). \tag{9.12}$$

In a general interferometric process, one state would accumulate a phase ϕ relative to the other, which would be determined by interfering the components of the BEC together. This process would result in a superposition of the type given in (9.1). Two measurement are required in order to determine the phase difference ϕ. However, the creation of the superposition state puts each BEC component in a state of non-uniform density. Subsequently, as demonstrated in the previous section, the fidelity rapidly decreases, and therefore a second measurement is thus prohibited.

An alternative scheme is to seek initial states that do not have uniform atomic densities, but still negate the effect of the nonlinearity. The availability of a second BEC component makes this possible; one example is

$$\psi_1(\theta, t = 0) = \sin\left(n\theta\right), \tag{9.13a}$$

$$\psi_2(\theta, t = 0) = \cos\left(n\theta\right), \tag{9.13b}$$

for which the corresponding nonlinear terms in (7.3), given by $\mathcal{N}_i = g_{ii}|\psi_i|^2 + g_{ij}|\psi_j|^2$ $(i, j = 1, 2 \text{ and } i \neq j)$ are,

$$\mathcal{N}_1 = g_{11}\sin^2(n\theta) + g_{12}\cos^2(n\theta), \tag{9.14a}$$

$$\mathcal{N}_2 = g_{22}\cos^2(n\theta) + g_{21}\sin^2(n\theta). \tag{9.14b}$$

In the special case where $g_{11} = g_{12} = g_{22} = g$, the identity $\sin^2(x) + \cos^2(x) \equiv 1$ implies that the nonlinearities are equal with $\mathcal{N}_1 = \mathcal{N}_2 = g$. The dynamics are then regular and predictable, enabling a description in terms of a simple phase evolution. However, the g_{ij} are inherent properties of the atom, and are not always easily adjusted. Fortunately, ^{87}Rb has three hyperfine sublevels, which can be used as trapping states, whose scattering lengths differ by less than 6% [see Table. 8.1], and therefore presents itself as an ideal candidate. It remains, therefore, to explore the effect of the small discrepancy between interaction strengths on the dynamical stability of the initial states (9.13).

9.2.2 Choice of Parameters

For typical parameter sets, the interaction strength g is very large, which can become problematic when implementing numerical methods. Although this can be alleviated by considering BECs containing fewer atoms, this would be disadvantageous in practical applications where many atoms are preferred to generate more easily observed signals.

In the numerical algorithm used in this work (see Appendix C), it is necessary to use more space-points, and correspondingly more timesteps, to obtain properly converged solutions for large g. This is because high interaction strengths induce high energy motions which require a finer space-time mesh to describe the kinetic energy. Although the necessary computational resources are available to do this for most parameters of interest, it is not feasible to perform extensive explorations over large parameter spaces.

The CGPEs are invariant under the rescaling $\{x, t, g, \psi\} \rightarrow \{sx, s^2t, g/s, \psi/\sqrt{s}\}$. The reduction of a high interaction strength to unity, therefore, is consistent with a corresponding increase in the spatial periodicity of the system, with correspondingly slower dynamics. The periodicity is held fixed here, and therefore high-interaction strength dynamics cannot be rescaled to describe equivalent low-interaction strength dynamics, due to the non-trivial way that nonlinear excitations manifest in this system. The focus here, however, is on dynamics where these excitations have little effect. Therefore, once regimes have been identified for weakly-interacting systems, there should be a corresponding regime for larger g. Consequently, the essential physics will be investigated for few atom numbers, and large atom numbers will be investigated for specific cases of interest.

9.2.3 Time-Evolution

The introduction of a second BEC component creates a situation of two qualitatively different dynamical regimes, depending on the miscibility $\alpha = g_{12}^2/g_{11}g_{22}$ of the BEC mixture. For $\alpha > 1$, the BEC components spontaneously separate (assuming they were spatially overlapped), and the system is said to be in the immiscible regime, whereas for $\alpha < 1$, the BEC components are able to fully interpenetrate, and the system is said to be miscible.

Figures (9.6) and (9.7) show a range of dynamics in the miscible and immiscible

regimes, respectively, for the initial conditions (9.13) with the two intraspecies interaction strengths equal. In both cases, $g_{11} = g_{22}$, and therefore $\psi_1 = \psi_2$ except for a phase shift of π; consequently, only ψ_1 is shown. In the miscible regime, the atomic density rapidly spreads to fill the space around the nodes of the wavefunction. For $g_{12} \approx g_{11} = g_{22}$, the dynamics of the system appear regular over the time-scales shown, whereas for much lower g_{12} the BEC components essentially decouple, and the dynamics begin the resemble the one-component case. For small, but nonzero g_{12}, the excitations of the system appear to retain their soliton-like characteristics. It is interesting to consider if these excitations are examples of the topological winding and unwinding described in Ref. [217], and whether a sophisticated experimental realisation of this system could, in principle, tune g_{12} to observe varying degrees of this effect. As for GPE, the CGPEs preserve the symmetry of their individual initial states, ensuring the preservation of the number and the position of the nodes in their wavefunctions.

In the immiscible regime, it is less reasonable that the dynamics may be considered to be a combination of soliton-like excitations. What is clear, however, is that the individual components are almost completely separated for high g_{12}. For g_{12} similar to g_{11} and g_{22}, the atomic density appears to evolve in a manner that suggests that their nonlinear interaction has little effect.

The degree of excitation can be characterised by examining the BEC components in an angular momentum basis. Figures (9.8) and (9.9) show the populations of the lowest significantly-occupied angular momentum modes in BEC component j, calculated as

$$c_k^j = \frac{1}{\sqrt{2\pi}} \int_0^{2\pi} d\theta \exp(ik\theta)\psi_j. \tag{9.15}$$

For the same fractional change of g_{12}, the degree of excitation in the immiscible regime is less severe than in the miscible regime. Trivially, this follows from the fact that the two BEC components in the immiscible regime are rigidly interlocked, and unable to tunnel through each other which strong encourages the localisation of their respective densities. It is tempting to believe that high g_{12} is advantageous for interferometry because it rigidly interlocks the two BEC components so that the atomic densities are not greatly dissimilar to the initial state. However, Fig. (9.9) shows that this aggressive confinement populates many angular momentum states, which would be a significant source of error in interferometry as well leading to considerable depletion of the condensate mode.

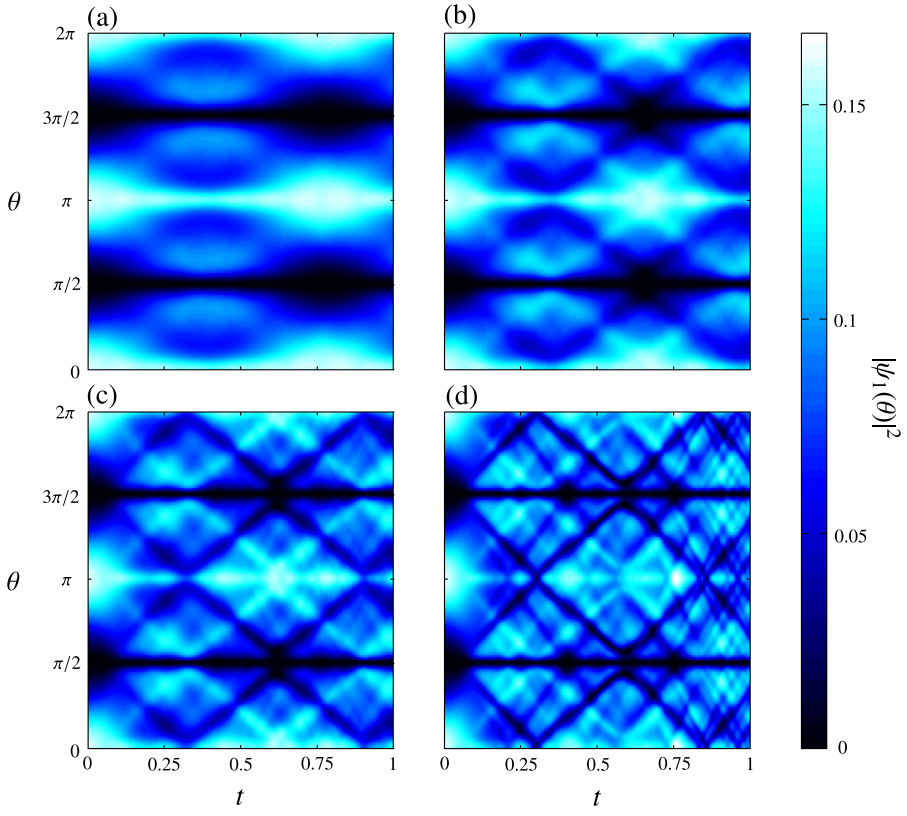

Figure 9.6: The time-evolved atomic density of a two-component BEC in a ring trap in the miscible regime for $g_{11} = g_{22} = 1000$ and (a) $g_{12} = 900$, (b) $g_{12} = 800$, (c) $g_{12} = 700$, and (d) $g_{12} = 500$, with each component equally populated and normalised to 1/2. Since $g_{11} = g_{22}$, $|\psi_1|^2 = |\psi_2|^2$ except for an angular shift of π, and therefore only the atomic density $|\psi_1|^2$ is shown. For g_{12} much less than 1000, the excitations resemble the soliton-like excitations observed in the one-component case whereas for g_{12} approaching 1000, the excitations not only lose their soliton-like character but also significantly diminish. Parameters correspond to one dimensionless time-unit equivalent to 0.14 seconds, and $N \approx 2800$, and the zero-magnetic field s-wave scattering lengths of ^{87}Rb [see Table (8.1]. Units are dimensionless.

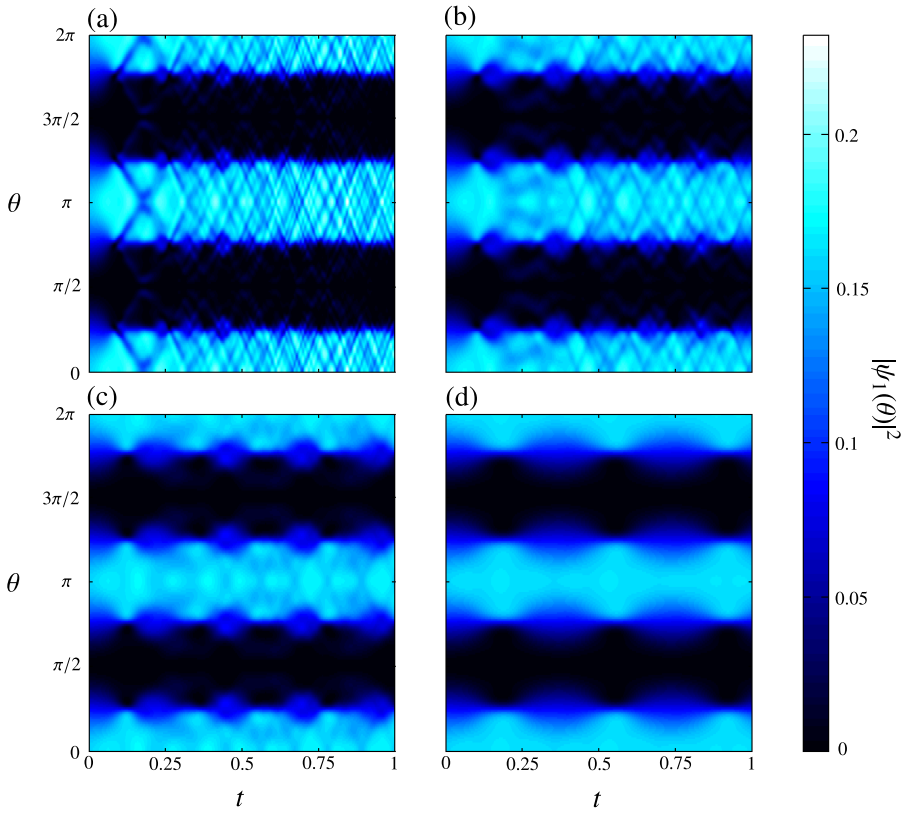

Figure 9.7: The time-evolved atomic density of a two-component BEC in a ring trap in the immiscible regime for $g_{11} = g_{22} = 1000$ and (a) $g_{12} = 1500$, (b) $g_{12} = 1300$, (c) $g_{12} = 1200$, and (d) $g_{12} = 1100$, with each component equally populated and normalised to 1/2. Since $g_{11} = g_{22}$, $|\psi_1|^2 = |\psi_2|^2$ except for an angular shift of π, and therefore only the atomic density $|\psi_1|^2$ is shown. For g_{12} much greater than 1000, traces in the density manifest, but the dynamics are not resolved sufficiently to compare them to the soliton-like excitations seen in the one-component case. For g_{12} approaching 1000, the excitations significantly diminish, and the initial state appears to persist. Parameters correspond to one dimensionless time-unit equivalent to 0.14 seconds, and $N \approx 2800$, and the zero-magnetic field s-wav scattering lengths of ^{87}Rb [see Table (8.1]. Units are dimensionless.

Despite being far from equality of the three interaction strengths, it is interesting that these states still represent superpositions of counter-propagating flow, despite being in an immiscible regime. This apparent contradiction may be resolved by realising that the creation of the two-component system results in a superposition of an equal superposition of flows. Therefore, prior to a measurement, the position of an atom is completely undetermined since the atom is assumed to be well-described by an angular momentum eigenstate. Furthermore, it is impossible to know what component an atom occupies, or the sense of its rotation. Specifically, a measurement of the internal state of the atom does not yield the direction of propagation, and similarly, a measurement of the direction of propagation does not yield the state, and in both instances one can never know where the atom is on the ring until it is measured directly. Consequently, it is permissble to consider this system as two distinct vortex superpositions coupled by their respective atomic densities - the miscibility does not prohibit, therefore, a state describing counter-propagating flow.

9.2.4 Fidelity with Respect to the Initial State

The regime where the interaction strengths are similar, but not equal, can be examined by calculating the fidelity of the initial state, in the same way as for a one-component BEC. The fidelity of the j-th component is given by,

$$F_j(t) = \left| \int_0^{2\pi} d\theta \psi_j(\theta, t) \psi_j(\theta, 0) \right|^2, \tag{9.16}$$

where the maximum of $F_j(t)$ is $1/4$ since the wavefunctions are normalised to $1/2$.

Figure 9.10(a) shows the fidelity of the state for $g_{11} = g_{22} = 1000$ whilst varying g_{12}. In the immiscible regime, the fidelity is generally higher, and has maxima that occur quasi-periodically. Similar revivals of the fidelity are observed in the miscible regime, except these are separated by regions of particularly low fidelity. In these instances, this is accompanied by greater occupation of higher angular momentum modes, which may facilitate decoherence of the system.

For equal interaction strengths, there is a significant range of g_{12} where the fidelity is persistently high. For the range $g_{12} = [958, 1056]$, the fidelity is never lower than 0.24, i.e., it does not decay by more than 4%. Moreover, this interval is larger than the regime of dynamical stability found in a one-component BEC

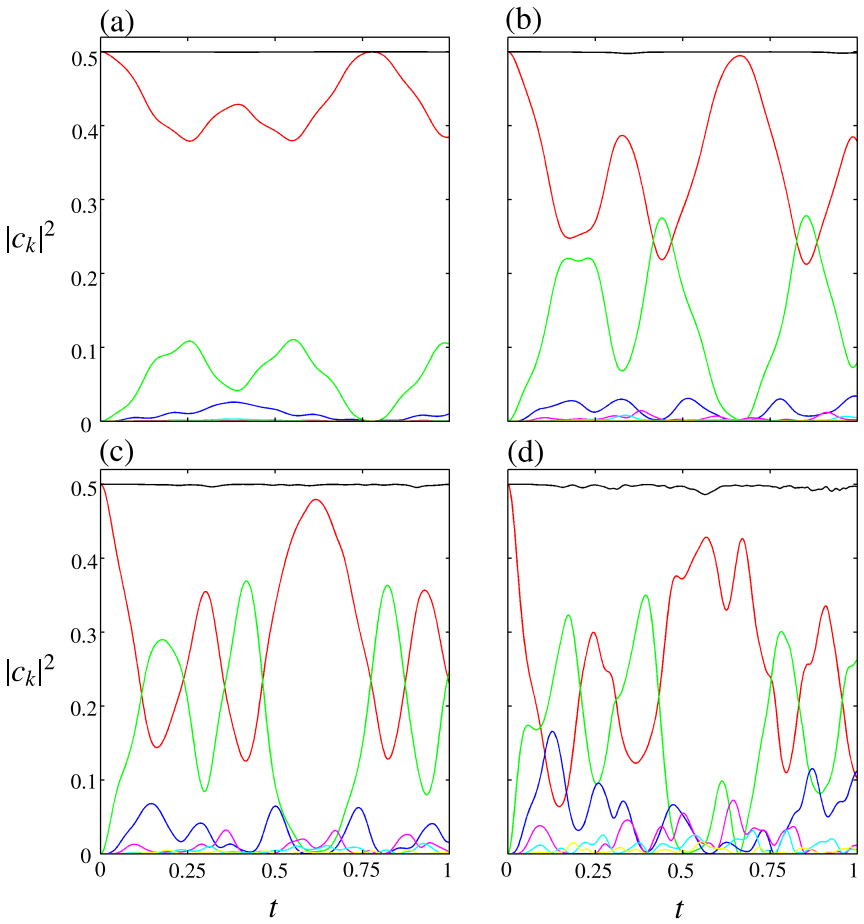

Figure 9.8: The time-evolution of the angular momentum components of a two-component BEC for $g_{11} = g_{22} = 1000$ and (a) $g_{12} = 900$, (b) $g_{12} = 800$, (c) $g_{12} = 700$, and (d) $g_{12} = 500$, for angular momentum eigenstates with eigenvalues (–) $k = 1$, (–) $k = 3$, (–) $k = 5$, and (–) $k = 7$, (–) $k = 9$, and (–) $k = 11$. As for the one-component case, only angular momentum states with $\Delta k = 2$ are coupled, and the conservation of angular momentum ensures this occurs symmetrically, e.g., $|C_k|^2 = |C_{-k}|^2$, and therefore only overlaps with angular momentum with $k > 0$ are shown. Each BEC component is equally populated and normalised to 1/2. Since $g_{11} = g_{22}$, $|C_k^1|^2 = |C_k^2|^2 \equiv |C_k|^2$. The solid black line shows the total of the angular momentum components, which has a maximum of 1/2. For g_{12} much less than 1000, the occupation of higher-angular momentum states becomes more significant, and is accompanied by rapid oscillatory behaviour. Quasi-periodic revivals of the initial state are observed for low interaction strengths. One dimensionless time-unit corresponds to a time of 0.14 seconds. Units are dimensionless.

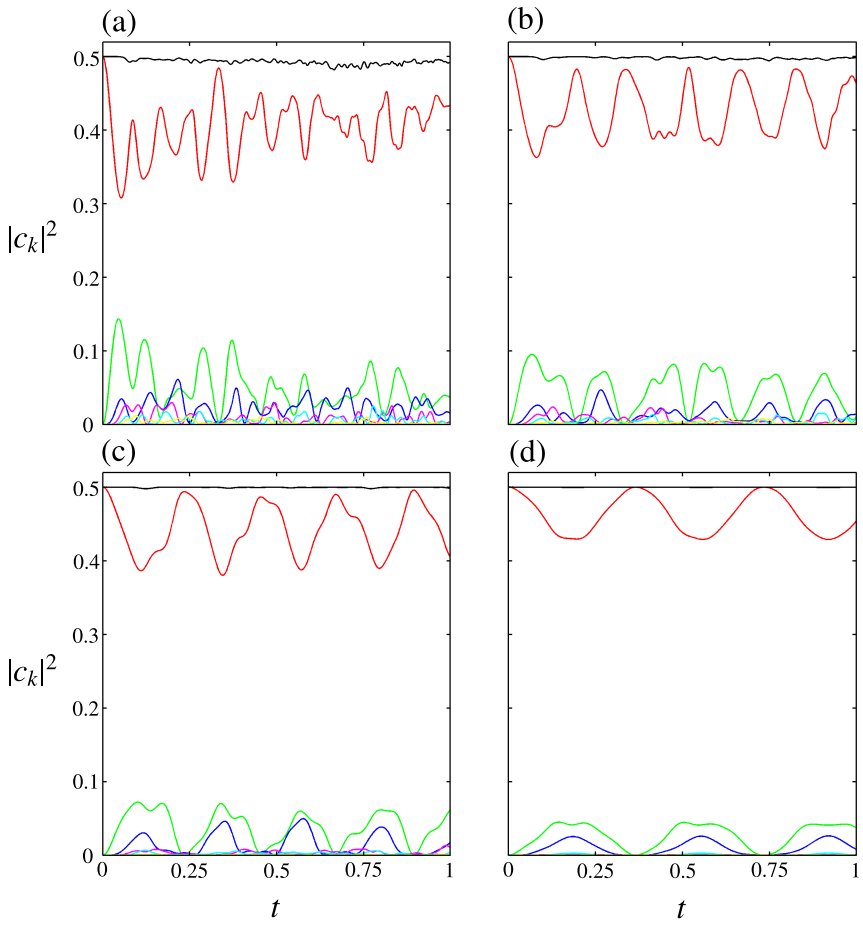

Figure 9.9: The time-evolution of the angular momentum components of a two-component BEC for $g_{11} = g_{22} = 1000$ and (a) $g_{12} = 1500$, (b) $g_{12} = 1300$, (c) $g_{12} = 1200$, and (d) $g_{12} = 1100$, for angular momentum eigenstates with eigenvalues (–) $k = 1$, (–) $k = 3$, (–) $k = 5$, and (–) $k = 7$, (–) $k = 9$, and (–) $k = 11$. As for the one-component case, only angular momentum states with $\Delta k = 2$ are coupled, and the conservation angular momentum ensures this occurs symmetrically, e.g., $|C_k|^2 = |C_{-k}|^2$, and therefore only overlaps with angular momentum with $k > 0$ are shown. Each BEC component is equally populated and normalised to 1/2. Since $g_{11} = g_{22}$, $|C_k^1|^2 = |C_k^2|^2 \equiv |C_k|^2$. The solid black line shows the total of the angular momentum components, which has a maximum of 1/2. For g_{12} much less than 1000, the occupation of higher-angular momentum states becomes more significant, and is accompanied by rapid oscillatory behaviour. Quasi-periodic revivals of the initial state are observed for low interaction strengths. One dimensionless time-unit corresponds to a time of 0.14 seconds. Units are dimensionless.

in the previous section, implying that the presence of interactions may help to preserve the initial state.

Figure 9.10(b) shows the time-averaged fidelity with respect to the initial state, given by,

$$\overline{F}_j = \int_0^T dt \left| \int_0^{2\pi} d\theta \psi_j(\theta, t) \psi_j(\theta, 0) \right|^2 , \tag{9.17}$$

with $T = 10$ and $g_{12} = 1000$. Note that, due to the normalisation of ψ_j being $1/2$, the maximum fidelity is $1/4$. The region of dynamical stability appears to extend over a significant neighbourhood around exact equality of the interaction strengths. As, expected, the mean fidelity is generally lower in the miscible regime than in the immiscible regime. Interestingly, dynamical stability appears to be preferred for interaction strengths that are close to the transition from a miscible to immiscible regime, i.e., where $\alpha = 1$. However, it is clear that even for $\alpha = 1$, the fidelity cannot be maximal because the initial states are identical except for a phase shift and the interaction strengths are asymmetric. The parameter regime corresponding to an implementation using ^{87}Rb under the typical experimental conditions using 2800 atoms [see Table 8.1] is marked, and can clearly seen to lie within the stability region. The time-averaged fidelity at this point for $T = 10$ is 0.2432, suggesting that the dynamics are extremely dynamical stable.

9.2.5 ^{87}Rb BEC

Dynamical Stability

The interaction strengths considered so far correspond to a two-component BEC with relatively few atoms. Figures 9.10(b) and (c) indicate the fidelity of the dynamics for a ^{87}Rb BEC of 2800 atoms for typical trapping frequencies. Although many BEC experiments have similarly low atom numbers, greater atom numbers may be preferable from an experimental point of view. In considering the application of this system in atom-interferometry, it is prudent therefore to consider if the regime of dynamical stability persists for many atoms, i.e., for stronger interactions. The experiment by Ryu *et al* [166] is the closest realisation of the system studied here, and the BECs that were used in that work contained approximately 280,000 atoms, which corresponds to $g_{12} \approx 100,000$ in the dimensionless units used here [see Table 8.1].

Figure 9.11(a-b) shows the dynamics for ^{87}Rb of 280,000 atoms for $T = 10$ (1.4

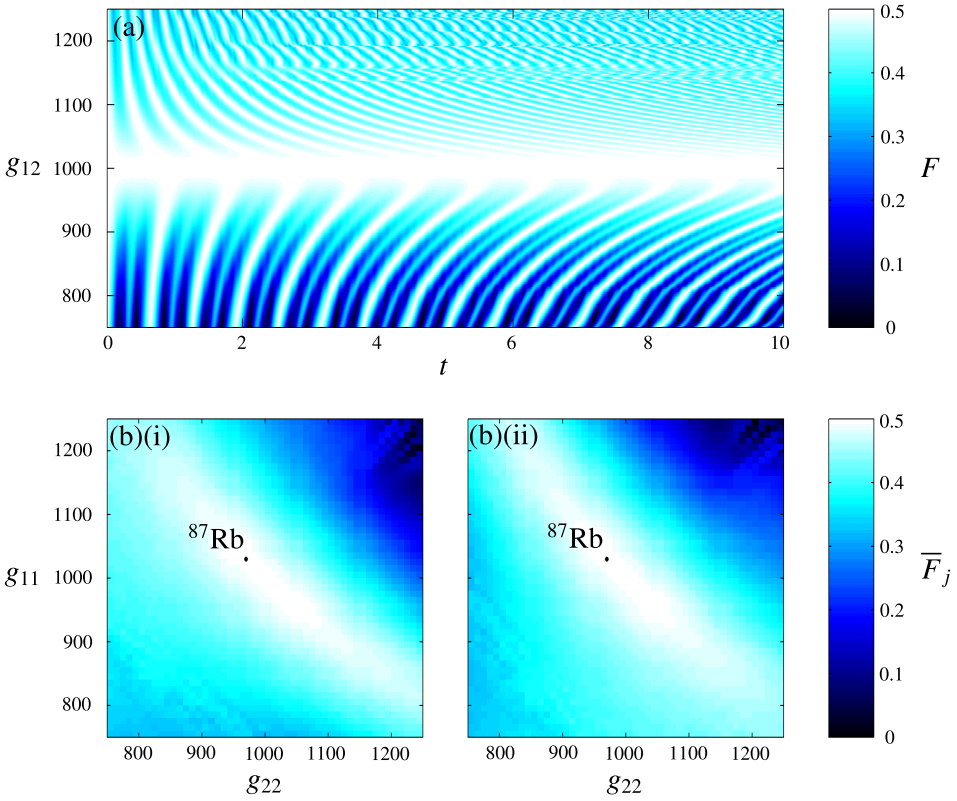

Figure 9.10: The fidelity of a two-component BEC subject to the initial conditions (9.13) for a dimensionless time $T = 10$, corresponding to 1.4 seconds. Shown is (a) the fidelity $F_1 = F_2 = F$ [see Eq. (9.16)] for $g_{11} = g_{22}$, and (b) the time-averaged fidelity, $\overline{F}_j$, with $g_{12} = 1000$ for (i) $\psi_1(\theta, t)$ and (ii) $\psi_2(\theta, t)$, with the parameter regime corresponding to a typical implementation of ^{87}Rb marked for comparison [see Table 8.1]. Note that, as expected, figures (b)(i-ii) are identical under a reflection through $g_{11} = g_{22}$. Units are dimensionless.

seconds). The dynamics appear stable, and do not exhibit any of the soliton-like excitations that accompany low fidelities. There are small oscillations in the atomic densities that were not easily visible in the few-atom case, however, and these persist for the duration of the dynamics. Subsequently, the mean fidelity is 0.23, which is lower, and suggests that the region of stability shrinks for larger atom numbers. Figure 9.11(c) demonstrates that the degree of excitation in this system is low, inferred from the low occupation of high angular momentum states, but the oscillation frequency of the states is high, suggesting the presence

of fast, but very shallow, sound waves or grey-soliton excitations. Therefore, the region of dynamical stability identified for weak interactions appears to remain for stronger interactions, and suggests that this system would be suitable for atom-interferometry.

Self-Stabilising Interaction Regime

Conceptually, one can consider the atomic densities associated with each component to be interleaved with each other, but in a manner that results in a constant total mean-field interaction. It is interesting to consider whether this interleaving also contributes a restorative force that could be exploited, for example, in the scenario where the initial states are imperfectly aligned. For example, for the initial states,

$$\psi_1(\theta, t=0) = \cos(n\theta) \tag{9.18a}$$

$$\psi_2(\theta, t=0) = \sin(n\theta + \delta), \tag{9.18b}$$

the nonlinear terms are no longer constant, and the regular dynamics in Fig. 9.11 will not be reproduced, even for equal interaction strengths. However, for equal g_{ij} and small δ, the nonlinear terms (9.14) are approximately

$$\mathcal{N} \approx g\left[1 + \delta \sin(2n\theta)\right] \tag{9.19a}$$

The effect of small angular shifts in the initial condition is therefore equivalent to introducing a small angular potential around the ring trap. This nonlinear potential does not remain constant, however, and the initially sinusoidal angular potential evolves nonlinearly into a more complicated form. For small angular shifts, the effect of the nonlinearity will be weak, and it is reasonable to assume that the nonlinear terms will remain constant for a time determined by $g\delta$. In some sense, this introduces a roughness to the trapping potential albeit one that is time-dependent, and the examination of such a scenario therefore provides some insight into sensitivity of the dynamics to an imperfect trapping potential as well directly examining the case of imperfect alignment.

Fig. 9.12 shows the fidelity of the atomic density for a range of initial angular shifts, corresponding to using ^{87}Rb with 280,000 atoms [see Table 8.1]. It can be inferred that the two-components are oscillating out of phase with each other, and undergoing "sloshing" motion in the mean-field potential of the opposite component. The observation of damping in this sloshing behaviour, however,

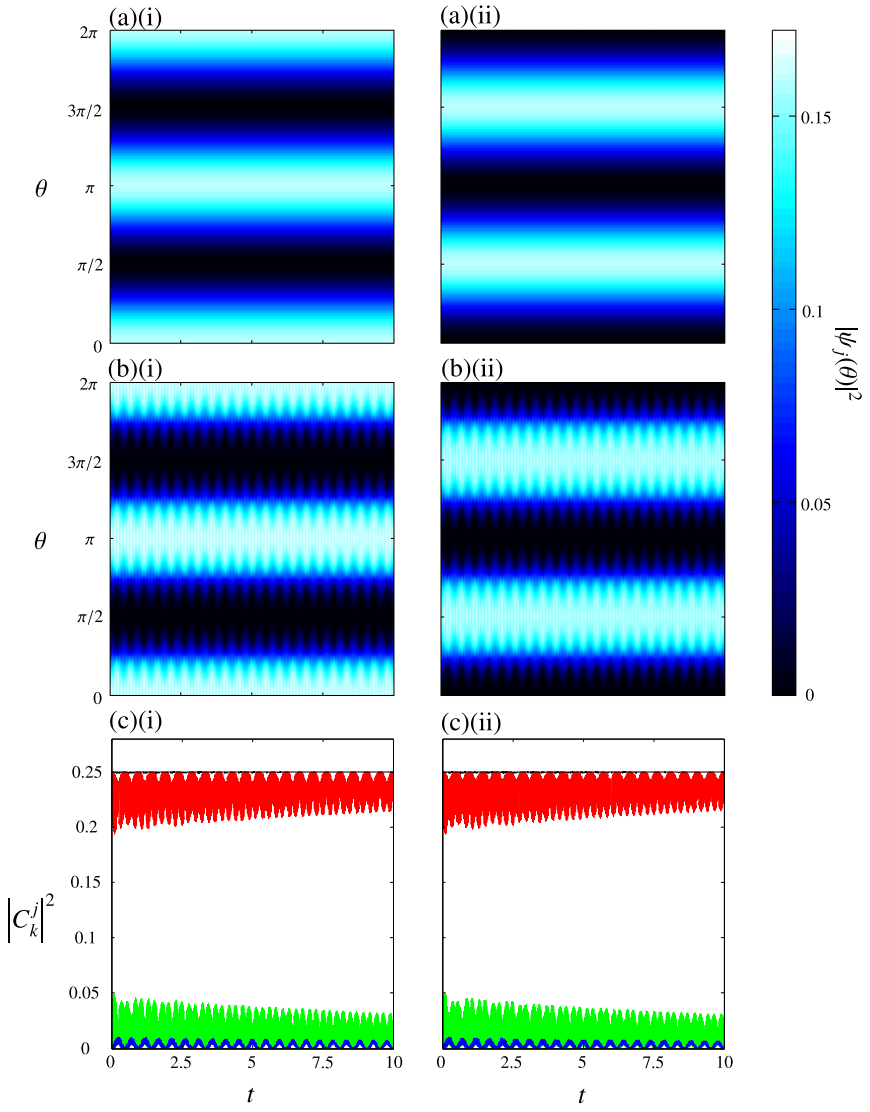

Figure 9.11: The time-evolved dynamics of a two-component ^{87}Rb BEC of 280,000 atoms under typical experimental parameters in (a) the ideal case where $g_{ij} = 100,000$, and (b) the case corresponding to $g_{11} = 97,000$, $g_{12} = 100,000$, and $g_{22} = 103,000$, where the occupied hyperfine sublevels are $|1\rangle = |F = 1, m_F = -1\rangle$ and $|2\rangle = |F = 2, m_F = 1\rangle$. Compared to the ideal case, the density fringes undergo regular breathing motions, with the extreme of the fringes preserved by symmetry. (c) The time-evolution of the angular momentum components [see Eq. (9.5)] with the eigenvalues (–) $k = 1$, (–) $k = 3$, and (–) $k = 5$. The solid black line is the sum of these three angular momentum components. The breathing motion in panel (b) is associated with rapid oscillations in the amplitudes of the angular momentum components, but relatively few modes are involved indicating that excitation of the state is weak. Units are dimensionless.

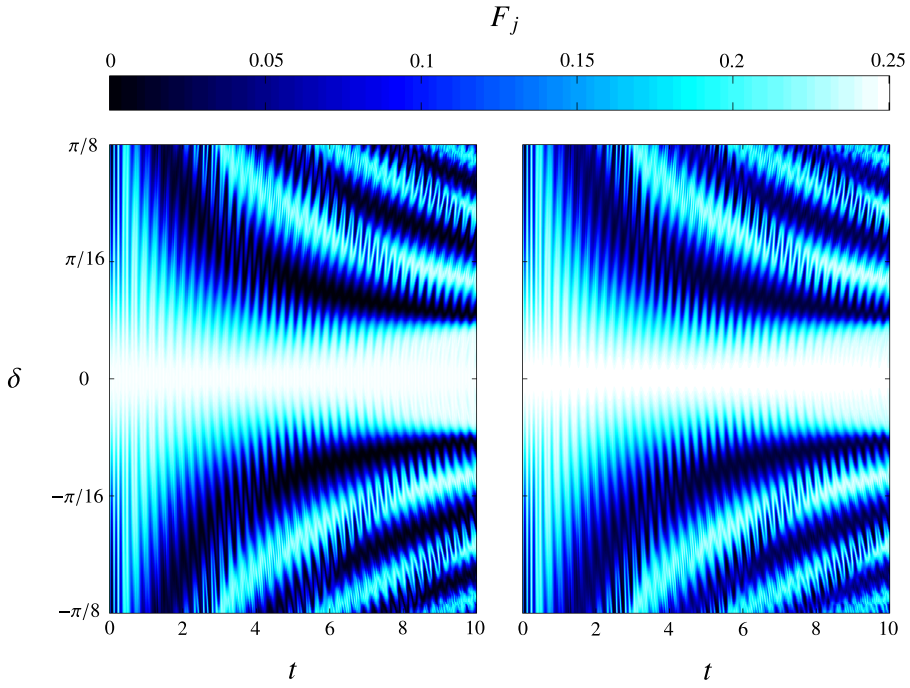

Figure 9.12: The fidelity of a two-component BEC [see Eq. (9.16)] with respect to the initial state (9.18) for (a) $\psi_1(\theta, t)$ and (b) $\psi_2(\theta, t)$. Parameters correspond to an experimentally feasible implementation of ^{87}Rb [see Table 8.1] with 280,000 atoms (i.e., $g_{11} = 97000$, $g_{12} = 100000$, and $g_{22} = 103000$) with $T = 10$ corresponding to 1.4 seconds [see Table 8.1]. Small angular displacement in the initial condition fall within an interval of high fidelity with a width of approximately 10 degrees. Units are dimensionless.

is an indication that some tunnelling (of the wavefunction of one-component through the atomic density of the second-component) occurs, resulting in complicated nonlinear dynamics.

The most pertinent observation, however, is the occurrence of an interval of notably high dynamical stability. This appears to narrow at first, before undergoing some damping, i.e., the fidelity decays. It is not clear if this the beginning of revival behaviour within the stability region, or if this would occur indefinitely. A conclusion that can be drawn, however, is that the system is not sensitive to perfect alignment of the initial states. An implication is the system also has the capability to withstand small perturbations that cause angular shifts between the BEC components during the dynamics, although that has not been shown explicitly.

9.2.6 Summary of Two-Component Dynamics

The inclusion of a second BEC component permits a regime of dynamical stability, identified by a persistently high fidelity with respect to the initial state, for which the inter- and intra-species interaction strengths are approximately equal, as is possible in ^{87}Rb. Numerical evidence has been given to suggest that this regime exists for a typical implementation of ^{87}Rb over an experimentally appreciable time. In addition, small angular displacements between the initial states of the components, as may be present following imperfect preparation, has been briefly examined. For small displacements, the fidelity remains high over an appreciable duration. One would not expect this to be the case in the miscible regime, and the lack of exact equality of the interaction strengths in ^{87}Rb can be seen to be advantageous in this respect. The existence of an accessible regime of stable dynamics suggest the possibility of exploiting a two-component BEC in a ring trap for the purposes of atom-interferometry.

Chapter 10

Sagnac Interferometry in a Ring Trap

10.1 Introduction

In the previous chapter, the dynamics of one- and two-component BECs was studied. In both cases, particular attention was paid to how the fidelity of the initial state varied with the mean-field interactions for a particular set of initial conditions. Of direct relevance is the result that ^{87}Rb lies in a regime where the fidelity is almost maximal for long times. In this chapter, a proof-of-principle Sagnac interferometer will be presented that exploits these dynamics to make measurements of rotation.

To begin, the Sagnac effect will be summarised. Then, two idealised protocols for implementing a Sagnac interferometer using a two-component BEC in a ring trap will be outlined. Both protocols are very similar, and only differ in the final measurement stage where either a position-dependent atomic density or a relative population measurement is made. Before concluding, an estimate of the sensitivity of these interferometers is given, with a brief discussion of how the proposed Sagnac interferometer differs from conventional implementations.

10.2 The Sagnac Effect

The Sagnac effect [204] is a rotational phenomenon that was originally discovered in optics. It describes the accumulation of a phase shift between two identical counter-propagating waves around the same closed path in a rotating frame. Although traditionally an optical effect, it is in fact more universal [205]. Specifically, the Sagnac effect is not a relativistic effect[1], and also applies to matter-waves [15, 178, 181, 182, 197, 218, 219]. Given that atom interferometry is especially suited to measuring inertial effects, this latter point has been exploited to use the Sagnac effect high-precision measurements of rotation. The sensitivity of a matter-wave Sagnac interferometry is expected to be sufficiently great that it has even been proposed as a method of testing general relativity [219]. At present, however, Sagnac atom-inteferometers use sources of cold [15, 181, 182, 197] or thermal atoms [178, 218, 219], and a Sagnac interferometer with BECs is yet to be demonstrated. Some schemes have been proposed [183, 198, 200, 220] but these assume negligible atom-atom interactions.

The phase difference between two counter-propagating beams of light traversing the same closed path, called the Sagnac phase, is given by

$$\Delta\theta_{\text{light}} = \frac{8\pi A}{\lambda v}\Omega, \tag{10.1}$$

where A is the enclosed area of the closed path, Ω is the rotation of the external system (orthogonal to enclosed area), λ is the wavelength, and v is the velocity of the wave. This expression elucidates an often-quoted characteristic of Sagnac interferometers, i.e., that the Sagnac phase is directly proportional to the product of the enclosed area, A, and the rotation of the external system. Consequently, efforts are made to design Sagnac interferometers to maximise the area they enclose to increase the sensitivity of the device.

An equivalent form of Eq. (10.1) for matter-waves can be obtained by substituting λ for the de Broglie wavelength, λ_{dB}, yielding,

$$\Delta\theta_{\text{matter}} = \frac{8\pi m v A}{h}\Omega. \tag{10.2}$$

where v is the velocity of the de Broglie wave. In this form it can be seen that the relative sensitivity to the Sagnac phase in both of its manifestations is

$$\frac{\Delta\theta_{\text{light}}}{\Delta\theta_{\text{matter}}} = \frac{mc\lambda}{h} \approx 10^{10}, \tag{10.3}$$

[1] Originally, the Sagnac effect was used in investigations of relative motion against a supposed aether.

where typical experimental parameters have been assumed. This huge increase in sensitivity is a strong motivating factor for performing Sagnac interferometry with atom-interferometers.

10.3 A Sagnac Interferometer with a Two-Component BEC

Sagnac interferometry with cold atoms has been demonstrated using magnetic waveguides [182, 183], launched atoms[15], and stimulated Raman transitions in MOTs [197, 219, 221]. In all of these implementations, atom-atom interactions contribute a deleterious effect to the measurement process [152], and efforts are made to avoid their effect. Theoretical work by Boxio *et al* has shown that, contrary to expectation, many-body interactions could be exploited to decrease the inherent uncertainty in an atom-interferometer by beating the Heisenberg limit [189].

A two-component BEC confined in a ring trap is an ideal configuration in which to consider Sagnac matter-wave interferometry. The previous chapter showed how, under certain conditions, the inherent atom-atom interactions can not only be included in a way which preserves the fidelity of the state, but that they also help to stabilise the dynamics against small imperfections in some cases. In this section, these results will be exploited in a proposal of Sagnac interferometry.

10.3.1 CGPEs in a Rotating Frame

The CGPEs (7.3) can be transformed into a rotated frame to yield

$$i\hbar\frac{\partial\Psi_j}{\partial t} = \left[-\frac{1}{2}\frac{\partial^2}{\partial\theta^2} - i\Omega\frac{\partial}{\partial\theta} + (-1)^j\frac{\hbar\omega}{2} + \sum_{k=1}^{2} g_{jk}|\psi_k|^2\right]\psi_j, \tag{10.4}$$

The explicit inclusion of rotation does not alter the conclusions of the previous chapter. The dynamics are identical except for a precession about the ring at the rate Ω, and therefore the regimes of dynamical stability are unchanged. This is obvious since the transition to a moving frame is performed with the application of a unitary operator, and therefore observables are not affected; only a relative motion is observed [220]. Clearly, however, non-zero values of Ω are required to observe the Sagnac effect, but this will not manifest in the dynamics; rather, it will be extracted using the protocols below.

10.3.2 Preparation of the State

The BEC-components can be considered to be described by the orthogonal basis elements $|\alpha\rangle$ and $|\beta\rangle$, which represent the internal states of the trapped atoms, so that a general wavefunction, $|\psi\rangle$, of the two-component BEC is described by,

$$|\psi\rangle = a|\alpha\rangle + b|\beta\rangle \tag{10.5}$$

where a and b are the probability amplitudes associated with the components α and β, respectively, and obey the normalisation condition $|a|^2 + |b^2| = 1$. It is convenient to introduce a vector notation using the basis $\{|\alpha\rangle, |\beta\rangle\}$, so that the general state (10.5) is written as

$$\boldsymbol{\psi} = \begin{pmatrix} a \\ b \end{pmatrix}. \tag{10.6}$$

The starting point for the idealised Sagnac interferometry described here will be a BEC in its motional ground state confined in the state $|F = 1, m_F = -1\rangle$ a ring trap, written as,

$$\boldsymbol{\psi}_0 = \begin{pmatrix} 1 \\ 0 \end{pmatrix}. \tag{10.7}$$

The second BEC-component may then be populated by the application of a resonant $\pi/2$ pulse to the relevant internal state transition, implemented as a microwave pulse or a Raman transition, for example. This operation is represented in the vector representation by the unitary matrix

$$U_{\pi/2} = \frac{1}{\sqrt{2}} \begin{pmatrix} 1 & 1 \\ 1 & -1 \end{pmatrix}, \tag{10.8}$$

and creates an equal superposition of both BEC-components, described by

$$\begin{aligned} \psi_{\pi/2} =& U_{\pi/2}\boldsymbol{\psi}_0 \\ =& \frac{1}{\sqrt{2}} \begin{pmatrix} 1 & 1 \\ 1 & -1 \end{pmatrix} \begin{pmatrix} 1 \\ 0 \end{pmatrix} \\ =& \frac{1}{\sqrt{2}} \begin{pmatrix} 1 \\ 1 \end{pmatrix}, \end{aligned} \tag{10.9}$$

Small errors in this stage will result in unequal populations, with their associated changes to the values of g_{ij}, but for sufficiently small imbalances this has already been shown to have little impact on the dynamics.

The state is then phase imprinted with orbital angular momentum (OAM). This has been demonstrated experimentally by using the Laguerre-Gauss mode of a laser to transfer a known amount of OAM of light to a BEC confined in a toroidal trap [135]. It is reasonable to model the imprinted state with an angular momentum eigenstate with an eigenvalue equal to the amount of OAM transferred. Since each BEC-component is associated with a different magnetic sublevel, they are separately addressable, in principle, and it is therefore assumed that the transfer of OAM to each component can take place independently. Considering a transfer of $m\hbar$ to component α, and $\ell\hbar$ to component β, where m and ℓ are integers, the transfer process is described in the matrix representation as

$$\begin{aligned}\vec{\psi}_{\ell m}(\theta) =& U_{\ell m}\psi_0 \\ \equiv& \frac{1}{\sqrt{2}}\begin{pmatrix} e^{i(m+\ell)\theta} & 0 \\ 0 & e^{i(m-\ell)\theta} \end{pmatrix}\begin{pmatrix} 1 \\ 1 \end{pmatrix} \\ =& \frac{1}{\sqrt{2}}\exp\left[im\theta\right]\begin{pmatrix} \exp(i\ell\theta) \\ \exp(-i\ell\theta) \end{pmatrix}.\end{aligned} \tag{10.10}$$

The resultant state describes a superposition of two angular momentum eigenstates of with a difference in OAM of 2ℓ, and will be used as the initial state for the following protocols. For $m = 0$, this state describes two counter-propagating flows with equal and opposite angular momentum.

Experimentally, it may be technically difficult to simultaneously transfer equal and opposite OAM in a state-selective way to a trapped two-component BEC. However, as will become clear below, this is not strictly necessary; one can, instead, transfer OAM to one component so that the relative motion describes counter-propagation. That is, either m or ℓ may be set to zero. Therefore, the creation of the state (10.10) is within current experimental capability. For clarity, however, the case where the angular momenta of the flows is equal and opposite, where $m = 0$, will be considered.

10.3.3 Free-Evolution

When the initial atomic density in each BEC-component is constant, the CGPEs (7.3) decouple, and the dynamics of a two-component BEC can be equivalently described by two uncoupled Schrödinger equations with constant potentials, regardless of the relative interaction strengths. Following an interrogation time,

$T/2$, the initial state (10.10) evolves to

$$\begin{aligned}\vec{\psi}_{T/2}(\theta) =& U_{T/2}\vec{\psi}_{\ell m}(\theta) \\ =& \frac{e^{-i\varphi_1 T/2}e^{im(\theta+\Omega T/2)}}{2\sqrt{\pi}} \begin{pmatrix} e^{i\varphi_2 T/2}e^{i\ell(\theta+\Omega T/2)} \\ e^{-i\varphi_2 T/2}e^{-i\ell(\theta+\Omega T/2)} \end{pmatrix},\end{aligned}$$

where $\varphi_1 = (m^2+\ell^2)/2 + (g_{11}+2g_{12}+g_{22})/8\pi$, and $\varphi_2 = \omega/2 - 2m\ell + (g_{22}-g_{11})/8\pi$, where $U_{T/2}$ is the time-evolution operator for the free-evolution. A resonant π pulse, represented by the unitary matrix

$$U_\pi = \frac{1}{\sqrt{2}} \begin{pmatrix} 0 & 1 \\ 1 & 0 \end{pmatrix}, \tag{10.11}$$

is then applied to the state (10.11) to exchange the BEC-components, before allowing the system to undergo a second time-evolution for $T/2$. This stage is the atom-optical equivalent of reflection. In this context, its use ensures that the phase evolution due to the (constant) mean-fields is experienced by both components equally. The resultant state is

$$\vec{\psi}^T(\theta) = \frac{e^{-i\varphi_1 T}e^{im(\theta+\Omega T)}}{2\sqrt{\pi}} \begin{pmatrix} e^{-i\ell(\theta+\Omega T)} \\ e^{i\ell(\theta+\Omega T)} \end{pmatrix}. \tag{10.12}$$

This final state continues to represent superposition of counter-propagating flows, except there is now a phase difference between the BEC-components by an amount ΩT. In principle, if the phase of the initial state (10.9) was accurately reproducible, then this phase shift could be determined by, for instance, observation of the atomic density fringes created by the further application of a resonant $\pi/2$ pulse, but such a measurement presumes knowledge of the initial phase. The reproducibility necessary to reliably ascertain the initial phase, however, may not be attainable in practice, and will vary from one preparation of the initial states to the next. The phase difference ΩT must therefore be determined by other means.

Relative Population Measurement

The combined preparatory process that occurs to the initial state (10.9) can be summarised as $U_{T/2}U_\pi U_{T/2}U_{\ell m}U_{\pi/2}$. It is instructive to consider the analogy with optics; $U_{\ell m}U_{\pi/2}$ represents a beam-splitting stage and U_π represents a reflection stage, with $U_{T/2}$ describing the phase evolution between them. The accumulation of the Sagnac phase is contained within the free-evolution part,

described by $U_{T/2}$. Clearly, a recombination stage necessary to determine the Sagnac phase, which can be achieved with the combined process $U_{\pi/2}U_{\ell m}$.

To perform this final recombination stage, the angular momentum imprinting is applied a second time to the state (10.12), and due to the previous application of a π pulse, the imprinting now acts in a sense opposite to the previously induced flow. Experimentally, the phase imprinting is simply repeated. This second transfer of OAM cancels the relative spatial phase of the states, so that the states are now in their motional ground states. A final $\pi/2$ pulse is applied to superpose the two states, producing the final state

$$\vec{\psi}_f(\theta) = \frac{e^{-i\varphi_1 T}e^{im(2\theta+\Omega T)}}{\sqrt{2\pi}} \begin{pmatrix} \cos(\ell\Omega T) \\ -i\sin(\ell\Omega T) \end{pmatrix}, \tag{10.13}$$

Figure 10.1(a) shows the expected signal using parameters corresponding to ^{87}Rb with high atom number. The populations of each BEC-component oscillates with a period $\pi/\ell\Omega$, with respect to the total interrogation time, T. A measurement of, for example, the population of the second BEC-component would yield $N_2 = N[1-\cos(2\ell\Omega T)]/2$. For typical parameters ($\ell = 1$, $T = 10$), and assuming a 1% difference in population would be observable, this would provide a suitable means to determine rotation frequencies of the order 10 mHz, which is comparatively large[2]. For more sophisticated experimental setups, an ambitious estimate using $\ell = 10$, and $T = 70$ (corresponding to one minute of interrogation time) would suggest rotations of the order 0.1 mHz would be observable.

Angular Displacement Measurement

The measurement of the relative populations protects the dynamics from the presence of atom-atom interactions in a trivial way. However, it allows only a single measurement of the rotation to be made; once the second $\pi/2$ pulse has been applied, the populations of the BEC-components are projected into their final states, and the superposition of counter-propagating flows is destroyed.

An alternative measurement may be obtained by omitting the second angular momentum imprinting, $U_{\ell,-\ell}$. Instead, a resonant $\pi/2$ pulse may be applied

[2]The most recent precision measurements are able to determine differences of rotation frequencies of the order 10^{-10} Hz [178], and commercially available fibre optic gyroscopes can achieve of the order 10^{-6} Hz.

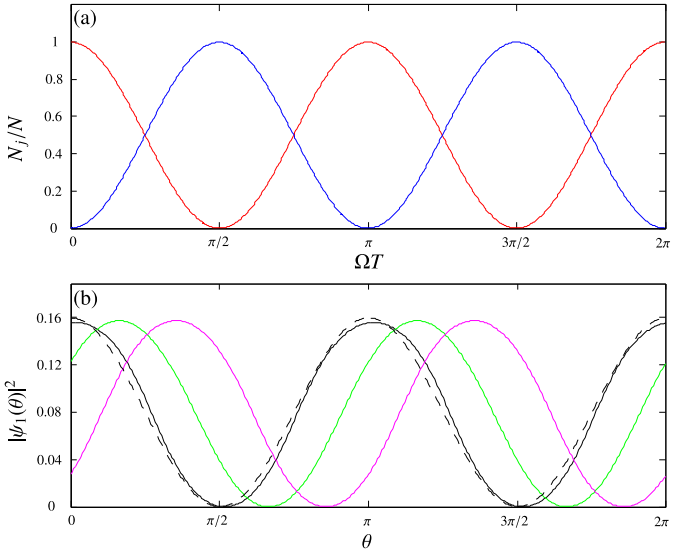

Figure 10.1: Ideal signals from typical implementations of ^{87}Rb with 280,000 atoms with typical experimental parameters [See Table 8.1]. (a) Population measurement following a sequence $U_{\pi/2}U_{\ell m}U_{\pi}U_{T/2}U_{\ell,m}U_{\pi/2}$. The relative populations oscillate with a period $\pi/\ell\Omega$, but any experimentally significant deviation from equal occupation would be an indication of nonzero rotation. (b) Angular precession of the atomic density in the first BEC-component for (–) $T = 0$, (-) $T = 0.1$, (–) $T = 1$, and (–) $T = 8.3$ at a rate $\Omega - m$, with $\ell = 1$, $m = 0$, and $\Omega = 1$. The precession of both BEC-components is identical. Units are dimensionless.

directly to the state (10.12) to produce

$$\vec{\psi}_{f'}(\theta) = \frac{e^{-i\varphi_1 T}e^{im(\theta+\Omega T)}}{\sqrt{2\pi}} \begin{pmatrix} \cos(\ell[\theta+\Omega T]) \\ -i\sin(\ell[\theta+\Omega T]) \end{pmatrix}. \tag{10.14}$$

Unlike the previous protocol, the population of each BEC-component is equal, but the atomic densities are no longer uniformly distributed around the ring. In the general case, following the sequence $U_{\pi/2}U_{T/2}U_{\pi}U_{T/2}U_{\ell,-\ell}U_{\pi/2}$ acting on the initial state (10.9), a complicated density evolutions ensues, and it is not clear how the Sagnac phase accumulates. An immediate measurement of the atomic density would not yield a determination of Ω because there is no information concerning the initial phase.

Except for an unimportant imaginary multiplicative factor, these initial states are exactly those studied in the previous chapter. When the interaction strengths are approximately equal, as for ^{87}Rb, the time-evolution can be predicted straightforwardly, and the atomic density fringes should be ade-

quately preserved for reasonable experimental times. For the ideal case where $g_{11} = g_{12} = g_{22} = g$, a subsequent evolution of (10.14), found using U_T on the state (10.14), yields

$$\vec{\psi}^t(\theta) = \frac{e^{-i\varphi_1 t}e^{im(\theta+\Omega t)}}{\sqrt{2\pi}} \begin{pmatrix} e^{i\varphi_2 t}\cos(\ell[\theta + (\Omega - m)t]) \\ -ie^{-i\varphi_2 t}\sin(\ell[\theta + (\Omega - m)t]) \end{pmatrix}, \tag{10.15}$$

where the phases simplify to $\varphi_1 = (m^2+\ell^2)/2+g/2\pi$ and $\varphi_2 = \omega/2-2m\ell$. The final state (10.15) implies that the fringes simply precess around the ring at a rate $\Omega - m$. Consequently, repeated *in situ* state selective measurements of the atomic density are possible, allowing the rotation frequency to be determined continuously, in principle.

A measurement specific to one internal state destroys the coherence between the internal states, but does not affect their densities, assuming the measurement is non-destructive. This is not in contradiction to usual quantum mechanics where one would expect a single measurement to project out the superposition onto a particular state. Rather, the crucial point here is that a measurement of the state of an atom leaves the direction of propagation completely uncertain. Hence, a superposition of counter-propagating flows associated with each BEC-component remains, and the Sagnac phase is continually aggregated by the system. Although the accuracy would not be expected to improve over the preceding population measurement protocol, it does illustrate the unusual capability to continuously measure an evolving interference pattern established between matter-waves.

10.3.4 Discussion

The proposed measurement protocols are summarised in Fig. (10.3). In both cases, the precision is not competitive with implementations in either optical or matter-wave Sagnac interferometry, at least under the assumed experimental parameters. However, this system does exhibit an unusual characteristic that is not found elsewhere that may prove to be advantageous in more advanced variations of this system. In contrast to other matter-wave Sagnac interferometers, the system proposed here is not limited to a minimum interrogation time corresponding to, for example, the time taken to split and recombine two atomic beams; measurements may be taken at any time, although the measurement is enhanced by longer interrogation times.

An intriguing feature of this Sagnac interferometer is its insensitivity to changes

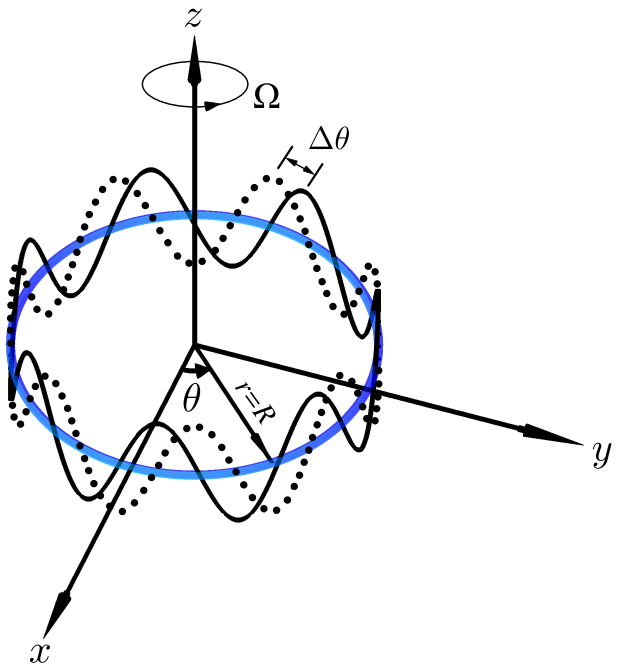

Figure 10.2: Precession of an atomic density fringe of a single BEC-component in a binary mixture in a ring trap of radius R. The nonzero external rotation of the system, Ω, causes a phase difference between two counter-propagating waves around a ring to be accumulated a rate $\Omega - m$, where m is the angular momentum difference between the two waves. Shown here is the interference pattern of two such waves by an amount $\Delta\theta$. Measurement of $\Delta\theta$ is possible by state selective fluorescence detection, for example. For counter-propagating waves of a fixed momentum, the radius of the ring trap does not affect the measurement, providing it is possible to create the initial state, i.e., $\Delta\Theta$ is insensitive to changes in r provided m is fixed.

to its area (within the validity of the model employed, i.e., it is assumed that the coherence length of the BEC is longer than the circumference of the ring trap). In a semi-classical picture, the phase shift $\Delta\theta = \Omega T$ may be related to the usual optical phase shift in Eq. (10.2), but in this system the OAM of the propagating waves is fixed, rather than their velocity as is often the case. By holding the OAM fixed, changes in the area of the ring (in the initial preparation) are not important. In a semi-classical picture, this is equivalent to adjusting the velocity of a pair of counter-propagating atoms so that, whilst the area varies, the time taken for the atoms to make a single revolution remains fixed. It should be

noted that changes to the area during the dynamics is equivalent to a rescaling of the spatial variable in the CGPEs (7.3), which clearly has ramifications on the effective interaction strengths and the time-units used. In the case where the radius of the ring trap varies by a multiplicative amount ϵ, the equivalent system is found by letting $g_{ij} \to \epsilon g_{ij}$ and $t \to \epsilon^2 t$. Changes in the area during the dynamics are therefore equivalent to time-dependent modulations in the interaction strengths as well in the time-unit used. However, the measurement of the Sagnac phase is robust to this effect provided $\epsilon \approx 1$, and the resulting dynamics are within the region of dynamical stability that has been identified previously. The property of area insensitivity may be particularly advantageous if it would be possible to couple multiple Sagnac atom-interferometers together in such a may that magnified their combined sensitivity.

For optical Sagnac interferometers, the light input into the interferometer arms is continuous, which also allows continuous measurement. However, optical Sagnac interferometry may be superseded in the future by matter-wave interferometers, and it would be advantageous to retain the capability of real-time measurement. At present, the most precise matter-wave Sagnac interferometer uses deflected slowed atomic beams in a Mach-Zehnder configuration, but the apparatus is very large, and offers few prospects for miniaturisation. BEC atom-interferometers, on the other hand, allow for the possibility of much smaller matter-wave Sagnac interferometers to be developed, with the possibility of not only permitting atom-atom interactions to be present, but also exploiting them to surpass the Heisenberg limit. The current proposal may be a useful step in achieving this ambition.

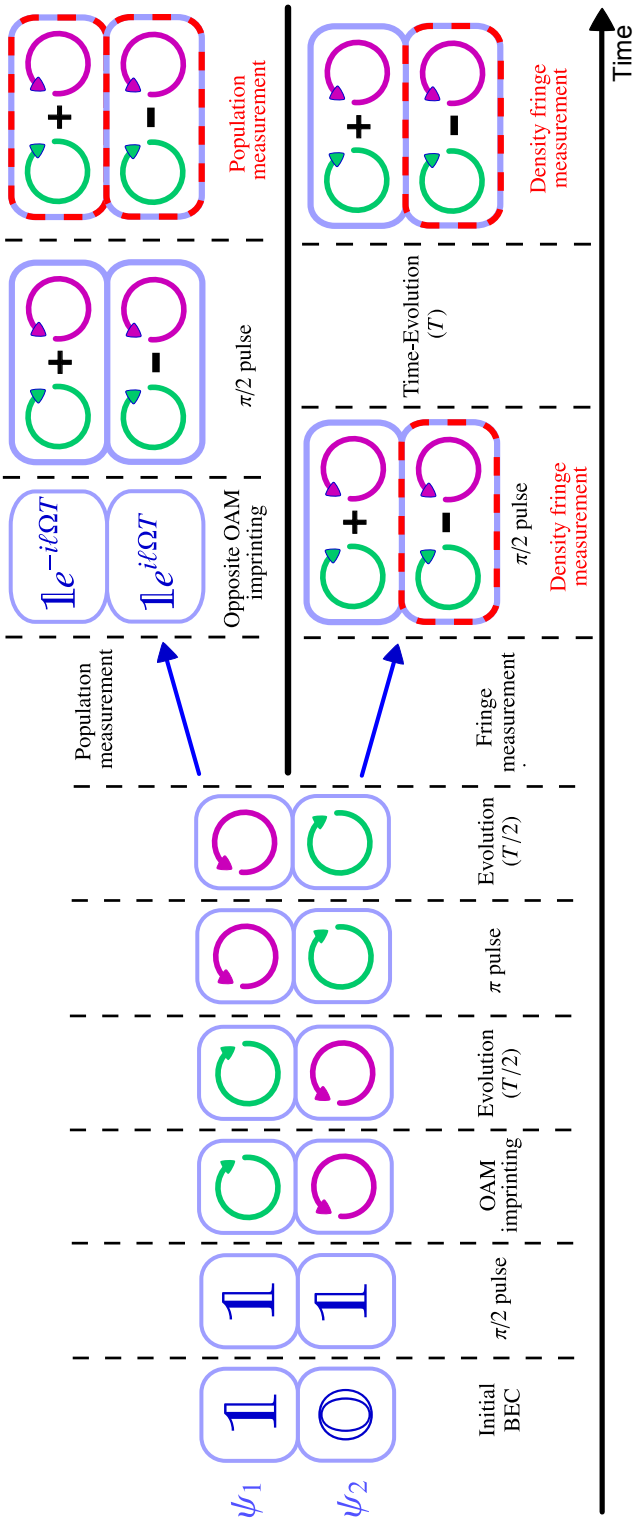

Figure 10.3: Schematic overview of the proposed protocols

10.4 Summary

In summary, two idealised experimental protocols for realising a Sagnac atom-interferometer using a two-component BEC in a quasi-1D toroidal trap have been presented. In both proposals, significant atom-atom interactions may be present without contributing deleterious effects. The first protocol describes a relative population measurement of the two BEC-components that allows the rotation frequency to be inferred, but requires restarting the system between successive measurements. The second protocol describes the angular precession of the density fringes associated with each BEC-component at a rate proportional to the rotation of the system. This protocol includes atom-atom interactions in a non-trivial manner, and permits successive *in situ* measurements to be taken. An implementation of this protocol would require the inter- and intra-species interactions to be approximately equal, whereas the former protocol has no such requirement.

Both protocols have the unusual property that they are insensitive to changes in their area prior to the measurement process, and it is speculated that this feature holds for time-dependent variations provided they are small. Such a feature in a Sagnac interferometer has not been commented upon previously, and may prove beneficial in future implementations.

Chapter 11

Conclusions

In the second part of this thesis, the dynamics of one- and two-component Bose-Einstein Condensates (BECs) in a quasi-1D toroidal trap (ring trap) have been investigated. The initial conditions selected for this study correspond to superpositions of counter-propagating flows, which also represent superpositions of vortex states, and permit the manifestation of the Sagnac effect. One-component BECs were studied firstly in order to develop insight into the dynamics, and also to motivate the requirement for using two-component BECs. A regime of dynamical stability using two-component BECs was identified, which contained a parameter set describing an experimentally feasible implementation using ^{87}Rb. An idealised proof-of-principle Sagnac atom-interferometer using ^{87}Rb was then examined, and two measurement protocols were presented. In both cases, nonlinear atom-atom interactions are explicitly included in a manner that does not deleteriously affect an ideal measurement, and in some cases, atom-atom interactions may actually stabilise the dynamics. The future prospects of using this system for Sagnac interferometry were discussed.

The physical implementation of this system relies upon tight radial and axial confinement in a toroidal trap, thus restricting these degrees of freedom to their zero-point motions. The radial and axial ground states were determined approximately, and projected out of the 1D coupled Gross-Pitaevskii equations (CGPEs), reducing the dimensionality of the dynamical equations from 3D to 1D. This simplified the numerics considerably, and allowed the CGPEs to be solved using the method outlined in Appendix C.

Throughout this work, a key motivation was exploiting BECs in ring traps

for atom-interferometry without precluding the presence of atom-atom interactions. The initial state for the investigations was chosen to be a superposition of counter-rotating flows; each oppositely directed flow would constitute a different interferometric path, thus allowing interferometry to occur without spatial separation of the associated atomic densities. To this end, regimes of dynamical stability were sought. The quantity used to identify such regimes was the fidelity with respect to the initial state. The simulations of one-component BECs in ring traps displayed interesting nonlinear dynamics, showing features reminiscent of grey and dark solitons, but did not endorse their suitability for atom-interferometry. The presence of such nonlinear effects was associated with significant excitation of the system, inferred by the occupation of energetic angular momentum modes, and ensured that the fidelity of the initial state rapidly decayed, except for occasional quasi-periodic revivals.

A two-component BEC was then examined for similar dynamics, except the initial conditions were contrived so that the combined mean-field potential was initially constant. In this instance, nonlinear effects are suppressed without requiring the absence of atom-atom interactions, and the time-evolution can be determined straightforwardly using the Schrödinger equation with a constant potential allowing the dynamics to be obtained analytically. To achieve this suppression, it is necessary to assume that the s-wave scattering lengths of atoms trapped in the relevant internal states are equal, which, fortuitously, is found approximately in ^{87}Rb. A range of combinations of s-wave scattering lengths were examined to explore the fidelity around the point of exact equality. The subsequent regime of dynamical stability was found to be appreciably broad, and contained within it a parameter set that describes a typical implementation using ^{87}Rb. In addition, the small inequality of the s-wave scattering lengths leads to the dynamics taking place in the weakly immiscible regime. It was shown that this could be potentially beneficial when certain imperfections in the preparation of the system are considered.

An idealised Sagnac atom-interferometer using a two-component ^{87}Rb BEC in a ring trap in a rotating frame was then considered. Two protocols for measuring the Sagnac phase accumulated between the two BEC-components were presented. The first utilised a relative population measurement to determine the rotation frequency, whereas the second depended on the precession of atomic density fringes. In the both cases, the protocols are insensitive to changes in the enclosed area from one experimental run to the next, which is a direct re-

sult of a fixed initial angular momentum rather than a fixed velocity, as is the case with other conventional Sagnac interferometers. In the second protocol, the precession of the atomic density fringes, where the atomic density of each BEC-component is interleaved with its partner, occurs at a rate proportional to the rotation frequency. This suggests, in principle, that non-destructive, state-selective measurements of the system could be performed continuously.

For the experimental configuration here, the precision of the proposed Sagnac atom-interferometer is relatively low compared to alternative schemes. The ultimate sensitivity of the system is limited by the requirement to use initial states with low angular momenta, relatively short interrogation times, and deviations from the delicate processes necessary to create the initial state. However, BEC atom-interferometers offer the possibility for miniaturisation and portability whereas atomic-beam atom-interferometers do not. Furthermore, the prospect of using nonlinear interactions to surpass the Heisenberg limit encourages the investigation of BEC atom-interferometers in regimes where atom-atom interactions may be present, even if at first they are not exploited to this end. Finally, it should be noted that closely-related, preliminary work [220] has recently suggested that BEC Sagnac interferometry using vortex superpositions also exhibits desirable stability properties and in very favourable conditions could achieve sensitivities comparable with the most precise Sagnac atom-interferometers demonstrated.

Future avenues of research on these themes may include investigating the feasibility using this system to couple multiple Sagnac interferometers, similar to that demonstrated in Ref. [179], to acquire enhanced sensitivity, or the time-dependent manipulation of s-wave scattering lengths to exploit atom-atom interactions in beating the Heisenberg limit. Other work exploring interesting nonlinear phenomena could focus on the manipulation of the inter- and intra-species scattering lengths to generate of dark-bright soliton trains, which are simply generalisations of the interleaving atomic densities already exploited in this work.

Part III

Appendices

Appendix A

Adiabatic Eliminations

There are some regimes where a two-level system coupled to a light-field may be partitioned into fast and slow dynamics in a such a way as to permit the elimination of the excited states. This relies upon the incident light-field being far-detuned from the atomic transition, so that it is weakly coupled to the rest of the system.

The Hamiltonian for a two-level system interacting with a light-wave in a standing-wave configuration, with a static external potential given by $V(\hat{x})$, may be written as,

$$\hat{H} = \frac{\hat{p}^2}{2M} + V_0(\hat{x}) + \frac{\hbar\Omega}{2}\cos(k_L\hat{x})\left[|e\rangle\langle g| + |g\rangle\langle e|\right] + \hbar\Delta|e\rangle\langle e|, \tag{A.1}$$

where $\Delta = \omega_0 - \omega_L$ is the detuning, and Ω is the Rabi frequency.

In the Schrödinger picture, the wavefunction describing the dynamics of the system is given by,

$$i\hbar\frac{d}{dt}|\psi(t)\rangle = \left[\hat{H}_0 + \hbar\Omega\hat{V}_L\left(|e\rangle\langle g| + |g\rangle\langle e|\right) + \hbar\Delta|e\rangle\langle e|\right]|\psi(t)\rangle, \tag{A.2}$$

where $\hat{H}_0 = \hat{p}^2/2M + V_0(\hat{x})$, and $\hat{V}_L(\hat{x}) = (1/2)\cos(k_L\hat{x})$. The corresponding dynamics in the interaction picture are obtained via the unitary transformation

$$\hat{U}_I(t) = \exp\left(-\frac{it}{\hbar}[\hat{H}_0 + \hbar\Delta|e\rangle\langle e|]\right), \tag{A.3}$$

giving,

$$i\frac{d}{dt}|\psi(t)\rangle = \Omega\hat{U}^\dagger(t)\hat{V}_L\left(|e\rangle\langle g| + |g\rangle\langle e|\right)\hat{U}(t)|\psi(t)\rangle. \tag{A.4}$$

The wavefunction is then expanded as $|\psi(t)\rangle = c_g(t)|g\rangle + c_e(t)|e\rangle$. Under this decomposition, the orthogonality of $|g\rangle$ and $\langle e|$ may be exploited to yield

$$\begin{aligned}\hat{U}|\psi\rangle &= \sum_{n=0}^{\infty}\left(\frac{-it}{\hbar}\right)^n\left[\hat{H}_0 + \hbar\Delta|e\rangle\langle e|\right]^n (c_g(t)|g\rangle + c_e(t)|e\rangle) \\ &= c_g e^{-it\hat{H}_0/\hbar}|g\rangle + c_e e^{-it(\hat{H}_0+\hbar\Delta)/\hbar}|e\rangle,\end{aligned} \tag{A.5}$$

and,

$$\begin{aligned}\langle g|\hat{U}^\dagger &= e^{it\hat{H}_o/\hbar}\langle g|, \\ \langle e|\hat{U}^\dagger &= e^{it(\hat{H}_o+\hbar\Delta)/\hbar}\langle e|.\end{aligned} \tag{A.6}$$

Using these expressions, Eq.(A.4) may be written as

$$i\frac{dc_g}{dt} = \Omega e^{-it\Delta}\hat{W}(t)c_e \tag{A.7}$$

$$i\frac{dc_e}{dt} = \Omega e^{it\Delta}\hat{W}(t)c_g, \tag{A.8}$$

where, for brevity, we omit the explicit time-dependence of c_g and c_e, and introduce the notation $\hat{W}(t) = \hat{U}^\dagger(t)\hat{V}_L\hat{U}(t)$.

Eq. (A.7) may now be formally integrated, giving,

$$c_g(t) = c_g(0) - i\Omega\int_0^t dt' e^{-i\Delta t'}\hat{W}(t)c_e(t'). \tag{A.9}$$

This expression may then be integrated by parts to give,

$$\begin{aligned}c_g(t) =& c_g(0) + \frac{\Omega}{\Delta}\left[e^{-i\Delta t'}\hat{W}(t')c_e(t')\right]_0^t - \frac{\Omega}{\Delta}\int_0^t dt' e^{-i\Delta t'}\frac{d}{dt'}\left[\hat{W}(t')c_e\right] \\ =& c_g(0) + \frac{\Omega}{\Delta}\left[e^{-i\Delta t}\hat{W}(t)c_e(t) - \hat{W}(0)c_e(0)\right] &\text{(A.10)} \\ &- \frac{\Omega}{\Delta}\int_0^t dt' e^{-i\Delta t'}\left[\frac{d\hat{W}(t')}{dt'}c_e(t') + \hat{W}(t')\frac{dc_e(t')}{dt'}\right]. &\text{(A.11)}\end{aligned}$$

Similarly,

$$\begin{aligned}c_e(t) =& c_e(0) - \frac{\Omega}{\Delta}\left[e^{i\Delta t}\hat{W}(t)c_g(t) - \hat{W}(0)c_g(0)\right] &\text{(A.12)} \\ &+ \frac{\Omega}{\Delta}\int_0^t dt' e^{i\Delta t'}\left[\frac{d\hat{W}(t')}{dt'}c_g(t') + \hat{W}(t')\frac{dc_g(t')}{dt'}\right]. &\text{(A.13)}\end{aligned}$$

It can be seen by inpsection that further expanding the integrals in these expressions will result in expressions of order $(\Omega/\Delta)^2$ and higher. In the far-detuned regime, we may neglect these higher orders, and truncate the expressions for c_g and c_e to obtain,

$$c_g(t) = c_g(0) + \frac{\Omega}{\Delta}\left[e^{-i\Delta t}\hat{W}(t)c_e(t) - \hat{W}(0)c_e(0)\right] \tag{A.14}$$

$$c_e(t) = c_e(0) - \frac{\Omega}{\Delta}\left[e^{i\Delta t}\hat{W}(t)c_g(t) - \hat{W}(0)c_g(0)\right]. \tag{A.15}$$

If the system is initially prepared with the population entirely in the ground state, then,

$$c_g(t) = 1 + \frac{\Omega}{\Delta}\left[e^{-i\Delta t}\hat{W}(t)c_e(t)\right] \tag{A.16}$$

$$c_e(t) = -\frac{\Omega}{\Delta}\left[e^{i\Delta t}\hat{W}(t)c_g(t) - \hat{W}(0)\right]. \tag{A.17}$$

By substituting $c_e(t)$ into $c_g(t)$ (or vice versa), a closed form for $c_g(t)$ could be obtained, and this would describe the dynamics in full. However, the intention of this work is to generalise these dynamics to the case where the laser-field is periodically flashed; therefore, a system Hamiltonian is sought from which such a generalisation can be made. To derive this Hamiltonian, $c_e(t)$ and $c_g(t)$ are substituted into Eqs. (A.7) and (A.8), giving,

$$i\frac{dc_g}{dt} = -\frac{\Omega^2}{\Delta}\hat{W}(t)\left[\hat{W}(t)c_g(t) - e^{-it\Delta}\hat{W}(0)\right] \tag{A.18}$$

$$i\frac{dc_e}{dt} = \Omega e^{it\Delta}\hat{W}(t)\left[1 + \frac{\Omega}{\Delta}\left(e^{-i\Delta t}\hat{W}(t)c_e(t)\right)\right]. \tag{A.19}$$

Now that the explicit interdependence of c_g and c_e has been removed, there exist further terms that, upon formal integration, yield orders of $(\Omega/\Delta)^2$ and higher. These are removed by omitting terms involving $e^{\pm i\Delta t}$, yielding,

$$i\frac{dc_g}{dt} = \frac{\Omega^2}{\Delta}\hat{W}^2(t)c_g(t) \tag{A.20}$$

$$i\frac{dc_e}{dt} = -\frac{\Omega^2}{\Delta}\hat{W}^2(t)c_e(t). \tag{A.21}$$

From these equations. it can be seen that the dynamics of the different levels are identical except for a π-phase shift, and decoupled, under these approximations. Furthermore, a general observation of the procedure above would reveal that the initial populations play no part in determining the effective dynamics of the system once they have begun. However, in the case where the entire population begins in the ground state, the excited state remains unoccupied, and does not contribute to the dynamics. Therefore, we eliminate it from the description, and describe the system dynamics through the ground state dynamics only. Unitarily transforming back into the Schrödinger picture, yields,

$$i\hbar\frac{d}{dt}|\psi\rangle = \left[\hat{H}_0 - \frac{\Omega^2}{\Delta}\hat{V}_L^2\right]|\psi\rangle. \tag{A.22}$$

Using the definition of $\hat{V}_L$, and the trigonometric identity $\cos(2x) = 2\cos^2(x)+1$, this may be simplified to give the effective Hamiltonian for this system as,

$$\hat{H} = \hat{H}_0 - \frac{\Omega^2}{8\Delta}\left[\cos(2k_L\hat{x}) + 1\right]. \tag{A.23}$$

Finally, we neglect the constant shift in the Hamiltonian (which may be formally removed by applying the unitary transformation $U = \exp(-it[\Omega^2|g\rangle\langle g|]/8\Delta)$), and write instead,

$$\hat{H} = \hat{H}_0 - \frac{\Omega^2}{8\Delta}\cos(2k_L\hat{x}). \tag{A.24}$$

Appendix B

Cosine Expansions

In calculating the momentum moments in chapter 5, it is frequently convenient to expand powers of $\sin(nx)/\sin(x)$ in cosines. To derive such an expansion for $\sin^2(nx)/\sin^2(x)$, first consider the summation

$$\begin{aligned} n + 2\sum_{q=1}^{n-1}(n-q)\cos(2qx) =& n + n\sum_{q=1}^{n-1} e^{i2qx} + n\sum_{q=1}^{n-1} e^{-i2qx} \\ & - \sum_{q=1}^{n-1} qe^{i2qx} - \sum_{q=1}^{n-1} qe^{-i2qx}. \end{aligned} \tag{B.1}$$

The exponential sums in Eq. (B.1) are related to geometric sums, either directly or through their derivatives. Hence,

$$\begin{aligned} n + 2\sum_{q=1}^{n-1}(n-q)\cos(2qx) =& n + n\frac{e^{i2xn} - e^{2ix}}{e^{2ix} - 1} \\ & - n\frac{e^{-i2x(n-1)} - 1}{e^{2ix} - 1} \\ & + \frac{i}{2}\frac{\partial}{\partial x}\frac{e^{i2xn} - e^{2ix}}{e^{2ix} - 1} \\ & - \frac{i}{2}\frac{\partial}{\partial x}\frac{e^{-i2xn} - e^{-2ix}}{e^{-2ix} - 1}. \end{aligned} \tag{B.2}$$

Differentiating Eq. (B.2), identifying a mutual denominator, and applying a little algebra then gives the desired result:

$$\begin{aligned} n + 2\sum_{q=1}^{n-1}(n-q)\cos(2qx) &= \frac{e^{2ix(n+1)} - 2e^{2ix} + e^{-2ix(n-1)}}{(e^{2ix} - 1)^2} \\ &= \frac{\sin^2(nx)}{\sin^2(x)}. \end{aligned} \tag{B.3}$$

In a similar fashion, it is found that

$$\begin{aligned}\frac{\sin^4(nx)}{\sin^4(x)} =& \frac{n}{3}(2n^2+1) \\ &+ \sum_{q=1}^{n-1}\left[q^3 - 2nq^2 - q + \frac{2n}{3}(2n^2+1)\right]\cos(2qx) \\ &- \sum_{q=n}^{2n-2}\left[\frac{q^3}{3} - 2nq^2 + (4n^2 - \frac{1}{3})q + \frac{2n}{3}(1-4n^2)\right] \\ &\times \cos(2qx).\end{aligned} \tag{B.4}$$

Appendix C

Numerical Method for Solving the Coupled GPEs

In Chapter 8, the dynamics of a two-component BEC in a quasi-1D toroidal trap are derived in terms of a set of coupled Gross-Pitaevskii equations (CGPEs), which are numerically solved in Chapter 9. This appendix will outline the numerical procedure used to compute the time-evolution of the 1D CGPEs. For clarity of presentation, the numerical solution to the Gross-Pitaevskii equation (GPE) will first be described before trivially generalising the procedure to include the CGPEs.

C.1 Crank-Nicolson Finite-Difference Method

The dimensionless 1D GPEs in a rotating frame are,

$$i\frac{\partial \Psi_j}{\partial t} = \left[-\frac{1}{2}\frac{\partial^2}{\partial \theta^2} - i\Omega\frac{\partial}{\partial \theta} + V_j(\theta) + \sum_{k=1}^{2} g_{jk}|\psi_k|^2\right]\psi_j, \tag{C.1}$$

where $j = 1, 2$ gives the component, $\theta \in [0, 2\pi)$ and t are the angular position and time coordinates, respectively, $V_j(\theta)$ is a state-dependent static potential, Ω is the rotational frequency, and g_{jk} describes the inter- and intra-component interaction strengths. Typically, g_{jk} are on the order of 10^4 to 10^6, whereas other parameters are of order unity. The GPE is obtained by simply neglecting one component, e.g., by setting $g_{12} = 0$, and considering only a single BEC component.

The CGPEs (C.1) can be solved conveniently using the Crank-Nicolson

method, which is a norm-conserving finite-difference method [222]. The method is, however, usually developed for linear systems, and it will become necessary to perform some additional computations to allow the nonlinearity in the CGPEs to be included. Similarly, some modifications will be made to enforce spatial periodicity.

The coordinates x and t are considered to be discretised as $\theta_j = (j-1)h$ and $t_n = (n-1)k$, with $j = 1, \ldots, , J$, and $n = 1, \ldots, N$, and the continuous wavefunction $\psi(\theta, t)$ is approximated by the discretised wavefunction $\psi_j^n = \psi(\theta_j, t_n)$. It is convenient to introduce the central-, backward- and forward-difference operators, δ_θ^2, D_θ^- and D_θ, respectively, where

$$\delta_\theta^2 \psi_j^n = \frac{1}{2}\left(\psi_{j+1}^n - 2\psi_j^n + \psi_{j-1}^n\right), \tag{C.2}$$

$$D_\theta^+ \psi_j^n = \psi_{j+1}^n, \tag{C.3}$$

$$D_\theta^- \psi_j^n = \psi_{j-1}^n. \tag{C.4}$$

Note that the operators may also be considered to act upon the time, t. The spatial and time derivatives in the GPE may be approximated at the point (θ_j, t_n) as

$$\frac{\partial^2 \psi(\theta,t)}{\partial \theta^2} \approx \frac{\delta_\theta^2}{h^2}\psi_j^n, \tag{C.5a}$$

$$\frac{\partial \psi(\theta_j,t_n)}{\partial t} \approx \frac{D_t - 1}{k}\psi_j^n, \tag{C.5b}$$

$$\frac{\partial \psi(\theta_j,t_n)}{\partial \theta} \approx \frac{D_\theta^+ - D_\theta^-}{2h}\psi_j^n. \tag{C.5c}$$

The accuracy of these approximations can be readily found by Taylor expanding the right-hand sides of (C.5); one finds that the first derivative (C.5b) is accurate up to $\mathrm{O}(h^2)$ and $\mathrm{O}(k^2)$, whilst (C.5a) and (C.5c) are accurate up to $\mathrm{O}(k^3)$. This increase in accuracy is due to the symmetry of the operators in the spatial coordinate, which cancels exactly all odd-ordered terms in its Taylor expansion. It is not advantageous to the solution at the $(n+1)$-th timestep would no longer depend on the solution at the n-th timestep in a straightforward manner.

The Euler method corresponds to using the approximations (C.5) with the GPE directly. Such a method, although accurate, does not guarantee stability of the numerical solution. For convergence, the method is required to be both accurate and stable, as stated in the Lax Equivalence theorem. A more sophisticated use of the approximations (C.5) can guarantee stability. The new approximations are found by replacing ψ_j^n with its time-average $(1/2)(\psi_j^n + 1 + \psi_j^n)$,

to yield

$$\frac{\partial^2\psi(\theta,t)}{\partial\theta^2} \approx \frac{\delta_\theta^2}{h^2}\left(\frac{\psi_j^{n+1}+\psi_j^n}{2}\right) \tag{C.6a}$$

$$\frac{\partial\psi(\theta_j,t_n)}{\partial\theta} \approx \frac{D_\theta^+ - D_\theta^-}{2h}\psi_j^n. \tag{C.6b}$$

Using (C.6) with C.5b in the GPE, and rearranging, implies the system of equations in the lattice points of ψ_j^n may be written

$$\begin{aligned}&\left[i-\frac{\mu}{2}-\frac{V(\theta_j)}{2}-\frac{g}{2}|\psi_j^{n+1}|^2\right]\psi_j^{n+1}+\left[\frac{\mu+i\Omega\nu}{4}\right]\psi_{j-1}^{n+1}+\left[\frac{\mu-i\Omega\nu}{4}\right]\psi_{j+1}^{n+1}\\ &=\left[i+\frac{\mu}{2}+\frac{V(\theta_j)}{2}+\frac{g}{2}|\psi_j^{n+1}|^2\right]\psi_j^{n+1}-\left[\frac{\mu-i\Omega\nu}{4}\right]\psi_{j-1}^{n+1}-\left[\frac{\mu+i\Omega\nu}{4}\right]\psi_{j+1}^{n+1}.\end{aligned} \tag{C.7}$$

where $V(\theta_j)\psi_j^n$ has been replaced with $V(\theta_j)(\psi_j^{n+1}+\psi_j^n)/2$, the nonlinear term has been replaced with $(1/2)(|\psi_j^{n+1}|^2\psi_j^{n+1}+|\psi_j^n|^2\psi_j^n)$, and the parameters $\mu = k/h^2$ and $\nu = k/h$ have been introduced for brevity. The system of equations (C.7) represents a tridiagonal system, which may be written as

$$A\vec{\psi}^{n+1} = B\vec{\psi}^n \tag{C.8}$$

where the j-th element of the vector $\vec{\psi}^{n+1}$ is ψ_j^{n+1}, A and B are $J\times J$ tridiagonal matrices. This system of equations represents the solution to the GPEs using the Crank-Nicolson method. It has the attractive property that it is norm-conserving and unconditionally stable provided $\mu < 1/2$. In this sense, conditional stability refers to conditions on the physical parameters, and not those in the numerical implementation. Norm-conservation can be readily seen by recognising that the above system of finite-difference equations are equivalent to

$$\vec{\psi}^{n+1} = \exp\left(-ik\hat{H}\right)\vec{\psi}^n \tag{C.9}$$

where $\hat{H}$ approximates the corresponding Hamiltonian of the system (see below regarding the inclusion of the nonlinear part), using Cayley's approximation,

$$\exp\left(-ik\hat{H}\right) \approx \frac{1-ik\hat{H}}{1+ik\hat{H}}, \tag{C.10}$$

with the replacements already specified. Cayley's form of the time-evolution operator is unitary, and accurate up to second order in time; hence, these properties are manifest in the Crank-Nicolson method.

The numerics proceed by solving the tridiagonal matrix system for $\vec{\psi}^{n+1}$ using $\vec{\psi}^n$. However, the nonlinearity means that conventional numerical methods are

not directly applicable since A depends on $\vec{\psi}^{n+1}$. This can be easily overcome by using the approximation $|\psi_j^{n+1}|^2 \approx (\psi_j^n)^2$ to generate a trial solution [223, 224] $\vec{\psi}_\alpha^{n+1}$. This can be repeated, so that the trial solution $\vec{\psi}_\alpha^{n+1}$ is used to generate a second trial solution $\vec{\psi}_\beta^{n+1}$, using the approximation $|(\psi_j^{n+1})_\beta|^2 \approx |(\psi_j^n)_\beta|^2$. By repeating this a number of times, the wavefunction at the $n+1$-th timesteps can be reliably found. In typical numerical solutions, only one trial wavefunction needs to be generated for good convergence.

C.2 The Numerov Approximation

Generally, a denser space- and time-coordinate mesh is required for increased accuracy . Decreasing h, however, requires more memory, whereas decreasing k means that the algorithm will be slower. It is often more convenient to wait longer, and to use less memory. Given this observation, it is desirable to focus on increasing the spatial accuracy rather than temporal accuracy.

The Numerov approximation [223, 224] permits allow an alternative approximation to (C.6a) to be derived. Essentially, it is a modification to (C.5a) that removes the fourth-order dependence, thereby allowing accuracy up to $\mathrm{O}(h^6)$. The modification can be motivated by considering the Taylor expansion of (C.5a) up to fourth-order, and approximating the fourth-order derivative of ψ as

$$\frac{\partial^4 \psi}{\partial \theta^4} \approx \frac{\delta_\theta^2}{h^2} \frac{\partial^2 \psi}{\partial \theta^2}, \tag{C.11}$$

It is then possible to obtain an algebraic expression for the second-order derivative at the point (θ_j, t_n), given by

$$\left(1 + \frac{\delta_\theta^2}{12}\right) \frac{\partial^2 \psi}{\partial \theta^2} \approx \frac{\delta_\theta^2}{h^2}. \tag{C.12}$$

In a similar manner, the first derivative can also be approximated as

$$\left(1 + \frac{\delta_\theta^2}{6}\right) \frac{\partial \psi}{\partial \theta} \approx \frac{D_\theta^+ - D_\theta^-}{2h}. \tag{C.13}$$

Using these approximations in the GPE, with considerable algebraic manipula-

tion, yields

$$\begin{aligned}
&[2-6i\mu+3\nu\Omega]\,\psi_{j+2}^{n+1}+[28-12i\mu+30\nu\Omega]\,\psi_{j+1}^{n+1}\\
&+\left[84+36i\mu+W_j+G_j^{n+1}\right]\psi_j^{n+1}+[28-12i\mu-30\nu\Omega]\,\psi_{j-1}^{n+1}\\
&+[2-6i\mu-3\nu\Omega]\,\psi_{j-2}^{n+1}\\
=&[2+6i\mu-3\nu\Omega]\,\psi_{j+2}^{n+1}+[28+12i\mu-30\nu\Omega]\,\psi_{j+1}^{n+1}\\
&+\left[84-36i\mu-W_j-G_j^{n}\right]\psi_j^{n+1}+[28+12i\mu+30\nu\Omega]\,\psi_{j-1}^{n+1}\\
&+[2+6i\mu+3\nu\Omega]\,\psi_{j-2}^{n+1},
\end{aligned} \tag{C.14}$$

where

$$W_j = ik\left[V(\theta_{j+2})+14V(\theta_{j+1})+42V(\theta_j)+14V(\theta_{j-1})+V(\theta_{j-2})\right], \tag{C.15}$$

and

$$G_j^n = gik\left[|\psi_{j+2}^n|^2+14|\psi_{j+1}^n|^2+42|\psi_j^n|^2+14|\psi_{j-1}^n|^2+|\psi_{j-2}^n|^2\right]. \tag{C.16}$$

This system is now pentadiagonal, and requires slightly more memory to store A and B, as well as the use of more sophisticated algorithms to solve the system of equations. However, numerical investigations suggest that the gain in computational accuracy greatly outweighs these disadvantages. For $g = 1000$, good convergence is found for $J = 100$ with $\mu = 0.49$, and most of the simulations produced in this work used $J = 200$. For stronger interactions, such $g = 100000$, $J = 1000$ resulted in good convergence. In all cases, $\mu = 0.49$ and the number of estimator loops for the nonlinear part was one. The finite-difference method was implemented in Matlab, and used the built-in routine `mldivide`. Simulations for a $J = 100$ and $T = 10$ took less than three minutes on a standard desktop computer.

C.3 Imposing Spatial Periodicity

The finite-difference equations do not couple spatial point at the end of the mesh in the same way as elsewhere. The consequence of this is that the boundaries of the spatial interval are infinitely hard, and the dynamics therefore evolve in an infinite square well potential.

Spatial periodicity can be enforced by including additional entries in the matrices A and B that couple the $j = 1$- and $j = J$-th points in same way that all other spatial points are coupled. For the finite-difference equations (C.14), one

simply makes the modifications

$$A(1, J-1) = A(2, J) = 2 - 6i\mu - 3\nu\Omega \tag{C.17a}$$

$$A(1, J) = 28 - 12i\mu - 30\nu\Omega \tag{C.17b}$$

$$A(J-1, 1) = A(J, 2) = 2 - 6i\mu + 3\nu\Omega \tag{C.17c}$$

$$A(J, 1) = 28 - 12i\mu + 30\nu\Omega \tag{C.17d}$$

$$B(1, J-1) = B(2, J) = 2 + 6i\mu + 3\nu\Omega \tag{C.17e}$$

$$B(1, J) = 28 + 12i\mu + 30\nu\Omega \tag{C.17f}$$

$$B(J-1, 1) = B(J, 2) = 2 + 6i\mu - 3\nu\Omega \tag{C.17g}$$

$$B(J, 1) = 28 + 12i\mu - 30\nu\Omega \tag{C.17h}$$

to the (p, q)-th entries of A and B. The finite-difference equations are no longer strictly pentadiaogonal following this modification, but still retain a high-degree of sparsity. The enforcement of spatial periodicity can therefore cause not inconsiderable slowing of the numerical algorithm, but the memory requirements are essentially the same. In numerical simulations, it is found that the increase in accuracy is worthwhile compared to the slowdown in execution time.

C.4 Generalisation to Two-Component BECs

The generalisation to multi-component BECs is relatively straight-forward since different components are coupled only through their nonlinear terms. For a binary mixture, the system of finite-difference equations reads

$$A_c \vec{\psi}_c^{n+1} = B_c \vec{\psi}_c^{n+1} \tag{C.18}$$

where $c = 1, 2$ indicates the component, and the matrices A_c and B_c differ only in their nonlinear terms (and state-dependent potentials, in general). For example, using the Numerov method above and considering the dynamics of component $c = 1$, one simply replaces $g|\psi_j^n|^2$ with $g_{11}|(\psi_j^n)_1|^2 + g_{12}|(\psi_j^n)_2|^2$. The estimator loop that is used to generate trial wavefunctions proceeds exactly as before. The dynamics of each component therefore proceed exactly as in the one-component case, except the matrices A_j and B_j are updated with the latest $(\psi_j^n)_c$ at each timestep. Since the nonlinear terms require A and B to be reconstructed at each timestep even in the one-component case, this poses no significant additional computational overhead.

Bibliography

[1] C. J. Foot, *Atomic Physics* (Oxford, New York, 2008).

[2] C. S. Adams and E. Riis, Prog. Quant. Electr. **21**, 1 (1997).

[3] M. Saunders, P. L. Halkyard, K. J. Challis, and S. A. Gardiner, Phys. Rev. A. **76**, 043415 (2007).

[4] P. L. Halkyard, M. Saunders, K. J. Challis, and S. A. Gardiner, Phys. Rev. A **78**, 063401 (2008).

[5] M. Saunders, P. L. Halkyard, S. A. Gardiner, and K. J. Challis, Phys. Rev. A. **79**, 023423 (2009).

[6] P. L. Halkyard, M. P. A. Jones, and S. A. Gardiner, Phys. Rev. A. **81**, 061602 (2010).

[7] B. H. Bransden and C. J. Joachain, *Physics of Atoms and Molecules* (Prentice Hall, 2003).

[8] C. J. Foot, Contemp. Phys. **32**, 369 (1991).

[9] W. D. Phillips, Rev. Mod. Phys. **70**, 721 (1998).

[10] C. Cohen-Tannoudji, Rev. Mod. Phys. **70**, 707 (1998).

[11] S. Chu, Rev. Mod. Phys. **70**, 685 (1998).

[12] C. S. Adams, M. Sigel, and J. Mlynek, Phys. Rep. **240**, 143 (1994).

[13] T. Könemann *et al.*, App. Phys. B **89**, 431 (2007).

[14] R. A. Nyman *et al.*, App. Phys. B **84**, 673 (2006).

[15] B. Canuel *et al.*, Phys. Rev. Lett. **97**, 010402 (2006).

[16] K. Takase, *Precision Rotation Rate Measurements with a Mobile Atom Interferometer*, PhD thesis, Stanford University, 2008.

[17] S. Inouye *et al.*, Nature (London) **392**, 151 (1998).

[18] J. L. Roberts *et al.*, Phys. Rev. Lett. **81**, 5109 (1998).

[19] S. L. Cornish, N. R. Claussen, J. L. Roberts, E. A. Cornell, and C. E. Wiemanld.

[20] T. Köhler, K. Góral, and P. S. Julienne, Rev. Mod. Phys. **78**, 1311 (2006).

[21] M. Gustavsson *et al.*, Phys. Rev. Lett. **100**, 080404 (2008).

[22] D. S. Weiss, B. C. Young, and S. Chu, Appl. Phys. B **217**, 59 (1994).

[23] A. Wicht, J. M. Hensley, E. Sarajlic, and S. Chu, Physica Scripta **T102**, 82 (2002).

[24] S. Fray, C. A. Diez, T. W. Hänsch, and M. Weitz, Phys. Rev. Lett. **93**, 93 (2004).

[25] K. Bongs and K. Sengstock, Rep. Prog. Phys. **67**, 907 (2004).

[26] C. H. Bennett and D. P. DiVicenzo, Nature **404**, 247 (2000).

[27] I. Bloch, J. Dalibard, and Z. Wilhelm, Rev. Mod. Phys. **7**, 885 (2008).

[28] A. J. Lichtenberg and M. A. Lieberman, *Regular and Chaotic Dynamics*, 2nd ed. ed. (Springer, New York, 1992).

[29] R. Blümel and W. P. Reinhardt, *Chaos in Atomic Physics* (Cambridge, 2005).

[30] E. N. Lorenz, *The Essence of Chaos* (University of Washington Press, Seattle, 1995).

[31] L. E. Reichl, *Quantum Signatures of Chaos*, Second ed. (Springer, 2004).

[32] S. H. Strogatz, *Nonlinear Dynamics and Chaos* (Westview, 2000).

[33] T. Tél and M. Gruiz, *Chaotic Dynamics* (Cambridge, 2006).

[34] P. S. Laplace, *A Philosophical Essay on Probabilities*, 1951, Translated by F. W. Truscott and F. L. Emory (Dover, New York).

[35] F. Haake, *Quantum Signatures of Chaos* (Springer, 2004).

[36] M. C. Gutzwiller, *Chaos in Classical and Quantum Mechanics* (Springer, New York, 1990).

[37] E. N. Lorenz, J. Atmos. Sci. **20**, 130 (1963).

[38] J. Banks, J. Brooks, G. Cairns, G. Davis, and P. Stacey, Am. Math. Mon. **99**, 332 (1992).

[39] B. Devaney, *An Introduction to Chaotic Dynamical Systems* (Addisson-Wesley, 1989).

[40] A. Crannell, Am. Math. Mon. **102**, 788 (1995).

[41] M. Toda, Phys. Rep. C **18**, 1 (1975).

[42] H. Goldstein, C. P. Poole, and J. L. Safko, *Classical Mechanics*, Third ed. (Addison-Wesley, 2002).

[43] G. Casati, B. V. Chirikov, F. M. Izraelev, and J. Ford, *Stochastic Behavior in Classical and Quantum Hamiltonian Systems*, New York, 1979, Springer.

[44] B. V. Chirikov, Phys. Rep. **52**, 263 (1979).

[45] J. M. Greene, J. Math. Phys. **20**, 1183 (1979).

[46] F. M. Izrailev and D. L. Shepelyanskii, Sov. Phys. Dokl. **24**, 996 (1979).

[47] F. M. Izrailev and D. L. Shepelyanskii, Theor. Math. Phys. **43**, 553 (1980).

[48] D. A. Steck, *Quantum Chaos, Transport, and Decoherence in Atom Optics*, PhD thesis, University of Texas at Austin, 2001.

[49] S. A. Gardiner, *Quantum Measurement,Quantum Chaos, and Bose-Einstein Condensates*, PhD thesis, Leopold-Franzens-Universität Innsbruck, 2000.

[50] H.-J. Stöckmann, *Quantum Chaos: An Introduction* (Cambridge University Press, 1999).

[51] G. Casati, *Quantum Chaos*, Chaos **6**, 391 (1996).

[52] M. B. d'Arcy, *Quantum Chaos in Atom Optics*, PhD thesis, Balliol College, University of Oxford, 2002.

[53] W. H. Zurek and J. P. Paz, Phys. Rev. Lett. **72**, 2508 (1994).

[54] H. W. Lee, Phys. Rep. **259**, 147 (1995).

[55] M. V. Berry, Proc. R. Soc. Lond. A **413**, 183 (1987).

[56] M. V. Berry, Physica Scripta **40**, 335 (1989).

[57] F. M. Izrailev, Phys. Rep. **196**, 299 (1990).

[58] U. Smilansky, Physica D **109**, 153 (1997).

[59] O. Bohigas, M. J. Giannoni, and C. Schmit, Phys. Rev. Lett **52**, 1 (1984).

[60] G. Casati, B. V. Chirikov, and D. L. Shepelyansky, Phys. Rep. **154**, 77 (1987).

[61] S. Fishman, D. R. Grempel, and R. E. Prange, Phys. Rev. Lett. **49**, 509 (1982).

[62] P. W. Anderson, Phys. Rev. **109**, 1492 (1958).

[63] R. Graham, M. Schlautmann, and P. Zoller, Phys. Rev. A **45**, R19 (1992).

[64] J. C. Robinson *et al.*, Phys. Rev. Lett. **74**, 3963 (1995).

[65] J. C. Robinson *et al.*, Phys. Rev. Lett. **76**, 3304 (1996).

[66] F. L. Moore, J. C. Robinson, C. Bharucha, P. E. Williams, and M. G. Raizen, Phys. Rev. Lett. **73**, 2974 (1994).

[67] F. L. Moore, J. C. Robinson, C. F. Bharucha, B. Sundaram, and M. G. Raizen, Phys. Rev. Lett. **75**, 4598 (1995).

[68] B. G. Klappauf, W. H. Oskay, D. A. Steck, and M. G. Raizen, Physica D **131**, 78 (1999).

[69] C. F. Bharucha *et al.*, Phys. Rev. E **60**, 3881 (1999).

[70] D. A. Steck, V. Milner, W. H. Oskay, and M. G. Raizen, Phys. Rev. E **62**, 3461 (2000).

[71] V. Milner, D. A. Steck, W. H. Oskay, and M. G. Raizen, Phys. Rev. E **61**, 7223 (2000).

[72] W. H. Oskay, D. A. Steck, and M. G. Raizen, Chaos, Solitons & Fractals **16**, 409 (2003).

[73] H. Ammann, R. Gray, I. Shvarchuck, and N. Christensen, Phys. Rev. Lett. **80**, 4111 (1998).

[74] K. Vant, G. Ball, and N. Christensen, Phys. Rev. E **61**, 5994 (2000).

[75] A. C. Doherty, K. M. D. Vant, G. H. Ball, N. Christensen, and R. Leonhardt, J. Opt. B **2**, 605 (2000).

[76] M. B. d'Arcy, R. M. Godun, M. K. Oberthaler, D. Cassettari, and G. S. Summy, Phys. Rev. Lett. **87**, 074102 (2001).

[77] I. Dana, E. Eisenberg, and N. Shnerb, Phys. Rev. E **54**, 5498 (1996).

[78] B. G. Klappauf, W. H. Oskay, D. A. Steck, and M. G. Raizen, Phys. Rev. Lett. **81**, 4044 (1998).

[79] M. K. Oberthaler, R. M. Godun, M. B. d'Arcy, G .S. Summy, and K. Burnett, Phys. Rev. Lett. **83**, 4447 (1999).

[80] R. M. Godun, M. B. d'Arcy, M. K. Oberthaler, G. S. Summy, and K. Burnett, Phys. Rev. A **62**, 013411 (2000).

[81] M. B. d'Arcy *et al.*, Phys. Rev. E **64**, 056233 (2001).

[82] S. Schlunk *et al.*, Phys. Rev. Lett. **90**, 054101 (2003).

[83] S. Schlunk, M. B. d'Arcy, S. A. Gardiner, and G. S. Summy, Phys. Rev. Lett. **90**, 124102 (2003).

[84] Z.-Y. Ma, M. B. d'Arcy, and S. A. Gardiner, Phys. Rev. Lett. **93**, 164101 (2004).

[85] A. Buchleitner *et al.*, Phys. Rev. Lett. **96**, 164101 (2006).

[86] W. H. Oskay, D. A. Steck, V. Milner, B. G. Klappauf, and M. G. Raizen, Opt. Comm. **179**, 137 (2000).

[87] G. A. Askar'yan, Sov. Phys. JETP **15**, 1088 (1962).

[88] V. Letokhov, JETP Lett. **7**, 272 (1968).

[89] A. Ashkin, Phys. Rev. Lett. **24**, 156 (1970).

[90] A. Ashkin, Phys. Rev. Lett. **40**, 729 (1978).

[91] T. W. Hänsch and A. L. Schawlow, Opt. Comm. **13**, 68 (1975).

[92] D. Wineland and H. Dehmelt, Bull. Am. Phys. Soc. **20**, 637 (1975).

[93] V. Letokhov, V. Minogin, and B. Pavlik, Opt. Comm. **19**, 72 (1976).

[94] J. V. Prodan and W. D. Phillips, Prog. Quant. Electr. **8**, 231 (1984).

[95] W. Ertmer, R. Blatt, J. Hall, and M. Zhu, Phys. Rev. Lett. **54**, 996 (1985).

[96] W. D. Phillips, J. Prodan, and H. J. Metcalf, J. Opt. Soc. Am. B **2**, 1751 (1985).

[97] S. Chu, L. Hollberg, J. E. Bjorkholm, A. Cable, and A. Ashkin, Phys. Rev. Lett. **55**, 48 (1985).

[98] P. D. Lett *et al.*, Phys. Rev. Lett. **61**, 169 (1988).

[99] P. D. Lett *et al.*, J. Opt. Soc. Am. B **6**, 2084 (1989).

[100] D. S. Weiss, E. Riis, Y. Shevy, P. J. Ungar, and S. Chu, J. Opt. Soc. Am. B **6**, 2072 (1989).

[101] A. Aspect, E. Arimondo, R. Kasier, N. Vansteenkiste, and C. Cohen-Tannoudji, Phys. rev. Lett. **61**, 826 (1988).

[102] M. Kasevich and S. Chu, Phys. Rev. Lett. **69**, 1741 (1992).

[103] E. L. Raab, M. Prentiss, A. Cable, S. Chu, and D. E. Pritchard, Phys. Rev. Lett. **59**, 2631 (1987).

[104] M. L. Bellac, *Quantum Physics* (Cambridge University Press, New York, 2006).

[105] Claude Cohen-Tannoudji and Jacques Dupont, *Atom-photon Interactions : Basic Processes and Applications* (J. Wiley, 1992).

[106] P. S. Jessen and I. H. Deutsch, Adv. Atom. Mol. Opt. Phys **37**, 95 (1996).

[107] K. B. Davis *et al.*, Phys. Rev. Lett. **75**, 3969 (1995).

[108] S. Franke-Arnold *et al.*, Optics Express **15**, 8620 (2007).

[109] R. Bach, K. Burnett, M. B. d'Arcy, and S. A. Gardiner, Phys. Rev. A **71**, 033417 (2005).

[110] J. Reslen, C. E. Creffield, and T. S. Monteiro, Phys. Rev. A **77**, 043621 (2008).

[111] J. Hecker Denschlag *et al.*, J. Phys. B **35**, 3095 (2002).

[112] W. H. Oskay, D. A. Steck, B. G. Klappauf, and M. G. Raizen, Laser Physics **9**, 265 (1999).

[113] N. W. Ashcroft and N. D. Mermin, *Solid State Physics* (Brooks/Cole, 1975).

[114] S. Fishman, I. Guarneri, and L. Rebuzzini, Phys. Rev. Lett. **89**, 084101 (2002).

[115] S. Fishman, I. Guarneri, and L. Rebuzzini, J. Stat. Phys. **110**, 911 (2003).

[116] E. Hecht, *Optics* (Addison-Wesley, San Francisco, 2002).

[117] C. Ryu *et al.*, Phys. Rev. Lett. **96**, 160403 (2006).

[118] J. F. Kanem, S. Maneshi, M. Partlow, M. Spanner, and A. M. Steinberg, Phys. Rev. Lett. **98**, 083004 (2007).

[119] A. Tonyushkin and M. Prentiss, Phys. Rev. A **78**, 053625 (2008).

[120] A. Tonyushkin, S. Wu, and M. Prentiss, Phys. Rev. A **79**, 051402(R) (2009).

[121] M. Abramowitz and I. A. Stegun, *Handbook of Mathematical Functions with Formulas, Graphs, and Mathematical Tables* (U.S. Government Printing Office, Washington, 1964).

[122] I. Guarneri, L. Rebuzzini, and S. Fishman, Nonlinearity **19**, 1141 (2006).

[123] I. Dana and V. Roitberg, Phys. Rev. E **76**, 015201(R) (2007).

[124] B. C. Berndt and R. J. Evans, Bull. Am. Math. Soc. **5**, 107 (1981).

[125] M. V. Berry and J. Goldberg, Nonlinearity **1**, 1 (1988).

[126] V. Armitage and A. Rogers, J. Phys. A **33**, 5593 (2000).

[127] M. Gilowski *et al.*, Phys. Rev. Lett. **100**, 030201 (2008).

[128] T. J. Rivlin, *The Chebyshev Polynomials* (Wiley, New York, 1974).

[129] J. C. Mason and D. C. Handscomb, *Chebyshev Polynomials* (Chapman & Hall, Boca Raton, 2003).

[130] T. M. Apostol, *Introduction to Analytic Number Theory* (Springer-Verlag, New York, 1976).

[131] J. V. Uspensky, *Introduction to Mathematical Probability*, 1st ed. ed. (McGraw-Hill, New York, 1937).

[132] C. W. Gardiner, *Handbook of Stochastic Methods*, 2nd ed. (Springer, Berlin, 1996).

[133] F. L. Moore, J. C. Robinson, C. F. Bharucha, B. Sundaram, and M. G. Raizen, Phys. Rev. Lett. **75**, 4698 (1995).

[134] D. A. Steck, W. H. Oskay, and M. G. Raizen, Science **293**, 274 (2001).

[135] C. Ryu *et al.*, Phys. Rev. Lett. **96**, 160403 (2006).

[136] I. S. Gradshteyn and I. M. Ryzhik, *Table of Integrals, Series, and Products*, Seventh ed. (Academic Press, 2007).

[137] M. Sadgrove, M. Horikoshi, T. Sekimura, and K. Nakagawa, Eur. Phys. J. D **45**, 229 (2007).

[138] J.-A. Currivan, A. Ullah, and M. D. Hoogerland, Euro. Phys. Lett. **85**, 30005 (2009).

[139] S. J. Wu, A. Tonyushkin, and M. Prentiss, Phys. Rev. Lett. **103**, 034101 (2009).

[140] D. Bouwmeester *et al.*, Nature **390**, 575 (1997).

[141] A. Aspect, P. Grangier, and G. Roger, Phys. Rev. Lett. **49**, 91 (1982).

[142] Q. J. Chen, J. Stajic, S. Tan, and K. Levin, Phys. Rep. **412**, 1 (2005).

[143] S. Viefers, J. Phys.-Cond. Matt. **20**, 123202 (2008).

[144] S. Levy, E. Lahoud, I. Shomroni, and J. Steinhauer, Nature **449**, 579 (2007).

[145] M. Albiez *et al.*, Phys. Rev. Lett. **95**, 010402 (2005).

[146] P. Mandel *et al.*, Nature **425**, 937 (2003).

[147] K. E. Strecker, G. B. Partridge, A. G. Truscott, and R. G. Hulet, Nature **417**, 150 (2002).

[148] L. Khaykovich *et al.*, Science **296**, 1290 (2002).

[149] S. Burger *et al.*, Phys. Rev. Lett. **83**, 5198 (1999).

[150] A. L. Fetter and A. A. Svidzinsky, J. Phys.Condens.Matt. **13**, R135 (2001).

[151] M. R. Matthews *et al.*, Phys. Rev. Lett. **83**, 2498 (1999).

[152] M. Horikoshi and K. Nakagawa, Phys. Rev. A **74**, 031602(R) (2006).

[153] Y.-J. Wang *et al.*, Phys. Rev. Lett. **94**, 090405 (2005).

[154] J. A. Stickney and A. A. Zozulya, Phys. Rev. A **66**, 053601 (2002).

[155] E. Timmermans, P. Tommasini, M. S. Hussein, and A. Kerman, Phys. Rep. **315**, 199 (1999).

[156] C. Chin, R. Grimm, P. Julienne, and E. Tiesinga, Rev. Mod. Phys. **82**, 1225 (2010).

[157] W. Hänsel, J. Reichel, P. Hommelhoff, and T. W. Hänsch, Phys. Rev. A **64**, 063607 (2001).

[158] J. Stenger *et al.*, Phys. Rev. Lett. **82**, 2422 (1999).

[159] I. Bloch, T. W. Hänsch, and T. Esslinger, Phys. Rev. Lett. **82**, 3008 (1999).

[160] A. J. Leggett, Rev. Mod. Phys. **73**, 307 (2001).

[161] F. Dalfovo, S. Giorgini, L. P. Pitaevskii, and S. Stringari, Rev. Mod. Phys. **71**, 463 (1999).

[162] W. Ketterle, Rev. Mod. Phys. **74**, 1131 (2002).

[163] E. A. Cornell and C. E. Wieman, Rev. Mod. Phys. **74**, 875 (2002).

[164] J. F. Allen, Nature **141**, 75 (1938).

[165] P. Kapitza, Nature **141**, 74 (1938).

[166] C. Ryu *et al.*, Phys. Rev. Lett. **99**, 260401 (2007).

[167] J. Williams, R. Walser, J. Cooper, E. Cornell, and M. Holland, Phys. Rev. A **59**, R31 (1999).

[168] D. S. Jin, J. R. Ensher, M. R. Matthews, C. E. Wieman, and E. A. Cornell, Phys. Rev. Lett. **77**, 420 (1996).

[169] M. Kasevich *et al.*, Phys. Rev. Lett. **66**, 2297 (1991).

[170] O. Carnal and J. Mlynek, Phys. Rev. Lett. **2689**, 66 (1991).

[171] D. W. Keith, C. R. Ekstrom, Q. A. Turchette, and D. E. Pritchard, Phys. Rev. Lett. **2693**, 66 (1991).

[172] M. R. Andrews *et al.*, Science **275**, 637 (1997).

[173] E. M. Rasel, M. K. Oberthaler, H. Batelaan, J. Schmiedmayer, and A. Zeilinger, Phys. Rev. Lett. **75**, 2633 (1995).

[174] T. Schumm *et al.*, Nat. Phys. **57**, 1 (2005).

[175] F. Riehle, Th. Kisters, A. Witte, J. Helmcke, and C. J. Bordé, Phys. Rev. Lett. **67**, 177 (1991).

[176] A. Peters, K. Y. Chung, and S. Chu, Nature **400**, 6747 (1999).

[177] Y. Shin *et al.*, Phys. Rev. Lett. **050405**, 92 (2004).

[178] T. L. Gustavson, A. Landragin, and M. A. Kasevich, Class. Quantum. Grav. **17**, 2385 (2000).

[179] D. J. Dayon, J. R. E. Toland, and C. P. Search, J. Phys. B **43**, 115302 (2010).

[180] D. S. Weiss, B. C. Young, and S. Chu, Phys. Rev. Lett. **2706**, 70 (1993).

[181] D. S. Durfee, Y. K. Shaham, and M. A. Kasevich, Phys. Rev. Lett. **97**, 240801 (2006).

[182] S. Wu, E. Su, and M. Prentiss, Phys. Rev. Lett. **99**, 173201 (2007).

[183] J. H. T. Burke and C. A. Sackett, Phys. Rev. A **80**, 061603(R) (2009).

[184] M. Fattori *et al.*, Phys. Rev. Lett. **080405**, 100 (2008).

[185] R. J. Sewell *et al.*, J. Phys. B **43**, 051003 (2010).

[186] O. Garcia, D. Deissler, K. J. Hughes, J. M. Reeves, and C. A. Sackett, Phys. Rev. A **74**, 031601(R) (2006).

[187] M. Holland, K. Burnett, C. Gardiner, J. I. Cirac, and P. Zoller, Phys. Rev. A **54**, R1757 (1996).

[188] R. J. Ballagh, K. Burnett, and T. F. Scott, Phys. Rev. Lett. **78**, 1607 (1997).

[189] S. Boxio *et al.*, Phys. Rev. Lett. **101**, 040403 (2008).

[190] D. S. Hall, M. R. Matthews, J. R. Ensher, C. E. Wieman, and E. A. Cornell, Phys. Rev. Lett. **81**, 1539 (1998).

[191] G. Modugno, F. Riboli, G. Roati, and M. Inguscio, Phys. Rev. Lett. **89**, 190404 (2002).

[192] S. B. Papp, J. M. Pino, and C. E. Wieman, Phys. Rev. Lett. **101**, 040402 (2008).

[193] J. Stenger *et al.*, Nature **396**, 345 (1998).

[194] D. M. Stamper-Kurn *et al.*, Phys. Rev. Lett. **80** (1998).

[195] S. Ishino, H. Takeuchi, and M. Tsubota, arXiv:1006.4488v1.

[196] M. Trippenbach, K. Góral, K. Rzążewski, B. Malomed, and Y. B. Band, J. Phys. B **33**, 4017 (2000).

[197] P. Wang, R-B. Li, H. Yan, J. Wang, and M-S. Zhan, Chin. Phys. Lett. **24**, 27 (2007).

[198] P. M. Baker *et al.*, Phys. Rev. A **80**, 063615 (2009).

[199] P. F. Griffin, E. Riis, and A. S. Arnold, Phys. Rev. A **77**, 051402 (2008).

[200] A. S. Arnold, J. Phys. B , 37 (2004).

[201] A. S. Arnold, C. S. Garvie, and E. Riis, Phys. Rev. A **73**, 041606 (2006).

[202] S. Gupta, K. W. Murch, K. L. Moore, T. P. Purdy, and D. M. Stamper-Kurn, Phys. Rev. Lett. **95**, 143201 (2005).

[203] J. A. Sauer, M. D. Barrett, and M. S. Chapman, Phys. Rev. Lett. **87**, 270401 (2001).

[204] E. J. Post, Rev. Mod. Phys. **39**, 475 (1967).

[205] E. Varoquaux and G. Varoquaux, Physics-Uspekhi **51**, 205 (2008).

[206] S. E. Olson, E. Spencer, M. L. Terraciano, M. Bashkansky, and F. K. Fatemi, Phys. Rev. A **061404**, 76 (2007).

[207] N. Houston, E. Riis, and A. S. Arnold, J. Phys. B **41**, 211001 (2008).

[208] W. H. Heathcote, E. Nugent, B. T. Sheard, and C. J. Foot, New J. Phys. **10** (2008).

[209] K. Henderson, C. Ryu, C. MacCormick, and M. G. Boshier, New J. Phys. **11**, 043030 (2009).

[210] V. B. Gostev, V. S. Mineev, and A. R. Frenkin, Russian Physics Journal **30** (1987).

[211] E. Tiesinga *et al.*, J. Res. Natl. Inst. Stand. Technol. **505**, 101 (1996).

[212] P. A. Altin *et al.*, Phys. Rev. A **012713**, 81 (2010).

[213] H. J. Lewandowski, *Coherences and correlations in an ultracold Bose gas*, PhD thesis, University of Colorado, 2005.

[214] K. T. Kapale and J. P. Dowling, Phys. Rev. Lett. **95** (2005).

[215] L. Salasnich, A. Parola, and L. Reatto, Phys. Rev. A **59**, 2990 (1999).

[216] L. D. Carr, C. W. Clark, and W. P. Reinhardt, Phys. Rev. A **62**, 063610 (2000).

[217] R. Kanamoto, L. D. Carr, and M. Ueda, Phys. Rev. Lett. **100** (2008).

[218] A. Lenef *et al.*, Phys. Rev. Lett. **760**, 78 (1997).

[219] S. Dimopoulos, P. W. Graham, J. M. Hogan, and M. A. Kasevich, Phys. Rev. D **78**, 041003 (2008).

[220] S. Thanvanthri, K. T. Kapale, and J. P. Dowling, arXiv:0907.1138v1.

[221] T. L. Gustavson, P. Bouyer, and M. A. Kasevich, Phys. Rev. Lett. **78**, 2046 (1997).

[222] W. H. Press, S. A. Teukolsky, W. T. Vetterling, and B. P. Flannery, *Numerical Recipes in Fortran* (Cambridge University Press, Cambridge, 1992).

[223] A. D. Martin, *Theoretical Studies of Bright Solitons in Trapped Atomic Bose-Einstein Condensates*, PhD thesis, Durham University, 2008.

[224] N. Parker, *Numerical Studies of Vortices and Dark Solitons in Atomic Bose-Einstein Condensates*, PhD thesis, Durham University, 2004.